

**Investigations into the fundamentals of gas-phase and  
gas-surface chemistry prevalent in growth of  
Chemical Vapour Deposited diamond films**

Andrew Cheesman, July 2006

A dissertation submitted to the University of Bristol in accordance with the requirements of the degree of Doctor of Philosophy in the Faculty of Science.

# Abstract

This thesis reports studies of fundamental gas-phase chemistry within Hot Filament (HF) and microwave plasma enhanced chemical vapour deposition (CVD) reactors used for depositing diamond as well as computational investigations into the incorporation of gas-phase species, present within the CVD environment, into a growing {100} diamond surface.

Resonance enhanced multiphoton ionisation studies of atomic boron and atomic hydrogen in HF activated  $B_2H_6 / CH_4 / H_2$  gas mixtures are described. These results suggest that boron does not form a stable gas-phase reservoir species with borane ( $B_2H_y$ ) species and only combines with carbon species (when present) in cooler regions of the reactor. The physical properties of the tantalum filament, particularly its surface are considered to have a major influence on the gas-phase  $BH_x$  concentrations.

A high pressure CVD microwave reactor has been installed and its operation optimised. Under base operating conditions, Cavity Ringdown Spectroscopy measurements of  $C_2$  rotational temperature show the plasma temperature to be  $3520 \pm 260$  K and  $C_2(a, v=0)$  column densities are found to be  $\sim 3.6 \times 10^{12} \text{ cm}^{-2}$ .  $C_2(a)$  column and number densities have been calculated as a function of process conditions.

$CH_4$  and  $C_2H_2$  molecules, and their interconversion, have been monitored by line-of-sight single pass absorption methods, as a function of process conditions (e.g. choice of input hydrocarbon ( $CH_4$  or  $C_2H_2$ ), hydrocarbon mole fraction, total gas pressure, and applied microwave power) using a quantum cascade laser.

Computational studies have focussed upon the addition and loss processes of gaseous methyl and boron hydride ( $BH_x$ ) radical species to a DFT model of the {100} diamond surface. Mechanisms for direct insertion of surface bound BH (and B) species into a growing {100} face of diamond have been identified, as has an alternative ring opening / closing sequence for incorporating BH.

Studies of the incorporation of methyl radical upon the {100} surface have been expanded by the use of a QM / MM approach.

# **AUTHOR'S DECLARATION**

I declare that the work in this dissertation was carried out in accordance with the Regulations of the University of Bristol. The work is original except where indicated by special reference in the text and no part of the dissertation has been submitted for any other degree. Any views expressed in the dissertation are those of the author and in no way represent those of the University of Bristol. The dissertation has not been presented to any other University for examination either in the United Kingdom or overseas.

Andrew Cheesman

## Acknowledgements

I would like to thank Mike for being a fantastic supervisor, and for being so patient with reading drafts of the various chapters. I would like to acknowledge Jeremy Harvey for all the help that he has provided to the computational side of the work, especially with the creation of the QM / MM program. I am indebted to James Smith, Keith Rosser, the Bristol University Diamond Group (Budgies) and the Mechanical Workshop for all their help, patience and ideas with all the practical aspects of the work contained within the thesis. I would like to thank Joe Dodson and John Brandon from Element Six Ltd for their assistance with the high pressure microwave reactor and many helpful discussions.

The Snowplains community have been excellent in helping me with randomness ([www.snowplains.org](http://www.snowplains.org)). Caffeine sustaining the creation of this thesis has been provided by the most excellent Coffee dude at a fair cup ([www.afaircup.com](http://www.afaircup.com))

And finally Samm : Szerelek.

# Contents

Contents . . . . .	iv
List of Figures . . . . .	v
<b>1 Introduction</b>	<b>1</b>
1.1 Diamond structure and properties . . . . .	1
1.2 Diamond Synthesis . . . . .	4
1.3 Chemical Vapour Deposition of Diamond . . . . .	5
1.3.1 Gas-phase Chemistry . . . . .	6
1.3.2 Hot Filament Reactors . . . . .	7
1.3.3 Microwave Plasma Reactors . . . . .	8
1.3.4 DC Arc-jet Reactors . . . . .	11
1.4 CVD Growth Mechanisms . . . . .	13
1.4.1 Growth species . . . . .	13
1.4.2 Growing surfaces . . . . .	14
1.4.3 Growth on the {100} surface . . . . .	15
1.4.4 Growth on other diamond surfaces . . . . .	21
1.4.5 Etching . . . . .	24
1.5 Defects in Diamond . . . . .	26
1.5.1 Doping of Diamond . . . . .	28
1.5.2 p-type doping . . . . .	29
1.5.3 n-type doping . . . . .	30
1.5.4 Application of dopant technology . . . . .	32
1.6 Aims . . . . .	32
Bibliography . . . . .	33

<b>2</b>	<b>Resonance Enhanced Multiphoton Ionisation studies of atomic Boron in B<sub>2</sub>H<sub>6</sub> / H<sub>2</sub> and B<sub>2</sub>H<sub>6</sub> / CH<sub>4</sub> / H<sub>2</sub> gas mixtures relevant to Boron doped CVD diamond growth</b>	<b>42</b>
2.1	Introduction . . . . .	43
2.1.1	History of Borane research . . . . .	43
2.1.2	The properties of Boranes . . . . .	43
2.2	Resonance Enhanced Multiphoton Ionisation (REMPI) . . . . .	47
2.2.1	Theory . . . . .	47
2.2.2	Previous HF CVD REMPI Studies . . . . .	48
2.2.3	Boron REMPI . . . . .	49
2.3	Experimental . . . . .	50
2.4	Results . . . . .	52
2.4.1	(1+1) REMPI of Boron Atoms . . . . .	52
2.4.2	(2+1) REMPI of Boron Atoms . . . . .	53
2.5	Conclusions . . . . .	64
	Bibliography . . . . .	65
<b>3</b>	<b>BH<sub>x</sub> Addition to the {100} surface of Diamond.</b>	<b>68</b>
3.1	Introduction . . . . .	68
3.1.1	<i>Ab-Initio</i> Computational Chemistry Theory . . . . .	68
3.1.2	Density functional theory . . . . .	72
3.1.3	Potential Energy Surface . . . . .	75
3.1.4	Thermodynamics . . . . .	75
3.1.5	Transition State Theory (TST) . . . . .	76
3.2	Method . . . . .	77
3.3	Results . . . . .	78

3.3.1	Boron addition to the cluster surface . . . . .	79
3.3.2	Boron insertion into the diamond surface . . . . .	82
3.3.3	Loss processes from the diamond surface . . . . .	85
3.3.4	Conclusions . . . . .	90
	Bibliography . . . . .	92
<b>4</b>	<b>Quantum Mechanical / Molecular Mechanical Studies of Diamond growth</b>	<b>94</b>
4.1	Introduction . . . . .	95
4.1.1	Molecular Mechanics . . . . .	95
4.1.2	Quantum Mechanics / Molecular Mechanics . . . . .	98
4.1.3	Previous Work . . . . .	101
4.2	Experimental. . . . .	107
4.3	Results & Discussions . . . . .	110
4.3.1	Initial Tests . . . . .	111
4.3.2	Incorporation into the reconstructed surface carbon-carbon bond. . . . .	114
4.3.3	The dimer trough bridging mechanism . . . . .	124
4.3.4	New row nucleation . . . . .	136
4.3.5	Surface carbon migration reactions . . . . .	141
4.4	Conclusions . . . . .	147
	Bibliography . . . . .	148
<b>5</b>	<b>Preliminary diagnostic studies of a high pressure microwave CVD dia- mond reactor.</b>	<b>150</b>
5.1	Spectroscopy . . . . .	150
5.1.1	Optical Emission Spectroscopy (OES) . . . . .	158
5.1.2	Absorption Spectroscopy . . . . .	158

5.1.3	Cavity Ring-Down Spectroscopy . . . . .	159
5.1.4	Applying spectroscopy to plasmas used in Diamond CVD .	161
5.2	Experimental construction . . . . .	164
5.3	Optimisation of process conditions for CVD diamond growth in CRDS Microwave Reactor by the Taguchi method . . . . .	165
5.3.1	Identification of quality control . . . . .	166
5.3.2	Design of experimental conditions and control parameters .	167
5.3.3	Data Analysis & Predictions . . . . .	169
5.4	Optical Emission Spectroscopy . . . . .	173
5.4.1	Experimental Method . . . . .	173
5.4.2	Results . . . . .	173
5.5	Cavity Ring-Down spectroscopy . . . . .	177
5.5.1	Experiment . . . . .	177
5.5.2	Results . . . . .	178
5.6	Initial thermodynamical and kinetic modelling of gas-phase chem- ical processes . . . . .	187
5.7	Conclusions . . . . .	190
	Bibliography . . . . .	191
<b>6</b>	<b>Monitoring of CH<sub>4</sub> and C<sub>2</sub>H<sub>2</sub> column densities in CH<sub>4</sub> / Ar / H<sub>2</sub> and C<sub>2</sub>H<sub>2</sub> / Ar / H<sub>2</sub> gas mixtures in the microwave CVD reactor using an Infrared Quantum Cascade Laser</b>	<b>194</b>
6.1	Introduction . . . . .	195
6.2	Experimental Details . . . . .	198
6.3	Results . . . . .	199
6.4	Discussion . . . . .	214
6.5	Conclusions . . . . .	218

Bibliography . . . . .	219
<b>Appendices</b>	<b>221</b>
<b>A Coupled cluster calculation of boron-carbon bond fission reaction</b>	<b>221</b>
<b>B Optimised structures for DFT cluster models for the incorporation of CH<sub>3</sub> and BH<sub>x</sub> into a diamond surface</b>	<b>223</b>
<b>C Canonical Transition State Theory rate coefficients for inclusion of carbon and boron species into the {100} diamond reconstructed surface</b>	<b>245</b>
<b>D Thermochemical Data for BH<sub>x</sub>, x = 0 – 4</b>	<b>248</b>
<b>E Raman spectroscopy of thin diamond films grown for the Taguchi optimisation of the CVD microwave plasma reactor</b>	<b>254</b>
<b>F Photos of Plasma ball as a function of process conditions</b>	<b>264</b>
Bibliography . . . . .	268

## List of Figures

1.1	Elemental forms of $sp^2$ carbon: (a) graphite, showing the layer structure; (b) $C_{60}$ molecule . . . . .	2
1.2	The unit cell of diamond with the corner atom removed for clarity . . . . .	2
1.3	Major morphologies of diamond with carbon-hydrogen bonds terminating the growth direction indicated. . . . .	3
1.4	The phase diagram for elemental carbon from ref [3] . . . . .	4
1.5	The growth of polycrystalline diamond films from isolated nucleation sites from ref [12] . . . . .	5
1.6	The systematic diagram of the HF reactor . . . . .	8
1.7	The schematic diagram of a microwave reactor . . . . .	9
1.8	The change in morphology from polycrystalline diamond (a) to UNCD (b) by increasing the percentage of Ar in a $CH_4 / H_2 / Ar$ gas-phase plasma, from ref [39] . . . . .	10
1.9	Reactions occurring with the DC Arc-Jet torch head from ref [43]. Cathode degradation is shown by the emission of metal atoms, M, from the surface. . . . .	11
1.10	A two head CVD DC arc-jet set up for Cavity Ring down Spectroscopy from ref [45]. . . . .	12
1.11	Idiomorphic crystal shapes for different values of the growth parameter $\alpha$ . The arrows indicate the the direction of fastest growth (from ref [59]) . . . . .	15
1.12	SEMs of $\{100\}$ cubic diamond planes from ref [30] . . . . .	16
1.13	Schematic of epitaxial growth: (a) Hillock growth upon a well-aligned sample from ref [61] (b) Formation of a single domain surface for a mis-aligned sample from ref [16]. . . . .	16
1.14	Surface dimer reconstructions arrangement for Group XIV semiconductors showing the (a) Row arrangement (b) Staggered dimer arrangement. Adapted from ref [65] . . . . .	17

1.15	(a) Scanning tunnelling Microscopy (STM) image of the topography of the hydrogen terminated {100} diamond reconstruction surface from ref [63] : (b) a proposed mechanism for formation of isolated reconstructed surface dimers for the hydrogen terminated {100} surface from ref [71] (energy in kcal mol <sup>-1</sup> ). . . . .	18
1.16	Cross section through the {100} plane showing the dimer reconstruction (A) and the trough (B) insertion points. . . . .	19
1.17	Mechanism for i) Hydrogen abstraction and surface activation (A → B) ii) Carbon incorporation into the diamond {100} surface (C → G). . . . .	20
1.18	The HH mechanism, showing the conversion of BCN (A) to adamantane (F) modelling the incorporation of an adsorbed methyl radical across a dimer trough from ref [79]. . . . .	21
1.19	The (2×1) reconstruction for the {111} surface, from ref [91] . . . . .	22
1.20	Suggested pathway of CH <sub>y</sub> and C <sub>2</sub> H <sub>y</sub> incorporation into the {111} diamond surface (modified from ref [94] . . . . .	23
1.21	(a) Addition of two methyl radicals to the {110} diamond surface from ref [56]; (b) Proposed fate of the adsorbed ethyl chain from ref [56]; (c) Proposed C <sub>2</sub> incorporation into the {110} diamond surface from ref [104] . . . . .	25
1.22	Figure showing the twinning effect at the atomic level with (a) regular and (b) eclipsed position. Figure reproduced from ref [106]. . . . .	27
1.23	Figure showing the twinning effect upon the crystal structures are (a) the regular and (b) the twinned stacking pattern. The chair and boat conformations of cyclohexane structure are highlighted within the appropriate stacking pattern. Figure reproduced from ref [106]. . . . .	27
1.24	Common interstitial geometries (a) Hexagonal and tetrahedral holes; (b) The bond centred form; (c) The {100} split interstitial, showing the change in geometry, all from ref [108]. . . . .	28
1.25	The band structures of diamond showing the energy levels of dopants. All values are in eV and quoted relative to the nearest band. . . . .	29

2.1	Structure of $B_2H_6$ showing the three centre – two electron bridging hydrogen bonds . . . . .	44
2.2	Schematic showing how borane clusters can be generated in the gas phase and upon surfaces and the subsequent interactions between the two phases, from ref [29]. . . . .	46
2.3	Grottrian diagram for atomic boron, showing the possible (1+1) and (2+1) REMPI process . . . . .	48
2.4	Predicted variation in equilibrium constant as a function of temperature for diborane dissociation equation (2.2) and hydrogen abstraction reactions from $BH_x$ , $x = 1 - 3$ species, equation (2.5). . . . .	50
2.5	Experimental setup for REMPI studies of boron atoms in CVD reactor. Two side arms of the reactor have been omitted for clarity. . .	51
2.6	(1+1) REMPI spectra of B atoms in HF reactor at 0.0475 % $B_2H_6$ / $H_2$ , with a $T_{fil}$ of 2273° C at 20 Torr. . . . .	53
2.7	Grottrian diagram showing the competitive processes for atomic boron (1+1) REMPI process. . . . .	54
2.8	$2s^24p^1 \leftarrow 2s^22p^1$ B atom (2+1) REMPI signal of 0.0475% $B_2H_6$ , filament temperature ( $T_{fil}$ ) = 2273 K at 20 Torr and a laser focus at $d = 0.5$ mm from the filament. Red line is a Lorentzian least square fit to the experimental data. . . . .	54
2.9	Fundamental Tests of (2+1) REMPI signal of B Atoms in the HF–CVD environment . . . . .	57
2.10	Graph showing the relationship between the distance between the laser focus and the HF and REMPI signal for boron atoms (laser frequency of $28885.9\text{ cm}^{-1}$ ) and H atoms (laser frequency of $41128.5\text{ cm}^{-1}$ ) with a gas mixture of 0.0475% $B_2H_6$ / $H_2$ with $T_{fil} = 2273$ K. . . . .	58
2.11	Temperature profiling of HF reactor operating with pure $H_2$ and a filament temperature of 2673 K using H atom Doppler broadened line shapes and equation 2.8 to estimate local gas temperature [49]. . .	58
2.12	Filament temperature effect on (2+1) REMPI signal for B atoms ( $28885.9\text{ cm}^{-1}$ ) and H atoms ( $41128.5\text{ cm}^{-1}$ ) for 0.0475% $B_2H_6$ in $H_2$ with a laser focus at $d = 2$ mm from the filament. . . . .	59

2.13	(a) SEM cross section of a borodised filament. (b) the borodised surface showing evidence of localised melting. . . . .	60
2.14	(a) SEM image consistent with borodation of a carborised filament (b) Close up view of the boron carbon interface. . . . .	61
2.15	(a) The relation between % B <sub>2</sub> H <sub>6</sub> and REMPI signal at T <sub>fil</sub> = 2273 K. (b) Correlation between T <sub>fil</sub> and atomic boron REMPI signal for 0.0475% B <sub>2</sub> H <sub>6</sub> : Both recorded in 1 % CH <sub>4</sub> / H <sub>2</sub> gas mixtures with a laser frequency of 28885.6 cm <sup>-1</sup> and a laser focus at d = 2 mm from the filament. . . . .	62
2.16	Correlation between distance between the laser focus and HF and signal for 0.0475% B <sub>2</sub> H <sub>6</sub> in CH <sub>4</sub> / H <sub>2</sub> : laser frequency of 28885.6 cm <sup>-1</sup> and T <sub>fil</sub> = 2273K, 2673K. . . . .	63
3.1	Cross section through a bimolecular PES. . . . .	75
3.2	Mechanism for i) Hydrogen abstraction and surface activation ii) Carbon incorporation into the diamond {100} surface. Process energies (in kJ mol <sup>-1</sup> ) for inter-conversion between the various species via addition and / or elimination reactions as defined in the figure are indicated in italics. . . . .	79
3.3	Figures showing the optimised geometries for the C <sub>9</sub> H <sub>14</sub> cluster with adsorbed (a) BH species (with the empty orbital (LUMO) highlighted) (b) BH <sub>3</sub> species. . . . .	80
3.4	Overview of the reaction pathways for BH <sub>x</sub> addition to, incorporation into, and loss from, the diamond {100} surface. Process energies (in kJ mol <sup>-1</sup> ) for inter-conversion between the various species via addition and/or elimination reactions as defined in the figure are indicated in italics. . . . .	83
3.5	Calculated temperature dependent Gibbs free energies of activation (G <sub>act</sub> ) for selected key steps in the incorporation of BH <sub>x</sub> species into a diamond {100} surface: × insertion of B; * direct insertion of BH; ■ ring opening for BH insertion; ◆ ring closing for BH insertion. Calculated values for the □ ring opening for CH <sub>2</sub> insertion; ◇ ring closing for CH <sub>2</sub> insertion are included for comparison. . . .	84

3.6	$\beta$ -scission reaction pathways leading to a. & b. $\text{HBCH}_2$ or c. $\text{C}_2\text{H}_4$ loss from a diamond $\{100\}$ surface. $\text{HBCH}_2$ loss can occur either via C–C bond fission (a.) or via B–C bond fission (b.). . . . .	87
3.7	Calculated temperature dependent free energies of reaction for dissociation processes at a diamond $\{100\}$ surface. $\blacktriangleright \text{Surf}-\text{BH}_2 + \text{H} \longrightarrow \text{Surf}-\text{BH}_3$ ; $\blacksquare \text{Surf}-\text{BH}_2 + \text{H} \longrightarrow \text{Surf} + \text{BH}_3$ ; $\bullet \text{Surf}-\text{BH}_3 \longrightarrow \text{Surf} + \text{BH}_3$ ; $\blacklozenge \text{Surf}-\text{BH}_3 \longrightarrow \text{Surf}-\text{BH} + \text{H}_2$ ; $\times \text{Surf}-\text{C}_2\text{H}_4 \longrightarrow \text{Surf} + \text{C}_2\text{H}_4$ ; $\triangle \text{Surf}-\text{BHCH}_2 \longrightarrow \text{Surf} + \text{CH}_2\text{BH}$ (Figure 3.6b.); $\nabla \text{Surf}-\text{CH}_2\text{BH} \longrightarrow \text{Surf} + \text{CH}_2\text{BH}$ (Figure 3.6c.) . . . . .	88
4.1	(a) Example showing the bond stretching and angle bending in propane (b) Example of the torsion interaction about the central bond of a hypothetical rotomer of butane. . . . .	96
4.2	QM / MM region splitting examples using $\text{M}(\text{P}(\text{CH}_3)_3)_2$ (a) QM core with hydrogen link atoms (b) The real system (adapted from ref [8]). . . . .	101
4.3	Sketch showing different features for a generic surface from [13]. . . . .	102
4.4	The transformation of an adsorbed $\text{C}=\text{CH}_2$ group into a reconstructed dimer at a $\text{S}_\text{B}$ step from ref [22] . . . . .	105
4.5	Images of $\{100\}$ films during simulated growth at 1200 K (a) without and (b) with etching. Light grey atoms are carbons in the diamond film. The hydrogen atoms are shaded according to their height. Two gray levels (dark grey and white) are used, and cycle every two layers, from ref [26]. . . . .	107
4.6	The QM / MM model for the reconstructed diamond $\{100\}$ surface used for modelling the inclusion of carbon and boron species into the reconstructed dimer bond. QM region highlighted in red. . . . .	109
4.7	The common artifacts upon a growing $\{100\}$ diamond surface. . . . .	110
4.8	Two reactions used to compare the relative energetics of PM3 and B3LYP calculations . . . . .	112
4.9	Recapitulation of Figure 1.17 showing one mechanism by which carbon can be incorporated into the $\{100\}$ surface . . . . .	114

4.10	(a) Figure showing the QM region and the surrounding MM region (truncated for clarity) of structure G from Figure 4.9, (b) The transition state for the post insertion hydrogen abstraction reaction from structure G, Figure 4.9. . . . .	117
4.11	CH <sub>3</sub> bound to a surface site after an initial carbon insertion into a dimer reconstruction. Note the induced displacement from the normal geometries for hydrogen bound to neighbouring dimer reconstructions. . . . .	118
4.12	Recapitulation of mechanism shown in Figure 4.9 . . . . .	120
4.13	Cross sections through QM / MM models showing the MM modifications for modelling the effects on incorporation energetics (a) insertions into a neighbouring reconstructed dimer (b) 1D chain, growing across dimers and troughs. . . . .	122
4.14	Recapitulation of Figure 1.18 showing the mechanism by which carbon can be incorporated into the {100} surface across a dimer row. . . . .	125
4.15	The three environments used for modelling the row bridging mechanism for carbon incorporation: (a) nucleation; (b) propagation; (c) the termination step. The structure shown relates to step D from Figure 4.14 with the QM region highlighted in red. . . . .	126
4.16	(a) The larger QM region used to model the propagation step in the trough bridging mechanism; (b) The “mirrored” arrangement. QM region highlighted in red. . . . .	127
4.17	Surface radical sites investigated for methyl addition in [17] . . . . .	133
4.18	(a) Recapitulation of Figure 1.15(b) showing a proposed intermediate for formation of the dimer reconstruction from ref [43] (b) The transition state of the ring closing reaction (E → F, Figure 4.18(c)) as part of the incorporation of carbon into a dimer reconstruction (left) next to a row of previously incorporated carbons (c) Recapitulation of the ring opening / closing mechanism (Section 4.3.2). . . . .	137

4.19	Proposed mechanism for nucleation of a new dimer reconstruction layer by incorporation of CH <sub>3</sub> . Process energies (in kJ mol <sup>-1</sup> ) for inter-conversion between the various species via addition and/or elimination reactions as defined in the figure are indicated in italics .	139
4.20	The CH <sub>2</sub> surface migration mechanism along a dimer chain from ref [21]. The mechanism is highlighted by optimised QM structures from the relevant IMOMM calculation with the QM atoms represented by spheres and the link hydrogen atoms by sticks. . . . .	143
4.21	The CH <sub>2</sub> surface migration mechanism along a dimer row from ref [21]. The mechanism is highlighted by optimised QM structures from the relevant IMOMM calculation. . . . .	144
4.22	Possible termination step for methyl radical migration along a dimer row. . . . .	146
5.1	Three different ways in which electromagnetic radiation can interact with two energy levels (a) Spontaneous emission (b) Absorption (c) Stimulated emission. Colours are used for identification only. . .	151
5.2	The more commonly observed electronic series of atomic hydrogen [17]. . . . .	163
5.3	The MO electronic structure for the (a) $X^1\Sigma_g^+$ ground state (b) first excited state, $a^3\Pi_u$ , for the C <sub>2</sub> diatomic. Core 1s electrons omitted. .	164
5.4	Photos showing the reverse of a Molybdenum substrate (a) the groove (b) spacer mounted upon a substrate. . . . .	168
5.5	Low resolution optical emission spectra from a 4.4% CH <sub>4</sub> / 7% Ar / balance H <sub>2</sub> plasma generated within the microwave system, sustained at 1.45 kW, measured at a height of 4 mm above the substrate, at pressures of (a) 50 (b) 100 (c) 150 Torr. The H <sub>α</sub> OES signals have been truncated to retain clarity. . . . .	174

5.6	The measured optical emissions from the $C_2$ Swan band, $H_\alpha$ and $H_\beta$ transitions as a function of distance from the substrate (distance = 0 mm) at (a) 50 Torr (b) 100 Torr (c) 150 Torr. All emission spectra were recorded under the standard condition with a gas mixture of 4.4 % $CH_4$ / 7% Ar in a balance of $H_2$ at a total flow rate of 565 sccm with 1.50 kW of microwave power. . . . .	175
5.7	High Resolution optical emission spectrum of the $C_2$ $d^3\Pi_g - a^3\Pi_u$ Swan band emission from a plasma resulting from a 4.4 % $CH_4$ / 7 % Ar in a balance of $H_2$ gas mixture, sustained at 1.45 kW microwave power, at a pressure of 150 Torr. . . . .	176
5.8	(a) Systematic drawing showing CRDS set up (b) experimental apparatus (guiding optics omitted for clarity). . . . .	177
5.9	CRDS spectra of the $C_2$ $d^3\Pi_g - a^3\Pi_u$ origin band under typical operating conditions of power of 1.5 kW, with gas composition of 4.4% $CH_4$ ; 7 % Ar; balance of $H_2$ at a pressure of 150 Torr measured at a distance of $\sim 10$ mm from the substrate. . . . .	179
5.10	A Boltzmann plot comparing $C_2$ line intensity, the calculated line strength and the energy of rotational transitions. The studied plasma is running under the typical operating conditions, with gas composition of 4.4% $CH_4$ ; 7 % Ar; balance of $H_2$ at a pressure of 150 Torr sustained at 1.5 kW. The line of sight column was measured at a distance of $\sim 10$ mm from the substrate. . . . .	180
5.11	CRD spectrum of of a small portion of the $C_2$ $d^3\Pi_g - a^3\Pi_u$ origin band under typical operating conditions, with gas composition of 4.4% $CH_4$ ; 7 % Ar; balance of $H_2$ at a pressure of 150 Torr, maintained with an input power of 1.5 kW. The column probed was a distance of $\sim 10$ mm from the substrate. A PGOPHER simulation of this region of the spectrum, assuming $T_{rot} = 3500$ K, is shown above. . . . .	181

5.12	Variation of $C_2(a)$ column density with (a) % methane (7 % Ar, balance $H_2$ ) and (b) % argon (4.4% $CH_4$ , balance $H_2$ ), at a total pressure 150 Torr (c) total pressure, $p$ , ( $P = 1.5$ kW) and (d) applied microwave power, $P$ , ( $p = 150$ Torr) . The effect of the individual variables was assessed as a deviation from the standard conditions of a gas composition of 4.4% $CH_4$ ; 7 % Ar; balance of $H_2$ at a pressure of 150 Torr sustained at 1.5 kW and the column density measurements were made at a distance of $\sim 10$ mm above the substrate surface. . . . .	183
5.13	Photo of the side view of a plasma operating under standard conditions (i.e gas composition of 4.4% $CH_4$ ; 7 % Ar; balance of $H_2$ at a pressure of 150 Torr sustained at 1.5 kW). The bar shows the path along which the plasma is measured and all subsequent plasma images are scaled to this image. . . . .	184
5.14	Comparison of the variation of $C_2(a)$ number densities from probing on the $J'' = 8$ transition, using the scaled absorption path length $l$ and a fixed $l$ of 30 mm for (a) total pressure, $p$ , (b) applied microwave power and (c) % $CH_4$ . These results were obtained from deviations from the standard conditions of 4.4 % $CH_4$ , 7 % Ar, balance $H_2$ gas mixture at a gas pressure of 150 Torr with an input power of 1.5 kW. Measurements were performed at a distance of $\sim 10$ mm above the substrate surface. . . . .	186
5.15	Calculated (r,z) distribution for (a) gas temperature, $T_g$ (left) and electron distribution (right) (b) hydrogen (left) and $C_2$ (right), within microwave reactor under standard conditions. . . . .	189
6.1	Schematic of the quantum cascade laser energy profile from ref [7] .	197
6.2	Line-of-sight absorption spectra of MW activated 4.4 % $C_2H_2$ 7% Ar / $H_2$ (upper panel) and 8.8% $CH_4$ / 7% Ar / $H_2$ (lower panel) gas mixtures. The carbon fraction, the total flow rate (565 sccm), total pressure (150 Torr), and applied MW power (1.5 kW) are the same in both cases. $C_2H_2$ and $CH_4$ absorptions are present in both spectra, with different relative intensities. Features due to $C_2H_2$ and to $CH_4$ are indicated in the upper and lower panels respectively. Details of these assignments are given in Tables 6.1 & 6.2. . . . .	200

- 6.3 Absorption spectra measured over the range  $1276.2 - 1274.6 \text{ cm}^{-1}$  for (a)  $\text{CH}_4 / \text{Ar} / \text{H}_2$  and (b)  $\text{C}_2\text{H}_2 / \text{Ar} / \text{H}_2$  gas mixtures containing, respectively, C input fractions of 1%, 4.4%, and 8.8%. The respective spectra have been offset vertically, by 0.1 absorbance unit, for clarity. . . . . 203
- 6.4 Semilogarithmic plot showing the temperature dependence of  $S$ , the intensity per molecule in units of  $\text{cm}^{-1} / (\text{molecule cm}^{-2})$  when probing  $\text{C}_2\text{H}_2$  ( $\diamond$ ) via the P (23) line of the  $4_0^1 5_0^1$  band at  $1275.5122 \text{ cm}^{-1}$  and  $\text{CH}_4$  ( $\circ$ ) by the  $4\text{F}_2\text{-}5\text{F}_{1,2}$  transition of the  $4_0^1$  band at  $1275.0417 \text{ cm}^{-1}$  (left-hand axis). Also shown is the ratio of the respective  $S$  (T) values (\*), plotted on a linear scale (right-hand axis). 206
- 6.5 Absorption spectra measured over the range  $1276.2\text{-}1274.6 \text{ cm}^{-1}$  for (a)  $\text{CH}_4 / \text{Ar} / \text{H}_2$  and (b)  $\text{C}_2\text{H}_2 / \text{Ar} / \text{H}_2$  gas mixtures containing 4.4% C input fractions at total gas pressures of 50, 100, and 150 Torr (as indicated at the right-hand end of each spectrum). The respective spectra have each been offset vertically by 0.1 absorbance unit for ease of display. . . . . 208
- 6.6 (a) Example spectra demonstrating the quality of the Lorentzian fits to the  $1275.0417 \text{ cm}^{-1}$  ( $\text{CH}_4$ ) line shapes measured using the 2.2%  $\text{C}_2\text{H}_2 / \text{Ar} / \text{H}_2$  gas mixture at  $p = 100$  and 150 Torr. (b) The pressure dependence of the full width half-maximum (fwhm) values obtained by fitting the  $1275.9585$  ( $\text{C}_2\text{H}_2^\ddagger \triangle$ ),  $1275.5122$  ( $\text{C}_2\text{H}_2 \diamond$ ), and  $1275.0417 \text{ cm}^{-1}$  ( $\text{CH}_4 \circ$ ) line shapes in spectra obtained using the same mixing ratio as in Figure 6.6(a). . . . . 210
- 6.7 Plots showing the  $p$  dependence of the respective  $\text{C}_2\text{H}_2^\ddagger$ ,  $\text{C}_2\text{H}_2$ , and  $\text{CH}_4$  absorbances when using (a) 4.4%  $\text{CH}_4 / \text{Ar} / \text{H}_2$  and (b) 2.2%  $\text{C}_2\text{H}_2 / \text{Ar} / \text{H}_2$  input gas mixtures. . . . . 211

6.8	Absorption spectra measured over the range 1276.2-1274.6 $\text{cm}^{-1}$ , as a function of time (in s, indicated at the right-hand end of each trace) following addition of 4.4% $\text{C}_2\text{H}_2$ (upper traces in each panel) and 8.8% $\text{CH}_4$ (lower traces) to a pre-established Ar / $\text{H}_2$ plasma. Spectra shown in panels a, b, and c (on the following page) were recorded at progressively later times after the instant of hydrocarbon addition to the mixing manifold, and the spectra displayed in any one panel have been coloured and offset vertically for display purposes. . . . .	213
6.9	Plot showing variation of $\text{CH}_4$ ( $\circ$ ), $\text{C}_2\text{H}_2$ ( $\diamond$ ), and $\text{C}_2\text{H}_2^\ddagger$ ( $\triangle$ ) absorbances with time after the introduction (at $t = 0$ s) of 8.8% $\text{CH}_4$ to a pre-established 7% Ar in $\text{H}_2$ plasma and, below, the subsequent fall in these signals from their equilibrium values when the hydrocarbon feed is cut (at $t = 70$ s). . . . .	215
B.1	The optimised geometry for structure A in Figure 3.2 . . . . .	223
B.2	The optimised geometry for structure B in Figure 3.2 . . . . .	225
B.3	The optimised geometry for structure C in Figure 3.2 . . . . .	225
B.4	The optimised geometry for structure D in Figure 3.2 . . . . .	225
B.5	The optimised geometry for structure E in Figure 3.2 . . . . .	229
B.6	The optimised geometry for structure F in Figure 3.2 . . . . .	229
B.7	The optimised geometry for structure G in Figure 3.2 . . . . .	229
B.8	The optimised geometry for surface bound $\text{BH}_3$ on the diamond {100} surface (Figure 3.4) . . . . .	233
B.9	The optimised geometry for surface bound $\text{BH}_2$ on the diamond {100} surface (Figure 3.4) . . . . .	233
B.10	The optimised geometry for surface bound BH on the diamond {100} surface (Figure 3.4) . . . . .	233
B.11	The optimised geometry for surface bound B on the diamond {100} surface (Figure 3.4) . . . . .	234

B.12	The optimised geometry for unsaturated ring opened boron intermediate for boron inclusion on diamond {100} surface (Figure 3.4)	239
B.13	The optimised geometry for boron containing radical intermediate involved in boron inclusion on diamond {100} surface (Figure 3.4)	239
B.14	The optimised geometry for boron containing intermediate involved in boron inclusion on diamond {100} surface (Figure 3.4)	239
B.15	The optimised geometry for atomic boron inclusion on diamond {100} surface (Figure 3.4)	243
E.1	Raman spectra of (a) diamond (b) graphite with insets showing the respective nuclear motions associated with each band, from ref [4].	255
E.2	Raman spectrum of sample 1.	255
E.3	Raman spectrum of sample 2.	256
E.4	Raman spectrum of sample 3.	256
E.5	Raman spectrum of sample 4.	257
E.6	Raman spectrum of sample 5.	257
E.7	Raman spectrum of sample 6.	258
E.8	Raman spectrum of sample 7.	258
E.9	Raman spectrum of sample 8.	259
E.10	Raman spectrum of sample 9.	259
E.11	Raman spectrum of sample 10.	260
E.12	Raman spectrum of sample 11.	260
E.13	Raman spectrum of sample 12.	261
E.14	Raman spectrum of sample 13.	261
E.15	Raman spectrum of sample 14.	262
E.16	Raman spectrum of sample 15.	262
E.17	Raman spectrum of sample 16, with curve fitting highlighted.	263

F.1	Side image of plasma sustained under the standard conditions of a gas composition of 4.4% CH <sub>4</sub> ; 7 % Ar; balance of H <sub>2</sub> at a pressure of 150 Torr sustained at 1.5 kW. . . . .	264
F.2	Side image of plasma sustained with a gas composition of 8.8% CH <sub>4</sub> ; 7 % Ar; balance of H <sub>2</sub> at a pressure of 150 Torr sustained at 1.5 kW. . . . .	265
F.3	Side image of plasma sustained with a gas composition of 2% CH <sub>4</sub> ; 7 % Ar; balance of H <sub>2</sub> at a pressure of 150 Torr sustained at 1.5 kW. . . . .	265
F.4	Side image of plasma sustained with a gas composition of 7 % Ar; balance of H <sub>2</sub> at a pressure of 150 Torr sustained at 1.5 kW. . . . .	265
F.5	Side image of plasma sustained with a gas composition of 4.4% CH <sub>4</sub> , 7 % Ar; balance of H <sub>2</sub> at a pressure of 175 Torr sustained at 1.5 kW. . . . .	266
F.6	Side image of plasma sustained with a gas composition of 4.4% CH <sub>4</sub> , 7 % Ar; balance of H <sub>2</sub> at a pressure of 100 Torr sustained at 1.5 kW. . . . .	266
F.7	Side image of plasma sustained with a gas composition of 4.4% CH <sub>4</sub> , 7 % Ar; balance of H <sub>2</sub> at a pressure of 150 Torr sustained at 1.75 kW. . . . .	266
F.8	Side image of plasma sustained with a gas composition of 4.4% CH <sub>4</sub> , 7 % Ar; balance of H <sub>2</sub> at a pressure of 150 Torr sustained at 1.0 kW. . . . .	267
F.9	Side image of plasma sustained with a gas composition of 4.4% CH <sub>4</sub> , 7 % Ar; balance of H <sub>2</sub> at a pressure of 150 Torr sustained at 1.25 kW. . . . .	267

*“Writing in English is the most ingenious torture  
ever devised for sins committed in previous lives.”*

— James Joyce

*“If it was easy, It would have already been done.”*

— Anon

# Chapter 1

## Introduction

Diamond is an ancient gem material whose plethora of extreme physical properties are only just being industrially realised. This chapter explores the known properties, synthesis methods and growth mechanisms of chemical vapour deposited diamond.

### 1.1 Diamond structure and properties

Atomic carbon has three major elemental forms, graphite, cages (e.g. fullerenes) and diamond. Each allotrope has vastly different properties, due to the ability of carbon to adopt various electronic hybridisation forms by mixing of the valence s and p orbitals.

$sp^2$  carbon atoms typically adopt hexagonal patterns with the non-hybridised carbon p orbital perpendicular to the pattern. Carbon hexagons can be arranged to form a graphitic sheet structure, Figure 1.1(a). The planar arrangement of the  $sp^2$  carbon atoms leads to a distributed  $\pi$  electronic system which enables electronic conduction. 3D isolated cage structures formed from hexagonal and pentagonal carbon rings are found to be stable for structures with more than 60 carbon atoms [1], Figure 1.1(b).

Diamond is a 3D cubic crystal of covalently bound  $sp^3$  carbon, Figure 1.2, with each carbon bound to the four neighbouring atoms.

The carbon atoms are interlocked into a perfect tetrahedral arrangement, with bond lengths of 1.5445 Å and bond angles of  $109^\circ$ , with a point group of  $T_d$  that forms a face centre cubic crystal with local  $O_h^7$  symmetry in the  $Fd\bar{3}m$  space group.

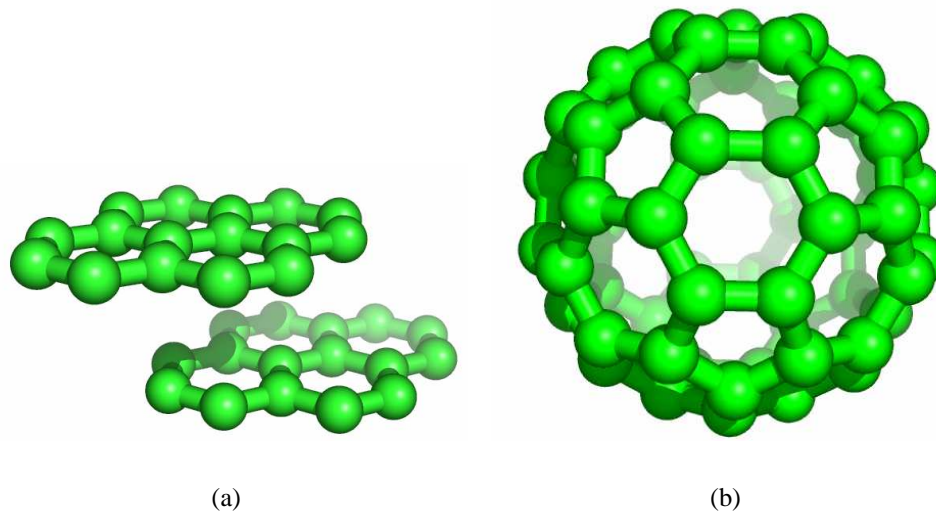


**Figure 1.1:** Elemental forms of  $sp^2$  carbon: (a) graphite, showing the layer structure; (b)  $C_{60}$  molecule

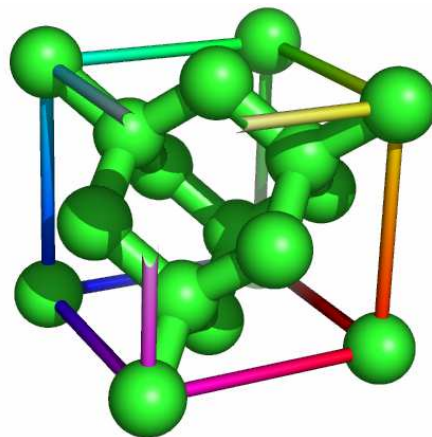


**Figure 1.2:** The unit cell of diamond with the corner atom removed for clarity

The combination of the strong carbon–carbon covalent bonds, rigid geometry and high level of symmetry leads to the physical properties listed in Table 1.1.

In combination with these extreme physical properties, diamond also affords a wide window of optical transparency, from the far IR to UV light (255 nm), making it an ideal material for windows in extreme chemical environments. (There are weak IR absorptions within the small region of 2.5 to 6  $\mu\text{m}$  due to the two phonon absorption). The symmetric nature of diamond means that there are various morphologies which a sample can adopt with the most common planes, identified by

their respective Miller indices, shown in Fig. 1.3

Mechanical hardness	$\sim 90$ GPa
Bulk modulus	$1.2 \times 10^{12}$ N / m <sup>2</sup>
Compressibility	$8.3 \times 10^{-13}$ m <sup>2</sup> / N
Thermal conductivity (Type IIa, 293K)	$2 - 2.2 \times 10^3$ W / m / K
Thermal expansion coefficient (293K)	$0.8 \times 10^{-6}$ / K

**Table 1.1:** Physical properties of diamond from ref [2]

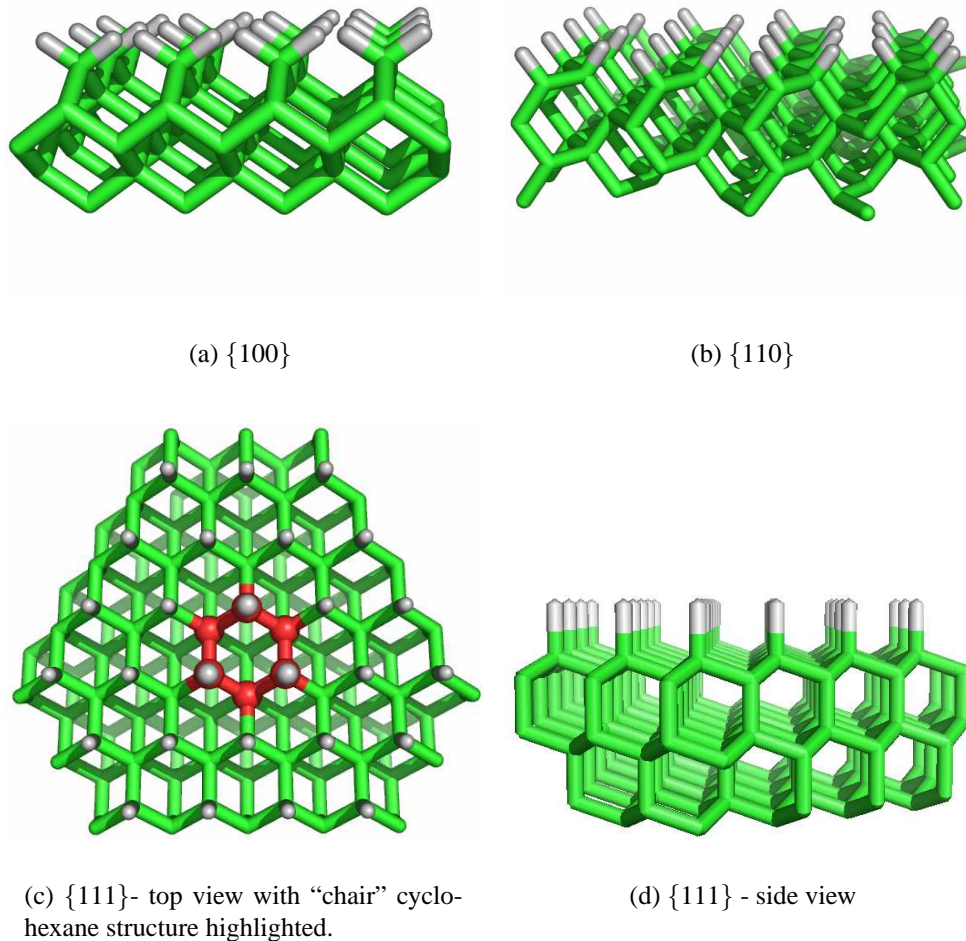


**Figure 1.3:** Major morphologies of diamond with carbon-hydrogen bonds terminating the growth direction indicated.

## 1.2 Diamond Synthesis

Under standard conditions (298 K, 1 atm), graphite is the stable form of carbon and diamond is metastable. There is a small difference in free energies between the two phases ( $2.9 \text{ kJ mol}^{-1}$  [3]) but interconversion is hindered by the presence of a large energy barrier, resulting in the phase diagram for carbon, Figure 1.4. In order to circumvent the large kinetic barrier, diamond growth must occur under conditions where diamond is the preferred product, using non-graphitic reagents.

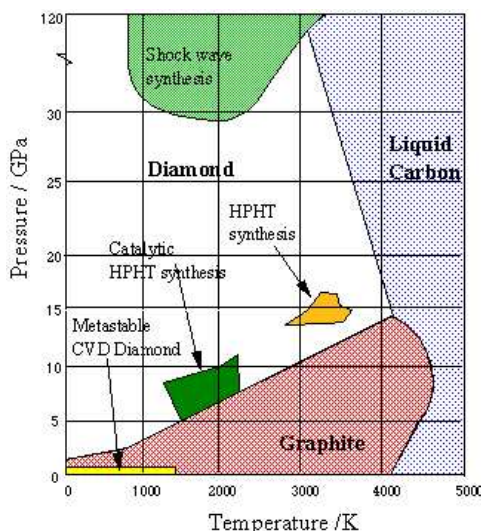


**Figure 1.4:** The phase diagram for elemental carbon from ref [3]

The first successful attempts at synthetic diamond growth were developed as a mimic of geological diamond growth conditions [4], using high pressure and high temperatures (HPHT) to convert graphite to diamond [5]. Small diamond crystallites form under these extreme conditions and this is the major industrial process for producing diamond grits (60 tons; 90% of industrial diamond in 1990 [6]). Catalytic solvents are used to lower the activation energy of dissolving graphite and hence reduce the extreme growth conditions to more feasible and viable levels. These solvents can be molten metal (Group VIII metals [5]) or a molten metal carbide isoelectronic with group VIII elements [7]. There are numerous factors which affect the growth quality of HPHT diamonds [8] and the mechanism for conversion from the liquid carbon to diamond phase is not well known [9]. Choundary *et al.* have produced an excellent review of the development of HPHT synthesis techniques for the purpose of growing larger single crystals of diamond [10].

### 1.3 Chemical Vapour Deposition of Diamond

The fundamental principle of Chemical Vapour Deposition (CVD) growth of diamond is to use gas-phase carbon species to combine in a stepwise manner on a substrate to form a diamond lattice, thus avoiding the large interconversion barrier between graphite and diamond. The process has been widely tried throughout the history of chemistry, with major progress occurring in the 1950s, and the technique being realised with the use of carbon-containing gas precursors in the 1980s [11].

CVD growth can occur upon a single diamond seed (homoepitaxial growth) and polycrystalline films can be formed from growth from multiple nucleation sites upon non-diamond substrates, Figure 1.5. The polycrystalline diamond films have many similarities to single crystal samples but the formation of grain boundaries can introduce subtle bulk mechanical and electronic defects.

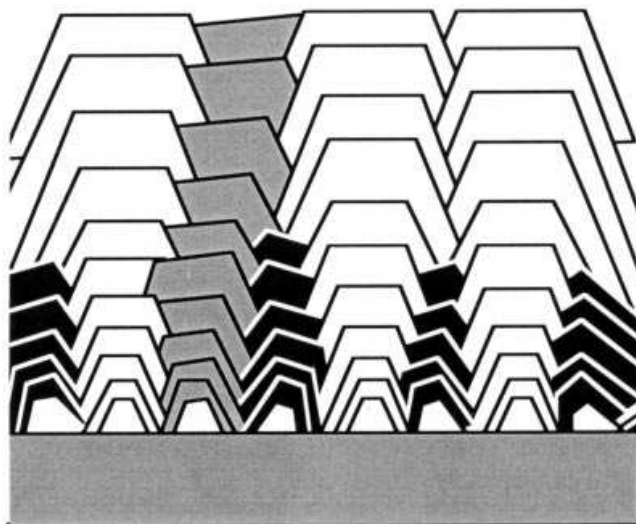


**Figure 1.5:** The growth of polycrystalline diamond films from isolated nucleation sites from ref [12]

Successful CVD growth processes have three fundamental stages for incorporating gaseous material into the growing solid phase. These can be loosely classified as activation of the gaseous reagents, gas-phase reactions and diffusion of reagents onto the surface, where further chemistry may occur, and growth of the solid. Despite the wide variations in methods of activation of the gaseous precursors, which strongly relate to the design of the particular reactor, all diamond CVD gas-phase chemistry is similar.

### 1.3.1 Gas-phase Chemistry

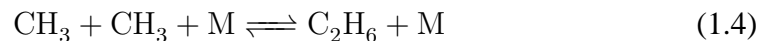
Diamond CVD growth from hydrocarbon / hydrogen gas mixtures occurs within a harsh reductive environment dominated by reactions involving atomic hydrogen. Atomic hydrogen can be produced from dissociation of  $H_2$  either as a surface mediated thermal process (Hot Filament reactors) (1.1), or as the result of energy transfer from gas-phase collisions with excited free electrons (Microwave and Arc-Jet reactors) (1.2).



Dynamic atomic hydrogen abstraction / hydrogen addition reactions with hydrocarbons are the dominant process within a CVD reactor, leading to the production of a variety of carbon radical species, (1.3).



Third-body mediated reactions can also occur between carbon radicals leading to the formation of  $C_2H_y$  species. Production of these species occurs at a slower rate than the hydrogen abstraction reactions (1.4). Hydrogen addition / abstraction reactions involving  $C_2H_y$  species can also occur, (1.5), as with the  $CH_y$  species.



Modelling by Mankelevich *et al.* [13], [14], using a 3D model of a HF reactor (see section 1.3.2 for more experimental details) showed that the conversion of acetylene to methane by hydrogen addition was only favourable at low gas temperature (< 1000 K) while the reverse reaction was dominant at high temperatures comparable with CVD conditions. The interconversion between these two species is discussed further in Chapter 6.

There is the possibility of the formation of carbon containing species larger than  $C_2H_y$  by further carbon radical addition reactions similar to reaction (1.4),

however mass spectrometry studies suggest that these species are present in very low mole fractions in comparison to  $\text{CH}_y$  and  $\text{C}_2\text{H}_y$  species [15]. Experimental measurements on these larger species would be difficult as the large number of degrees of freedom available to the molecules combined with high temperatures would lead to broadening of any spectroscopic features.

Studies show that the methane / hydrogen gas-phase mixing ratio is critical in determining the level of nucleation on the growing diamond surface. Low percentages of methane (< 2%) encourage smooth film formation whilst higher percentages (> 4%) cause an increase in the secondary nucleation on the growing diamond surface which results in a faster growth rate, but smaller grain size (poorer quality) diamond films [16], [17].

### 1.3.2 Hot Filament Reactors

The thermal activation of gas-phase chemistry underpins the oldest and simplest design for a CVD diamond reactor [18]. In a typical hot filament reactor, a coil of metal is resistively heated, to the order of 2000 °C, in a reduced pressure atmosphere (~ 20 Torr) of hydrogen with a small amount of methane (typically 1%). A substrate, usually silicon or diamond, is maintained at a temperature between 600 – 900 ° C, and placed within 20 mm of the filament, (Figure 1.6) and diamond growth occurs on the hot substrate at typical rates of  $1 \mu\text{m hr}^{-1}$ .

The critical design features in the HF reactor are the choice of the metal wire, and the gas flow design as diffusion is the dominant transportation process of active reagents to the substrate. Under CVD conditions, a metal carbide layer forms around the filament upon which molecular hydrogen adsorbs. The thermal energy of the carbide layer is transferred to the molecular hydrogen which promptly dissociates and diffuses into the gas-phase. The production rate of atomic hydrogen is limited by the surface area of the filament and the availability of suitable dissociation sites upon the filament. The thermal and mechanical stability of the metal carbide layer is critical for extended growth of diamond. Tantalum is one of the preferred metals for filaments as it readily forms a carbide whilst maintaining rigidity at high temperature. Experimental parameters have been investigated for the HF reactor looking at optimisation of the growth rate of CVD diamond films [19].

HF assisted CVD technology is the cheapest way of growing CVD diamond, with the ability to grow large areas of diamond [20] and to coat novel structures

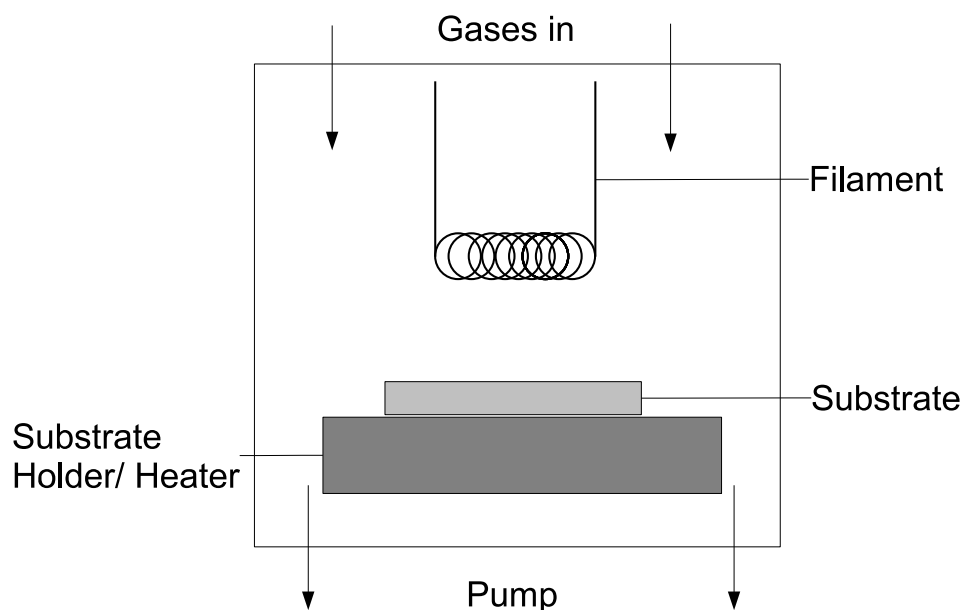


**Figure 1.6:** The systematic diagram of the HF reactor

and surfaces. However, the applications of this technology are limited by the low quality of the the final product and the possible inclusion of the filament source material in the growing diamond films [21].

### 1.3.3 Microwave Plasma Reactors

Microwave plasma activation of hydrocarbon / hydrogen gas mixtures has become the industrial standard for production of high quality diamond, Figure 1.7. Microwaves (usually at 2.45 GHz) from a generator are coupled into the microwave reactor through a quartz window via a waveguide and an antenna. A stub tuner is used to fine tune the microwave matching. Within the reactor, a few free electrons are heated by coupling with the electric component of the microwave field. The oscillating electrons rapidly gain energy and transfer it to the system through gas-phase collisions with molecular hydrogen, causing vibrational excitation, ionisation and molecular dissociation. This generates a non-equilibrated plasma where the excited atomic hydrogen initiates the radical gas-phase chemistry [22], [23]. At high microwave power densities, atomic hydrogen is also generated by thermal dissociation processes [24] and collisional induced dissociation can also occur at high

pressures (1.6).



Microwave plasma CVD reactors are designed so that there is a local maximum in the microwave field intensity above the water cooled substrate thus ensuring the stability and location of the plasma within the reactor [25].

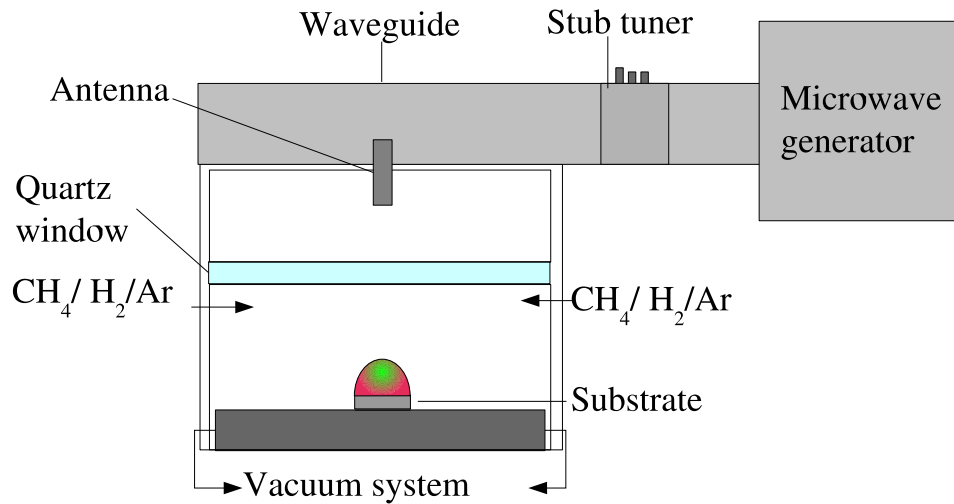


**Figure 1.7:** The schematic diagram of a microwave reactor

Initial designs for microwave plasma reactors used a quartz hemisphere (bell jar) for the reactor (e.g. [26]) but most modern research is performed in metal-walled reactors to minimise silicon contamination into the growing diamond film. There have been studies of the morphology and growth rate of the deposited diamond films [27], [28] and species present in the plasma ball during diamond growth using optical [29], [30] and mass spectrometry techniques [31] – [34]. These results have been used for comparison with theoretical modelling of the dynamics of microwave plasma [35] – [37].

Addition of noble gases to gas mixtures used in CVD deposition of semiconductors is a well-known practice, and the inclusion of such gases (especially argon) in diamond growth has been widely studied. Polycrystalline films of diamond can grow with addition of argon to  $\text{CH}_4/\text{H}_2$  gas mixtures with the grain size and orientation of the resulting crystals being highly dependent upon the argon concentration [29], [38].

Methane containing microwave plasma with high levels of Ar ( $> 90\%$ ) with reduced hydrogen levels ( $< 1\%$ ; only present to stabilise the plasma) leads to the formation of a crystalline film of diamond with exceptionally small sized grains. This fine-patterned “diamond-esque” material is known as Ultra Nano Crystalline Diamond (UNCD) as shown in Figure 1.8(b).

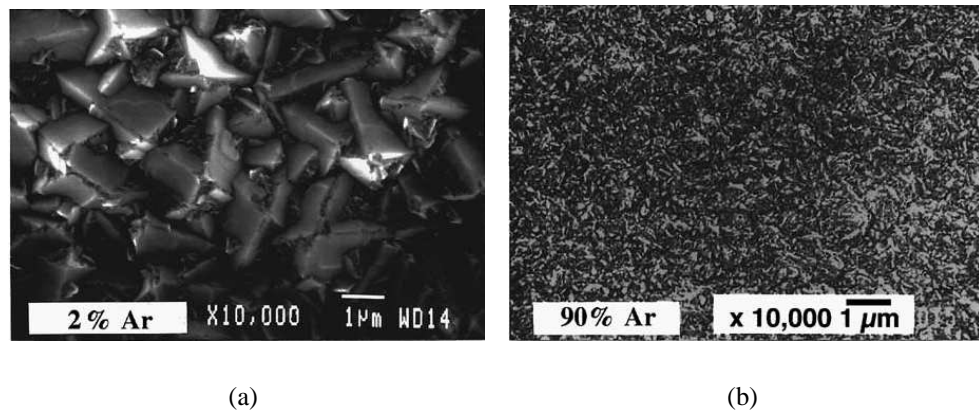


**Figure 1.8:** The change in morphology from polycrystalline diamond (a) to UNCD (b) by increasing the percentage of Ar in a  $\text{CH}_4 / \text{H}_2 / \text{Ar}$  gas-phase plasma, from ref [39]

Argon has two suggested roles in MWCVD plasma processes for UNCD production; the first is to act as a dilution factor, by reducing the number of hydrocarbon / hydrogen interactions and the second role is to activate molecular species via Penning effects [40]. This second use is a questionable mechanism as UNCD can also be formed in the less activated HF reactor where these processes do not occur [41] suggesting that argon affects the level of nucleation of growing diamond films. UNCD growth can also be attributed to the shift in hydrogen abstraction gas-phase equilibria due to an increased plasma temperature with the unique patterning due to high levels of etching due to atomic hydrogen generated in the vicinity of the substrate [42].

The main advantage of using microwave activation is that the process creates an electrode-free discharge, eliminating the possibility of electrode degradation and sample contamination. This enables a large window of process conditions to be investigated including high gas temperatures / pressures without the degradation of equipment and experimental stability. The inherent problems with microwave technology is the high cost of design and manufacture of the systems as well as the effective integration of analytical techniques without changing the CVD environ-

ment.

### 1.3.4 DC Arc-jet Reactors

Arc-jet reactors are the extreme diamond growing machine using high electrostatic potentials to induce species breakdown. Argon (and Hydrogen depending on the design) flow through a plasma torch head which consists of two electrodes biased at high voltages. Free electrons are electrostatically accelerated towards the anode, causing excitation and ionisation by collision with Ar species. The generated ions are attracted to the cathode and the process cascades, forming a plasma jet, which expands into a chamber maintained at reduced pressure. The torch head reactions are summarised within Figure 1.9.

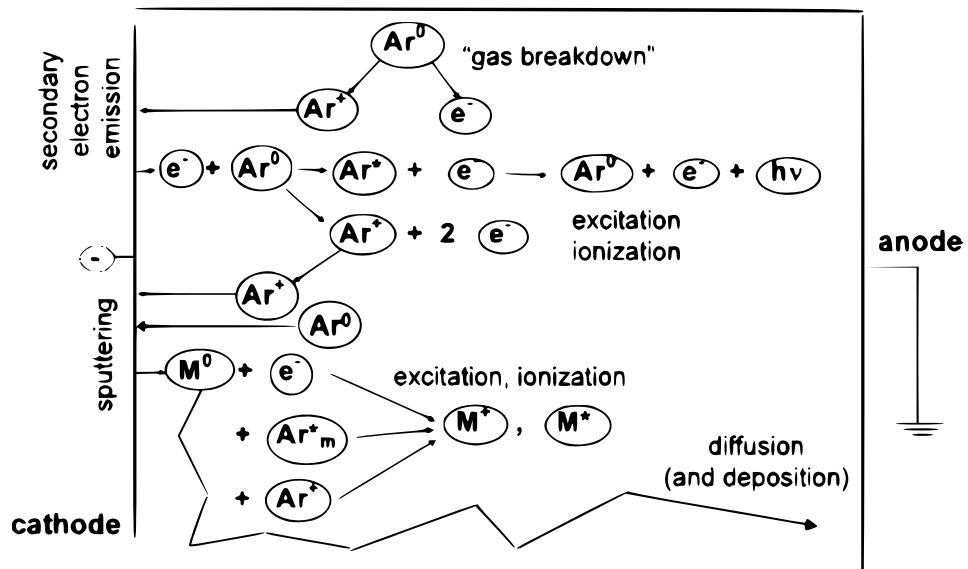


**Figure 1.9:** Reactions occurring with the DC Arc-Jet torch head from ref [43]. Cathode degradation is shown by the emission of metal atoms, M, from the surface.

A secondary torch may be added to increase the stability of the plasma and methane is usually added to the system downstream via an injection ring to avoid amorphous carbon clogging the nozzle head. The methane diffuses into the plasma whilst undergoing chemical breakdown reactions and the resulting plasma flows towards a water cooled substrate upon which grows diamond, Figure 1.10. This technique was first demonstrated for growing diamond in 1998 with a growth rate of  $80 \mu \text{ hr}^{-1}$  [44] though the growth rate is highly dependent on reactor design and

experimental conditions.

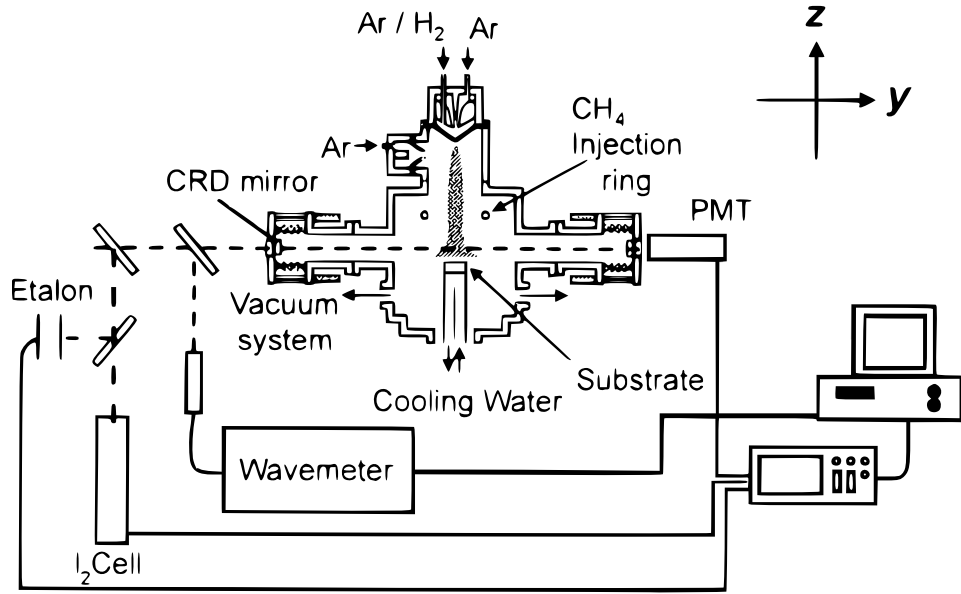
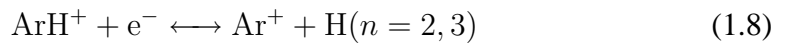


**Figure 1.10:** A two head CVD DC arc-jet set up for Cavity Ring down Spectroscopy from ref [45].

Optical emission spectroscopy (OES) revealed that the plasma jet forms an annular structure using optical emission spectroscopy of the C<sub>2</sub> species [46]. The chemistry within the arc-jet reactor is controlled by the high levels of excited Ar<sup>+</sup> ions which causes the decomposition of molecular hydrogen [47].



The formation of the highly excited states of atomic hydrogen arises from the decomposition of the ArH<sup>+</sup> species in the plasma. These species are very prone to relaxation via the n=3 → n=2, Balmer α emission. However, any spontaneous optical emission from the H(n=3) state is subsequently re-absorbed by neighbouring H(n=2) atoms such that the level of H(n=3) atoms is maintained with minimal optical emissions and H(n=3) atoms are detectable downstream from the methane injection ring.

The arc-jet process is not used as a major method for diamond synthesis as there is a vast radial variation in the quality of diamond produced, electrode sputtering causes a short lifetime of the torch heads and the extreme gas temperatures gen-

erated within the system can be produced within high power microwave reactors. However, DC arc-jet reactors do offer a system with highly energetic plasma based species which can be easily probed without degradation to the experimental conditions.

## 1.4 CVD Growth Mechanisms

CVD diamond growth follows a classical crystal growth process of nucleation, propagation, followed by a termination step. Most CVD diamond studies either focus on the expansion of a small diamond seed (usually from HPHT synthesis) or on heteroepitaxial growth from a suitable substrate, where growth occurs from seeding the surface with diamond particulates. The origins of the nucleation of diamond are important as this can lead to the introduction of many common growth faults.

Gas-phase nucleation has been suggested as playing a role in diamond growth but most studies have been performed in relatively low power and low pressure systems [48]. Studies also show that large hydrocarbon species are not stable at CVD temperatures [49].

Any diamond particulates formed in the gas-phase have been found to be of such low concentrations that they would have minimal effects on nucleation [50]. This leads to the suggestion that simple molecular species which can survive the harsh CVD environment are required for diamond growth.

### 1.4.1 Growth species

A growth species is a molecular reagent, derived from the source gas material, which diffuses to the surface where it is incorporated into the growing diamond phase. The exact chemistry of these growth species is a complex issue to resolve as it is hard to probe the active surface region of a CVD system (which is located in the millimetre or so just above the substrate) experimentally.

In the simplest case, the HF-CVD reactor, the relatively low CVD gas temperatures lead to minimal species activation in the region of the substrate, yet diamond growth is still possible. The dominant activated species within the substrate region are H atoms and CH<sub>3</sub> radicals (which can typically approach  $\sim 10^{16}$  cm<sup>-3</sup> and

$\sim 10^{14} \text{ cm}^{-3}$ , respectively). Numerous studies have independently shown that  $\text{CH}_3$  is responsible for low-temperature, low power growth of diamond [15], [51], [52]. In more energetic plasmas where gas temperatures can reach  $3500 \text{ }^\circ\text{C}$ , methyl radicals can still be found but there is a wider variety of  $\text{CH}_y$  and  $\text{C}_2\text{H}_y$  species present.

$\text{C}_2$  has been suggested as a growth species in the literature [53] especially as it is easily recognisable by a distinctive green optical emission at  $526 \text{ nm}$ . Proposed  $\text{C}_2$  insertion mechanisms into the growing diamond surface do not require a hydrogen abstraction activation step. This mechanism is especially relevant to the growth process of UNCD films which grow in a hydrogen-deficient plasma environment.

However, in pulsed microwave systems (which grow diamond of comparable quality to continuous wave systems), optimum conditions are found when  $\text{C}_2$  species (taken to be a measure of  $\text{C}_2\text{H}_y$  distributions) are minimised during the power off stage of the duty cycle. CH and H concentrations remained constant during this period resulting in diamond growth [54]. Studies on the effects of acetylene and methane addition also show that minimising the optical emission from  $\text{C}_2$  species increases the quality of the sample [51].

## 1.4.2 Growing surfaces

Diamond growth under CVD conditions requires that diamond is deposited at a faster rate than graphitic material. Atomic hydrogen is an essential part of the CVD diamond growth process as it stabilises the growing diamond surface by maintaining the  $\text{sp}^3$  hybridisation by saturating the surface radical sites, forming Carbon-Hydrogen bonds. Hydrogen atoms also preferentially etch  $\text{sp}^2$  carbon faster than  $\text{sp}^3$  carbon, ensuring that the diamond is the predominant phase of carbon grown [55].

The generic picture for CVD diamond growth is site-activation by a surface hydrogen abstraction reaction, (1.9), followed by addition of a hydrocarbon radical, (assumed to be  $\text{CH}_3$  in this case), (1.10) [56] – [58].



The lifetime of the surface radical,  $C_d^*$ , is effectively independent of the rate of methyl addition due to the relatively low concentration of carbon radicals in comparison with atomic hydrogen. The competition between surface activation and H-atom re-combination with the surface radical site (1.11) determines the number of active sites available [56].



The morphology of a growing diamond surface depends on the different rates at which diamond planes grow. The morphology assessment of the diamond sample grown is made by the growth parameter  $\alpha$ , (1.12).

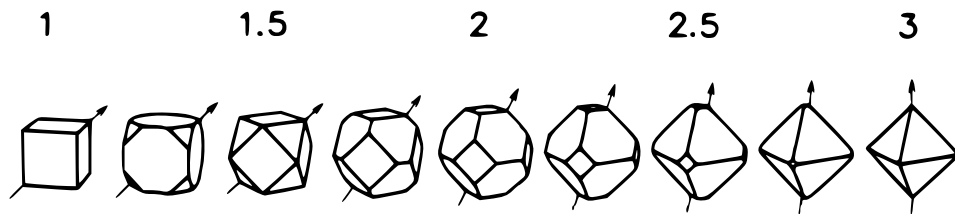


**Figure 1.11:** Idiomorphic crystal shapes for different values of the growth parameter  $\alpha$ . The arrows indicate the the direction of fastest growth (from ref [59])

$$\alpha = \sqrt{3} \frac{v_{100}}{v_{111}} \quad (1.12)$$

where  $v_{100}$  and  $v_{111}$  are the normal growth velocity of the respective diamond planes [59], [60]. This results in the change in shape from the  $\{100\}$  cubic structure to octahedral  $\{111\}$  diamond crystals, Figure 1.11.

### 1.4.3 Growth on the $\{100\}$ surface

CVD growth of  $\{100\}$  diamond produces a cubic morphology ( $\alpha < 1.5$ ) which is extremely flat and smooth, Figure 1.12. Diamond samples which are mainly  $\{100\}$  aligned generally have less defects (section 1.5) than the other planes making it the focus of intensive experimental and theoretical studies.

The level of different terracing depends upon the orientation of the growing diamond surface. Well-oriented substrates show evidence for a hillock growth process, Figure 1.13(a), [61]. Microwave CVD epitaxial diamond growth upon off-angle Ib

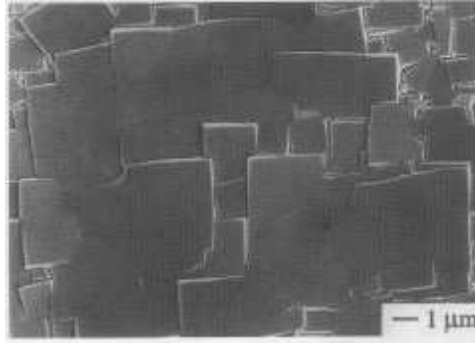


**Figure 1.12:** SEMs of  $\{100\}$  cubic diamond planes from ref [30]

diamond substrates suggests that step-growth is occurring upon the  $\{100\}$  surface, resulting in the formation of large terraces of  $(2 \times 1)$  reconstructed diamond, Figure 1.13(b), [16]. Increased methane concentrations within the reactor resulted in an increase of nucleation sites culminating in the generation of double-domain surfaces, [16]. Both these suggested mechanisms are based upon adsorption of a growth species upon the surface and its subsequent diffusion across the growing surface to step edges and / or other adsorbed atoms.

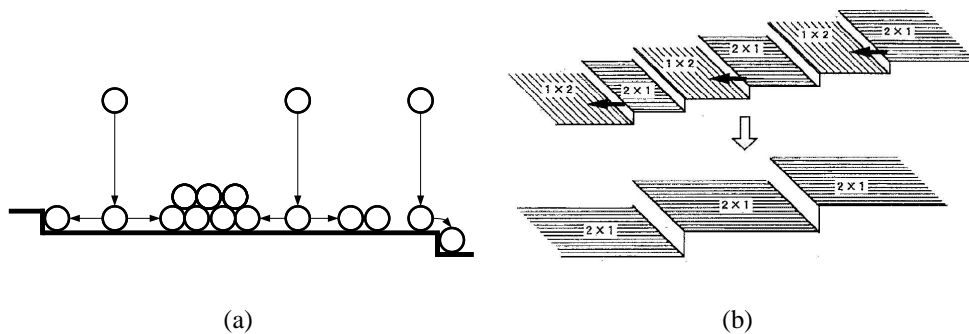


**Figure 1.13:** Schematic of epitaxial growth: (a) Hillock growth upon a well-aligned sample from ref [61] (b) Formation of a single domain surface for a mis-aligned sample from ref [16].

The  $\{100\}$  surface of diamond has a well known visible  $(2 \times 1)$  reconstruction where two surface carbon atoms relax from the bulk geometry positions and move together to form a carbon-carbon bond in the plane of the growing surface [16], [62], [63]. The diamond surface can be covered with multiple dimers which are neatly arranged into rows, Figures 1.14(a) & 1.15(a). This behaviour is unlike any other group XIV semiconductors which also undergo  $(2 \times 1)$  reconstructions

but form patterns of alternate dimers in both directions along the surface, Figure 1.14(b).

Periodic Density Functional Theory calculations (LDA, see chapter 3 for more information) confirm experimental evidence that carbon forms a symmetric configuration of dimer rows. The arrangement of the individual dimers into rows is due to the strong interaction between the  $\pi$  electrons on the reconstructed carbons due to the localised nature of the carbon's p orbitals [64]. This effect is weakened descending down the group XIV period and hence all other semiconductors from the same group have the staggered configuration.

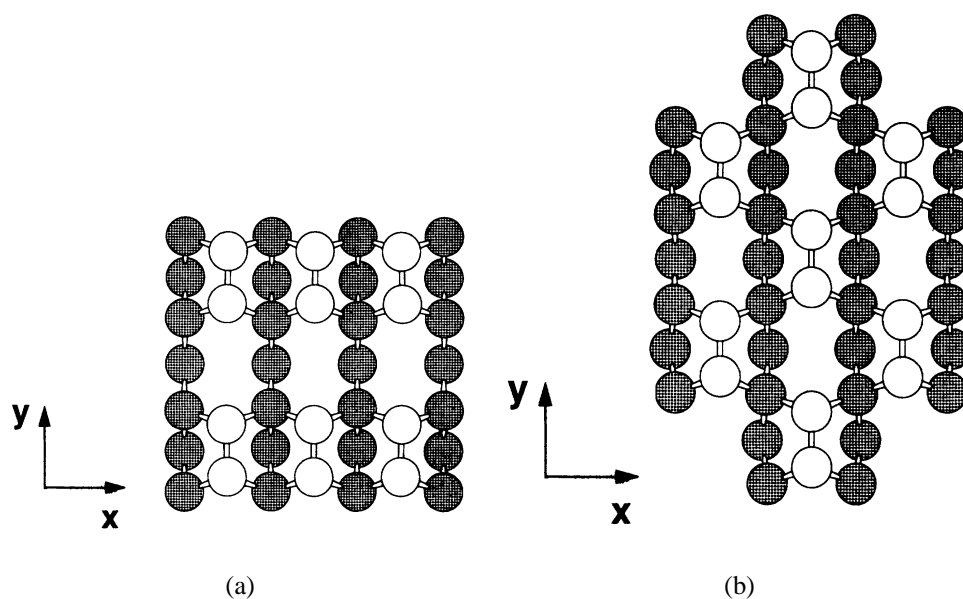


**Figure 1.14:** Surface dimer reconstructions arrangement for Group XIV semiconductors showing the (a) Row arrangement (b) Staggered dimer arrangement. Adapted from ref [65]

The extent to which growing surfaces are covered with reconstructed dimers is not clear as there are numerous scanning tunnelling (STM) and atomic force (AFM) microscopy studies which confirm the formation of the  $(2 \times 1)$  reconstructions, the mirror counterpart the  $(1 \times 2)$  reconstructions and other derivatives like the  $(3 \times 1)$  reconstruction which incorporates one reconstructed dimer with an isolated surface dihydride [62] – [68]. However, there are also suggestions that the surface reconstructions and the formation of the large domains of smooth (100) diamond surface is a post-growth feature either caused by annealing in hydrogen in sample preparation for surface studies [69] or surface etching / annealing that occurs during the

shutdown process of a CVD reactor [70].

Diamond surfaces growing under CVD conditions will be hydrogen terminated and the steric interaction between H atoms on neighbouring {100} surface carbon atoms may drive the creation of hydrogen terminated surface reconstructions. The formation of the reconstructed dimer is an overall energetically favoured process (Figure 1.15(b)). The close proximity of the two neighbouring hydrogen atoms enables them to associate (at a slight energy cost) and then to dissociate as molecular hydrogen, resulting in formation of a C-C bond in the {100} plane [71]. It is also energetically feasible that the reconstruction process can be initiated by hydrogen abstraction of a pendant surface hydrogen and the resultant lowest energy structure results in the expulsion of atomic hydrogen and the formation of the reconstructed bond. The study by Huang and Frenklach does not address the issue of the origin of the reconstructions, whether they are formed as part of the growth mechanism or as a post-process surface relaxation of carbon.

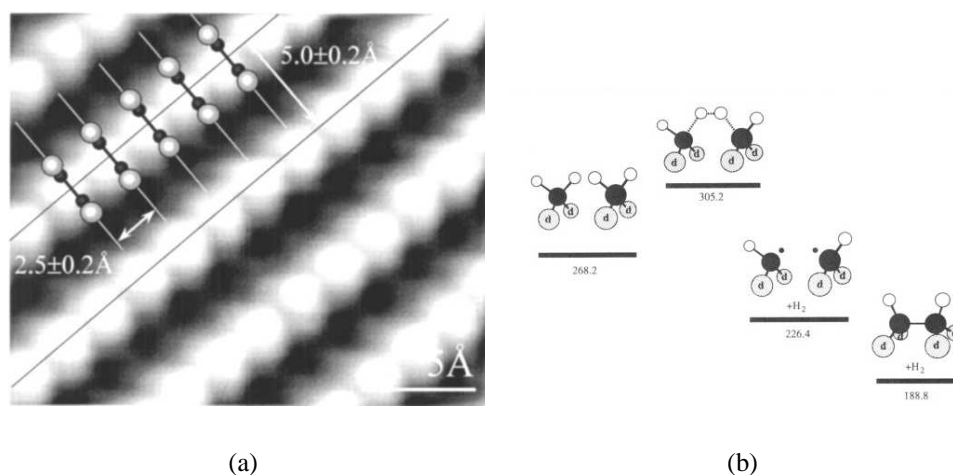


**Figure 1.15:** (a) Scanning tunnelling Microscopy (STM) image of the topography of the hydrogen terminated {100} diamond reconstruction surface from ref [63] : (b) a proposed mechanism for formation of isolated reconstructed surface dimers for the hydrogen terminated {100} surface from ref [71] (energy in kcal mol<sup>-1</sup>).

Most theoretical studies have focused on the incorporation of the CH<sub>3</sub> radical into the growing surface and in the remainder of this thesis, CH<sub>3</sub> will be assumed as the carbon growth species unless stated otherwise.

The diamond CVD growth process is initiated by hydrogen abstraction of one of the hydrogens pendant on the dimer reconstruction. Methyl radicals can diffuse

from the gas-phase towards the diamond surface and form strong bonds to the surface radical sites. The resulting bound methyl group can be incorporated in two different places, either by formation of a carbon–carbon bond at the neighbouring end of a reconstructed dimer bond to which the methyl group is bound or by addition to the neighbouring reconstructed carbon dimer by bridging the trough between the two dimer rows (Sites A and B respectively in Figure 1.16).

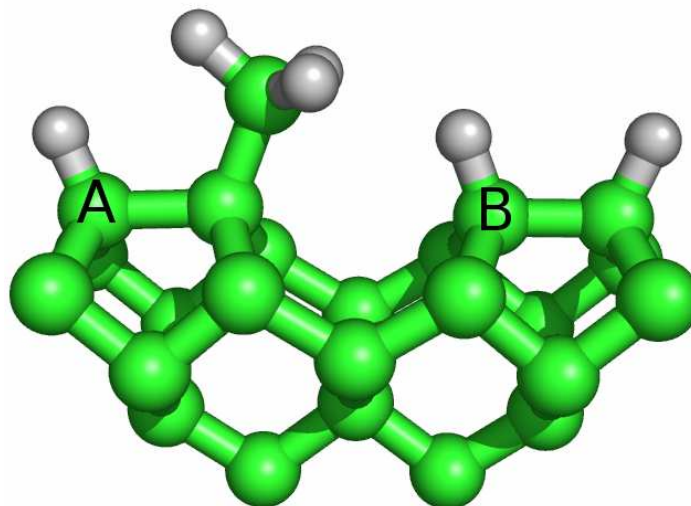


**Figure 1.16:** Cross section through the  $\{100\}$  plane showing the dimer reconstruction (A) and the trough (B) insertion points.

Figure 1.17 shows the mechanism for carbon insertion into the dimer bond, (A), initially proposed by Garrison *et al.* from molecular dynamics studies of diamond surfaces [72]. The process is initiated by hydrogen abstraction from a pendant surface bound  $\text{CH}_3$  (i.e.  $\text{C} \rightarrow \text{D}$  in Figure 1.17). The newly formed  $\text{CH}_2$  radical then incorporates into the diamond structure via a ring opening mechanism ( $\text{D} \rightarrow \text{E} \rightarrow \text{F}$ ) rather than by direct insertion of  $\text{CH}_2$  into the carbon – carbon bond which has a very large barrier (ca  $200 \text{ kJ mol}^{-1}$ ) [72], [73]. The mechanism has been studied with numerous different environments including isolated clusters [73], larger QM / MM clusters [74], [75] and under periodic boundary conditions [76], [77]. The ring opening and closing mechanism for incorporation can also model lateral  $\{100\}$  diamond growth from a step on the  $\{111\}$  surface [78].

Alternatively, a surface bound  $\text{CH}_3$  species could be incorporated across the trough which separates dimers (site B in Figure 1.16). Incorporation across the dimer trough was first suggested by Harris and was based upon results obtained from studies upon bicyclo-[3, 3, 1] nonane (BCN) [79]. The process, known as the

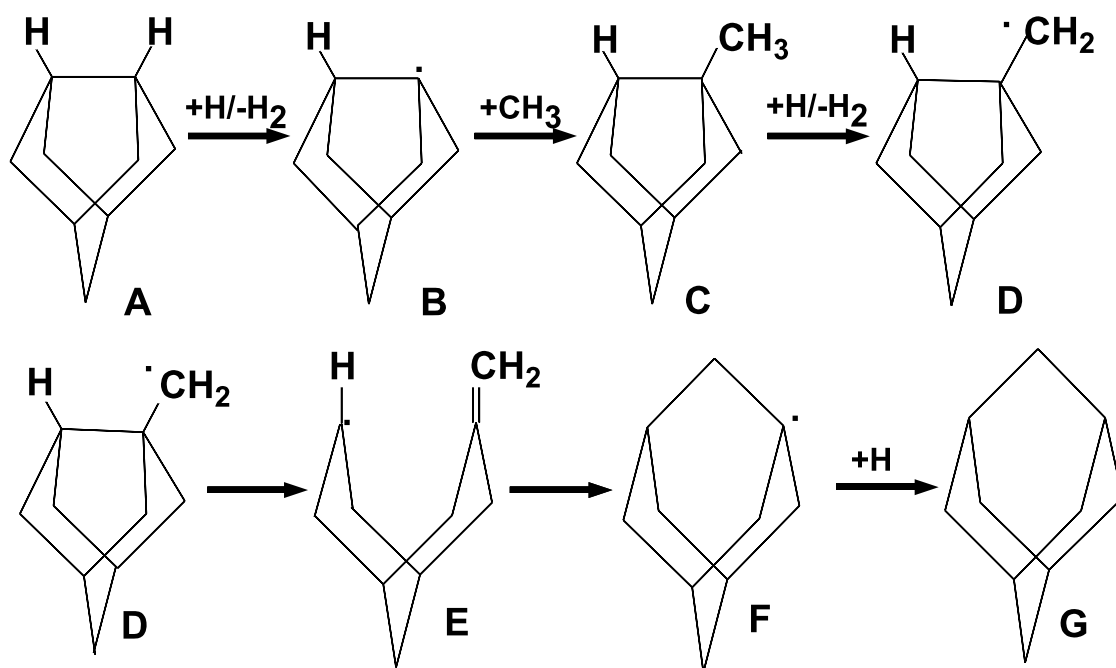


**Figure 1.17:** Mechanism for i) Hydrogen abstraction and surface activation (A → B) ii) Carbon incorporation into the diamond {100} surface (C → G).

HH mechanism, is initiated by surface hydrogen abstraction followed by methyl adsorption. The neighbouring hydrogen atom is abstracted and then followed by ring closure, Figure 1.18.

In order for growth of a complete new monolayer of diamond to occur, carbon species must be incorporated into the reconstructed dimer as well as across the trough linking the dimer rows, Figure 1.16. Neither mechanism adequately describes the effective growth rates and process for a whole new layer of diamond. This has led to suggestions that the overall growth mechanism must involve a combination of the two processes [80], or that one should introduce the possibility of surface migration of reactive species. These ideas are discussed in more detail in Chapter 4.

C<sub>2</sub>H<sub>2</sub> / H<sub>2</sub> gas mixtures have been used to grow {100} diamond, and C<sub>2</sub>H<sub>2</sub> has been considered as a growth species [71], [81]. C<sub>2</sub> has also been investigated for possible incorporation into a non-hydrogenated (2×1) reconstructed {100} surface. This incorporation process is energetically feasible [82] with the stable non-hydrogenated dimer bond [74], but is unlikely to be a major contributor to the growth process as the lifetime of a surface radical site is not long enough to endure for a second hydrogen abstraction reaction.

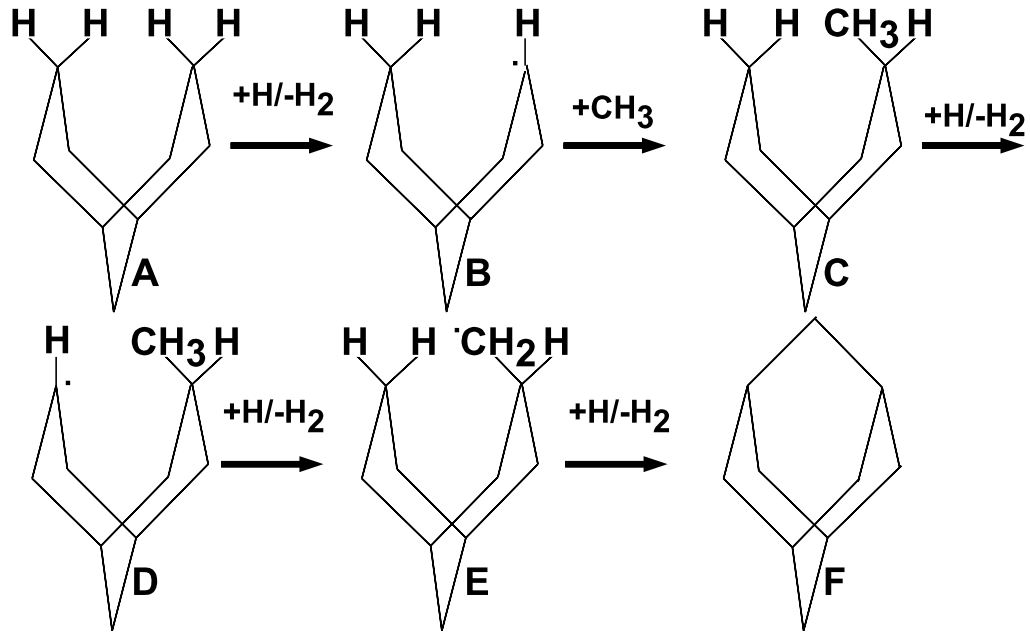


**Figure 1.18:** The HH mechanism, showing the conversion of BCN (A) to adamantane (F) modelling the incorporation of an absorbed methyl radical across a dimer trough from ref [79].

#### 1.4.4 Growth on other diamond surfaces

##### {111} diamond surfaces

In stark contrast to growth on the {100} surface, diamond growth on the {111} plane is considered to be a quicker yet more complicated process. The open cyclohexane nature (Figure 1.3(c)) of the growing surface has led to suggestions that this face is more accommodating for inclusion of defects as well as larger hetero atom species. Normal growth of {111} diamond produces octahedral crystallites ( $\alpha > 2$ ).

The {111} surface can also undergo a reconstruction process, and there have been numerous experimental [83], [84] and theoretical studies [85] – [89] on the shape and electronic properties of the reconstruction. The reconstruction consists of a distortion of the cyclohexane pattern of the surface layer which enables the formation of  $\pi$  bonds between two carbon atoms. This results in the formation of a chain structure across the surface. Figure 1.19 shows the surface reconstruction for the {111} diamond surface which, unlike other group XIV semiconductors, does not show any tilting of  $\pi$  bonds. Unlike the {100} surface, the hydrogenated {111}

surface is stable (Figures 1.3(c) & 1.3(d)) and the reconstruction only occurs when surface hydrogen is removed, usually by annealing in UHV conditions [90].

Methyl radical addition to a radical site on the  $\{111\}$  surface is an exothermic reaction which is less energetic than  $\text{CH}_3$  addition on the  $\{100\}$  reconstructed surface [92]. The initial suggestion for the mechanism of  $\text{CH}_3$  addition into the growing  $\{111\}$  diamond surface was for the surface to be covered in a monolayer of adsorbed methyl groups to which  $\text{CH}_3^\dagger$  is finally added to form a new layer [93]. However, the large steric interaction between the adsorbed methyl groups makes this pathway very unfavourable.  $\{111\}$  diamond growth modelled using  $\text{CH}_3$  radicals as the sole growth species has been found to be a slow process because of the relatively poor rate of new layer nucleation. The slow layer nucleation has been proposed as the rate limiting step of  $\{111\}$  CVD growth [94], [95]. However, addition of  $\text{CH}_y$  species into the lateral growth on this surface has been successfully modelled from isolated nucleation points, step edges and kinks [95] – [98] leading to a step-flow process for monolayer growth [99]. Studies of the new layer nucleation mechanisms include  $\text{C}_2\text{H}_y$  species as a way of avoiding the complications of multiple  $\text{CH}_y$  additions, Figure 1.20.

The inclusion of these growth species in calculations increases the rate of diamond deposition to levels comparable with that observed experimentally [99], [100]. There are suggestions that  $\text{C}_2\text{H}$  may be a more favourable growth species than acetylene on the  $\{111\}$  surface because of a slower surface desorption rate

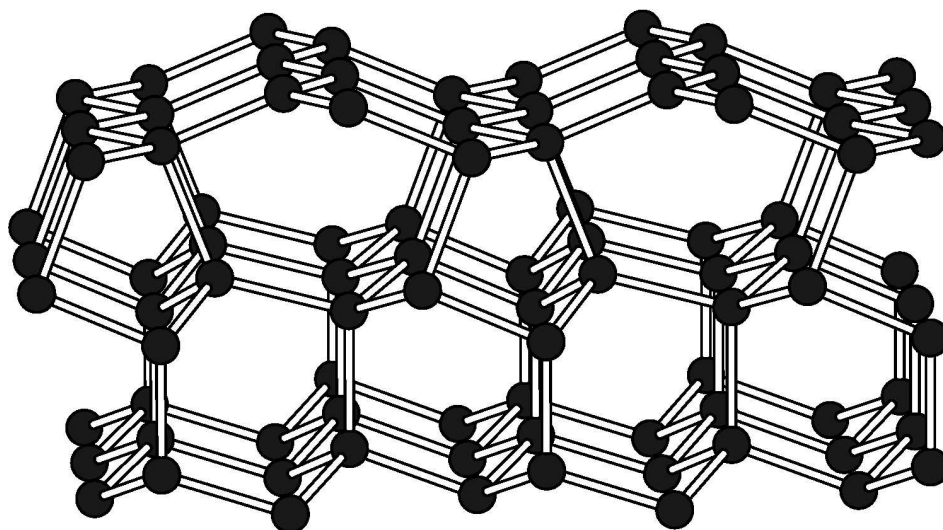


**Figure 1.19:** The  $(2 \times 1)$  reconstruction for the  $\{111\}$  surface, from ref [91]

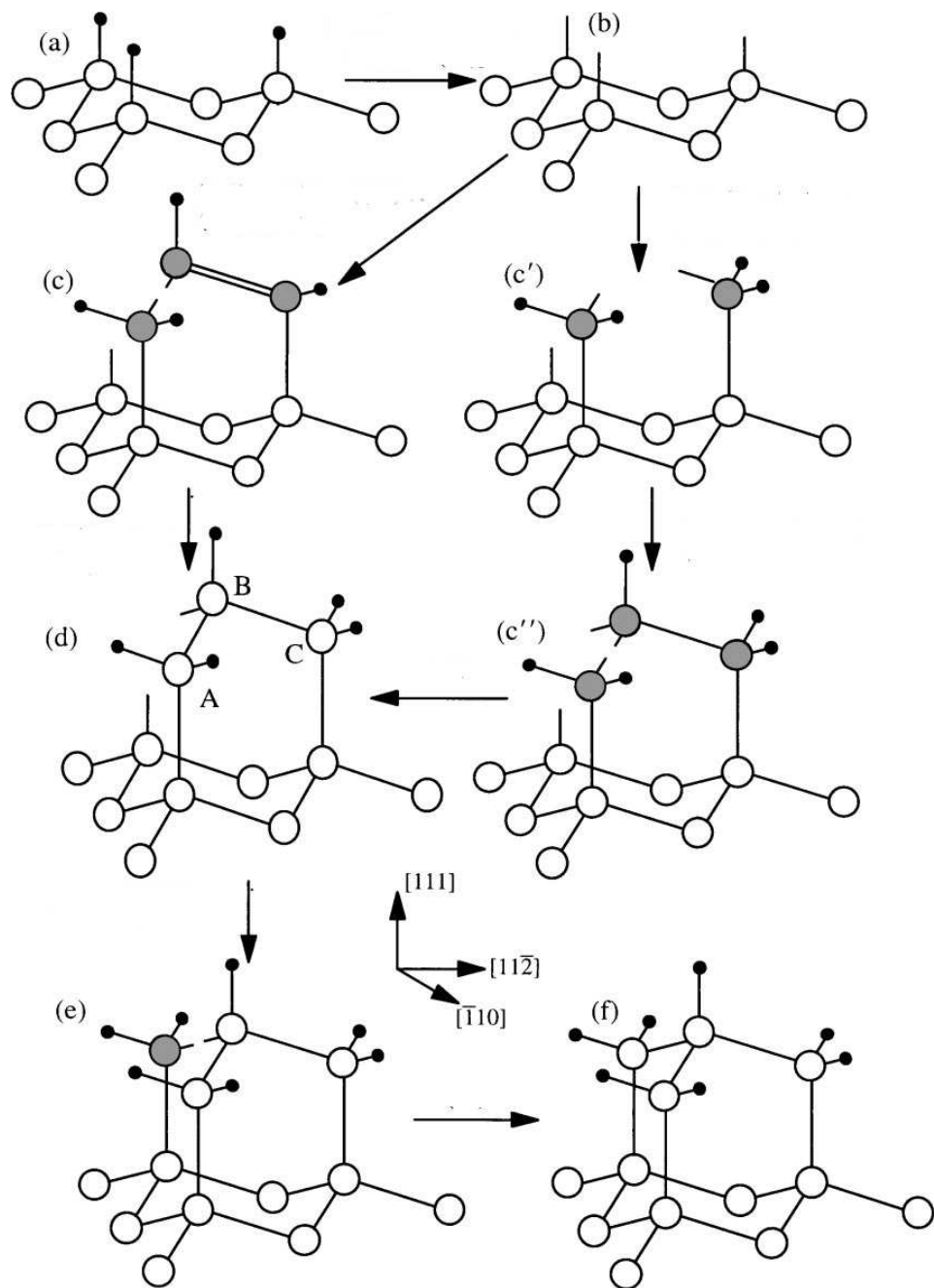


**Figure 1.20:** Suggested pathway of  $\text{CH}_y$  and  $\text{C}_2\text{H}_y$  incorporation into the  $\{111\}$  diamond surface (modified from ref [94])

[96], [101]. There have also been suggestions of possible ionic species mechanism involving a surface charged site [102].  $C_2$  has also been suggested as a growth species on the hydrogen free  $(2 \times 1)$  reconstructed surface by forming a bridge between rows of the  $\pi$ -bond chains [103].

### **{110} diamond surfaces.**

The {110} diamond face is the fastest growing diamond surface and hence has been subjected to few experimental and theoretical studies. The main mechanism suggested for growth on this surface involves the bridging of the large ridges present on the growing {110} surface. This can occur by two sequential methyl radical additions with the necessary hydrogen abstraction reactions, Figures 1.21(a) & 1.21(b) [56], or by the direct insertion of  $C_2$  which, theoretically at least, can insert into a carbon–hydrogen bond via an exothermic process with only a small activation barrier [104].

$C_2$  insertion is also possible upon non-hydrogenated {110} surfaces in a similar manner [105]. These mechanisms appear to be energetically plausible reaction pathways but both require many stepwise reactions in conjunction with neighbouring addition / abstraction reactions in order for incorporation.

## **1.4.5 Etching**

So far, mechanisms have only been discussed which focus upon the incorporation of carbon species into the diamond. Etching and the removal of non-diamond material is also a critical process in ensuring the prevalence of diamond growth. In most gas-surface bond forming steps, like the initial addition of the methyl radical to the active surface site, there is the unlikely possibility of bond fission and disassociation of the reagent back into the gas-phase. This is due to the highly exothermic nature of the addition reaction and these direct desorption processes are highly unlikely unless the resulting carbon–carbon bond is very weak. Etching processes occur by the active removal of carbon material by a gas-phase reagent bonding with a pendant surface species, then dissociating.

Most studies have focused on the removal of pendant methyl groups. The simplest way for removal of the surface methyl group is for a direct radical displacement reaction involving atomic hydrogen, resulting in methane dissociating into

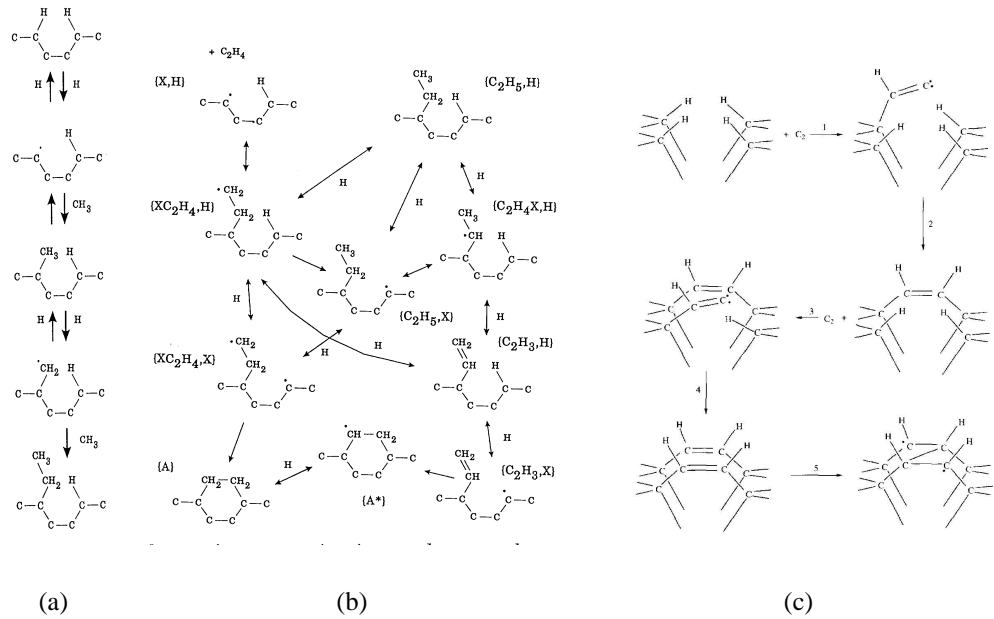


**Figure 1.21:** (a) Addition of two methyl radicals to the {110} diamond surface from ref [56]; (b) Proposed fate of the adsorbed ethyl chain from ref [56]; (c) Proposed  $\text{C}_2$  incorporation into the {110} diamond surface from ref [104]

the gas-phase. This reaction is unlikely despite the high flux of atomic hydrogen under CVD conditions as there is a very high barrier of activation [74]. Another form of radical displacement reaction involves the formation of a surface radical (by gas-phase hydrogen abstraction) from a carbon dimer to which a methyl radical is attached at the other end. The liberation of the  $\text{CH}_3$  radical into the gas-phase is driven by the formation of a non-hydrogenated  $\pi$  reconstructed dimer carbon-carbon surface bond [81].

### The $\beta$ -Scission reaction

Growth of diamond so far has assumed that methyl radical – surface reactions are isolated incidents based upon the concentrations of atomic hydrogen and methyl radical in the gas-phase. However, during the growth process, there is the possibility of formation of surface bound alkyl chains by  $\text{CH}_3$  radical addition to a pendant  $\text{CH}_2$  species. Such processes are suppressed under typical diamond CVD conditions, however, by so-called  $\beta$ -scission reactions. Hydrogen abstraction from the  $\beta$  carbon leads to formation of an unsaturated radical species, which dissociates

to form a gas-phase species (e.g. ethene) and a surface radical site – thereby preventing incorporation of longer alkyl chains into the growing diamond surface [80]. This is the most common etching scheme included in Monte Carlo modelling of diamond growth.

## 1.5 Defects in Diamond

Despite the robust nature of diamond, faults can be found in crystals due to the growth process or post-growth damage. Some of these processes can account for the wide variety in colour of natural diamond. These defects can manifest themselves as vacancies; dislocations and twinning. All of these defects can appear throughout the crystal, affecting the bulk diamond physical properties and introducing new undesirable features into the diamond electronic structure. The introduction of defects into a diamond causes new characteristics by distorting the crystal and reducing the high level of symmetry of the diamond unit cell, all which can be monitored by absorption spectroscopy.

### Twinning

Twinning is a common stacking fault found in synthetic and natural diamond resulting from a disruption in the growth process. Diamond usually adopts an *abcabc* stacking pattern, Figure 1.23(a), however twinning is introduced into the system by the formation of a carbon–carbon bond in the mirror position of the normal bond, Figure 1.22, thereby resulting in a boat rather than chair form of cyclohexane. This inclusion changes the stacking pattern to *abcba* where *c* has become the mirror plane. Figure 1.23(b) shows this effect with the twin plane introduced between the aB Ba layer, leading to the formation of two symmetric crystals with shared points. The twinning can occur in the form of a reflection of a mirror plane, a symmetric inversion or around a rotational axis.

### Interstitials

Interstitials defects are formed by the displacement of a species from the normal lattices position into a stable but higher energy confirmation. Figure 1.24 shows a diamond model highlighting the common locations for interstitial defects. In dia-

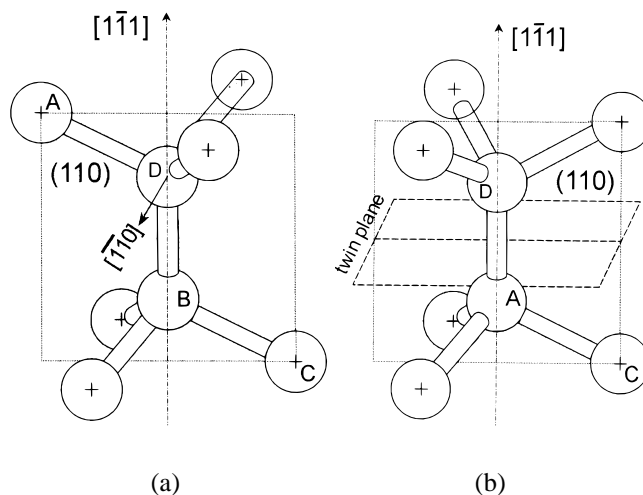


**Figure 1.22:** Figure showing the twinning effect at the atomic level with (a) regular and (b) eclipsed position. Figure reproduced from ref [106].

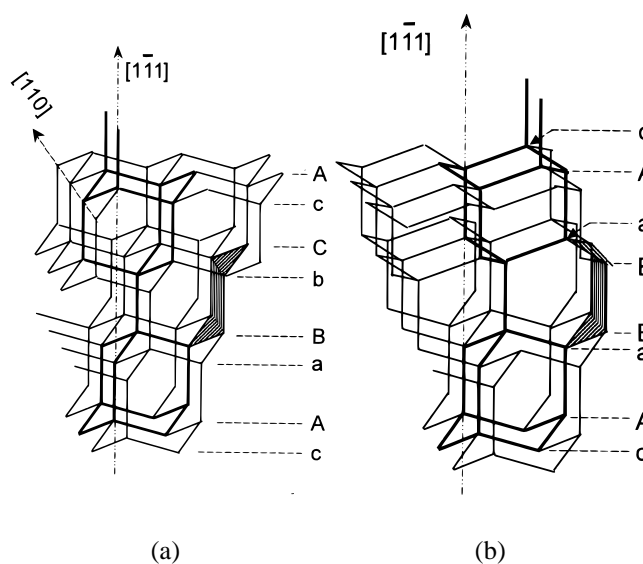


**Figure 1.23:** Figure showing the twinning effect upon the crystal structures are (a) the regular and (b) the twinned stacking pattern. The chair and boat conformations of cyclohexane structure are highlighted within the appropriate stacking pattern. Figure reproduced from ref [106].

mond, it transpires that the most favourable arrangement is a split self-interstitial along the  $\{100\}$  axis, Figure 1.24(c). The split interstitial is formed when a normal diamond lattice site is replaced by two carbon atoms, symmetrically arranged around the now vacant site [107].

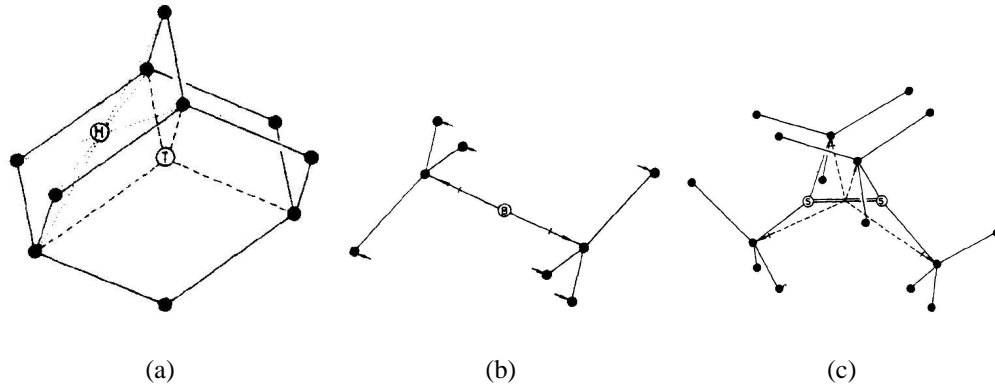


**Figure 1.24:** Common interstitial geometries (a) Hexagonal and tetrahedral holes; (b) The bond centred form; (c) The  $\{100\}$  split interstitial, showing the change in geometry, all from ref [108].

## Vacancies

A vacancy is a discontinuity in the diamond lattice caused by the complete displacement of a carbon atom from its normal site and the resultant interaction between the former bonding electrons located on neighbouring carbon atoms. These symmetry bound electronic states can be identified by optical absorption spectroscopy and Electron Paramagnetic Resonance (EPR) spectroscopy [110]. Absorptions due to singular vacancies have been assigned to neutral [111], [112], negatively [113] and positively charged [114] vacancies. There is the possibility of forming multi-component systems, especially with nitrogen impurities.

### 1.5.1 Doping of Diamond

Diamond is a semiconductor with a large gap between the conduction and valence bands (5.5 eV), Figure 1.25. The energy required for a promotion of an electron from the valence band into the conduction band is great enough to make diamond an electronic resistor (typically  $10^{16} \Omega \text{ cm}$ ) under normal conditions.

However, incorporation of hetero-atoms into the diamond lattice with slightly different electronic configurations from the host material leads to new energy levels in the band structure that enable conduction. The hetero-atoms can be incorporated during the growth cycle of diamond or as a post growth process, typically ion implantation or diffusion. The experimental problem with doping is ensuring that the

dopant remains active when inserted into the diamond structure. Hydrogen, a common impurity within CVD diamond, complicates issues as it can complex with the active dopant within the crystal. The complex species can either pacify (boron) or activate (sulphur) the dopant, [115] [116].

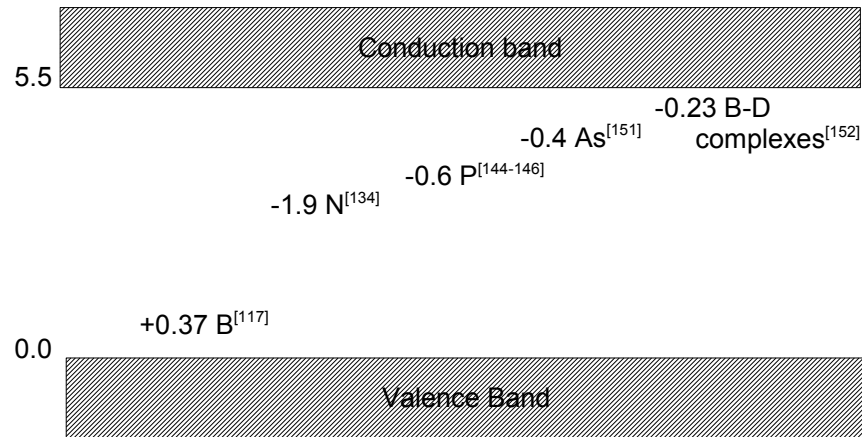


**Figure 1.25:** The band structures of diamond showing the energy levels of dopants. All values are in eV and quoted relative to the nearest band.

## 1.5.2 p-type doping

The introduction of a p-type dopant causes the formation of discrete acceptor levels above the valence band of diamond. The energy levels are accessible by electrons from the valence band. When promotion occurs into these levels, delocalised positive holes form in the valence band which enables conductance.

Boron naturally incorporates into diamond to create a (shallow) p-type semiconductor with a donor level of  $368.6 \pm 2.5 \text{ meV}$  [117]. Addition of trace amounts of a suitable boron-containing precursor to the process gas mixture enables deposition of doped material, in which B atoms have incorporated into both the diamond  $\{100\}$  and  $\{111\}$  surfaces. Sources used for boron inclusion during diamond CVD include diborane, trimethylboron and triethylboron [118] – [121].

Low level additions of boron in the gas-phase ( $< 500$  ppm B / C) increase the quality of CVD diamond samples with larger crystals, faster growth rates and better crystal morphology. Intermediate B / C values (1 000 – 5 000 ppm) produce diamond with similar characteristics to pure carbon CVD growth but p-type while high boron concentrations ( $> 4\,000$  ppm) lead to a breakdown in crystallinity and a general loss in quality [122], [123]. A graphitic phase is co-deposited with B / C gas-phase ratios above 8 000 ppm yet diamond can still grow up to B / C gas-phase ratios of 10 000 ppm. The increase in graphitic material at high boron levels is attributed to depleted atomic hydrogen number densities in the gas phase, due to reactions with  $B_2H_6$ , which effectively reduces the rate at which  $sp^2$  carbon is etched [124]. The relative efficiencies of boron and carbon incorporation into a growing film from a given B / C / H gas mixture can be highly dependent upon the system design and conditions [125]. There are indications that boron species may assist with the migration of carbon species across a growing diamond surface [126].

Several studies have highlighted the preferential incorporation of boron in  $\{111\}$  growth sectors [120], [127], [128] and the effects of the incorporation of boron on the CVD diamond crystallinity varies greatly with surface morphology [129], [130]. The elementary steps leading to B incorporation into diamond were not well characterised, new insights into the diborane / methane / hydrogen gas-phase chemistry are presented in Chapter 2, while Chapter 3 presents modelling studies of the incorporation of  $BH_x$  species into a growing diamond surface.

Other species have been considered to act as p-type donors (e.g. Al) but the incorporation levels are poor when compared to boron.

### 1.5.3 n-type doping

A hetero-atom inclusion causes n-type doping by forming a donor level whose electrons can be easily excited into the conduction band. There are no natural diamond samples which show n-type conductivity and finding the best donor is the “Holy Grail” of synthetic diamond research.

Nitrogen, with one more electron than carbon, would be the natural suggestion for a n-type dopant for diamond, as nitrogen is a common inclusion which historically has been used as a measure of quality by infrared absorption spectroscopy. Samples which only show higher order diamond absorption patterns are classified as IIa while semiconducting diamonds of comparable quality are labelled IIb [131].

Class I diamonds have a measurable level of nitrogen with type Ia diamond having aggregates of nitrogen whilst type Ib only has the isolated substitutional form of nitrogen. Numerous studies have shown that trace nitrogen addition into the gas-phase mixtures improves the quality of diamond samples [132], [133], while theoretically, it has been suggested that Nitrogen inclusion modifies the growth mechanism of diamond by activation of surface dimer reconstructions [77]. However, nitrogen provides a deep donor level (1.9 eV) below the conduction band which prevents conductivity, from thermal excitation of electrons, at room temperature [134].

Sulphur has been suggested theoretically as a prime candidate for shallow n-type donor [135], with growth mechanisms [136] and CVD gas-phase chemistry [137] well studied. However, reported n-type doping of diamond with an activation of 0.38 eV [138] has been questioned on the basis that the samples also contained a high level of boron and exhibited p-type semiconduction [139].

Phosphorus has been incorporated into the {111} surface of diamond as a substitutional donor [140] with mixed results [141] – [143]. The as-grown films showed n-type properties, but also showed poor carrier characteristics with an activation barrier of  $\sim 0.6$  eV [144] – [146], which is deeper than theory predicted. Theoretical studies predict that phosphorus is insoluble in bulk diamond [116], yet studies on the {111} surface reconstruction indicate that local near surface solubility is greatly enhanced [147].

In the search for better n-type dopants, more exotic species have been considered. Group I elements, lithium and sodium, looked theoretically promising as interstitial donors [148] but experimental results failed to yield any n-type properties, with lithium remaining at the near surface region [149], [150]. Arsenic has been suggested as a possible dopant [151], but there are no reports of any successful synthesis.

Much further interest has been stimulated by recent reports of n-type electrical conductivity from deuterated (100) B-doped diamond layers which exhibits the lowest activation barrier yet reported, of 0.23 eV [152]. Theory, thus far, has failed to validate initial suggestions that such conductivity might be associated with boron–deuterium complex defects within the diamond lattice [115], [153].

## 1.5.4 Application of dopant technology

The advent of B doped CVD diamond has led to the development of unipolar devices [154], [155], electrochemical detectors [128], [156] and, when combined with P (n-type) doped diamond, UV light sources [157]. Also, introduction of conductivity into diamond enables the material to be cut and shaped by traditional metal spark cutting tools. More recent, has been the discovery that B-doped diamond is a superconductor [158], however the critical temperature ( $T_c$ ) for superconductivity is  $\approx 4\text{K}$ .

## 1.6 Aims

This thesis has investigated the fundamental processes which major gas-phase species undergo within the framework of diamond growth under CVD conditions. This includes probing the complex gas-phase reaction dynamics as well as modelling the gas-surface reactions with subsequent incorporation steps required for CVD diamond growth.

Chapter 2 shows the spatially resolved measurements of atomic boron (derived from the degradation of the gas-phase dopant,  $\text{B}_2\text{H}_6$ ) within a thermally activated  $\text{CH}_4 / \text{H}_2$  gas mixture within a HF-CVD reactor as a function of process conditions. This experimental work led to the development of a DFT based computational model for the incorporation of boron hydride species into a small region of a  $\{100\}$  diamond surface. This work within Chapter 3 is expanded to investigate the incorporation of methyl (and  $\text{BH}_x$ ) radicals to numerous different surface environments by using a QM / MM system within Chapter 4. Experimentally, a new high pressure CVD microwave system has been installed. The optimum growth condition has been identified using the Taguchi protocol and initial profiling of the radiative species within the plasma has been performed using Optical Emission spectroscopy and Cavity Ring-Down Spectroscopy; these are reported in Chapter 5. This thesis concludes with the first reported simultaneous line of sight absorption spectroscopy measurement of  $\text{C}_2\text{H}_2$  and  $\text{CH}_4$  within a CVD diamond growing environment using a quantum cascade laser, Chapter 6.

## Bibliography

- [1] H. W. Kroto, J. R. Heath, S. C. O'Brien, R. F. Curl, and R. E. Smalley, *Nature* **318**, 162 (1985).
- [2] J. E. Field, *Properties of Natural and Synthetic Diamond* (Academic Press Limited, 1992).
- [3] F. P. Bundy, *J. Geophys. Res.* **85**, 6930 (1980).
- [4] S. E. Haggerty, *Nature* **320**, 34 (1986).
- [5] H. P. Bovenkerk, F. P. Bundy, H. T. Hall, H. M. Strong, and R. H. Wentorf, *Nature* **184**, 1094 (1959).
- [6] J. Martin, *Ind. Diamond Rev.* **59**, 291 (1990).
- [7] M. Wakatsuki, *Jpn. J. Appl. Phys.* **5**, 337 (1966).
- [8] H. Kanda and T. Sekine, in *Properties, Growth and Applications of Diamond*, (ed. M. H. Nazaré and A. J. Neves), Institution of Electrical Engineers, Michael Faraday House, Six Hills Way, Stevenage, Herts, SG1 2AY, UK (2001).
- [9] P. K. Bachmann, *Adv. Mater.* **5**, 137 (1993).
- [10] D. Choudhary and J. Bellare, *Ceramics International* **26**, 73 (2000).
- [11] R. C. DeVries, *Ann. Rev. Mater. Sci.* **17**, 161 (1987).
- [12] S. K. Han, M. T. McClure, C. A. Wolden, B. Vlahovic, A. Soldi, and S. Sitar, *Diamond Relat. Mater.* **9**, 1008 (2000).
- [13] Yu. A. Mankelevich, A. T. Rakhimov, and N. V. Suetin, *Diamond Relat. Mater.* **7**, 1133 (1998).
- [14] Yu. A. Mankelevich, N. V. Suetin, M. N. R. Ashfold, J. A. Smith, and E. Cameron, *Diamond Relat. Mater.* **10**, 364 (2001).
- [15] S. J. Harris, A. M. Weiner, and T. A. Perry, *J. Appl. Phys.* **53**, 1605 (1988).
- [16] T. Tsuno, T. Tomikawa, S. Shikata, T. Imai, and N. Fujimori, *Appl. Phys. Lett.* **64**, 572 (1994).
- [17] H. Kawarada, H. Sasaki, and A. Sato, *Phys. Rev. B* **52**, 11331 (1995).
- [18] S. Matsumoto, Y. Sato, M. Kamo, and N. Setaka, *Jpn. J. Appl. Phys.* **21**, L183 (1982).
- [19] S. Zhou, Z. Zhihao, X. Ning, and Z. Xiaofeng, *Mat. Sci. Eng. B.* **25**, 47 (1994).

- [20] D. M. Li, T. Mäntylä, R. Hernberg, and J. Levoska, *Diamond Relat. Mater.* **5**, 350 (1995).
- [21] M. Griesser, G. Stinger, M. Grasserbauer, H. Baumann, F. Link, P. Wurzing, H. Lux, R. Haubner, and B. Lux, *Diamond Relat. Mater.* **3**, 638 (1994).
- [22] K. Hassouni, O. Leroy, S. Farhat, and A. Gicquel, *Plasma Chem. Plasma P.* **18**, 325 (1998).
- [23] W. L. Hsu, *J. Appl. Phys.* **72**, 3102 (1992).
- [24] K. Hassouni, A. Gicquel, M. Capitelli, and J. Loureiro, *Plasma Sources Sci. Technol.* **8**, 494 (1999).
- [25] M. Föner, C. Wild, and P. Koidl, *Appl. Phys. Lett.* **72**, 1149 (1998).
- [26] A. Gicquel, E. Anger, M. F. Ravet, D. Fabre, G. Scatena, and Z. Z. Wang, *Diamond Relat. Mater.* **2**, 417 (1993).
- [27] K. Kobashi, K. Nishimura, Y. Kawate, and T. Horiuchi, *Phys. Rev. B* **38**, 4607 (1988).
- [28] J. Achard, A. Tallaire, R. Sussmann, F. Silva, and A. Gicquel, *J. Cryst. Growth.* **284**, 396 (2005).
- [29] V. Mortet, Z. Hubicka, V. Vorlicek, K. Jurek, and M. V. J. Rosa, *Phys. Stat. Sol. (a)* **201**, 2425 (2004).
- [30] T. Lang, J. Stiegler, Y. V. Kaenel, and E. Blank, *Diamond Relat. Mater.* **5**, 1171 (1996).
- [31] M. C. McMaster, W. L. Hsu, M. E. Coltrin, D. S. Dandy, and C. Fox, *Diamond Relat. Mater.* **4**, 1000 (1995).
- [32] S. M. Leeds, P. W. May, E. Bartlett, M. N. R. Ashfold, and K. N. Rosser, *Diamond Relat. Mater.* **8**, 1377 (1999).
- [33] S. M. Leeds, P. W. May, M. N. R. Ashfold, and K. N. Rosser, *Diamond Relat. Mater.* **8**, 226 (1999).
- [34] J. R. Petherbridge, P. W. May, S. R. J. Pearce, K. N. Rosser, and M. N. R. Ashfold, *J. Appl. Phys.* **89**, 1484 (2001).
- [35] E. Hyman, K. Tsang, A. Drobot, B. Lane, J. Casey, and R. Post, *J. Vac. Sci. Tech. A.* **12**, 1474 (1994).
- [36] K. Hassouni, T. A. Grotjohn, and A. Gicquel, *J. Appl. Phys.* **86**, 134 (1999).
- [37] G. Lombardi, K. Hassouni, G.-D. Stancu, L. Mechold, J. Röpcke, and A. Gicquel, *J. Appl. Phys.* **98**, 053303 (2005).

- [38] H. C. Shih, C. P. Sung, W. L. Fan, and W. T. Hsu, *Thin Solid Films* **232**, 41 (1993).
- [39] D. Zhou, D. M. Gruen, L. C. Qin, T. G. McCauley, and A. R. Krauss, *J. Appl. Phys.* **84**, 1981 (1998).
- [40] W. Zhu, A. Inspektor, A. R. Badzian, T. McKenna, and R. Messier, *J. Applied Phys.* **68**, 1489 (1990).
- [41] Y. F. Zhang, F. Zhang, Q. J. Gao, X. F. Peng, and Z. D. Lin, *Diamond Relat. Mater.* **10**, 1523 (2001).
- [42] G. Lombardi, K. Hassouni, F. Bénédic, F. Mohasseb, J. Röpcke, and A. Gicquel, *J. Appl. Phys.* **96**, 6739 (2004).
- [43] A. Bogaerts, E. Neyts, R. Gijbels, and J. van der Mullen, *Spectro. Acta. B* **57**, 609 (2002).
- [44] K. Kurihara, K. Sasaki, M. Kawarada, and N. Koshino, *Appl. Phys. Lett.* **52**, 437 (1988).
- [45] J. B. Wills, J. A. Smith, W. E. Boxford, J. M. F. Elks, M. N. R. Ashfold, and A. J. Orr-Ewing, *J. Appl. Phys.* **92**, 4213 (2002).
- [46] J. A. Smith, *Laser Diagnostics of a Diamond depositing Chemical Vapour Deposition gas-phase environment*, Ph.D thesis, Universty of Bristol, 2001.
- [47] C. J. Rennick, R. Engeln, J. A. Smith, A. J. Orr-Ewing, M. N. R. Ashfold, and Yu. A. Mankelevich, *J. Appl. Phys* **97**, 113306 (2005).
- [48] M. Frenklach, R. Kematick, D. Huang, W. Howard, and K. E. Spear, *J. Appl. Phys.* **66**, 395 (1989).
- [49] S. E. Stein, *Nature* **346**, 517 (1990).
- [50] H. Liu and D. S. Dandy, *Diamond Relat. Mater.* **4**, 1173 (1995).
- [51] M. P. D'Evelyn, J. D. Graham, and L. R. Martin, *J. Cryst. Growth* **231**, 506 (2001).
- [52] F. G. Celii, P. E. Pehrsson, H. t. Wang, and J. E. Butler, *Appl. Phys. Letts.* **52**, 2043 (1988).
- [53] D. M. Gruen, C. D. Zuiker, A. R. Krauss, and X. Pan, *J. Vac. Sci. Tech. A.* **13**, 1628 (1995).
- [54] L. de Poucques, J. Bougdira, R. Hugon, G. Henrion, and P. Alnot, *J. Phys. D: Appl. Phys.* **34**, 896 (2001).
- [55] C. M. Donnelly, R. W. McCullough, and J. Geddes, *Diamond Relat. Mater.* **6**, 787 (1997).

- [56] J. E. Butler and R. L. Woodin, *Phil. Trans. R. Soc. Lond. A* **342**, 209 (1993).
- [57] D. G. Goodwin and J. E. Butler, in *Handbook of Industrial Diamonds and Diamond Films*, (ed. M. A. Prelas, G. Popovici, and L. G. Bigelow), Marcel Dekker Inc. (1998).
- [58] J. E. Butler and D. G. Goodwin, in *Properties, Growth and Applications of Diamond*, (ed. M. H. Nazaré and A. J. Neves), Institution of Electrical Engineers, Michael Faraday House, Six Hills Way, Stevenage, Herts, SG1 2AY UK (2001).
- [59] C. Wild, P. Koidl, W. Müller-Sebert, H. Walcher, R. Kohl, N. Herres, R. Locher, R. Samlenski, and R. Brenn, *Diamond Relat. Mater.* **3**, 158 (1993).
- [60] C. Wild, R. Kohl, N. Herres, W. Müller-Sebert, and P. Koidl, *Diamond Relat. Mater.* (1994).
- [61] N. Lee and A. Badzian, *Diamond. Relat. Mater.* **6**, 130 (1997).
- [62] C. Nützenadel, O. M. Küttel, L. Diederich, E. Maillard-Schaller, O. Gröning, and L. Schlapbach, *Surf. Sci.* **396**, L111 (1996).
- [63] K. Bobrov, A. Mayne, G. Comtet, G. Dujardin, L. Hellner, and A. Hoffman, *Phys. Rev. B* **68**, 195416 (2003).
- [64] P. Krüger and J. Pollmann, *Phys. Rev. Lett.* **74**, 1155 (1995).
- [65] S. Skokov, C. S. Carmer, B. Weiner, and M. Frenklach, *Phys. Rev. B* **49**, 5662 (1993).
- [66] T. Tsuno, T. Imai, Y. Nishibayashi, K. Hamada<sup>1</sup>, and N. Fujimori, *Jpn. J. Appl. Phys.* **30**, 1063 (1991).
- [67] Y. L. Yang and M. P. D'Evelyn, *J. Am. Chem. Soc.* **114**, 2796 (1992).
- [68] Y. Kuang, N. Lee, A. Badzian, T. T. Tsong, T. Badzian, and C. Chen, *Diamond Relat. Mater.* **4**, 1371 (1995).
- [69] R. E. Stallcup II, L. M. Villarreal, S. C. Lim, I. Akwani, A. F. Aviles, and J. M. Perez, *J. Vac. Sci. Tech. B* **14**, 929 (1996).
- [70] S. Skokov, B. Weiner, M. Frenklach, Th. Frauenheim, and M. Sternberg, *Phys. Rev. B* **52**, 5426 (1995).
- [71] D. Huang and M. Frenklach, *J. Phys. Chem.* **96**, 1868 (1992).
- [72] B. J. Garrison, E. J. Dawnkaski, D. Srivastava, and D. W. Brenner, *Science* **255**, 835 (1992).
- [73] J. K. Kang and C. B. Musgrave, *J. Chem. Phys.* **113**, 7582 (2000).

- [74] H. Tamura and M. S. Gordon, *Chem. Phys. Lett.* **406**, 197 (2005).
- [75] C. C. Battaile, D. J. Srolovitz, I. I. Oleinik, D. G. Pettifor, A. P. Sutton, S. J. Harris, and J. E. Butler, *J. Chem. Phys.* **111**, 4291 (1999).
- [76] H. Tamura, H. Zhou, Y. Hirano, S. Takami, M. Kubo, R. V. Belosludov, A. Miyamoto, A. Imamura, M. N. Gamo, and T. Ando, *Phys. Rev. B.* **62**, 16995 (2000).
- [77] M. Kaukonen, P. K. Sitch, G. Jungnickel, R. M. Nieminen, Sami. Pöykkö, D. Porezag, and T. Frauenheim, *Phys. Rev. B.* **57**, 9665 (1998).
- [78] M. Frenklach, S. Skokov, and B. Weiner, *Nature* **372**, 535 (1994).
- [79] S. J. Harris, *Appl. Phys. Lett.* **56**, 2298 (1990).
- [80] S. J. Harris and D. G. Goodwin, *J. Phys. Chem.* **97**, 23 (1993).
- [81] S. Skokov, B. Weiner, and M. Frenklach, *J. Phys. Chem.* **99**, 5616 (1995).
- [82] M. Sternberg, P. Zapol, and L. A. Curtiss, *Phys. Rev. B* **68**, 205330 (2003).
- [83] S. Walter, J. Bernhardt, U. Starke, K. Heinz, F. Maier, J. Ristein, and L. Ley, *J. Phys.: Condens. Matter* **14**, 3085 (2002).
- [84] L. F. Sutcu, C. J. Chu, M. S. Thompson, R. H. Hauge, J. L. Margrave, and M. P. D'Evelyn, *J. Appl. Phys.* **71**, 5930 (1992).
- [85] K. C. Pandey, *Phys. Rev. B* **25**, 4338 (1982).
- [86] S. Iarlori, G. Galli, F. Gygi, M. Parrinello, and E. Tosatti, *Phys. Rev. Lett.* **69**, 2947 (1992).
- [87] Th. Frauenheima, U. Stephan, P. Blaudeck, D. Porezag, H. -G. Busmann, and W. Zimmermann-Edling, *Phys. Rev. B* **48**, 18189 (1993).
- [88] K. Kobayashi, *Phys. Rev. B* **68**, 075308 (2003).
- [89] M. Marsili, O. Pulci, F. Bechstedt, and R. D. Sole, *Phys. Rev. B* **72**, 115415 (2005).
- [90] A. V. Hamza, G. D. Kubiak, and R. H. Stulen, *Surf. Sci.* **206**, L833 (1988).
- [91] S. Han, J. Ihm, S. G. Louie, and M. L. Cohen, *Phys. Rev. Letts.* **80**, 995 (1998).
- [92] R. C. Brown, C. J. Cramer, and J. T. Roberts, *Diamond Relat. Mater.* **10**, 39 (2001).
- [93] M. Tsuda, M. Nakajima, and S. Oikawa, *J. Am. Chem. Soc.* **108**, 5780 (1986).

- [94] M. Grujicic and S. G. Lai, *J. Mater. Sci.* **35**, 5359 (2000).
- [95] M. Grujicic and S. G. Lai, *J. Mater. Sci.* **35**, 5371 (2000).
- [96] K. Larsson, *Phys. Rev. B* **56**, 15452 (1997).
- [97] D. Huang and M. Frenklach, *J. Phys. Chem* **95**, 3692 (1991).
- [98] K. Larsson and J. O. Carlsson, *Physica. Stat. Sol. A* **186**, 319 (2001).
- [99] C. C. Battaile, D. J. Srolovitz, and J. E. Butler, *Diamond Relat. Mater.* **6**, 1198 (1997).
- [100] C. C. Battaile, D. J. Srolovitz, and J. E. Butler, *J. Cryst. Growth.* **194**, 353 (1998).
- [101] J. Peploski, D. L. Thompson, and L. M. Raff, *J. Phys. Chem.* **96**, 8538 (1992).
- [102] S. Komatsu, K. Okada, Y. Shimizu, and Y. Moriyoshi, *J. Appl. Phys.* **89**, 8291 (2001).
- [103] S. W. Yang, X. Xie, P. Wu, and K. P. Loh, *J. Phys. Chem. B*, **107**, 985 (2003.).
- [104] D. A. Horner, L. A. Curtiss, and D. M. Gruen, *Chem. Phys. Letts.* **233**, 243 (1995).
- [105] M. Sternberg, M. Kaukonen, R. M. Nieminen, and T. Frauenheim, *Phys. Rev. B* **63**, 165414 (2001).
- [106] E. Blank, *Semiconductors and Semimetals* **76**, 49 (2003).
- [107] C. Weigel, D. Peak, J. W. Corbett, G. D. Watkins, and R. P. Messmer, *Phys. Rev. B* **8**, 2906 (1973).
- [108] A. Mainwood, F. P. Larkins, and A. M. Stoneham, *Solid-State Electron* **21**, 1431 (1978).
- [109] G. D. Watkins and R. P. Messmer, *Phys. Rev. Letts.* **32**, 1244 (1974).
- [110] M. E. Newton, J. M. Baker, and D. J. Twitchen, in *Properties, Growth and Applications of Diamond*, (ed. M. H. Nazaré and A. J. Neves), Institution of Electrical Engineers, Michael Faraday House, Six Hills Way, Stevenage, Herts, SG1 2AY UK (2001).
- [111] C. D. Clark and J. Walker, *Proc. R. Soc. Lond. A.* **234**, 241 (1973).
- [112] G. Davies and C. M. Petchina, *Proc. R. Soc. Lond. A.* **338**, 359 (1974).
- [113] G. Davies, *Nature* **269**, 498 (1977).

- [114] A. Mainwood and A. M. Stoneham, *J. Phys. Condense. Matter.* **9**, 2453 (1997).
- [115] E. B. Lombardi, A. Mainwood, and K. Osuch, *Phys. Rev. B.* **70**, 205201 (2004).
- [116] L. G. Wang and A. Zunger, *Phys. Rev. B* **66**, 161202(R) (2002).
- [117] A. T. Collins and A. W. S. Williams, *J. Phys. C: Solid State Phys* **4**, 1789 (1971).
- [118] Z. Y. Xie, J. H. Edgar, T. L. McCormick, and M. V. Sidorov, *Diamond Relat. Mater.* **7**, 1357 (1998).
- [119] S. Yamanaka, H. Watanabe, S. Masai, D. Takeuchi, H. Okushi, and K. Kajimura, *Jpn. J. Appl. Phys.* **37**, L1129 (1998).
- [120] P. Wurzinger, P. Pongratz, P. Hartmann, R. Haubner, and B. Lux, *Diamond Relat. Mater.* **6**, 763 (1997).
- [121] A. Deneuve, *Semiconductors and Semimetals* **76**, 183 (2003).
- [122] P. Hartmann, S. Bohr, R. Haubner, B. Lux, P. Wurzinger, M. Griesser, A. Bergmaier, G. Dollinger, H. Sternschulte, and R. Sauer, *Int. J. Refract. Met. Hard Mater.* **16**, 223 (1997).
- [123] X. H. Wang, G. H. M. Ma, W. Zhu, J. T. Glass, L. Bergman, K. F. Turner, and R. J. Nemanich, *Diamond Relat. Mater.* **1**, 828 (1992).
- [124] E. Gheeraert, A. Deneuve, and J. Mambou, *Carbon* **73**, 107 (1999).
- [125] P. Gonon, A. Deneuve, F. Fontaine, E. Gheeraert, A. Campargue, M. Chenevier, and S. Rodolphe, *J. Appl. Phys.* **78**, 7404 (1995).
- [126] M. Hata, M. Tsuda, N. Fujii, and S. Oikawa, *Appl. Surf. Sci.* **79/80**, 255 (1994).
- [127] R. Samlenski, C. Haug, R. Brenn, C. Wild, R. Locher, and P. Koidl, *Diamond Relat. Mater.* **5**, 947 (1996).
- [128] J. C. Angus, Y. V. Pleskov, and S. C. Eaton, *Semiconductors and Semimetals* **77**, 97 (2004).
- [129] R. Locher, J. Wagner, F. Fuchs, M. Maier, P. Gonon, and P. Koidl, *Diamond Relat. Mater.* **4**, 678 (1995).
- [130] J. H. Edgar, Z. Y. Xie, and D. N. Braski, *Diamond Relat. Mater.* **7**, 35 (1998).
- [131] J. F. H. Custers, *Physica* **18**, 489 (1952).
- [132] S. Bohr, R. Haubner, and B. Lux, *Applied Physic Letters* **68**, 1075 (1996).

- [133] R. Locher, C. Wild, N. Herres, D. Behr, and P. Koidl, *Applied Physics Letters* **65**, 34 (1994).
- [134] R. G. Farrer, *Solid State Commun.* **7**, 685 (1969).
- [135] D. Saada, J. Adler, and R. Kalish, *Applied Physics Letters* **77**, 878 (2000).
- [136] H. Zhou, Y. Yokoi, H. Tamura, S. Takami, M. Kubo, A. Miyamoto, N. M. Gamo, and T. Ando, *Jpn. J. Appl. Phys.* **40**, 2830 (2001).
- [137] J. R. Petherbridge, P. W. May, G. M. Fuge, G. F. Robertson, K. N. Rosser, and M. N. R. Ashfold, *J. Appl. Phys.* **91**, 3605 (2002).
- [138] I. Sakaguchi, M. N.-Gamo, Y. Kikuchi, E. Yasu, H. Haneda, T. Suzuki, and T. Ando, *Phys. Rev. B* **60**, R2139 (1999).
- [139] R. Kalish, A. Reznik, C. Uzan-Saguy, and C. Cytermann, *Appl. Phys. Lett.* **76**, 757 (2000).
- [140] M. Hasegawa, T. Teraji, and S. Koizumi, *Appl. Phys. Lett.* **79**, 3068.
- [141] S. Koizumi, M. Kamo, Y. Sato, H. Ozaki, and T. Inuzuka, *Appl. Phys. Lett.* **71**, 1065 (1997).
- [142] S. Koizumi, T. Teraji, and H. Kanda, *Diamond Relat. Mater.* **9**, 935 (2000).
- [143] M. Katagiri, J. Isoya, S. Koizumi, and H. Kanda, *Appl. Phys. Lett.* **85**, 6365 (2004).
- [144] E. Gheeraert, S. Koizumi, T. Teraji, H. Kanda, and M. Nesladek, *Physica Status Solidi A* **174**, 39 (1999).
- [145] Y. Koide, S. Koizumi, H. Kanda, M. Suzuki, H. Yoshida, N. Sakuma, T. Ono, and T. Sakai, *Appl. Phys. Lett.* **86**, 232105 (2005).
- [146] O. Gaudin, D. K. Troupis, R. B. Jackman, C. E. Nebel, S. Koizumi, and E. Gheeraert, *J. Appl. Phys.* **94**, 5832 (2003).
- [147] Y. Yan, S. B. Zhang, and M. M. Al-Jassim, *Phys. Rev. B* **66**, 201401.
- [148] S. A. Kajihara, A. Antonelli, and J. Bernholc, *Phys. Rev. Lett.* **66**, 2010 (1991).
- [149] C. Uzan-Saguy, C. Cytermann, B. Fizegeer, V. Richter, R. Brener, and R. Kalish, *Physica Status Solidi (a)* **193**, 508 (2002).
- [150] R. Kalish, *Diamond Relat. Mater.* **10**, 1749 (2001).
- [151] J. P. Goss, P. R. Briddon, R. Jones, and S. Sque, *Diamond Relat. Mater.* **13**, 684 (2004).

- [152] Z. Teukam, J. Chevallier, C. Saguy, R. Kalish, D. Ballutaud, M. Barbé, F. Jomard, A. Tromson-Carli, C. Cytermann, J. E. Butler, M. Bernard, C. Baron, and A. Deneuve, *Nature Materials* **2**, 482 (2003).
- [153] J. P. Goss, P. R. Briddon, S. J. Sque, and R. Jones, *Phys. Rev. B* **69**, 165215 (2004).
- [154] J. Isberg, J. Hammersberg, E. Johansson, T. Wikström, D. J. Twitchen, A. J. Whitehead, S. E. Coe, and G. A. Scarsbrook, *Science* **297**, 1670 (2002).
- [155] A. Gicquel, K. Hassouni, F. Silva, and J. Achard, *Curr. Appl. Phys.* **1**, 479 (2001).
- [156] M. N. Latto, D. J. Riley, and P. W. May, *Diamond Relat. Mater* **9**, 1181 (1999).
- [157] S. Koizumi, K. Watanabe, F. Hasegawa, and H. Kanda, *Science* **292**, 1899 (2001).
- [158] E. A. Ekimov, V. A. Sidorov, E. D. Bauer, N. N. Mel'nik, N. J. Curro, J. D. Thompson, and S. M. Stishov, *Nature* **428**, 542 (2004).

## **Chapter 2**

# **Resonance Enhanced Multiphoton Ionisation studies of atomic Boron in $B_2H_6 / H_2$ and $B_2H_6 / CH_4 / H_2$ gas mixtures relevant to Boron doped CVD diamond growth**

This study looks at the roles of atomic hydrogen, boron atoms and methane in HF activated  $B_2H_6 / CH_4 / H_2$  gas mixtures such as are used for the growth of boron doped diamond. Variables investigated include filament temperature, %  $B_2H_6$ , the presence (or not) of  $CH_4$  and the distance of the laser focus from the filament, all of which are studied by measuring relative concentrations of boron and hydrogen atoms using a multiphoton ionisation technique.

## 2.1 Introduction

### 2.1.1 History of Borane research

Investigations in borane chemistry started at the turn of the 20th century with the development of air free synthesis techniques by Alfred Stock who, over 20 years, identified and categorised a wide range of species from diborane ( $B_2H_6$ ) to  $B_{10}H_{14}$ . The main bulk of research in borane chemistry was performed around the space race era with the development of boron based rocket fuels, as oxidation reactions of  $B_zH_x$  species are highly exothermic due to the formation of strong Boron-Oxygen bonds, (2.1) [1].



Research into borane combustion is progressing with the development of high power combustion systems fuelled by boron containing slurries [2] and accurate theoretical combustion models [3]. An excellent review of borane oxidation chemistry is by Bauer [4]. Important areas of contemporary borane research are metal hardening, usually steel, by boron diffusion from a borane plasma; production of hard boron nitride / boron carbide coatings and films [5] – [9], and studies of  $MgB_2$  superconductors [10].

### 2.1.2 The properties of Boranes

Atomic boron, with an electronic configuration of  $1s^2 2s^2 2p^1$ , is considered to be the classic example of an electron deficient species.  $sp^2$  hybridisation is energetically affordable and thus boron typically forms tri-valent species with an empty p orbital localised on the boron atom.

Diborane is one of the more common forms of borane, Figure 2.1. The main feature of this molecule is the bridging H atoms which undergo a three centre – two electron bond. These ‘non traditional’ covalent bonds are formed to satisfy the electron deficient nature of the boron atom and X-ray crystallography that proved their existence resulted in the award of the 1976 Nobel prize to W. M. Lipscomb [11].

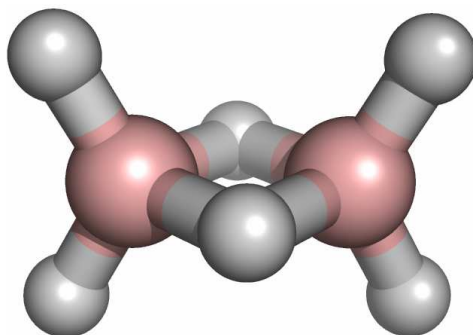


**Figure 2.1:** Structure of  $B_2H_6$  showing the three centre – two electron bridging hydrogen bonds

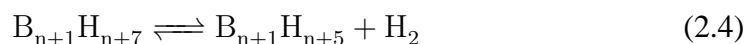
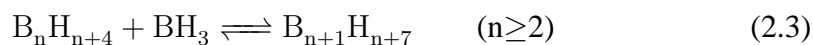
Diborane readily dissociates into two unstable  $BH_3$  components by breaking the weaker bonds holding the bridging hydrogen atoms in place, equation (2.2). This can be instigated by photolysis (e.g. with UV laser light) or by pyrolysis. Thermal decomposition of diborane has been reported over a wide range of temperatures, ranging from 273 K to 1073 K [12] – [15].



Historically, borane compounds have been the focus of intense spectroscopic and theoretical studies including work on the boron atom [16] – [19], and BH [20] – [22],  $BH_2$  [23],  $BH_3$  [24] and  $BH_4$  [25] species.

There have been intensive investigations of boron cluster production using diborane precursors. These reactions occur at low temperatures and high diborane

concentrations and can lead to clusters of various sizes (2.3) [26], [27]. The mechanism and kinetics of these gas phase inter conversions is highly debated and a good recent review is by Greenwood [28].



Studies into dissociation of diborane within a IR activated silicon epitaxial film reactor show that the diborane dissociation can be mediated on the internal surfaces of the reactor. This causes the formation of boron clusters of various sizes, which can desorb from the reactor walls, Figure 2.2 [29]. The equilibria between the gas-phase and surface bound borane clusters can regulate the levels of  $BH_x$  species within the reactor.

Theoretical studies of thermal decomposition of  $BCl_3 / H_2$  gas mixtures show, indirectly, the  $BH_3$  degradation reactions with hydrogen species [30], [31]. Harris *et al.* have calculated reaction mechanisms and rates for hydrogen abstraction from, and insertions into,  $BH_x$ ,  $x = 0 - 3$  species using standard transition state theory at the G2 level of theory. (The G2 level of computational theory is based upon the parameterised results of *ab-initio* calculations of 125 species [32] – [34]). Transition state theory is discussed in more detail in Chapter 3.

For hydrogen addition and abstraction reactions with  $BH_x$ , there are two competing processes; a direct mechanism (the equivalent reactions of (1.3) from Chapter 1) and a pathway occurring through a low energy  $BH_{x+1}$  intermediate formed from coordination of the atomic hydrogen with the valence p orbital on the boron atom, Eq. (2.5). Molecular hydrogen incorporation / abstraction reactions occur

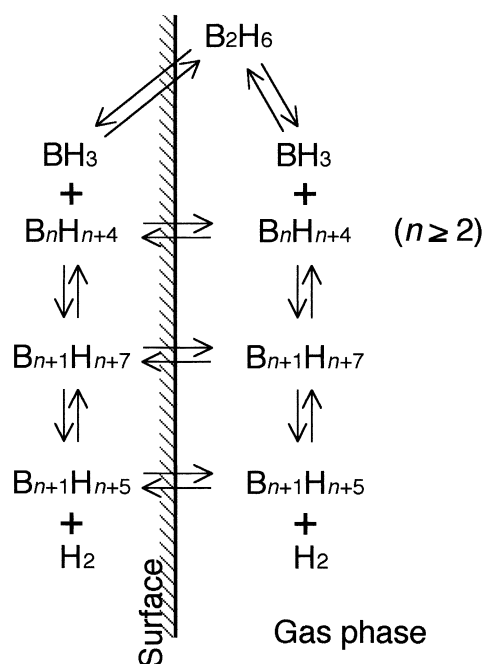
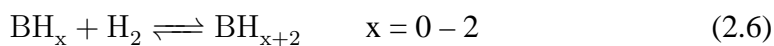
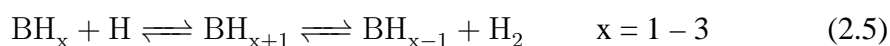


**Figure 2.2:** Schematic showing how borane clusters can be generated in the gas phase and upon surfaces and the subsequent interactions between the two phases, from ref [29].

in a similar manner, via a distorted transition state, via coordination to an empty orbital, Eq. (2.6). These reactions have been studied for BH [22] and related carbyne reactions [35], [36]. Reactions involving atomic hydrogen are feasible up to  $x = 3$ , where the empty orbital on the boron atom and trigonal geometry enables the formation of  $\text{BH}_4$ .



Harris *et al.* showed that for  $\text{BH}_3$ , hydrogen abstraction reactions only occur via the co-ordination of the abstracting atom (2.5) at low temperatures but, above 1900 K, the direct abstraction reaction is more prevalent. BH species have been

detected by optical emission spectroscopy in microwave plasmas growing doped diamond from  $B_2H_6 / CH_4 / H_2$  gas mixtures [37], [38].

## 2.2 Resonance Enhanced Multiphoton Ionisation (REMPI)

### 2.2.1 Theory

Ionisation of species requires an electron to absorb enough energy to raise it above the ionisation potential (I. P.). In most situations, the I.P. of a system is too large to be directly accessible by absorption of a single photon of visible / UV light but absorption of multiple photons can make ionisation viable. Direct multiple photon ionisation is a relatively unlikely process unless using extremely intense short pulsed lasers, as it requires a very high photon density.

However, the probability of a multiphoton ionisation process is greatly enhanced if there is an intermediate ‘stepping stone’ electronic state of the system resonant at the energy of one (or two) absorbed photons. The resulting ion or electron can be detected in multiple ways including time of flight mass spectrometry or electrostatic interactions with a biased wire.

The multiphoton absorption is usually described as an  $(m + n)$  REMPI process where  $m$  is the number of photons needed to excite the species to the ‘stepping stone’ electronic state and  $n$  is the number of photons required for the final ionisation step. Figure 2.3 shows the most commonly used multiphoton ionisation processes for atomic boron.

The REMPI process is highly species selective as ionisation depends upon the internal electronic structures and the I.P. of the probed sample. In the case of molecular species, rotation–vibration excitation spectra can be recorded by REMPI by

selective population of a vibrational state by tuning the probing laser light to the appropriate frequency. The REMPI process is also a localised technique because tight focusing to a small volume is required to generate the high photon density required for the multiphoton absorption process.

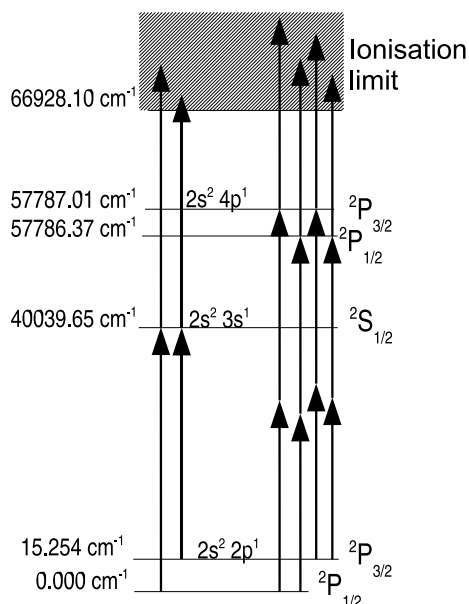


**Figure 2.3:** Grotrian diagram for atomic boron, showing the possible (1+1) and (2+1) REMPI process

## 2.2.2 Previous HF CVD REMPI Studies

The current Bristol REMPI reactor was designed [39] to investigate the local distribution of H atoms in the vicinity of a hot filament [40] using a (2+1) REMPI detection process. The method showed that the surface of the filament was critical in the production of H atoms with hydrogen molecules adsorbing onto the hot filament surface and undergoing bond dissociation, catalysed by the metal, and atomic hydrogen atoms dissociating from the filament surface with high thermal energy, contributing to the localised gas heating. This confirmed the observed trends from the earlier (3+1) REMPI studies by Celii and Butler [41].

CH<sub>3</sub> distributions have been measured using 2+1 REMPI via the  $3p_z: {}^2A_2'' \leftarrow \tilde{X}^2A_2''$  transition from HF activated CH<sub>4</sub> / H<sub>2</sub> [42], [43] and C<sub>2</sub>H<sub>2</sub> / H<sub>2</sub> [44] gas mixtures which shows that there is a gas phase chemical interconversion between the two species. A more detailed discussion of methane-acetylene interconversion chemistry can be found in Chapter 6. The work reported here is, to the best of our knowledge, the first study of B atoms in such an HF CVD environment.

### 2.2.3 Boron REMPI

Boron hydride compounds have strong boron–hydrogen bonds ( $\text{BH}_2 + \text{H} \longrightarrow \text{BH}_3$ ;  $\Delta\text{H} = 312.1 \text{ kJ mol}^{-1}$ ) which are approximately  $100 \text{ kJ mol}^{-1}$  weaker than the corresponding carbon hydride bond ( $\text{CH}_3 + \text{H} \longrightarrow \text{CH}_4$ ;  $\Delta\text{H} = 438.6 \text{ kJ mol}^{-1}$ ). (Bond strengths are derived from the experimental values for the enthalpy of formation of the CH<sub>3</sub>, CH<sub>4</sub>, BH<sub>2</sub>, BH<sub>3</sub> & H species from ref [45]). This suggests that boron hydrides should behave similarly to methane in a diamond CVD environment but that boron–hydrogen bond breaking reactions should be more facile.

Simple thermodynamical analysis of B<sub>2</sub>H<sub>6</sub> / H<sub>2</sub> gas mixtures in the presence of H atoms indicates that, at low temperatures (<500 °C), diborane is the most thermodynamically stable species. At HF–CVD gas temperatures (~1800 °C, in the immediate vicinity of the filament), reactions (2.2) and (2.5) will favour the products and the equilibrium overall should shift in favour of boron atoms. Figure 2.4 shows the variation in equilibrium constant as function of temperature, relevant to CVD diamond growth, for the hydrogen abstraction reaction (2.5), using data from Appendix D. A more detailed discussion of the statistical mechanics and methods will be presented in Chapter 4.

Atomic boron ( $1s^2 2s^2 2p^1$ ) has two possible ground state configurations ( ${}^2P_{1/2}^0$ ,  ${}^2P_{3/2}^0$ ) separated by  $15.254 \text{ cm}^{-1}$  [46] from which the REMPI process can occur.

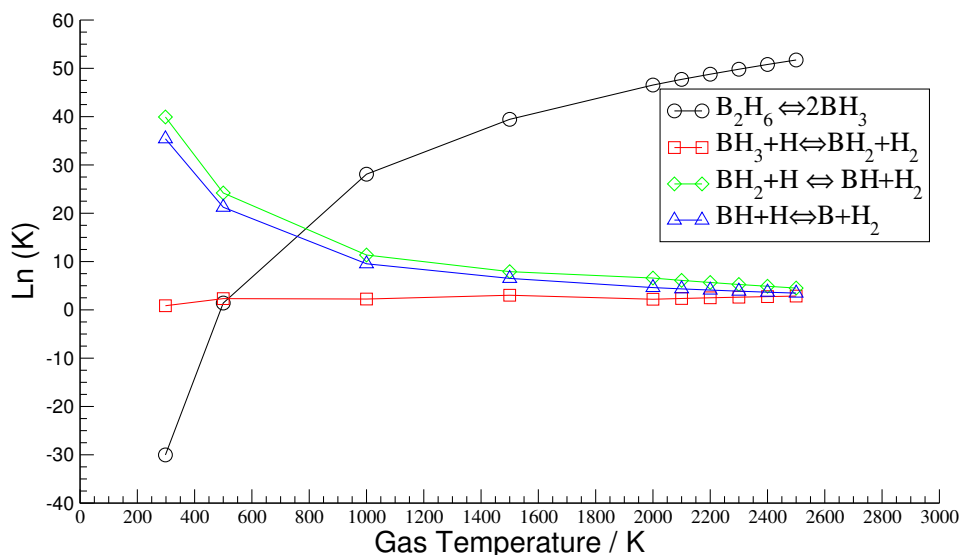


**Figure 2.4:** Predicted variation in equilibrium constant as a function of temperature for diborane dissociation equation (2.2) and hydrogen abstraction reactions from  $\text{BH}_x$ ,  $x = 1 - 3$  species, equation (2.5).

This can be achieved by a 3 colour double resonance scheme [17] or more simply, by 1 colour REMPI via the  $2s^23s^1$  state ((1+1) REMPI,  $^2\text{S}_{1/2}$ ,  $40040 \text{ cm}^{-1}$ ) or the  $2s^24p^1$  state ((2+1) REMPI,  $^2\text{P}_{3/2}^0$ ,  $57787.0 \text{ cm}^{-1}$ ;  $^2\text{P}_{1/2}^0$ ,  $57786.3 \text{ cm}^{-1}$ ), Figure 2.3 [18].

## 2.3 Experimental

The experimental set up has been described previously [47] and is shown in Figure 2.5. The CVD chamber consists of a 6-way cross (baseline pressure  $10^{-2}$  Torr) fitted with quartz windows to enable transmission of the probing laser. The filament (Ta,  $250 \mu\text{m}$  dia. 7 coils,  $\sim 3 \text{ mm}$  coil dia.) is attached to the top flange, via a mount which moves normal to the incident laser beam. The temperature of the filament is measured by a 2 colour pyrometer (Landmark X) mounted perpendicular to the filament laser plane. Hydrogen (98-99 sccm), Methane (0-5 sccm) and Diborane (4.75% in  $\text{H}_2$ ; 0-1 sccm) are mixed before introduction to the chamber and the

pressure is regulated at 20 Torr.

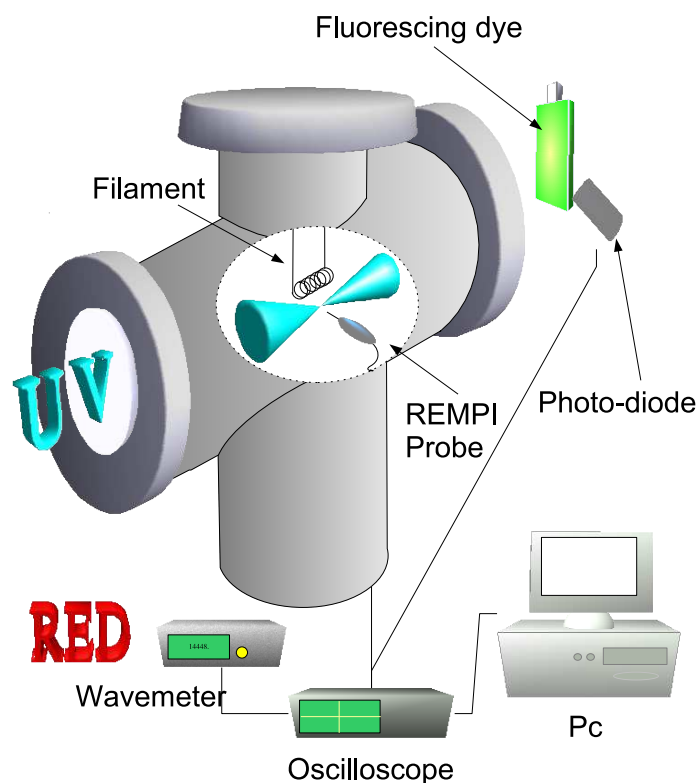


**Figure 2.5:** Experimental setup for REMPI studies of boron atoms in CVD reactor. Two side arms of the reactor have been omitted for clarity.

1+1 REMPI detection occurs at a wavelength of 249 nm generated by a Nd:YAG pumped dye laser (Surelight 11-10, third harmonic (355 nm), pumping a PDL3) at 10 Hz using LD490 dye mixture and a BBO doubling crystal. B atoms are detected using (2+1) REMPI with a wavelength  $\sim 346$  nm [18] using the same laser system but with an LDS 698 dye mixture (end pumped) and a KD\*P doubling crystal (in conjunction with the 2<sup>nd</sup> harmonic output from the Nd:YAG laser). H atom detection occurred at  $\sim 243.1$  nm using a Coumarin 480 dye mixture and a BBO double crystal, together with 355 nm pumping.

The fundamental and frequency doubled dye laser light are separated using a Pellin Broca prism and the doubled light (pulse energy 1-3 mJ), is steered via a right angle prism and focused with a 25 cm Quartz lens to a spot about 1 mm

above a probe wire (Pt, 0.5 mm dia) in the centre of the chamber. The wire is biased to -50 V so as to detect positive ions generated in the laser focal volume. Any transient pulse so detected is passed onto an oscilloscope (LeCroy 9450) and recorded on a PC via a GPIB interface. UV light passing through the chamber is reflected into a cuvette of fluorescent dye (Rhodamine 6G). The fluorescence is measured using a photodiode and the values are used for power normalisation. Undoubled light, (exiting along a different axis) from the Pellin-Broca prism, was passed through a beam splitter which reflected a fraction of the light into a wave meter (Coherent Wavemaster). The signal from this photodiode was monitored as the laser wavelength was scanned using a boxcar averager (SRS) and recorded on the PC. Data were recorded using the in house “Drive” program.

For investigations involving  $B_2H_6 / H_2$  gas mixtures, filaments were first baked in  $H_2$  background, then for a further hour after the introduction of diborane to the system at 2100 °C prior to making any measurements. For experiments using  $CH_4 / B_2H_6 / H_2$  gas mixtures, the filament was preconditioned in  $CH_4 / H_2$  at 2100 °C for 6 hours. Diborane was then introduced before experimenting 1 hour later.

## 2.4 Results

### 2.4.1 (1+1) REMPI of Boron Atoms

Initial studies focused on the (1+1) REMPI of boron atoms using the  $3s \leftarrow 2p$  transition at  $40040 \text{ cm}^{-1}$ . Figure 2.6 shows a typical broad spectrum.

Recalling the Grotrian diagram (Figure 2.3), we can see that this should be a strongly allowed one-photon transition satisfying all elements of the Laporte selection rules. This is confirmed by the short radiative lifetime of the  $\dots 3s^1 ({}^2S_{1/2})$  excited state,  $\tau \sim 4 \text{ ns}$  [48]. Population excited to the  $\dots 3s^1$  state by one photon

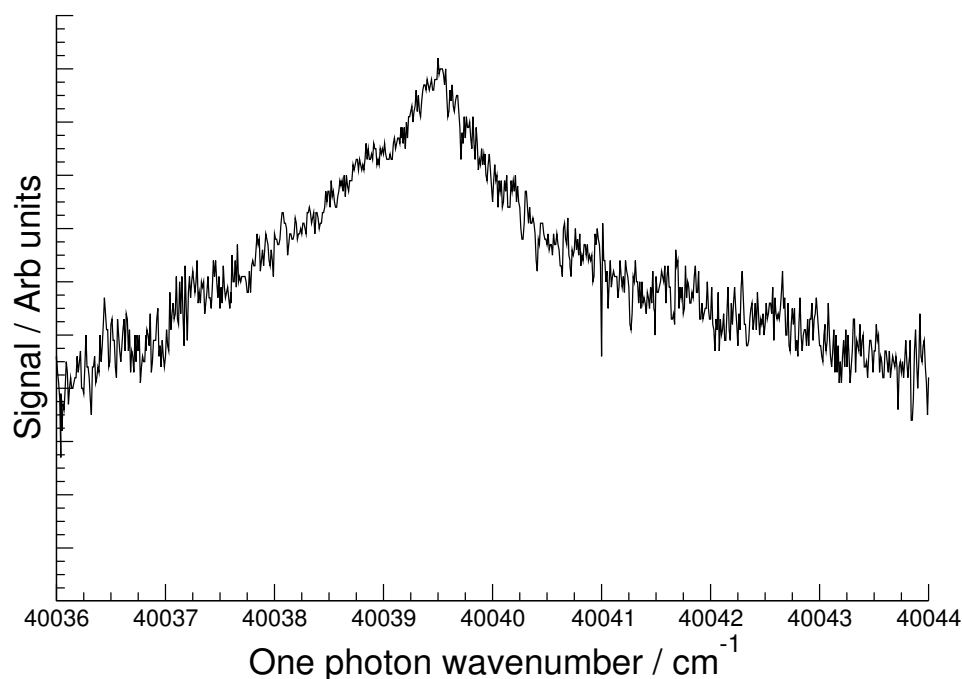


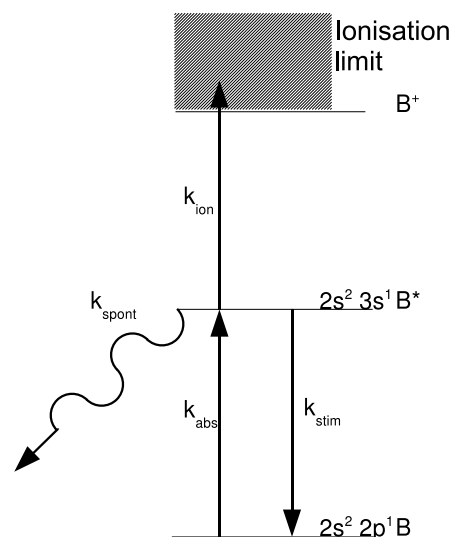
**Figure 2.6:** (1+1) REMPI spectra of B atoms in HF reactor at 0.0475 %  $\text{B}_2\text{H}_6 / \text{H}_2$ , with a  $T_{\text{fil}}$  of  $2273^\circ \text{C}$  at 20 Torr.

absorption can thus be lost by spontaneous fluorescence with rate constant ( $k_{\text{spont}}$ ) or by interacting with a further photon ( $k_{\text{ion}}$ ). The large width of the observed transition can be understood by assuming that the rate of stimulated emission ( $k_{\text{stim}} [\text{B}^*]$ ) back to the ground state is much greater than the ionisation rate, Figure 2.7. Both processes have linear dependencies with the laser intensity whilst only the latter process generates the  $\text{B}^+$  ions we depend on for detection.

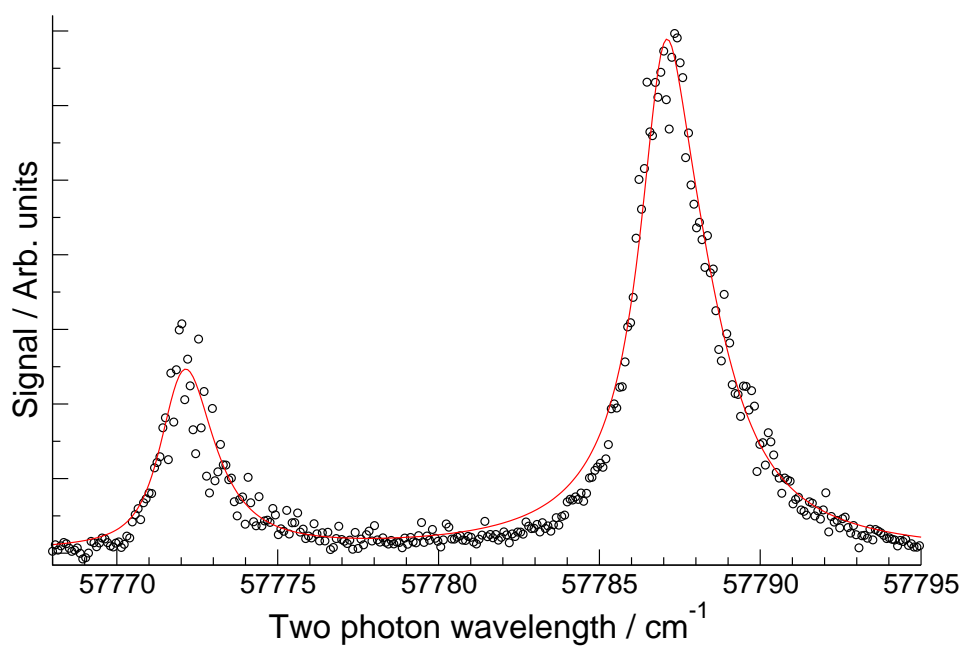
## 2.4.2 (2+1) REMPI of Boron Atoms

Figure 2.8 shows a composite power-normalised (2+1) REMPI spectrum of the  $2s^14p^1 \leftarrow 2s^12p^1$  transition of the boron atom, using 0.0475 %  $\text{B}_2\text{H}_6$  in  $\text{H}_2$  gas probed at a distance of 0.5 mm below the filament maintained at 2273 K.

The lineshapes consist of two closely-spaced and incompletely resolved transitions to the  $J = \frac{1}{2}$  and  $\frac{3}{2}$  spin-orbit components of the excited  $4p^1$  state. There is



**Figure 2.7:** Grotrian diagram showing the competitive processes for atomic boron (1+1) REMPI process.



**Figure 2.8:**  $2s^2 4p^1 \leftarrow 2s^2 2p^1$  B atom (2+1) REMPI signal of 0.0475%  $B_2H_6$ , filament temperature ( $T_{fil}$ ) = 2273 K at 20 Torr and a laser focus at  $d = 0.5$  mm from the filament. Red line is a Lorentzian least square fit to the experimental data.

a corresponding feature from the  $^2P_{3/2}$  level of the ground ( $2p^1$ ) state  $15.25 \text{ cm}^{-1}$  to lower wavenumber. The different populations of the two spin-orbit components

(2.7) of the ground state, in combination with the wavelength dependant variation in UV output (due to the fixed KD\*P crystal experimental setup), leads to the two peaks having different intensities. However, as studies focused on changes in relative intensities, both transitions could be used to monitor process conditions.

$$\frac{N_{3/2}}{N_{1/2}} = \frac{2J' + 1}{2J'' + 1} \exp(-\Delta E/kT) \quad (2.7)$$

Each of the major features is fitted to two Lorentzian functions, by means of a least squares fitting algorithm, indicating that the lineshape is dominated by a homogeneous broadening mechanism. It is instructive to consider the various possible line broadening contributions to the measured lineshape. The laser linewidth itself is  $< 0.2 \text{ cm}^{-1}$  in the UV and negligible on the scale of the present measurements. Equation (2.8) describes the Doppler contribution to the Full Width Half Maximum (FWHM) of a transition whilst probing a volume in local thermodynamic equilibrium (i.e. a Maxwellian velocity distribution).

$$\Delta\nu_D = \frac{\nu_0}{c} \sqrt{\frac{8kT \ln 2}{M}} \quad (2.8)$$

where  $\nu_0$  is the central line transition frequency,  $c$  is the speed of light and  $M$  is the mass of the probed species in kg.

At typical near filament gas temperatures (1800 K), the Doppler contribution to the FWHM would be  $\sim 0.53 \text{ cm}^{-1}$  (c.f the total FWHM of  $1.9 \text{ cm}^{-1}$ ). Pressure broadening will be negligible under the prevailing experimental conditions. The Lorentzian broadened boron signal is thus most readily attributed to the effects of power broadening whereby the second step of the (2+1) REMPI process is assumed to be partially saturated. This is not uncommon in (m+1) REMPI processes ( $m > 1$ ) that the one photon transitions from the  $2s^1 4p^1$  state to the ionisation continuum is much more probable than the initial 2 photon absorption. The (probable) one

photon ionisation reduces the excited state lifetime and thus increases the FWHM because of the Heisenberg uncertainty principle (2.9).

$$\Delta\nu\Delta t \sim \frac{1}{2\pi} \quad (2.9)$$

This effectively reduces the stabilising resonance effect of the  $2s^14p^1$  excited state and masks both the Doppler broadening and the  $0.638 \text{ cm}^{-1}$  excited state splitting. Figure 2.9(a) shows the relationship between the (2+1) REMPI signal for B atoms at  $57771.760 \text{ cm}^{-1}$  and the incident laser pulse energy, and provides further support for the idea that the (2+1) REMPI process is partially saturated under experimental conditions.

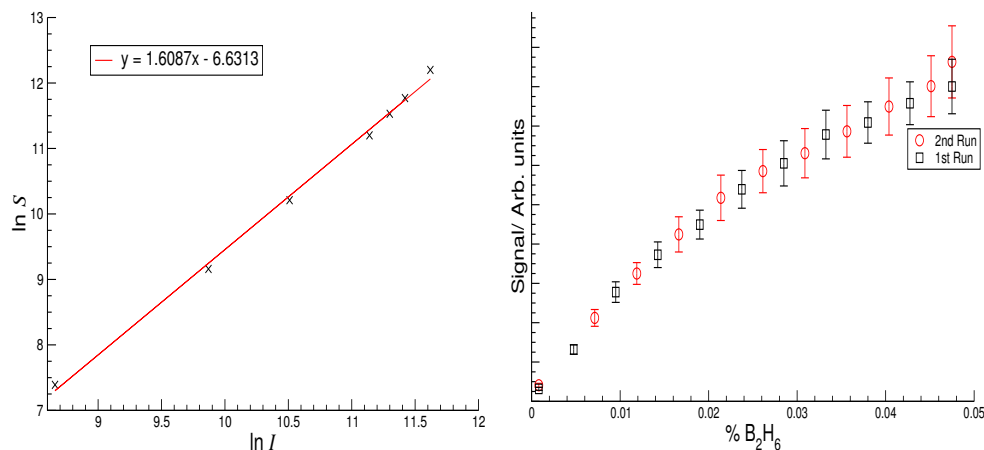
For an ideal (m+1) REMPI system, where the m-photon step is rate limiting, the ion yield signal  $S$  should scale with the laser intensity  $I$  (and thus the pulse energy) according to:

$$S \propto I^m \quad (2.10)$$

Thus for a (2+1) REMPI system,  $m$  should have a value of 2, but in this system, as Figure 2.9(a) shows, the measured gradient is 1.61 which is consistent with the previous discussion. Analogous studies of H atoms using (2+1) REMPI centred at 243.1 nm under similar conditions gave  $S \propto I^2$  and Doppler widths consistent with eq (2.8) [40]. (Note that the Doppler broadening is  $\sim \sqrt{10}$  greater in the case of H atoms because of their much lighter mass).

### **B<sub>2</sub>H<sub>6</sub> / H<sub>2</sub> gas mixtures**

B atom REMPI signals have been characterised as functions of process conditions with all data being power normalised according to Figure 2.9(a). Results show



(a) The measured REMPI signal versus laser power relationship at a laser frequency of  $28885.9 \text{ cm}^{-1}$ ,  $T_{\text{fil}}$  of 2273 K and a laser focus at  $d=2 \text{ mm}$  from the filament.

(b) The correlation between (2+1) REMPI signal at a laser frequency of  $28885.6 \text{ cm}^{-1}$  and % Diborane,  $T_{\text{fil}}$  of 2273 K and a laser focus at  $d= 2 \text{ mm}$  from the filament.

**Figure 2.9:** Fundamental Tests of (2+1) REMPI signal of B Atoms in the HF-CVD environment

that REMPI can easily detect B atoms in a HF activated 0.00475 %  $B_2H_6 / H_2$  gas mixture (Figure 2.9(b)) and that there is a positive correlation between B atom REMPI signal and diborane concentrations.

Figure 2.10 shows the measured variation in B and H REMPI signals with increasing distance from the hot filament. The observed decline in H atom REMPI signal with distance is consistent with atomic hydrogen dissociation mediated on the surface of the filament with a local maxim near the filament, as discussed in Section 2.2.2. The local gas temperature in the volume probed by the laser, can be deduced from the Doppler contribution to the FWHM using equation (2.8). Figure 2.11 shows a gradual decrease in temperature with increasing distance from the filament. The introduction of diborane reduces the temperature (deduced from the FWHM of the H REMPI scans) of the gas mixtures in the region of the filament by approximately 300 K. Measured B REMPI signal increases with distance which is in contrast to the results for H atoms (and  $CH_3$  radicals from previous studies

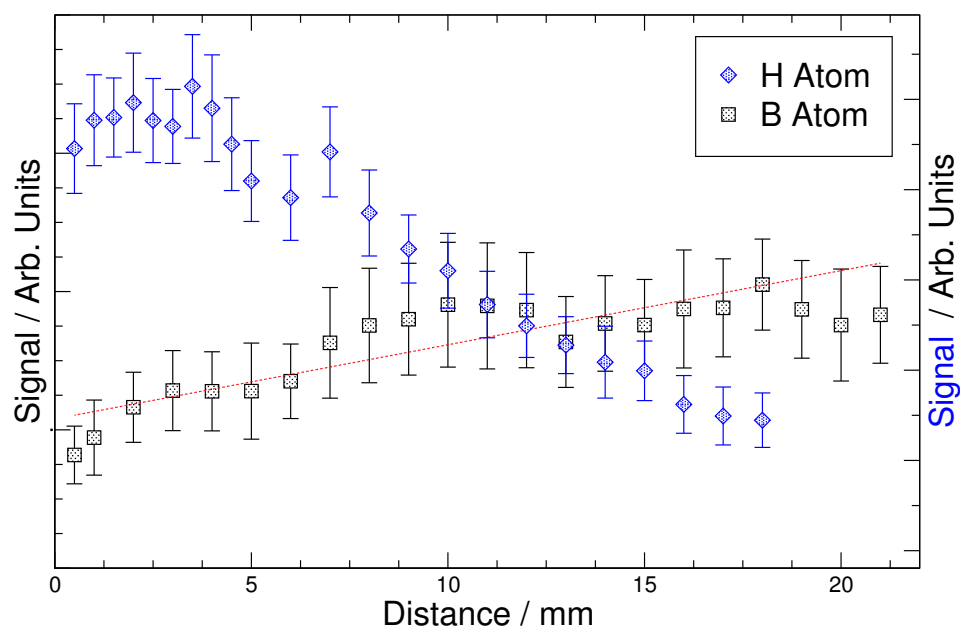


**Figure 2.10:** Graph showing the relationship between the distance between the laser focus and the HF and REMPI signal for boron atoms (laser frequency of  $28885.9 \text{ cm}^{-1}$ ) and H atoms (laser frequency of  $41128.5 \text{ cm}^{-1}$ ) with a gas mixture of  $0.0475\% \text{ B}_2\text{H}_6 / \text{H}_2$  with  $T_{\text{fil}} = 2273 \text{ K}$ .

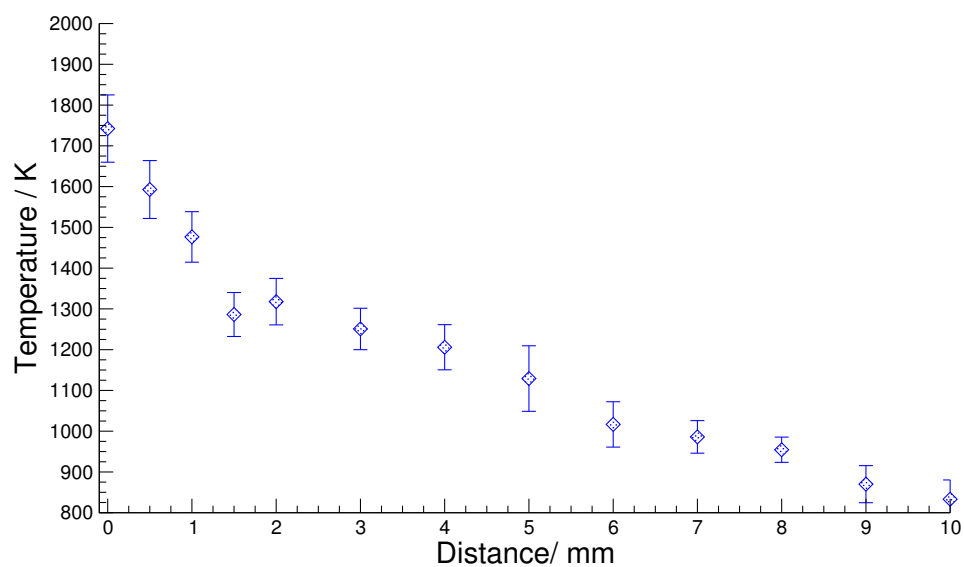


**Figure 2.11:** Temperature profiling of HF reactor operating with pure  $\text{H}_2$  and a filament temperature of  $2673 \text{ K}$  using H atom Doppler broadened line shapes and equation 2.8 to estimate local gas temperature [49].

[44]). This is unprecedented behaviour for a transient species in a HF reactor. Assuming ideal gas conditions for the reactor, it is a fair approximation that under

constant pressure, the local number density is inversely proportional to the local temperature. The local number density is proportional to the REMPI signal. Using the Smith *et al.* [49] temperature profiles, Figure 2.11, we suggest that the boron atom mole fraction will be almost constant across the whole chamber, with no local maximum near the filament.

Measurement of B REMPI Signal versus  $T_{\text{fil}}$  provides further insight into the role of the HF. Figure 2.12 shows that the B REMPI signal is highly dependent upon  $T_{\text{fil}}$  with a maximum in B REMPI signal at 2173 K. H REMPI measure-

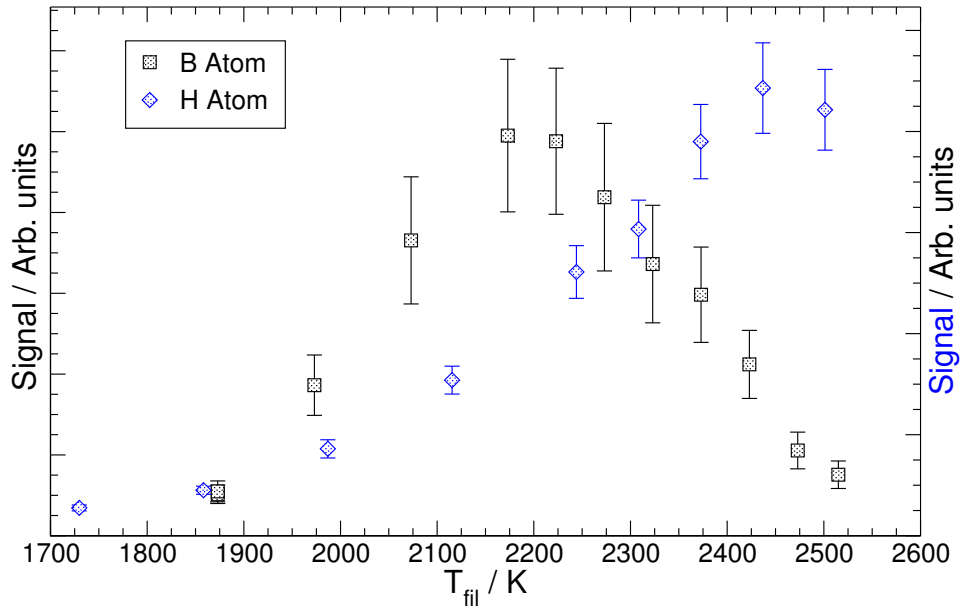
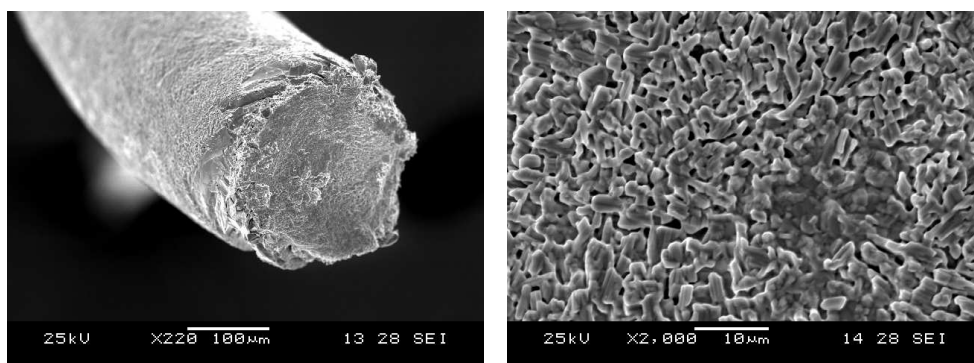


**Figure 2.12:** Filament temperature effect on (2+1) REMPI signal for B atoms ( $28885.9 \text{ cm}^{-1}$ ) and H atoms ( $41128.5 \text{ cm}^{-1}$ ) for 0.0475%  $\text{B}_2\text{H}_6$  in  $\text{H}_2$  with a laser focus at  $d = 2 \text{ mm}$  from the filament.

ments, under the same conditions, show that H atom production increases with the filament temperature, again consistent with surface enhanced  $\text{H}_2 \rightarrow 2 \text{ H}$  dissociation. The increase in atomic boron REMPI signal with  $T_{\text{fil}}$  can be attributed to a shift in the equilibria of hydride extraction reactions caused by the increase in H atom production (2.5) (2.6). The sharp decrease in [B] at high  $T_{\text{fil}}$  is very unusual and shows that boron production is directly related to filament properties because

there is no reduction in H atom production throughout the process window studied. We suggest this sharp decrease is due to a local surface melting of a tantalum boride layer present on the filament (TaB, melting point 2313K; B melting point 2349K [50]), causing the filament to become a reservoir for  $BH_x$  species. Despite this phase change, the surface continues to catalyse molecular hydrogen dissociation reactions resulting in an increase in H atoms in the system. This theory of surface activation is supported by SEM cross sectional images of spent filaments, which reveal an annular surface layer (conceivably tantalum boride) around the tantalum wire core, Fig 2.13. The outer surface structure shows evidence of localised melting and re-solidification, Fig 2.13(b).

These conditions under which B atoms are formed is very similar to a method of producing high purity boron by the thermal decomposition of  $BBr_3$  [51] and suggests that boron does not readily react with the hot metal surface and that the outer layer consists of  $BH_x$  rather than  $TaB_x$ .



(a)

(b)

**Figure 2.13:** (a) SEM cross section of a borodised filament. (b) the borodised surface showing evidence of localised melting.

## $B_2H_6 / CH_4 / H_2$ gas mixtures

Preconditioning treatment of the filament sequentially, first with methane and then with diborane, leads to formation of a double layer round the tantalum wire, Figure 2.14. The inner layer is presumed to be a tantalum carbide layer which reacts with  $B_2H_6$  in the second stage of the preconditioning to form an amorphous carboboride layer.

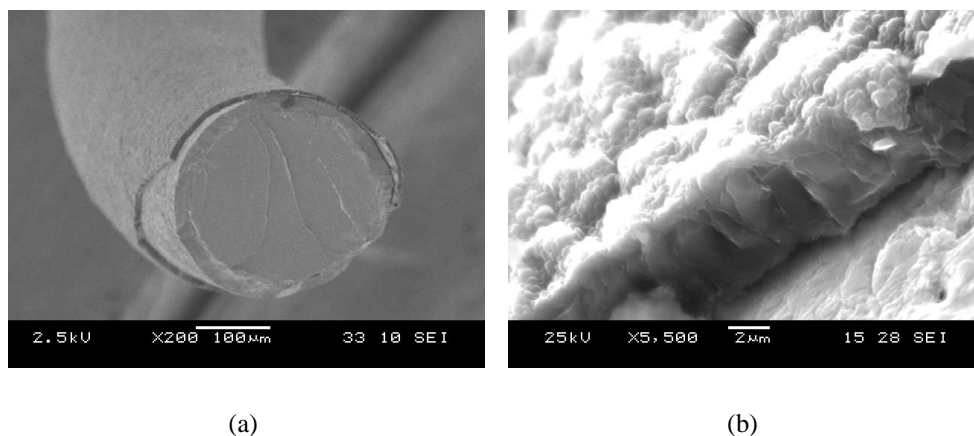


**Figure 2.14:** (a) SEM image consistent with borodation of a carborised filament (b) Close up view of the boron carbon interface.

Figure 2.15(a) shows how the measured boron REMPI signal varies with diborane input concentration with a background gas mixture of 1%  $CH_4 / H_2$  at 20 Torr. The results show the same trends as the  $B_2H_6 / H_2$  gas mixture with the same high level of sensitivity. With the carborised filament, an increase in filament temperature leads to an increase in B atom production, unlike the borodised filament, Figure 2.15(b).

We suspect that the observed differences in the filament properties are due to the difference in the melting points between the amorphous carboboride outer layer of the carborised filament (melting points  $B_4C$  2623 K [50]) and the  $TaB_x$  layer ( $TaB$ , melting points  $TaB$  2313 K [50] and B, melting point 2349 K). We suggest that the

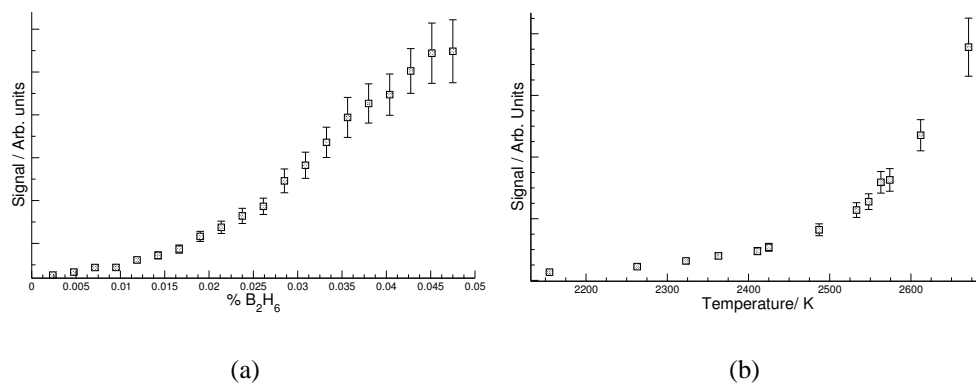


**Figure 2.15:** (a) The relation between % B<sub>2</sub>H<sub>6</sub> and REMPI signal at  $T_{\text{fil}} = 2273$  K. (b) Correlation between  $T_{\text{fil}}$  and atomic boron REMPI signal for 0.0475% B<sub>2</sub>H<sub>6</sub>: Both recorded in 1 % CH<sub>4</sub> / H<sub>2</sub> gas mixtures with a laser frequency of 28885.6 cm<sup>-1</sup> and a laser focus at  $d = 2$  mm from the filament.

carborised filament does not undergo a phase change for the temperature window investigated. These results suggest that the filament acts as a temperature dependent sink for BH<sub>x</sub> species.

Figure 2.16 shows effects of the carborised filament and methane in the gas mixture on B REMPI signal as a function of distance for two temperatures. At 2273K, the data indicates that there is a maximum in B number density at  $d = 4$  mm from the filament. In the regions close to the filament, the loss in B REMPI signal is ascribed to B atoms and other BH<sub>x</sub> species being adsorbed into the filament. In the cooler regions studied ( $d > 5$  mm), the atomic boron number density drops substantially, suggesting a loss mechanism. At 2673K, there is a major change in filament behaviour. The B REMPI signal peaks in the hotter gas regions of the reactor ( $d < 4$  mm), which correlates to B atoms evaporating from the filament. In the region where  $d$  is between 4 and 14 mm, there is an increase in B REMPI atom signal, which is similar to the trend shown in Figure 2.10 and when  $d > 14$  mm, the B REMPI signal decreases.

Experimental studies of B atom reactions with hydrocarbons mainly focus on

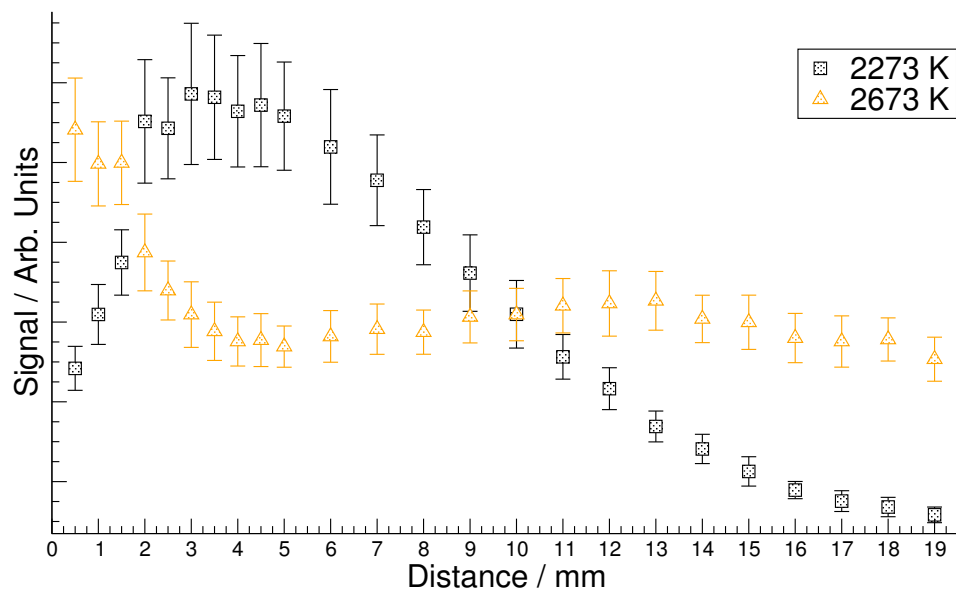


**Figure 2.16:** Correlation between distance between the laser focus and HF and signal for 0.0475%  $B_2H_6$  in  $CH_4 / H_2$ : laser frequency of  $28885.6 \text{ cm}^{-1}$  and  $T_{\text{fil}} = 2273\text{K}, 2673\text{K}$ .

methane insertion [52] and cross beam reactions with acetylene [53]. Boron reactions with methane are very unlikely as boron insertion reactions have an activation barrier of  $68.6 \text{ kJ mol}^{-1}$  and hydrogen abstractions have an even more unfavourable reaction activation barrier of  $149.0 \text{ kJ mol}^{-1}$  [52]. Methane, in the presence of H atoms and  $H_2$ , inter-converts to acetylene and other species in high temperature regions of a CVD reactor; the acetylene so formed then diffuses back into cooler regions [54]. Boron insertion reactions with acetylene occur via addition to the carbon  $\pi$  system and subsequent rearrangement to  $HBC_2$ , which is isoelectronic with  $C_3$ . This process is slightly exothermic by  $6.9 \text{ kJ mol}^{-1}$  [53]. We suggest that this is the loss mechanism for boron as acetylene concentrations are greater in the cooler regions of the reactor whereas in the hot regions the reaction favours the B and  $C_2H_2$  reagents.

## 2.5 Conclusions

These are the first recorded REMPI studies of the behaviour of atomic boron and atomic hydrogen, in HF activated  $B_2H_6 / CH_4 / H_2$  gas mixtures.

By probing the radial distribution of boron atoms from the HF, we have shown that, under CVD conditions, atomic boron does not form a stable reservoir species with other borane species ( $B_2H_y$ ) and only combines with carbon species (when present) most probably to form  $HBC_2$  in the cooler regions of the reactor.

These results suggests that for the same power into a tantalum filament processed in  $H_2$  or  $CH_4 / H_2$ , a borodised filament will run at a lower  $T_{fil}$  and give rise to a relative higher H atom number density, which implies that the filament provides an efficient catalytic surface for mediating hydrogen dissociation at low  $T_{fil}$  i. e. more of the filament's power is used in hydrogen dissociation rather than increasing  $T_{fil}$ .

The tantalum filament also acts as a sink for  $BH_x$  species resulting in the formation of boride layer. However, when a borodised filament undergoes a phase change, which occurs within the temperature range studied, there is an increase in the efficiency of  $BH_x$  species incorporation into the HF. This results in a decrease in the atomic boron number density in local vicinity of the HF.

This pioneering study of B atom number density in HF activated  $B_2H_6 / H_2$  and  $B_2H_6 / CH_4 / H_2$  gas mixtures has been repeated and extended by Ph.D student Dane Comerford, along with complementary modelling of  $BH_x$  interconversion reactions by Mankelevich [55]. It has also served to trigger preliminary modelling studies of  $BH_x$  addition to a simplified version of the diamond  $\{100\}$  surface – this forms the subject of the next chapter.

## Bibliography

- [1] F. A. Cotton and G. Wilkinson, *Advanced Inorganic Chemistry* (John Wiley & Sons Inc., 605 Third Avenue, New York, NY., 5th edition, 1988).
- [2] W. Zhou, R. A. Yetter, F. L. Dryer, H. Rabitz, R. C. Brown, and C. E. Kolb, *Combust. Flame*. **117**, 227 (1999).
- [3] P. R. P. Barreto, A. F. A. Velela, and R. Gargano, *Int. J. Quant. Chem.* **103**, 659 (2005).
- [4] S. H. Bauer, *Chem. Rev.* **96**, 1907 (1996).
- [5] K.-W. Lee and S. J. Harris, *Diamond Relat. Mater.* **7**, 1539 (1998).
- [6] R. Weissenbacher, R. Haubner, K. Aigner, and B. Lux, *Diamond Relat. Mater.* **11**, 191 (2002).
- [7] S. J. Harris, G. L. Doll, D. C. Chance, and A. M. Weiner, *Appl. Phys. Letts.* **67**, 2314 (1995).
- [8] S. J. Harris, A. M. Weiner, G. L. Doll, and W.-J. Meng, *J. Mat. Res.* **12**, 412 (1997).
- [9] Z. Y. Xie, J. H. Edgar, T. L. McCormick, and M. V. Sidorov, *Diamond Relat. Mater.* **7**, 1357 (1998).
- [10] C. Buzea and T. Yamashita, *Supercond. Sci. Tech.* **14**, R115 (2001).
- [11] W. N. Lipscomb, *Science* **196**, 1047 (1977).
- [12] H. I. Schlesinger and A. B. Burg, *J. Am. Chem. Soc.* **53**, 4321 (1931).
- [13] M. L. Yu, D. J. Vitkavage, and B. S. Meyerson, *J. Appl. Phys* **52**, 4032 (1986).
- [14] D. A. Grützmacher, K. Eberl, A. R. Powell, B. A. Ek, T. O. Sedgwick, and S. S. Iyer, *Thin Solid Films* **225**, 163 (1993).
- [15] Y. Kiyota, T. Nakamura, and T. Inada, *Appl. Surf. Sci.* **82/83**, 400 (1994).
- [16] G. A. Odintzova and A. R. Striganov, *J. Phys. Chem. Ref. Data.* **8**, 63 (1979).
- [17] E. B. Saloman, *Spectrochim. Acta B* **45**, 1 (1990).
- [18] K. Irikura, R. Johnson, and J. Hudgens, *J. Opt. Soc. Am. B.* **10**, 763 (1993).
- [19] W. Glab and A. M. Falleur, *J. Quant. Spect. Ra.* **73**, 121 (2002).
- [20] J. Clark, M. Konopka, L.-M. Zhang, and E. R. Grant, *Chem. Phys. Letts.* **340**, 45 (2001).
- [21] S. H. Bauer, G. Herzberg, and J. W. C. Johns, *J. Mol. Spect.* **13**, 256 (1964).

- [22] N. J. Caldwell, J. K. Rice, H. H. Nelson, G. F. Adams, and M. Page, *J. Chem. Phys.* **93**, 479 (1990).
- [23] G. Herzberg and J. W. C. Johns, *Proc. Roy. Soc. Lond. A.* **298**, 142 (1967).
- [24] B. Ruscic, C. A. Mayhew, and J. Berkowitz, *J. Chem. Phys.* **88**, 5580 (1988).
- [25] L. Andrews and X. Wang, *J. Am. Chem. Soc.* **124**, 7280 (2002).
- [26] K. Sato, N. Kanda, T. Ogata, and Y. Kumashiro, *Chem. Phys. Letts.* **325**, 453 (2000).
- [27] J. F. Stanton, W. N. Lipscomb, and R. J. Bartlett, *J. Am. Chem. Soc.* **111**, 5165 (1989).
- [28] N. N. Greenwood, *Chem. Soc. Rev.* **21**, 49 (1992).
- [29] H. Habuka, S. Akiyama, T. Otsuka, and W. F. Qu, *J. Cryst. Growth.* **209**, 807 (2000).
- [30] H. B. Schlegel, A. G. Baboul, and S. J. Harris, *J. Phys. Chem.* **100**, 9774 (1996).
- [31] S. J. Harris, J. Kiefer, Q. Zhang, A. Schoene, and K. W. Lee, *J. Electrochem. Soc.* **145**, 3203 (1998).
- [32] L. A. Curtiss, K. Raghavachari, G. W. Trucks, and J. A. Pople, *J. Chem. Phys.* **94**, 7221 (1991).
- [33] L. A. Curtiss, P. C. Redfern, K. Raghavachari, and J. A. Pople, *J. Chem. Phys.* **109**, 42 (1998).
- [34] L. A. Curtiss, K. Raghavachari, P. C. Redfern, and J. A. Pople, *J. Chem. Phys.* **106**, 1063 (1997).
- [35] M. Aoyagi, R. Shepard, A. F. Wagner, and T. H. Dunning Jr., *J. Phys. Chem.* **94**, 3236 (1990).
- [36] B. R. Brooks and H. F. Schaefer III., *J. Chem. Phys.* **67**, 5146 (1977).
- [37] P. Gonon, A. Deneuve, F. Fontaine, E. Gheeraert, A. Campargue, M. Chenevier, and S. Rodolphe, *J. Appl. Phys.* **78**, 7404 (1995).
- [38] M. Rayar, P. Veis, C. Foissac, P. Supiot, and A. Gicquel, *J. Phys. D. Appl. Phys.* **39**, 2151 (2006).
- [39] S. A. Redman, *Spectroscopic Studies of the Diamond Chemical Vapour Deposition Environment*, Ph.D thesis, University of Bristol, 1999.
- [40] S. A. Redman, C. Chung, K. N. Rosser, and M. N. R. Ashfold, *Phys. Chem. Chem. Phys.* **1**, 1415 (1999).

- [41] F. G. Celii and J. E. Butler, *Appl. Phys. Letts.* **54**, 1031 (1989).
- [42] V. Zumbach, J. Schäfer, J. Tobai, M. Ridder, T. Dreier, T. Schaich, J. Wolfrum, B. Ruf, F. Behrendt, O. Deutschman, and J. Warnatz, *J. Chem. Phys.* **107**, 5918 (1997).
- [43] E. J. Corat and D. G. Goodwin, *J. Appl. Phys.* **74**, 2021 (1993).
- [44] J. A. Smith, *Laser Diagnostics of a Diamond depositing Chemical Vapour Deposition gas-phase environment*, Ph.D thesis, Universty of Bristol, 2001.
- [45] M. Chase Jr., *J. Phys. Chem. Ref. Data* (1998).
- [46] G. A. Odintzova and A. R. Striganov, *J. Phys. Chem. Ref. Data.* **8**, 63 (1979).
- [47] J. A. Smith, E. Cameron, M. N. R. Ashfold, Yu. A. Mankelevich, and N. V. Suetin, *Diamond Relat. Mater.* **10**, 358 (2001).
- [48] T. R. O'Brian and J. E. Lawler, *Astron. Astrophys.* **255**, 420 (1992).
- [49] J. A. Smith, M. A. Cook, S. R. Langford, S. A. Redman, and M. N. R. Ashfold, *Thin Solid Films* **368**, 169 (2000).
- [50] G. V. Samsonov and L. Ya. Markivskii, *Usp. Khim.* **25**, 190 (1956).
- [51] M. Vlasse, R. Naslain, J. S. Kasper, and K. Ploog, *J. Solid. State. Chem.* **28**, 289 (1979).
- [52] W. H. Fang and S. D. Peyerimhoff, *Mol. Phys.* **93**, 329 (1998).
- [53] N. Balucani, O. Asvany, Y. T. Lee, R. I. Kaiser, N. Galland, M. Rayez, and Y. Hannachi, *J. Comp. Chem.* **22**, 1359 1365 (2001).
- [54] M. N. R. Ashfold, P. W. May, J. R. Petherbridge, K. N. Rosser, J. A. Smith, Yu. A. Mankelevich, and N. V. Suetin, *Phys. Chem. Chem. Phys.* **3**, 3471 (2001).
- [55] D. W. Comerford, A. Cheesman, T. P. F. Carpenter, D. M. E. Davies, N. A. Fox, R. S. Sage, J. A. Smith, M. N. R. Ashfold, and Yu. A. Mankelevich, *J. Phys. Chem. A* **110**, 2868 (2006).

## Chapter 3

# **BH<sub>x</sub> Addition to the {100} surface of Diamond.**

The aims of the preliminary theoretical investigations reported here were to identify likely boron growth species and to investigate plausible mechanisms for both B incorporation into, and B loss from, the reconstructed {100} surface during diamond CVD.

### **3.1 Introduction**

#### **3.1.1 *Ab-Initio* Computational Chemistry Theory**

The term computational chemistry covers a broad spectrum of work. There are two broad areas of computational chemistry research, *ab-initio* and molecular mechanics calculations. *Ab-initio* methods model electronic interactions within species, with a quantum mechanical description, whilst the molecular mechanics approach uses empirical potentials to describe atomic interactions and is discussed further in

## Chapter 4.

The scientific foundation of *ab-initio* calculations is the Schrödinger wave equation, which links the kinetic and potential energy of a system into a Hamiltonian,  $\hat{H}$ . This leads to an unsolvable yet true wavefunction equation, (3.1).

$$\hat{H}\Psi = E\Psi \quad (3.1)$$

To attempt approximate solutions of eq (3.1), the Hamiltonian can be broken down into the more important constituent components: The kinetic energies of the electrons and nuclei,  $\hat{T}_e$ ,  $\hat{T}_n$ , and the Coulombic interactions between similar and opposite charges,  $\hat{V}_{ee}$ ,  $\hat{V}_{nn}$ ,  $\hat{V}_{en}$ ; equation (3.2).

$$\hat{H} = \hat{T}_e + \hat{V}_{ee} + \hat{V}_{en} + \hat{T}_n + \hat{V}_{nn} \quad (3.2)$$

The Born-Oppenheimer approximation states that there is a large distinction between the timescales of the nuclear and electronic motion and thus the electronic component of the wavefunction can be decoupled for any fixed nuclear distance, (3.3). The electronic Hamiltonian can thus be expressed in terms which directly relate to the electron's coordinate systems ( $r$ ) for a fixed nuclear arrangement ( $R$ ).

$$\hat{H}_e\Psi_e(r, R) = E_e\Psi_e(r, R) \quad (3.3)$$

In practise, the variational method is used to refine the wavefunction starting from an initial approximation, usually a physically plausible guess. It can be shown that the expectation value of the Hamiltonian for any trial wavefunction must be greater than or equal to the true ground state energy of the system,  $E_0$ , (3.4) [1]. Hence by using an initial guess,  $\Psi_0$  then varying numerical coefficients determining this trial wavefunction, the expectational value of eq ( ) is at a minimum, giving the best

possible wavefunction.

$$\frac{\int \Psi^* \hat{H} \Psi d\mathbf{r}}{\int \Psi^* \Psi d\mathbf{r}} \geq E_0 \quad (3.4)$$

Using the variational method usually requires the adoption of an approximate form for the wavefunction. The most common approach is the the molecular orbital approximation, whereby, for a many-electron system, the overall electron wavefunction  $\Psi$  of equation (3.3), is written as a product of individual n -electron wavefunctions  $\Phi$  (3.5).

$$\Psi(r_1, r_2, \dots r_n) = \Phi_1(r_1)\Phi_1(r_2) \dots \Phi_1(r_n) \quad (3.5)$$

These individual 1-electron wavefunctions, usually referred to as molecular orbitals, can be described by basis sets and modelled by gaussian functions. For molecular species, it is usual to describe the wavefunction as a combination of molecular orbitals which in turn can be constructed from linear combinations of a set of atomic orbitals, (3.6). This set of atomic orbitals is usually referred to as the basis set.

$$\Phi = \sum_{i=1}^N a_i \varphi_i \quad (3.6)$$

Equation (3.5) does not account for the Pauli exclusion principle and the indistinguishability of electrons, but describing the wavefunction in the form of a Slater determinant overcomes these shortfalls, (3.7), where  $\alpha$  and  $\beta$  represent the

$M_s = \pm 1/2$  projection of the electronic spin.

$$\Psi = \frac{1}{\sqrt{n!}} \begin{vmatrix} \Phi_1(r_1)\alpha(1) & \Phi_1(r_1)\beta(1) & \Phi_2(r_1)\alpha(1) & \dots & \Phi_{\frac{n}{2}}(r_1)\beta(1) \\ \Phi_1(r_2)\alpha(2) & \Phi_1(r_2)\beta(2) & \Phi_2(r_2)\alpha(2) & \dots & \Phi_{\frac{n}{2}}(r_2)\beta(2) \\ \vdots & \vdots & \vdots & \ddots & \vdots \\ \Phi_1(r_n)\alpha(n) & \Phi_1(r_n)\beta(n) & \Phi_2(r_n)\alpha(n) & \dots & \Phi_{\frac{n}{2}}(r_n)\beta(n) \end{vmatrix} \quad (3.7)$$

One of the weaknesses of Hartree Fock calculations is the poor treatment of the correlation behaviour of electrons. This limits the accuracy of the calculations. One method of compensating for the electronic correlation deficiency is to simplify the mathematical descriptions of the wavefunction and to introduce empirical coefficients which can be optimised to experimental parameters. This semi-empirical approach, which includes the AM1 and PM3 methods, is favourable in systems with large number of atoms as the simplifications dramatically increase the speed of the calculation, but they lack high levels of accuracy.

The accuracy of the *ab-initio* calculations can be improved by explicitly including an electronic correlation functional in the HF calculation. Examples of this approach include the incorporation of Møller Plesset perturbation theory to produce the  $MP_n$  computational method.

The coupled cluster approach is an elegant and accurate computational method. Equation (3.8) shows the introduction of a cluster operator  $\mathbf{T}$ , which is the sum of all possible single-electron interactions for the number of electrons in the system,  $N$  [2].

$$\Psi = e^{\mathbf{T}}\Psi_{HF} \quad \text{where } \mathbf{T} = \sum_{i=1}^N \mathbf{T}_i \quad (3.8)$$

The exact solution of the summation of  $\mathbf{T}$  leads to the same results as a calculation that considered all possible electronic interactions. However, expanding the exponential as a Taylor series enables an easier mathematical method for truncating the extent of the electronic interaction, Equation (3.9)

$$\Psi = \left( 1 + \mathbf{T} + \frac{\mathbf{T}^2}{2!} + \frac{\mathbf{T}^3}{3!} + \dots \right) \Psi_{HF} \quad (3.9)$$

### 3.1.2 Density functional theory

All descriptions of molecular properties so far discussed have derived from electronic wavefunction definitions and manipulations. Electronic density,  $\rho$ , can also be used to compute molecular properties.

The foundations of density functional theory (DFT) calculations were laid by the Hohenberg-Kohn Theories [3], [4]. The first of these theories describes the nature of mapping of ground state electronic density to the ground state wavefunction while the second is a modification of the variational principle which enables the same principle to operate in a DFT system.

By combining these theories [5], a generic description for a DFT method can be formed, (3.10). This describes the combination of the kinetic energy ( $T[\rho(r)]$ ) and the electron-electron interaction ( $E_{ee}[\rho(r)]$ ) in terms of a system independent functional, the Hohenberg-Kohn functional,  $F_{HK}$ . This equation is essentially the Schrödinger equation (3.1) and thus can not be directly solved.

$$F_{HK}[\rho(r)] = T[\rho(r)] + E_{ee}[\rho(r)] \quad (3.10)$$

The electronic interaction term can be simplified into a known coulombic inter-

action,  $J[\rho(r)]$  and a non classical potential interaction,  $E_{ncl}[\rho(r)]$ .

$$E_{ee}[\rho(r)] = J[\rho(r)] + E_{ncl}[\rho(r)] \quad (3.11)$$

The Kohn-Sham approach bypasses the inherent problem in solving (3.10) by describing the kinetic energy functional of the electrons by comparison with a system where there are no electron-electron interactions. The non-interacting system accurately describes the kinetic energy,  $T_S$ , which is comparable to the real system, but leaves a small part of the energy,  $T_C$ , to be described by other methods. This leads to the formation of the Kohn-Sham functional, equation (3.12) and a new term, the exchange correlation energy,  $E_{XC}$ , which is defined as the combination of the non classical interactions and the residual kinetic energy, equation (3.13).

$$F_{HK}[\rho(r)] = T_S[\rho(r)] + J[\rho(r)] + E_{XC}[\rho(r)] \quad (3.12)$$

$$E_{XC}[\rho] = T_C[\rho] + E_{ncl}[\rho] \quad (3.13)$$

Different theories have arisen from different levels of describing the exchange correlation function as a function of electron density with the only requirement for the value of  $\rho$  being that it must be single valued at all positions. The Local Density Approximation (LDA) approach describes the exchange functional as being derived directly from the electron density of a system of free electrons at a particular position.

The generalised gradient approximation (GGA) uses the local density information (as in LDA) in conjunction with information regarding the density gradient in order to account for the non-uniform electron density distribution. In practice, the exchange correlation functional is often broken into its constituent parts for ease of

calculation and the general form is expressed in equation 3.14

$$E_{XC}^{GGA}[\rho(r)] = E_{XC}^{LDA}[\rho(r)] + \delta E_{XC} \left[ \frac{|\nabla\rho(r)|}{\rho^{4/3}(r)} \right] \quad (3.14)$$

The most common way of obtaining these functionals is to fit suggested empirically formulae to the experimental data for the exchange and correlation energies (usually the noble gases). This approach has led to the development of the more common functionals; The B exchange functional by Becke [6] and the correlation term LYP [7] (though strictly the latter term is not an LDA correction method, it is empirically calibrated to the helium atom values).

It can be shown that the exchange correlation energy can be expressed as a function of  $\lambda$ , the measure of inter-electronic interaction [5], (3.15).

$$E_{XC} = \int_0^1 E_{ncl}^\lambda d\lambda \quad (3.15)$$

When  $\lambda = 0$ , the system correlates to the Kohn-Sham non-interaction system, while when  $\lambda = 1$ ,  $E_{XC}$  is not known but can be described adequately by one of the GGA methods. Assuming that  $E_{ncl}$  has a linear dependence on  $\lambda$ , equation (3.15) can be approximated as equation 3.16.

$$E_{XC} = \frac{1}{2}E_{ncl}^{\lambda=0} + \frac{1}{2}E_{ncl}^{\lambda=1} \quad (3.16)$$

Becke [8] expanded the above ideas and used empirical coefficients to effectively weigh the contribution to each section using his B exchange functional and the PW91 correlation functional. The constants were optimised for a large number of molecular species. Equation 3.17 shows the expansion of the most popular DFT hybrid function, B3LYP [9], with the coefficients directly imported from Becke's BPW91 model combined with the LYP correlation term. B3LYP methods show a

good correlation with well studied experimental reactions [10].

$$E_{XC}^{B3LYP} = (1 - a)E_X^{LDA} + (1 - c)E_C^{LDA} + aE_{XC}^{\lambda=0} + bE_X^{B88} + cE_C^{LYP} \quad (3.17)$$

### 3.1.3 Potential Energy Surface

The Potential Energy Surface (PES) is a multi-dimensional surface which correlates the potential energy of a species with its geometry. These surfaces are often complex as the number of dimensions required scales with the degrees of freedom of the system. To enable easier visualisation, internal co-ordinates are restricted, typically along the reaction pathway. The main features of these surfaces are the identification of minima and transition states (first order saddle point) along reaction pathways, Figure 3.1. These features can be identified by gradient related iterative processes.

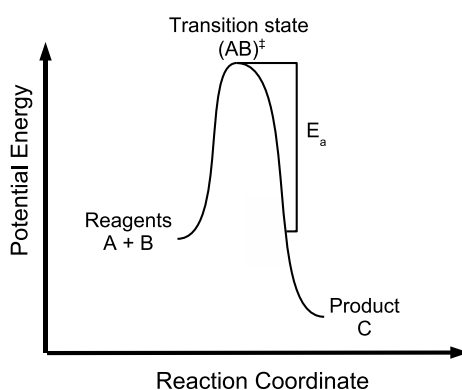


**Figure 3.1:** Cross section through a bimolecular PES.

### 3.1.4 Thermodynamics

The classic description of the thermodynamic feasibility of a reaction occurring is defined by the Gibbs energy of the process,  $G$ . (3.18). The Gibbs energy for a

given species is made up from an energy contribution, the enthalpy  $H$  (derived from the potential energy surface (PES)), and a temperature dependent entropic term,  $S$ , which can be calculated from the individual population of the energy levels of the species using statistical mechanics (??).

$$G = H + TS \quad (3.18)$$

In order for a reaction to occur, there must be a negative value for the change in Gibbs free energy from reactants to products.

### 3.1.5 Transition State Theory (TST)

For a bimolecular reaction sequence, (3.19), two reagents collide and react to form the product. This usually happens via an activated complex, the transition state. The rate at which product forms depends on the concentration of the two reagents and the rate coefficient at which these species react,  $k$ .



$k$  can be described by the experimentally determined Arrhenius law (3.20) showing that reaction rate depends on the activation energy of the reaction,  $E_a$  and the temperature of the system,  $T$  [11].

$$k = A e^{-E_a/RT} \quad (3.20)$$

Theoretical modelling of reaction dynamics focused on the interaction between the transition-state and the reagents is the key to understanding reaction rates. It can be shown that, for non-equilibrium situations, the rate coefficient using conven-

tional transition-state theory (CTST) can be described as a function of the various total partition functions ( $q$ ) of the reagents and the transition states, (3.21) [12].

$$k_{TST}(T) = \frac{k_B T}{h} \frac{q_{\ddagger}}{q_A q_B} e^{-E_a/RT} \quad (3.21)$$

The partition functions,  $q$ , can be expanded into their constituent parts (3.22) and evaluated separately using statistical mechanics.

$$q = q_e q_v q_r q_t \quad (3.22)$$

However, the construction of CTST includes many assumptions regarding the nature of the transition from reagents to products, for example CTST assumes that once activated, all reagents are completely converted into the products.

Variational Transition State Theory addresses this problem, and others, by calculating rate constants along different points on the reaction pathway and whichever position yields the lowest rate is considered to be the most accurate.

## 3.2 Method

As in previous modelling studies of the carbon growth step on a diamond ( $2 \times 1$ )  $\{100\}$  surface [13] our calculations are based on a unit cell model of diamond, a  $C_9H_{14}$  cluster (structure A in Figure 3.2: c.f. Figure 1.2). Potential energy minima and transition states were fully optimised using the standard B3LYP functional together with the 6-31G\* basis set within the Gaussian 03 program package [14]. Vibrational frequencies were computed to confirm the nature of the stationary points as either minima (all real frequencies) or transition states (one imaginary frequency). Single-point B3LYP energies were computed at the B3LYP / 6-31G\* ge-

ometries using the larger 6-311+G(2df,p) basis set. All reported energy differences ( $\Delta E$ ) and activation energies ( $E_a$ ) are based on B3LYP / 6-311+G(2df,p) energies with the B3LYP / 6-31G\* geometries and zero-point energy corrections. Based on the computed vibrational frequencies and rotational constants, rigid rotor-harmonic oscillator statistical mechanics was carried out at various temperatures using Gaussian 03 to generate free energy thermal corrections to the B3LYP / 6-311+G(2df,p) energies. The standard free energies of activation and free energies of reaction reported later in this work are derived in this way.

The computed  $E$  and  $G$  values, and the temperature dependence of the latter, are affected by various errors due to the use of approximate density functional theory (B3LYP), the use of a small model cluster for the diamond surface, and the use of the rigid rotor-harmonic oscillator approximation for computation of thermal effects. Taken together, these errors could, in principle, lead to a total error on relative energies of well over 50 kJ mol<sup>-1</sup>. However, the error is unlikely to be this large in all cases, and some error cancellation is expected.

As discussed later in Appendix A, benchmarking CCSD(T) calculations using the much larger cc-pVQZ basis have been carried out (at the B3LYP / 6-31G\* geometries) for one simple case, to calibrate the B3LYP method. These latter calculations were carried out using the MOLPRO program package [15].

Rate constants have been calculated using a custom “in-house” program using canonical transition state theory.

### 3.3 Results

Inclusion of the carbon-containing species into a diamond {100} surface has been well documented (section 1.4.3) and the various steps are summarised in Figure

3.2. This study looks at the possibility that borane incorporation mimics the carbon inclusion processes and hence focusses upon the feasibility of borane species addition to the diamond surface and their subsequent surface reactions. The geometries of all optimised structures for the inclusion of carbon and boron containing species can be found in Appendix B.

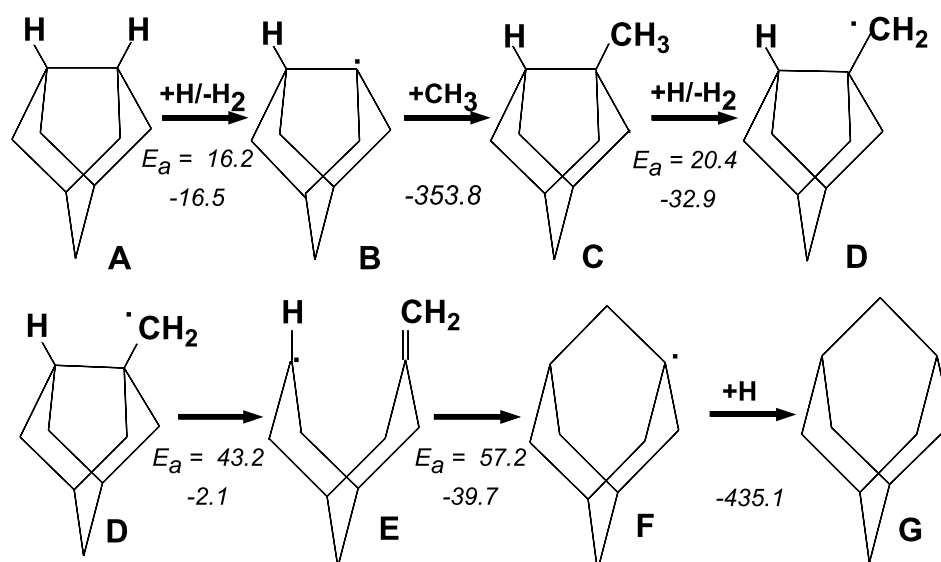


**Figure 3.2:** Mechanism for i) Hydrogen abstraction and surface activation ii) Carbon incorporation into the diamond {100} surface. Process energies (in  $\text{kJ mol}^{-1}$ ) for inter-conversion between the various species via addition and / or elimination reactions as defined in the figure are indicated in italics.

### 3.3.1 Boron addition to the cluster surface

The initial step in the carbon inclusion process is the formation of a surface radical site by a hydrogen abstraction from the diamond {100} surface (i.e. process A  $\rightarrow$  B in Figure 3.2). This reaction was calculated to be virtually thermoneutral, ( $\Delta E = -16.5 \text{ kJ mol}^{-1}$ ) and to have a low activation barrier ( $E_a = 16.2 \text{ kJ mol}^{-1}$ ), in good agreement with previous calculated values [13].

Addition of the various gaseous  $\text{BH}_x$  ( $x = 0-3$ ) species to a surface site radical has been modelled. Strong boron-carbon bonds result in the case that  $x = 0, 1$  or

2 ( $\Delta E = -363.0, -420.7$  and  $-408.3$  kJ mol<sup>-1</sup>, respectively), comparable to the energy release upon carbon bond formation when CH<sub>3</sub> adds to the same surface site ( $\Delta E = -353.8$  kJ mol<sup>-1</sup>).

The optimised structure for BH addition (Figure 3.3(a)) shows that the adsorbed boron atom aligns its empty valence p-orbital parallel to the strained {100} carbon-carbon bond, presumably due to a stabilising hyperconjugation interaction. BH<sub>3</sub> addition to the surface is calculated to be a much less exothermic ( $\Delta E = -46.9$  kJ mol<sup>-1</sup>) process, with the adsorbed BH<sub>3</sub> adopting a mildly distorted trigonal geometry, which coordinates to the diamond surface radical site through the unoccupied p orbital, Figure 3.3(b).

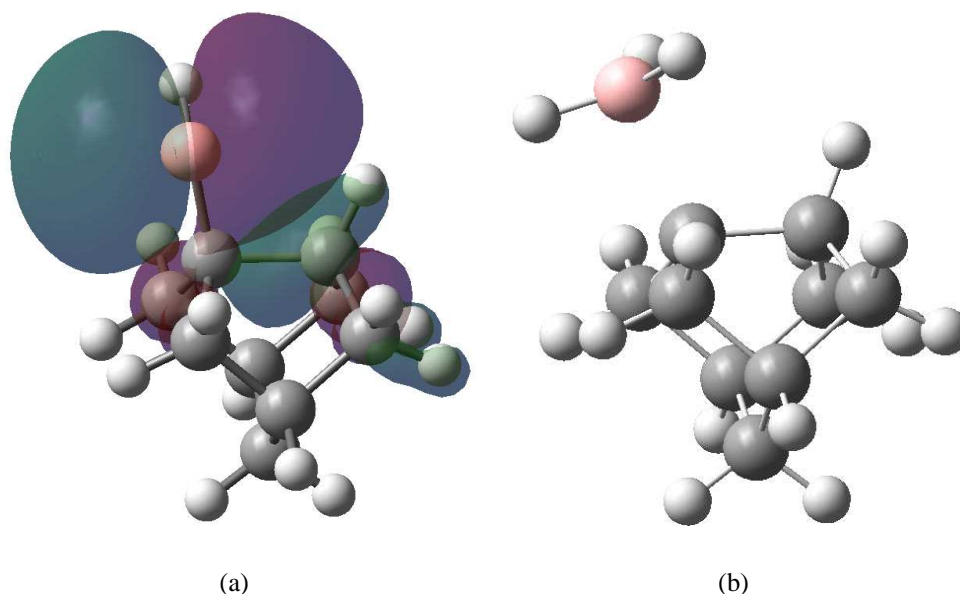


**Figure 3.3:** Figures showing the optimised geometries for the C<sub>9</sub>H<sub>14</sub> cluster with adsorbed (a) BH species (with the empty orbital (LUMO) highlighted) (b) BH<sub>3</sub> species.

Hydrogen abstraction from the surface bound BH<sub>x</sub>, x = 1,2, species occurs via analogues of reaction (2.5). As in the gas phase case [16], [17], abstraction may occur either directly, or via a sequential mechanism in which H atom addition is followed by loss of H<sub>2</sub>. In the case of surface bound BH<sub>2</sub>, H atom loss via the se-

quential mechanism involves an initial exothermic ( $\Delta E = -68.4 \text{ kJ mol}^{-1}$ ) addition to form a surface bound  $\text{BH}_3$ , followed by loss of  $\text{H}_2$  via an endothermic ( $\Delta E = 56.0 \text{ kJ mol}^{-1}$ ), barrier-less transition. The overall conversion is a mildly exothermic process ( $\Delta E = -12.4 \text{ kJ mol}^{-1}$ ). Abstraction from surface bound BH is much more exothermic ( $\Delta E = -120.9 \text{ kJ mol}^{-1}$ ). Transition states for both the direct and indirect abstraction processes have not been located but, by analogy with the reaction of H atoms with surface bound  $\text{BH}_2$ , neither pathway is expected to involve a significant energy barrier. Inter-conversion between surface-bound B, BH and  $\text{BH}_2$  is thus expected to be facile in the presence of H atom number densities (typically  $> 10^{13} \text{ cm}^{-3}$ ) and at temperatures (700 – 1200 K) prevailing in successful diamond CVD.

### 3.3.2 Boron insertion into the diamond surface

Once a  $\text{BH}_x$  species has attached to the surface, it then needs to be incorporated into the surface layer. These studies, performed on the small cluster model, only focus upon the insertion of boron into the dimer reconstruction. Boron incorporation requires that the strained reconstructed  $\{100\}$  carbon-carbon bond breaks, and a new boron-carbon bond be formed. Energetically feasible insertion pathways for surface bound BH and B species have been identified, and are described in this section.

As discussed previously (section 1.4.3), the preferred mechanism for the carbon insertion starts with the generation of the  $\text{CH}_2$  surface radical (D, Figure 3.2) by a hydrogen abstraction reaction, which initiates the breaking of the surface carbon-carbon bond to form an unsaturated methylene group (E, Figure 3.2) which then cyclizes with the surface radical to form the adamantane structure (F, Figure 3.2). The transition states (TSs) for these two steps lie fairly close in energy, at 43.2 and 57.2  $\text{kJ mol}^{-1}$  above that of the starting radical, similar to previously reported work [13]. Our studies also identified a pathway for direct insertion of the pendant  $\text{CH}_2$  group involving the surface dimer bond breaking as the new carbon-carbon bond forms. However, this direct insertion reaction is not a major path for carbon inclusion as the very high activation barrier ( $\sim 200 \text{ kJ mol}^{-1}$ ) makes this process unfeasible.

In contrast to the carbon case, the direct insertion mechanism with a pendant BH is found to be more favourable ( $E_a = 32.5 \text{ kJ mol}^{-1}$ ,  $\Delta E = -89.5 \text{ kJ mol}^{-1}$ ) than the indirect pathway (78.0 and 70.3  $\text{kJ mol}^{-1}$  for ring opening and closing activation energies respectively). The relatively low energy of the direct pathway is due to the availability of one empty (as well as the singly occupied) valence p-orbital present on the boron atom which can directly interact with the second

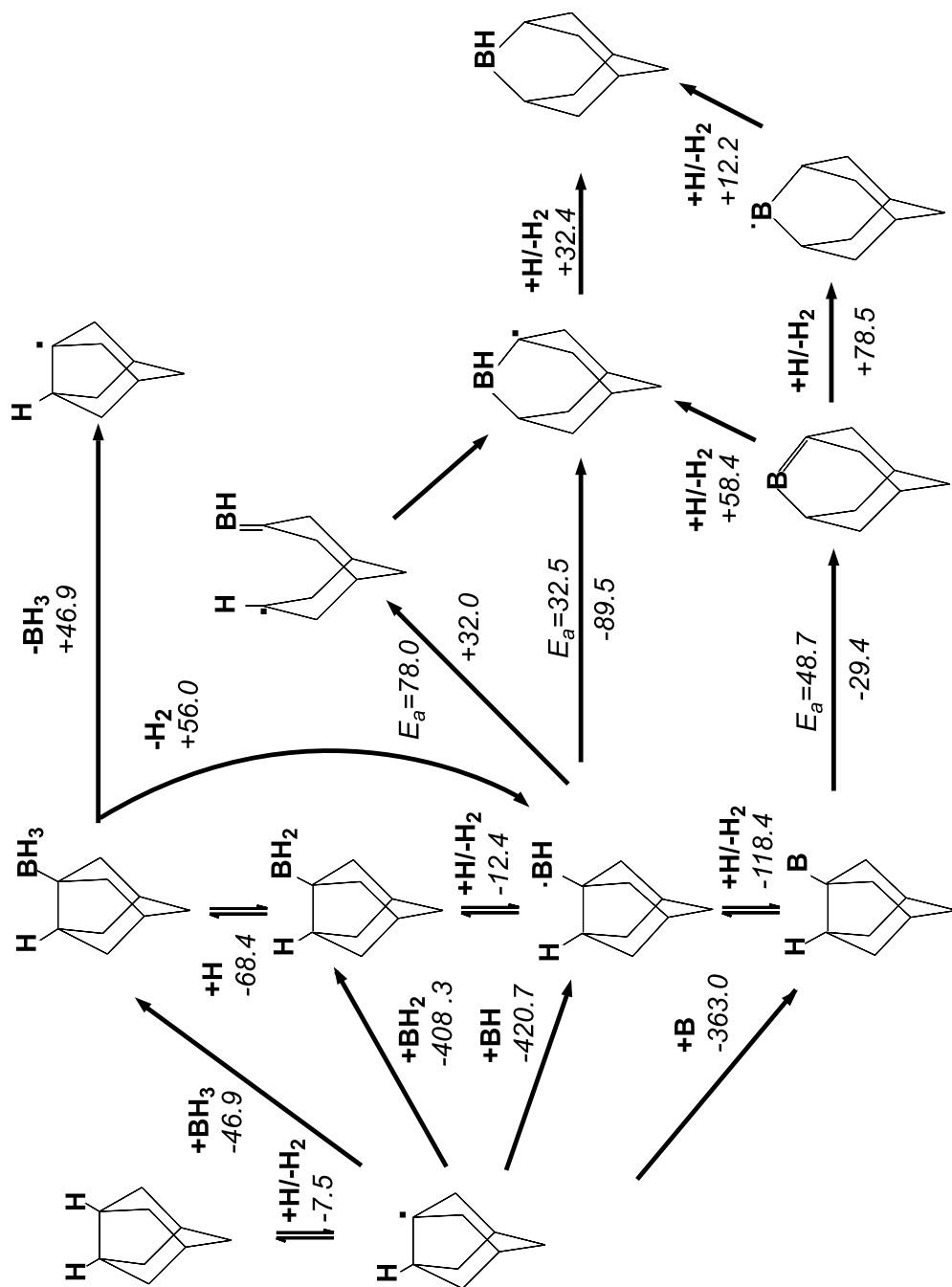


**Figure 3.4:** Overview of the reaction pathways for BH<sub>x</sub> addition to, incorporation into, and loss from, the diamond {100} surface. Process energies (in kJ mol<sup>-1</sup>) for inter-conversion between the various species via addition and/or elimination reactions as defined in the figure are indicated in italics.

carbon atom of the dimer reconstruction. This enables simultaneous bond breaking and formation. (Note that in the related all carbon sequence, (Figure 3.2, steps  $D \rightarrow E \rightarrow F$ ), there is no analogous vacant p orbital). Both the indirect and direct reaction mechanisms lead to the same species, which can undergo further H atom addition reactions which terminate the remaining surface radical site and conclude the B insertion process.

Figure 3.4 shows that there is also a direct insertion process starting from a surface bound B atom. This also has a low activation barrier ( $E_a = 48.7 \text{ kJ mol}^{-1}$ ) and is an exothermic process ( $\Delta E = -29.4 \text{ kJ mol}^{-1}$ ). Two subsequent H atom additions to the inserted species result in the same stabilised product as that obtained when starting from the surface bound BH species. The calculated energy barrier is sufficiently low to encourage the view that it, too, may play a role in the growth of B-doped diamond.

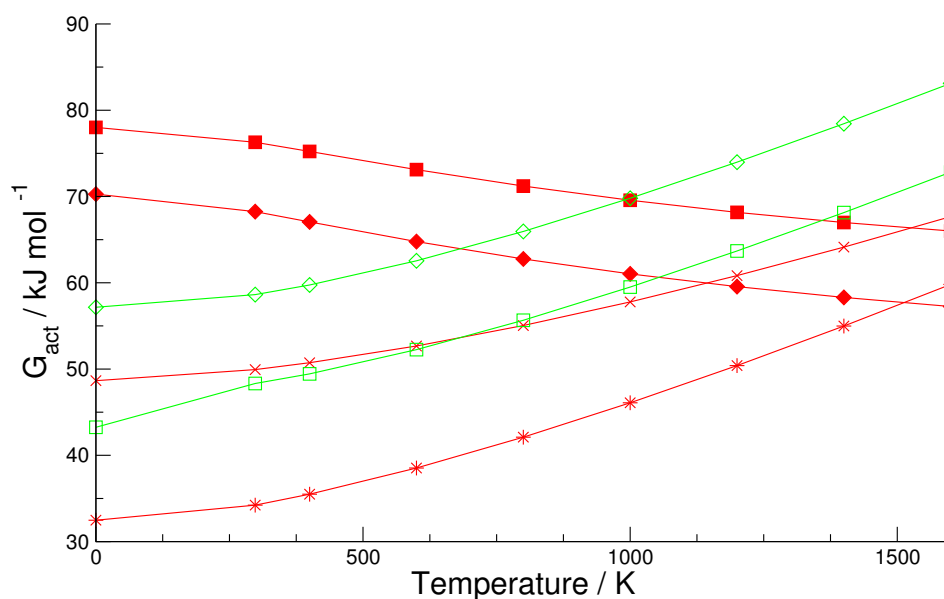


**Figure 3.5:** Calculated temperature dependent Gibbs free energies of activation ( $G_{\text{act}}$ ) for selected key steps in the incorporation of  $\text{BH}_x$  species into a diamond  $\{100\}$  surface:  $\times$  insertion of B;  $*$  direct insertion of BH;  $\blacksquare$  ring opening for BH insertion;  $\blacklozenge$  ring closing for BH insertion. Calculated values for the  $\square$  ring opening for  $\text{CH}_2$  insertion;  $\diamond$  ring closing for  $\text{CH}_2$  insertion are included for comparison.

Figure 3.5 shows the temperature dependence of the free energies of activation for the key TSs involved in these various B insertion processes, calculated relative to the respective surface bound activated species. The gradient of each line is caused by a change in vibrational entropy in forming the transition state with a positive value correlating to a decrease in entropy and *vice versa*. Direct insertion of BH is calculated to involve the transition state of lowest free energy at all temperatures <1500 K. Also shown, for comparison, are the corresponding temperature dependent activation free energies for carbon insertion starting from the surface bound CH<sub>2</sub> species (structure D in Figure 3.2).

Figure 3.5 shows that the transition states involved in all of the ring opening and closing reactions, for both boron and carbon, are calculated to lie higher in free energy than that for the direct BH insertion process.

Using simple TST, rate constants for the major carbon and boron inclusion reactions have been calculated. These are given in tables C.1 & C.2 in Appendix C. The reaction rates mirror observed trends in the activation energies.

The present mechanism would lead to the incorporation of a trivalent boron species into the diamond surface, yet boron is found to form 4-coordinate centres (similar in electronic and geometric structure to the BH<sub>4</sub> radical) in bulk boron-doped diamond [18]. Further work is needed to address this conversion and to monitor the sub-surface effect which boron species may have on the subsequent steps involved in further diamond growth [19].

### 3.3.3 Loss processes from the diamond surface

As shown above, B, BH and BH<sub>2</sub> species can readily attach to an activated surface site on the {100} reconstructed surface and interconversion between these species is likely to be facile under the conditions typically used for diamond CVD. Subsequent

boron insertion (as BH) involves a significantly lower energy transition state than those involved in CH<sub>2</sub> insertion. As previously discussed (section 1.4.5), diamond growth is a balance between growth and etching processes. The extent of boron incorporation into CVD diamond depends not only on the activation barriers for the insertion steps, discussed in the previous section, but also on the relative rates of carbon and boron loss.

The key intermediates in modelling possible loss processes are the surface bound BH<sub>x</sub> and CH<sub>x</sub> species. Loss mechanisms involving species inserted into the surface reconstructed dimers are unlikely processes because of the short lifetime of an isolated inserted species. Any direct loss mechanism of a species inserted into a dimer reconstruction will involve bimolecular reactions and these processes are several orders of magnitude slower than the reverse unimolecular reactions of the ring opening and closing mechanism. For example at 1200K, the lifetime for the hydrogen abstraction reaction is  $4.34 \times 10^{-2}$  s whilst the lifetime for the carbon ring opening and closing species are  $9.43 \times 10^{-11}$  s &  $7.35 \times 10^{-9}$  s respectively (Appendix C).

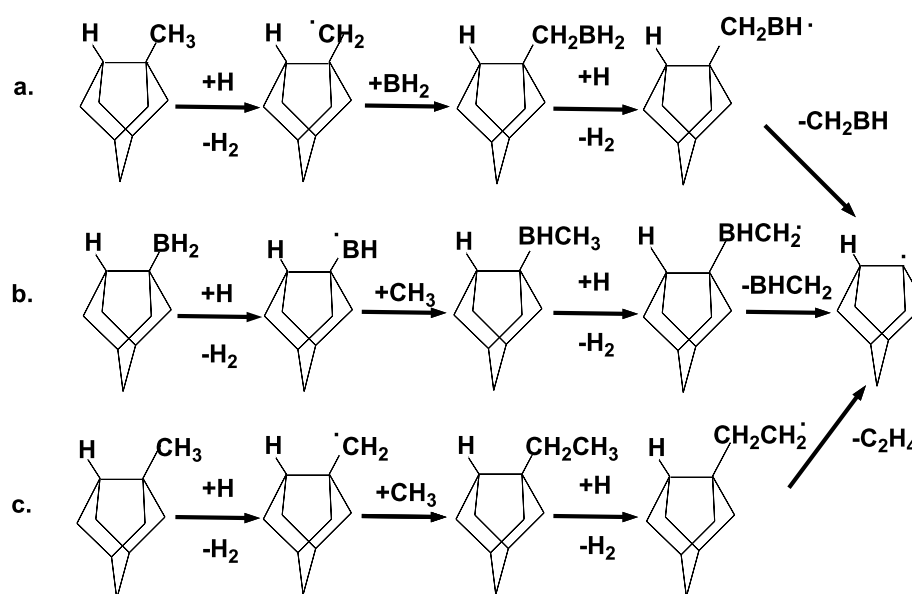


**Figure 3.6:**  $\beta$ -scission reaction pathways leading to a. & b.  $HBCH_2$  or c.  $C_2H_4$  loss from a diamond {100} surface.  $HBCH_2$  loss can occur either via C–C bond fission (a.) or via B–C bond fission (b.).

Pendant  $\text{CH}_y$  loss mechanisms from a dimer reconstruction are unlikely processes. A direct unimolecular carbon loss mechanism (3.23) for these species requires the breaking of a strong carbon–carbon bond which is very endothermic ( $\Delta E = 353.8 \text{ kJ mol}^{-1}$ ) and hence unfavourable.



Abstraction of methane by an H radical displacement reaction (3.24) is energetically favourable ( $\Delta E = -69.3 \text{ kJ mol}^{-1}$ ) but involves a very high activation barrier ( $E_a = 133.2 \text{ kJ mol}^{-1}$ ) [20].



The least energetically demanding way to remove carbon from the surface is by addition of a second carbon. This so-called  $\beta$ -scission mechanism is illustrated as process c. in Figure 3.6.  $\text{CH}_3$  addition to structure (D) in Figure 3.2 results in a pendant ethyl radical. Hydrogen abstraction by atomic hydrogen results in a surface bound  $\text{CH}_2\text{CH}_2$  species which can dissociate into the gas phase as ethene leaving the original surface site (B in Figure 3.2). This overall loss step is only  $172.6 \text{ kJ mol}^{-1}$  endothermic and is entropically favoured.

Figure 3.7 shows that the free energy for ethene elimination by the  $\beta$ -scission mechanism is calculated to become favourable at higher temperatures ( $>1100 \text{ K}$ ). The free energy of activation for this step or for the other loss processes has not been calculated, but as these are endothermic reactions with no energy barriers above the endothermicity, the free energy of reaction should be very similar to the free energy of activation.

There are a greater variety of mechanisms that could contribute to loss of sur-

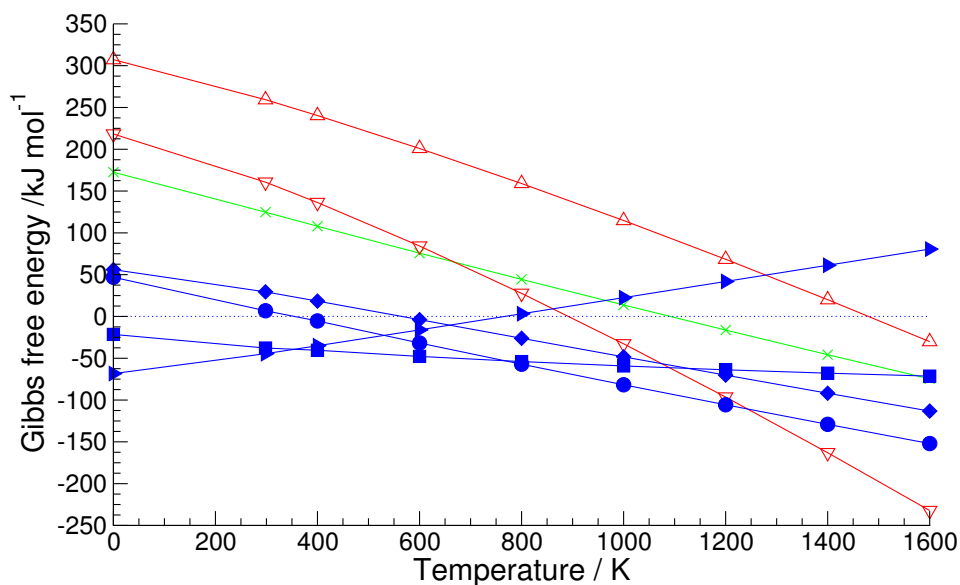


**Figure 3.7:** Calculated temperature dependent free energies of reaction for dissociation processes at a diamond {100} surface.  $\blacktriangleright$  Surf-BH<sub>2</sub> + H  $\rightarrow$  Surf-BH<sub>3</sub>;  $\blacksquare$  Surf-BH<sub>2</sub> + H  $\rightarrow$  Surf + BH<sub>3</sub>;  $\bullet$  Surf-BH<sub>3</sub>  $\rightarrow$  Surf + BH<sub>3</sub>;  $\blacklozenge$  Surf-BH<sub>3</sub>  $\rightarrow$  Surf-BH + H<sub>2</sub>;  $\times$  Surf-C<sub>2</sub>H<sub>4</sub>  $\rightarrow$  Surf + C<sub>2</sub>H<sub>4</sub>;  $\triangle$  Surf-BHCH<sub>2</sub>  $\rightarrow$  Surf + CH<sub>2</sub>BH (Figure 3.6b.);  $\nabla$  Surf-CH<sub>2</sub>BH  $\rightarrow$  Surf + CH<sub>2</sub>BH (Figure 3.6c.)

face bound boron, due to chemistry that is made accessible by the empty valence p-orbital located on the boron atom. There are two distinct  $\beta$ -scission routes, analogous to the all-carbon chemistry, shown in Figure 3.6, leading to loss of boron in the form of gas-phase CH<sub>2</sub>BH. The first process is the more important one, as it leads to cleavage of the surface carbon-boron bond. The alternative process, shown in Figure 3.6a., is less relevant as it only leads to carbon-carbon bond breaking. An interesting observation is that the final bond-breaking step is significantly more endothermic for process b. than for the carbon-carbon bond breaking steps in a. and c. This can be explained in terms of the stabilisation in the precursor radicals: the radical on the terminal CH<sub>2</sub> group in the case of b is stabilised by delocalization into the vacant p orbital on boron. There is no such stabilisation effect in the other two cases. Boron loss by the reaction shown in Figure 3.6 b. only becomes favourable above 1400 K (Figure 3.7), so probably does not play a role under CVD conditions.

A third mechanism has been identified for loss of a surface bound B species, which can compete with the above  $\beta$ -scission reactions. Figure 3.4 shows that a hydrogen atom addition to a surface bound  $\text{BH}_2$  species yields a surface bound  $\text{BH}_3$  in an exothermic step ( $\Delta E = -68.4 \text{ kJ mol}^{-1}$ ). The boron-carbon bond in the latter adduct is rather weak ( $\Delta E = 46.9 \text{ kJ mol}^{-1}$ ), so  $\text{BH}_3$  release into the gas phase, and reformation of the starting radical species (B in Figure 3.2), is a probable process. The surface bound  $\text{BH}_3$  species can also lose  $\text{H}_2$ , to form the surface bound BH species. The calculated endothermicity of this process ( $56.0 \text{ kJ mol}^{-1}$ ) is not dissimilar to that for  $\text{BH}_3$  loss from the surface; it represents another pathway for enabling the cycling between the various surface bound  $\text{BH}_x$  ( $x = 0-3$ ) species. These processes are included in Figure 3.4. Calculated temperature dependent free energy changes for the  $\text{BH}_3$  loss processes are shown in Figure 3.7.

$\text{BH}_3$  loss to the gas phase can be modelled simply as the release of a surface bound  $\text{BH}_3$  species, or as two successive steps involving, first, H atom addition to a surface bound  $\text{BH}_2$  species followed by fission of the boron-carbon bond. Both reactions are calculated to be exoergic at temperatures relevant to growth of B doped CVD diamond, though it is difficult to estimate their free energies of activation as the appropriate reference points are unclear. Given that the steady state concentration of surface bound  $\text{BH}_3$  species is likely to be low, we suggest that it is probably more reasonable to consider the latter (unimolecular) process as the rate limiting loss step at diamond growth temperatures.

The weakness of the boron-carbon bond in the surface bound  $\text{BH}_3$  species offers a B loss route for which there is no analogous carbon mechanism. Thus we conclude that B incorporation into, and B loss from, the diamond  $\{100\}$  surface are both more facile than is the case with carbon. However, a more complete elucidation of the competition between the various incorporation and loss steps identified here would require simulation of the full surface-growth kinetics, which is beyond the scope of

the present work.

### 3.3.4 Conclusions

$\text{BH}_x$  ( $x = 0-3$ ) species can bind to radical sites on the diamond  $\{100\}$  surface to form stable adducts. Inter-conversion between the surface bound  $\text{BH}_x$  species is facile at the H and  $\text{H}_2$  number densities and temperatures prevailing in typical diamond CVD conditions. Mechanisms for direct insertion of surface bound BH (and B) species into a growing  $\{100\}$  face of diamond have been identified, as has an alternative ring opening / closing sequence for incorporating BH. This latter process is the boron analogue of the mechanism by which carbon addition into the  $\{100\}$  surface is traditionally envisioned. Direct insertion of BH is calculated to involve the transition state of lowest free energy at all temperatures  $<1500$  K.

Several  $\text{BH}_x$  loss processes from the surface have also been identified. The calculated binding energy of a surface bound  $\text{BH}_3$  species is sufficiently weak that direct loss into the gas phase is likely under typical CVD conditions. Boron can also be lost from the surface as, for example,  $\text{CH}_2\text{BH}$ , by a  $\beta$ -scission mechanism. Both B incorporation into, and B loss from, the diamond  $\{100\}$  surface are thus deduced to be more facile than the corresponding carbon addition and loss processes. Estimates of the relevant energetics are a necessary precursor to any more complete description of B incorporation during diamond CVD, even into just the  $\{100\}$  surface, but a full description will eventually require proper simulation of both the gas-surface interactions and the surface-growth kinetics.

The present conclusions are based on computations at the B3LYP level of theory. Test calculations at the CCSD(T) level (Appendix A) for an even smaller model system show that the computed B3LYP energetics are fairly reliable. The use of such a small model for the diamond  $\{100\}$  surface is also a cause for concern.

Chapter 4 aims to resolve this by using a large hybrid DFT / MM procedure, encompassing the steric effects of the diamond surface, with the aim of looking at the energetics of the fundamental steps of growth of a new monolayer of diamond.

## Bibliography

- [1] P. W. Atkins and R. S. Friedman, *Molecular Quantum Mechanics* (Oxford University Press, Great Clarendon Street, Oxford, OX2 6DP, UK, 3rd. edition, 1997).
- [2] C. J. Cramer, *Essentials of Computational Chemistry: Theories and Models* (J. Wiley and Sons Inc., 605 Third Avenue, New York, NY., 2002).
- [3] W. Kohn and L. J. Sham, *Phys. Rev.* **140**, A1133 (1965).
- [4] P. Hohenberg and W. Kohn, *Phys. Rev.* **136**, B864 (1964).
- [5] W. Koch and M. C. Holthausen, *A Chemist's Guide to Density Functional Theory* (Wiley-VCH, Weinheim, 2nd edition, 2001).
- [6] A. D. Becke, *Phys. Rev. A* **38**, 3098 (1988).
- [7] C. Lee, W. Yang, and R. G. Parr, *Phys. Rev. B* **37**, 785 (1988).
- [8] A. D. Becke, *J. Chem. Phys.* **98**, 5648 (1993).
- [9] P. J. Stephens, F. J. Devlin, C. F. Chabalowski, and M. J. Frisch, *J. Phys. Chem* **98**, 11623 (1994).
- [10] J. Baker, M. Muir, and J. Andzelm, *J. Chem. Phys.* **102**, 2063 (1995).
- [11] S. Arrhenius, *Z. Phys. Chem.* **4**, 226 (1889).
- [12] K. J. Laidler, *Chemical Kinetics* (HarperCollins Publishers, New York, 3rd edition, 1987).
- [13] J. K. Kang and C. B. Musgrave, *J. Chem. Phys.* **113**, 7582 (2000).
- [14] M. J. Frisch, G. W. Trucks, H. B. Schlegel, G. E. Scuseria, M. A. Robb, J. R. Cheeseman, J. A. Montgomery Jr., T. Vreven, K. N. Kudin, J. C. Burant, J. M. Millam, S. S. Iyengar, J. Tomasi, V. Barone, B. Mennucci, M. Cossi, G. Scalmani, N. Rega, G. A. Petersson, H. Nakatsuji, M. Hada, M. Ehara, K. Toyota, R. Fukuda, J. Hasegawa, M. Ishida, T. Nakajima, Y. Honda, O. Kitao, H. Nakai, M. Klene, X. Li, J. E. Knox, H. P. Hratchian, J. B. Cross, C. Adamo, J. Jaramillo, R. Gomperts, R. E. Stratmann, O. Yazyev, A. J. Austin, R. Cammi, C. Pomelli, J. W. Ochterski, P. Y. Ayala, K. Morokuma, G. A. Voth, P. Salvador, J. J. Dannenberg, V. G. Zakrzewski, S. Dapprich, A. D. Daniels, M. C. Strain, O. Farkas, D. K. Malick, A. D. Rabuck, K. Raghavachari, J. B. Foresman, J. V. Ortiz, Q. Cui, A. G. Baboul, S. Clifford, J. Cioslowski, B. B. Stefanov, G. Liu, A. Liashenko, P. Piskorz, I. Komaromi, R. L. Martin, D. J. Fox, T. Keith, M. A. Al-Laham, C. Y. Peng, A. Nanayakkara, M. Challacombe, P. M. W. Gill, B. Johnson, W. Chen, M. W. Wong, C. Gonzalez, and J. A. Pople, *Gaussian 03, Revision B.04*, Gaussian, Inc., Pittsburgh PA, 2003.

- [15] R. D. Amos, A. Bernhardsson, A. Berning, P. Celani, D. L. Cooper, M. J. O. Deegan, A. J. Dobbyn, F. Eckert, C. Hampel, G. Hetzer, P. J. Knowles, T. Korona, R. Lindh, A. W. Lloyd, S. J. McNicholas, F. R. Manby, W. Meyer, M. E. Mura, A. Nicklass, P. Palmieri, R. Pitzer, G. Rauhut, M. Schütz, U. Schumann, H. Stoll, A. J. Stone, R. Tarroni, T. Thorsteinsson, and H.-J. Werner, *MOLPRO, a package of ab initio programs designed by H.-J. Werner and P. J. Knowles, Version 2002.1*, 2002.
- [16] H. B. Schlegel, A. G. Baboul, and S. J. Harris, *J. Phys. Chem.* **100**, 9774 (1996).
- [17] S. J. Harris, J. Kiefer, Q. Zhang, A. Schoene, and K. W. Lee, *J. Electrochem. Soc.* **145**, 3203 (1998).
- [18] J. P. Goss, P. R. Briddon, S. J. Sque, and R. Jones, *Phys. Rev. B* **69**, 165215 (2004).
- [19] M. Kaukonen, P. K. Sitch, G. Jungnickel, R. M. Nieminen, S. Pöykkö, D. Porezag, and T. Frauenheim, *Phys. Rev. B.* **57**, 9965 (1998).
- [20] H. Tamura and M. S. Gordon, *Chem. Phys. Lett.* **406**, 197 (2005).

## Chapter 4

# Quantum Mechanical / Molecular Mechanical Studies of Diamond growth

Two main models exist for the incorporation of carbon in the form of methyl radicals into a growing  $\{100\}$  diamond surface; the ring opening and closing insertion in a dimer, and insertion across trough dimer rows (the HH mechanism). These models form the basis of many Kinetic Monte-Carlo (KMC) simulations of diamond. The thermodynamics and kinetics of these incorporation reactions are based on studies performed upon models of the diamond surface, many of which incorporate a poor level of *ab-initio* theory resulting in uncertainty in the energetics of diamond growth. Our investigations have employed density functional theory (DFT) in conjunction with a large QM / MM cluster model to explore mechanisms for possible carbon incorporation in three major sites for growth on the  $\{100\}$  face of diamond as well as the corresponding direct insertion process for boron species (Chapter 3).

Our studies have also addressed the possibilities of neighbouring activation and surface migrations as a means for production of a smooth {100} diamond surface. Our results confirm, and also dramatically improve upon reported energetics and we discuss the validity of the main mechanisms in the light of our studies.

## 4.1 Introduction

### 4.1.1 Molecular Mechanics

The main challenges in computational chemistry are improving the accuracy of the calculations and the size of computational model which can be studied. Chapter 3 showed that application of quantum mechanics could yield high accuracy calculations with results comparable to experimental data. However, these techniques are not very practical for systems containing large number of atoms ( $n > 30$ ), due to their non-linear scaling nature.

Molecular mechanical (MM) calculations offer an alternative process which avoids complex electronic wavefunction calculations and originates from the early modelling of the PES of simple chemical species studied by spectroscopic techniques. The potential energy of the system is mapped out by a series of empirical functions which approximate the atomic electronic interactions. The main parameters which are used to define the PES are the changes in bond length, bond angles, torsion angles as well as non-bonding interactions, Equation (4.1).

$$E_{Total.} = \sum_{\substack{all \\ bonds}} E_{BondStretch} + \sum_{\substack{all \\ angles}} E_{BondAngle} + \sum_{\substack{all \\ dihedrals}} E_{Torsion} + \sum_{\substack{all \\ atoms}} E_{Non-Bonding} \quad (4.1)$$

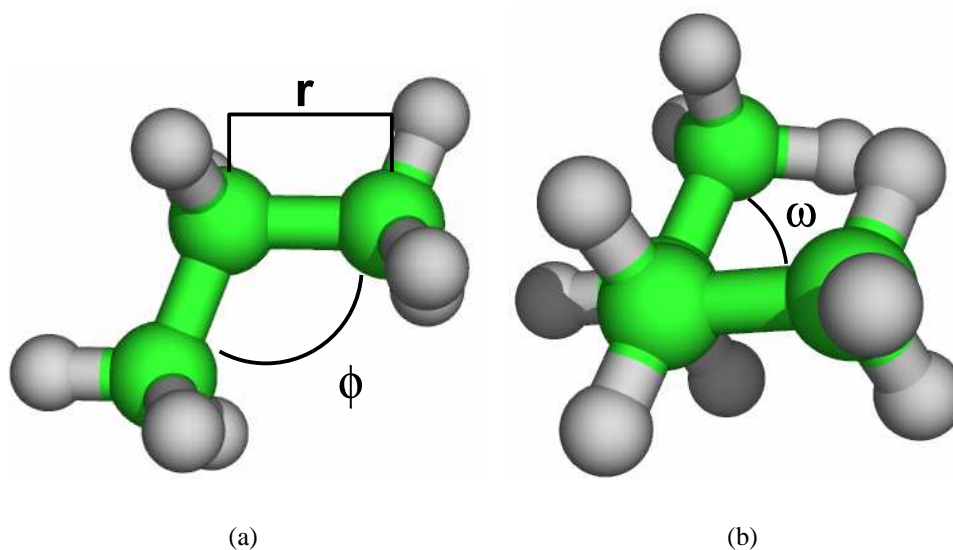


**Figure 4.1:** (a) Example showing the bond stretching and angle bending in propane (b) Example of the torsion interaction about the central bond of a hypothetical rotamer of butane.

The change in potential energy for a system due to the distortion of the bond lengths and angles, Figure 4.1(a), can be described by an harmonic oscillator function (4.2) based upon Hooke's law for the extension of a spring. The energy of the system directly relates to the displacement from the equilibrium geometry ( $x_0$ ) and has a force constant  $k$  for the respective motion.

$$E = \frac{1}{2}k_{ab(c)}(x_x - x_0)^2 \quad \text{where } x_x = r_{AB} \text{ or } \theta_{ABC} \quad (4.2)$$

However, this model is only valid at small displacements as these functions fail to describe dissociation into fragments adequately. Cubic and quartic expansion terms with their respective force constants are often included in calculations to increase accuracy, (4.3).

$$E = \frac{1}{2}[k + k_3(x_x - x_0) + k_4(x_x - x_0)^2](x_x - x_0)^2 \quad \text{where } x_x = r_{AB} \text{ or } \theta_{ABC} \quad (4.3)$$

Strain can be induced within a structure by the 3D arrangement of tertiary groups connected to two bonded atoms. This torsion strain energy results from the angle,  $\omega$ , between these groups, Figure 4.1(b), and is of the form shown in equation 4.4 [1]. The torsion potential energy is by definition periodic, with the minimum energy configuration usually being an antiperiplanar construct.

$$E_{Torsion} = \frac{1}{2}V_J [1 + (-1)^{J+1}\cos(J\omega + \phi)] \quad (4.4)$$

where  $V_J$  is the amplitude of the system,  $J$  reflects the local symmetry and the periodicity of the torsion environment and  $\phi$  is the phase angle which enables fine-tuning of the system.

Non-bonding interaction can be separated into two components, electrostatics, and steric interactions [2]. Electrostatic forms of interaction are included by the use of simple coulombic interaction between charges present upon atoms  $q_a$ ,  $q_b$ , separated by a distance  $r_{ab}$  with a certain electropermeability,  $\varepsilon_{ab}$ , (4.5). This simple equation can be expanded to include bond polarisation but this is beyond the scope of this study [1].

$$E_{electro} = \frac{q_a q_b}{\varepsilon_{ab} r_{ab}} \quad (4.5)$$

The non-electrostatic part of the non-bonding component of the MM energy has been classified as a steric interaction. These Van der Waals interactions are usually

described by Lennard–Jones type potentials between two atoms (4.6).

$$E_{vdw} = 4V_{ab} \left[ \left( \frac{\sigma_{ab}}{r_{ab}} \right)^{12} - \left( \frac{\sigma_{ab}}{r_{ab}} \right)^6 \right] \quad (4.6)$$

where  $V_{ab}$  is the attractive well depth for the atomic pair and  $\sigma$  is the value of  $r$  where there is no potential. For small to medium size systems, more realistic interatomic potentials (e.g. Buckingham potentials) can be used instead, resulting in better accuracy but these calculations require more computational resources.

All situations so far discussed have been in an ideal environment and further complications can arise as the defining parameters (bond length, angle and torsion angle) can couple together.

A key concept throughout MM theory is that, for each parameter, there is a system independent equilibrium value. In reality, these parameters vary according to the local environment, so MM models are parametrised for a selection of similar chemical models using experimental or *ab-initio* calculation results. This results in the formation of different MM forcefields and types of forcefields which are applicable to particular chemical environments.

### 4.1.2 Quantum Mechanics / Molecular Mechanics

Quantum Mechanics / Molecular Mechanics (QM / MM) is a hybrid technique which combines the accuracy of a high level of QM theory calculation with the large size advantages of MM calculations. A small region of the model, usually the centre of the reaction studied, is treated at QM theory, which is connected to the remainder of the model (usually a MM model).

The total Hamiltonian for the system, equation (4.7) (and hence the total energy, equation (4.8)) can be expressed in terms of Hamiltonian of the constituents

part, with the introduction of a term which describes the steric and electrostatic interactions between these layers ( $\hat{H}_{QM/MM}$ ) [3].

$$\hat{H} = \hat{H}_{QM} + \hat{H}_{MM} + \hat{H}_{QM/MM} \quad (4.7)$$

$$E_{total.} = E_{QM} + E_{MM} + E_{QM/MM} \quad (4.8)$$

Different levels of QM / MM theory arise from differing methods for describing  $\hat{H}_{QM/MM}$  (eq (4.9) provides an illustration [4]) and the coupling methods between the two different theory regions.

$$\hat{H}_{QM/MM} = E_{QM/MM}^{Steric} - \sum_{iM}^{Electronic} \frac{Q_M}{r_{iM}} + \sum_{\alpha M}^{Nuclei} \frac{Z_\alpha Q_M}{R_{\alpha M}} \quad (4.9)$$

where M represents the MM atoms; i and  $\alpha$  relates to the QM electrons and nuclei respectively.

Connecting the two different regions proves to be problematic, as the boundary between the two levels of theories usually occurs though a bond. Without modifications, this would lead to an unpaired electron in the QM region per bond connected to the MM region causing distortion of the QM calculations. The MM calculation would be unaffected as this level of theory explicitly neglects direct electronic interactions. Common solutions to this problem include manipulation of the QM region using a combination of hybrid and atomic orbitals to satisfy the valences (LSCF [5], [6]) and use of link atoms [4] (also known as junction dummy atoms [7]). These atoms (usually hydrogens) are added to the structure of the QM region to fulfil the electronic vacancies created by cleaving the MM region. The link atoms are explicitly included in the QM calculation but have no direct interaction with the MM

region.

The integrated molecular orbital and molecular mechanical (IMOMM) approach to QM / MM calculations uses internal geometry referencing to reduce the number of geometry variables used in the calculation [8]. This reduction occurs by redefining the coordinate system of the bridging MM atoms (represented by link atoms in the QM calculation), in terms of coordinates based upon the QM model and the remainder of the MM systems. This results in the bond and dihedral angles of the link atoms being identical to the MM atoms connected to the QM region, enabling any steric interactions from the MM region to be communicated into the QM region as well as for the results of electronic interactions in the QM region to be communicated to the MM bulk. The redefinition of internal coordinates based upon either the QM or MM regions enables the application of separate, standard energy and geometry optimisation processes for the QM and MM regions.

Figure 4.2 shows an example of the QM / MM separation of  $M(P(CH_3)_3)_2$  from ref [8] with Figure 4.2(a) showing the QM region capped with link atoms while Figure 4.2(b) shows the real system modelled. The bridging MM atoms in this example are the carbons in the pendant methyl groups.

Within the version of IMOMM used throughout this thesis [9], [10], the position of the link atoms along the bond connecting the QM and MM regions is maintained at a fixed ratio of the ideal QM-Hydrogen bond and the QM-MM bond length. The IMOMM calculations also ignore all of the electrostatic interaction components of the QM / MM Hamiltonian (4.9).

The IMOMM methodology can also be extended to include different levels of *ab-initio* theory instead of the MM region within the IMOMO protocol [11] and the N-layered Integrated MO and MM (ONIOM) protocol breaks the model down into further subsections with each section being calculated with a different level of

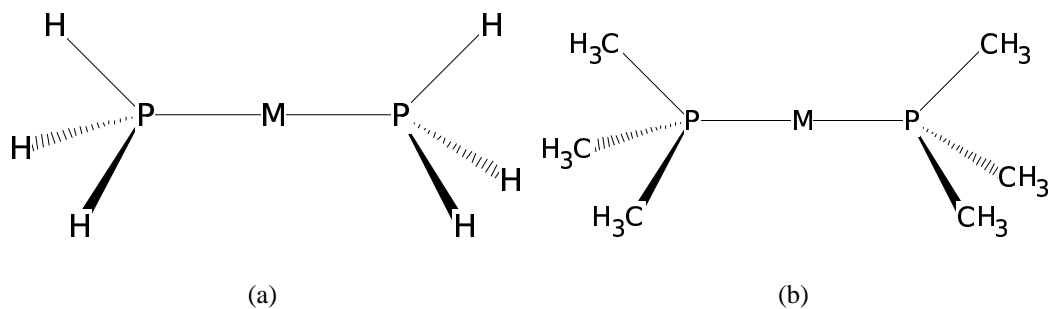


**Figure 4.2:** QM / MM region splitting examples using  $M(P(CH_3)_3)_2$  (a) QM core with hydrogen link atoms (b) The real system (adapted from ref [8]).

computational theory [12].

### 4.1.3 Previous Work

Incorporation of carbon from the gas-phase into the growing diamond surface within this thesis, so far, has focused upon the isolated adsorption of a gas-phase species upon a pristine diamond reconstructed surface and subsequent incorporation. However, Figure 4.3 shows that there are many different sites upon a growing surface, each with a different local environment, where different growth processes can occur.

Computational chemistry has been used to probe dynamics of the surface reactions. Initial work focussed upon the investigations of methyl radical incorporation into a growing surface, either into a dimer reconstruction by the ring opening closing mechanism (as discussed in Chapter 3) or via the trough bridging mechanism, Section 1.4.3.

M. Frenklach and collaborators have been at the forefront of resolving these issues and developing a consistent model for the growth of CVD diamond. Within the calculations performed by Frenklach *et al.*, the diamond surface is modelled using a

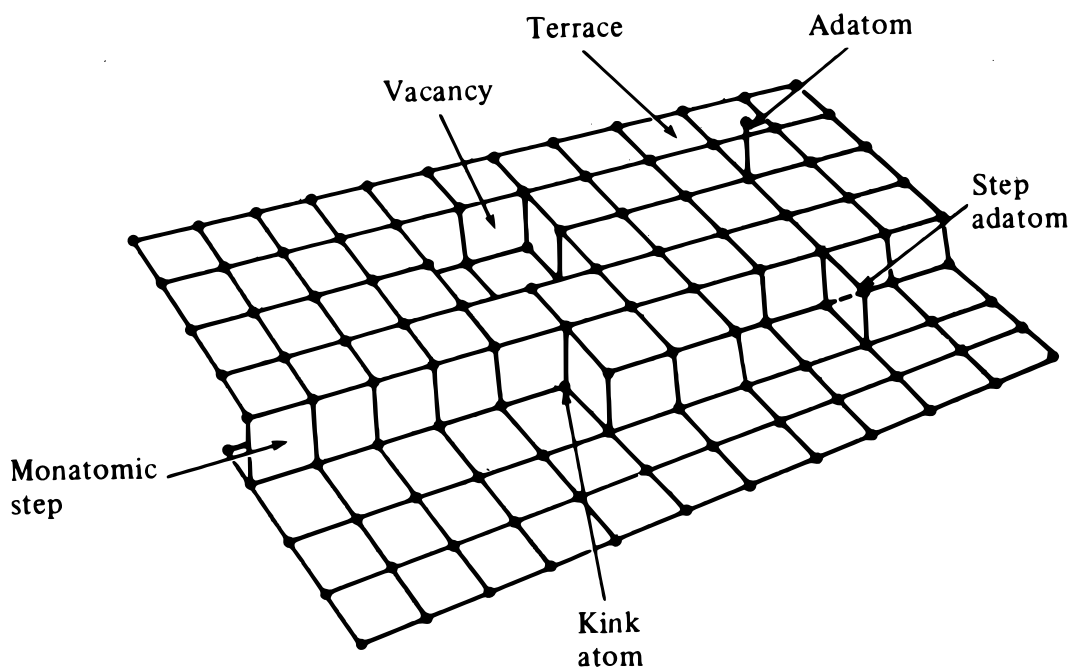


**Figure 4.3:** Sketch showing different features for a generic surface from [13].

two region system with an inner core described using the semi empirical PM3 [14] and the outer perimeter using an empirical potential parameterised to PM3 [15]. There have been various size models for the PM3 region ranging from an isolated cluster describing one reconstruction ( $C_9H_{14}$ ) to two rows of reconstructed dimer describing a  $3 \times 2$  section of the the diamond surface ( $C_{40}H_{52}$ ). Local minima upon the PES were calculated using unrestricted Hartree-Fock theory in conjunction with the combined-force molecular dynamics (CFMD) method for the outer perimeter. The energetics from these calculations have been used to calculate rate constants using non-variational transition-state theory (TST) and these form the basis for their Kinetic Monte Carlo model for diamond growth.

The main growth species considered within these incorporation studies are the methyl radical [16], [17] and acetylene [18] – [20]. The modelling shows that methyl addition to a pristine diamond surface is a barrier-less process and that there are energy barriers for  $CH_3$  radical addition at sites adjacent to previous incorpora-

tions. The results for  $\text{CH}_3$  addition were used to infer that the ring opening / closing mechanism is the more favourable process due to the inherent kinetic and thermodynamic stability of methyl absorption upon a pristine diamond surface.  $\text{C}_2\text{H}_2$  addition to a surface radical is calculated to be a feasible process and its subsequent addition results in the formation of the surface bound  $\text{C}=\text{CH}_2$  species. The authors discuss how this species can initiate the formation of a new layer of diamond, create a dimer reconstruction (see below) and the mechanism by which the  $\text{C}=\text{CH}_2$  species can be etched [18].

Investigations have been expanded to include the possibility that surface migration of carbon species might lead to the observed smooth diamond surface [21]. These studies were performed at similar theory levels to the incorporation energetics studies. The results show that hydrogen atoms can not migrate across a pristine diamond surface, as the migration process is prohibited by a large activation energy barrier (Calculated value  $\Delta E = 277.4 \text{ kJ mol}^{-1}$ , which is likely to be an underestimate) which originates from the large separations along and between the dimer rows. However, when the distance between a radical species and an H atom is reduced, (i.e. between a dimer reconstruction and an insertion or a pendant carbon species and a surface radical site), the migration of atomic hydrogen becomes a favourable process. These migration steps effectively reduce the lifetime of single radical species at certain sites and hence also reduce the feasibility of the trough bridging mechanism.

The migration of carbon species such as  $\text{CH}_2$  and  $\text{C}=\text{CH}_2$  is possible when a bi-radical site is formed from two neighbouring hydrogen abstractions and the rate of transportation is only limited by the hydrogen abstraction / addition processes. These carbon migration reactions are most favourable upon a pristine surface but the process becomes less favourable with increasing levels of neighbouring carbon incorporations as the steric interactions from the pendant  $\text{CH}_2$  groups increases the

activation energy for the migration reactions to unreasonable levels. The movement of carbon species upon the diamond surface typically ends with the coalescing of multiple moieties.

The well known observation of rows of reconstructed dimer has been a hallmark of diamond growth upon the  $\{100\}$  surface. Skokov *et al.* have proposed and discussed two possible mechanisms for the formation and geometrical arrangement of these dimers. The first mechanism assumes that there is a preferential absorption of methyl radicals at a neighbouring dimer site which results in the dimer propagation, and the second assumes that, under the right conditions, the surface migrations of  $\text{C}=\text{CH}_2$  species can result in the formation of the dimer pattern [22]. It was shown that there is no preference for adsorption of a gaseous methyl at the two common step edges ( $S_A$ ,  $S_B$ ) present upon the reconstructed diamond  $\{100\}$  surface and Figure 4.4 shows how the  $\text{C}=\text{CH}_2$  species can be incorporated into a dimer trough forming a new reconstruction [22].

Due to the large number of gas-phase and surface reactions possible, Kinetic Monte Carlo protocols have been used to see how the reaction energetics affect the growth of  $\{100\}$  diamond. The initial kinetic investigations of diamond growth looked at the direct incorporation of incident carbon species using simple adsorption models for carbon species [23], [24]. These models mapped the available experimentally published growth rates well, but offered little insight into the surface chemistry. However, the shortcomings of these initial models has led to an expansion of the modelling to include more complex reaction dynamics like surface migrations [25] and etching of surface atoms [26]. The KMC modelling process uses a time based probability algorithm to weigh the potential pathway from all the possible reactions. The model is initiated under a set of initial conditions to model CVD diamond growth and left to “grow”.

The Frenklach implementation of KMC modelled diamond growth [25], has

methyl radicals as the sole growth species with the incorporation into the diamond surface described by means of the ring opening / closing mechanism.  $\text{CH}_2$  migration along and across the dimer reconstructions was included as well as the reforming of dimer reconstructed bonds from two suitable adjacent surface radical sites. Etching was only considered to occur at isolated incorporated  $\text{CH}_2$  groups and reconstructed dimers. The former etching process is described by the removal of  $\text{CH}_2$  by the reverse of the ring opening / closing incorporation mechanism and the removal of isolated dimer reconstructions by a one or two carbon removal process. The energetics and kinetic data for these reactions are sourced from numerous calculations and experimental measurements.

The initial model failed to produce continuous rows of incorporated  $\text{CH}_2$  species (a similar observation is obtained in [27]) and all subsequent reported observations include a compensatory term to ensure saturation of these sites. This work high-

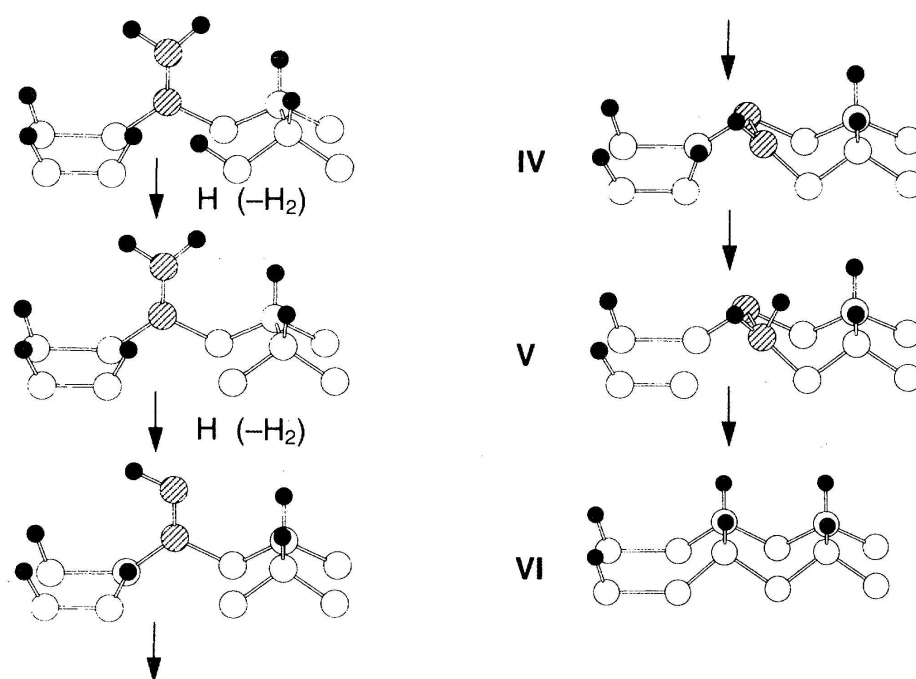


**Figure 4.4:** The transformation of an adsorbed  $\text{C}=\text{CH}_2$  group into a reconstructed dimer at a  $S_B$  step from ref [22]

lights the positive effect that the surface migration has upon the growth rates of diamond giving a roughly one order of magnitude enhancement of the growth rate over adsorption only diamond growth. The KMC model has studied the effects of numerous process conditions, including abundance of reagents and substrate temperature. The resultant films “grown” under these KMC conditions show wide variations in surface roughness, with the formation of  $\{111\}$  domains, most unlike the pristine starting diamond surface. This work also shows that, without the growth species present, etching reactions upon the rough  $\{100\}$  diamond surface can produce the smooth surfaces observed experimentally. The time-frame for this process to occur is short enough to coincide with annealing that can occur during the shutting down of a reactor.

Overall, the Frenklach model suggests that carbon, in the form of  $\text{CH}_3$ , can randomly incorporate upon a diamond surface and undergo migration across the surface until multiple species coalesce. During this process, the substrate surface can act as a template for migrating species to form new dimer reconstructions and, in combination with etching (especially under post-growth conditions), results in the smooth surface growth observed.

The KMC modelling work by Batialie *et al.* [28] is based upon previously reported energetics in the literature and considers diamond growth occurring by the methyl radicals via the trough bridging incorporation mechanism [24], [29] in conjunction with the incorporation of acetylene [18]. These studies highlight the importance of substrate orientations and the roles of  $\text{C}_2\text{H}_2$  in controlling the growth rate. By including the possibility of etching within the KMC calculations due to  $\text{CH}_3$  dissociation from the surface (calculated at the PM3 theory level), smooth terraces upon the  $\{100\}$  diamond surface can be produced, Figure 4.5 [26].

There are many other implementations of KMC to model diamond growth [27], [29], [30] but the main differences between models is due to differing KMC tech-

niques as most models use the existing literature energetics discussed above.

Tamura & Gordon [31] have used a  $(3 \times 3 \times 2)$  model ( $C_{140}H_{94}$ ) QM / MM model of the  $\{100\}$  diamond surface. Computations were performed using a Complete Active Space Self-Consistent Field (CASSCF) wavefunctions with the 6-31G (d,p) basis set to calculate the geometries of local energy minima upon the PES. The energies were corrected for dynamic correlation effects by the inclusion of a multi-reference second order perturbation theory (MRMP2) and for zero-point energy using the harmonic oscillator / rigid rotor approach. Their work mirrors that of Kang and Musgrave [32], focusing upon the insertion of methyl into a dimer reconstruction and they come to the similar conclusion that the ring opening /closing process is the rate-determining step within the dimer mechanism.

## 4.2 Experimental.

A QM / MM model of the diamond surface was set-up consisting of a 1586 atom system which describes a  $(5 \times 9 \times 4)$  section of the  $\{100\}$  diamond surface. The initial geometry of the model was formed from the bulk diamond lattice points. The

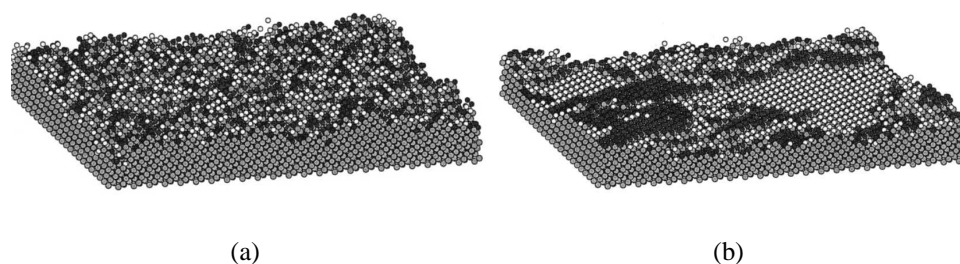


**Figure 4.5:** Images of  $\{100\}$  films during simulated growth at 1200 K (a) without and (b) with etching. Light grey atoms are carbons in the diamond film. The hydrogen atoms are shaded according to their height. Two gray levels (dark grey and white) are used, and cycle every two layers, from ref [26].

atoms on the perimeter of the model with a non-chemical stoichiometry are frozen in position during the calculations. The dimensions of the QM / MM model were chosen to reduce possible induced stresses from the frozen perimeter atoms (fixed at bulk geometry positions) affecting the region described at a high level of theory. The top diamond surface is terminated by a layer of bound hydrogens and the surface has been fabricated with the top layer following the observed surface reconstructions (Section 1.4.3). The initial geometry of the reconstructed surface layer was derived from the optimised geometry of the QM Cluster (Chapter 3) with the surface dimers arranged in rows and allowed to relax under the computation process. At the centre of the model is a QM region based upon the  $C_9H_{14}$  cluster described using DFT theory (B3LYP) with the 6-311G\*\* basis set. This small cluster model is connected to the remainder of the model through “link atoms” [4]. The majority of the atoms are described by molecular mechanics (MM2). The MM2 MM protocol is optimised for hydrocarbon species and has been parameterised using diamond within the subsets [33].

All calculations were performed using the “In-House” QoMMMa program [9], [10] which implements an IMOMM procedure. The corresponding QM calculations were performed using Jaguar [34], and the TINKER program [35] was used to model the molecular mechanics interactions. Optimisation calculations were performed using the B3LYP theory with the 6-31G\* basis set. Single point calculations of the geometry of the QM region were performed using the larger basis set of 6-311G\*\* and the resultant energies are incorporated into the QM / MM results reported. All energies quoted have no correction for zero point energies, and work quoted from Chapter 3 uses geometries and energies from comparable levels of theory.

To identify transition states upon the PES, the energy of the system is calculated at numerous points along the reaction coordinate. Constraints are imposed upon the

geometries of the key atoms so that the standard optimisation techniques can be applied to the system without returning to a global minimum. These constraints upon the geometries are typically a bond length or the difference in length between two bonds. By plotting the energies of these restricted calculations as a function of the frozen counterpart, a local energy maximum can be identified which is comparable to the transition states for the studied reaction.

By using DFT within an QM / MM protocol, total errors on all reported relative energies will be  $\sim 10 \text{ kJ mol}^{-1}$  but some cancellation of errors should occur. The present studies focus upon radical reactions at a diamond surface, hence no electrostatic interactions are included within the QM / MM model. All energies presented here are in  $\text{kJ mol}^{-1}$ , unless otherwise stated.

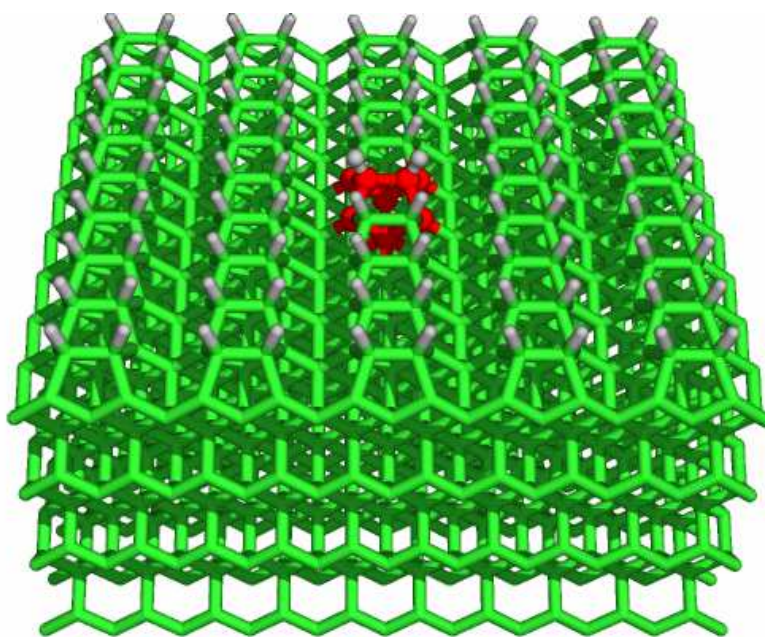


**Figure 4.6:** The QM / MM model for the reconstructed diamond {100} surface used for modelling the inclusion of carbon and boron species into the reconstructed dimer bond. QM region highlighted in red.

### 4.3 Results & Discussions

The QM/MM model used in the present work is shown in Figure 4.6. Three distinct environments for carbon incorporation into the  $\{100\}$  diamond surface have been modelled. These include modelling methyl insertion into a dimer reconstruction, the incorporation of  $\text{CH}_3$  into a dimer reconstruction across a dimer trough, and the formation of a new dimer row. Two proposed mechanisms for the surface migration of methylene groups across a pristine diamond surface have also been considered. The results obtained will be discussed in the light of the previously published work with particular attention paid to work produced by Frenklach.

The common terms used to describe carbon incorporation into the  $(2 \times 1)$  reconstructed  $\{100\}$  diamond surface are illustrated in Figure 4.7. Throughout this chapter, a smooth hydrogen terminated  $(2 \times 1)$  reconstructed  $\{100\}$  diamond surface with no carbon inclusion as shown in Figure 4.6 is referred to as a pristine diamond surface. This surface models a smooth terrace which are common upon the  $\{100\}$  diamond surface, Figure 1.12.

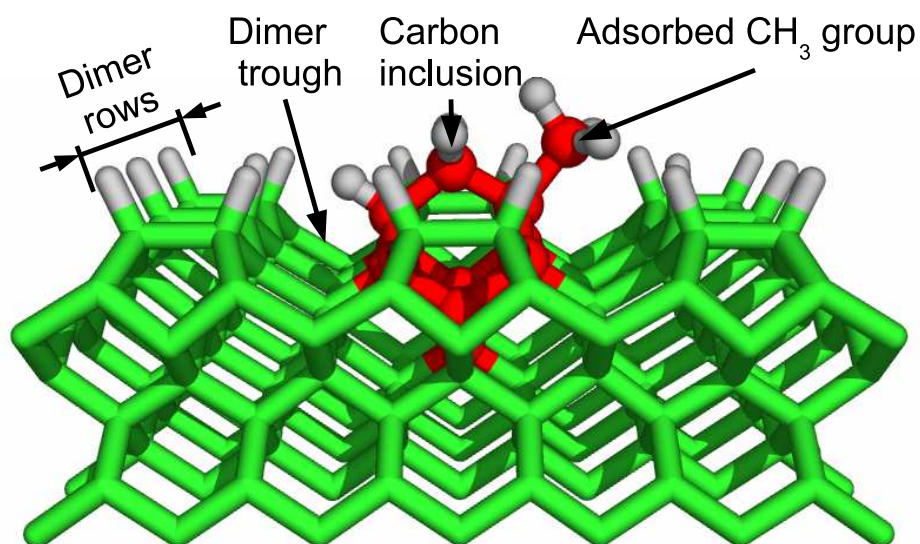


**Figure 4.7:** The common artifacts upon a growing  $\{100\}$  diamond surface.

### 4.3.1 Initial Tests

DFT QM / MM calculations were performed upon the pristine {100} diamond surface model with a C<sub>9</sub>H<sub>14</sub> QM cluster (identical to that used in Chapter 3, Figure 4.6). The reliability of the system was tested by modelling hydrogen abstraction from a dimer reconstruction by a gas-phase H atom. The energetics of abstraction should be similar to hydrogen abstraction from the small QM model (Chapter 3), as the abstracting hydrogen atom should not feel any steric interactions from the pristine surface. Also, the geometry of the QM region in the QM / MM calculation is constrained by being connected to the MM diamond surface.

Optimised geometries calculated using this QM / MM model show a high level of order permeating throughout the structure. This suggests that the reactions involving the {100} diamond surface have a very local effect on the bulk structure. The bulk MM carbon bond length is on average 1.54 Å, as opposed to the literature value of 1.51 Å for the bulk carbon-carbon bonds within a MM2 optimised diamond structure [33]. The difference in bond length results from the frozen nature of the perimeter atoms which prevents the MM region to relax adequately from the bulk positions. The extended bond lengths, will introduce strain into the diamond model but this should be constant through all models and any effects should cancel out. The length of the dimer surface reconstruction within the QM region is 1.64 Å which reflects the effects of the surrounding MM region as it prevents full relaxation to the preferable bond length for the reconstruction in the isolated cluster calculation (1.59 Å). The majority of the surface reconstructions optimised under MM conditions have carbon-carbon bond lengths of 1.58 Å. There are two exceptions to this trend, the two neighbouring parallel reconstructions which have a bond lengths of 1.63 Å. These larger values are comparable to the QM reconstruction bond length and the origins for the bond extension come from small distortions to the MM region caused from the optimisation of the QM region.

Despite this localised surface effect, all calculations have been performed using this large model as the majority of the atoms are treated by the MM level of theory and their inclusion has only a trivial effect on computational costs and running time.

As the majority of the computational work presented in the literature has calculated at the semi-empirical level of theory, tests have been proposed which compare and contrast experimental results with B3LYP and PM3 calculations. The small size of model within these tests enables modelling of the whole system with the DFT without any MM contributions. The two systems model a radical combination reaction with  $\text{CH}_3$  resulting in the formation of a carbon-carbon bond as shown in Figure 4.8, with Table 4.1 summarising the results.

Figure	Experiment	PM3		B3LYP	
		PM3	ZPE	B3LYP	ZPE
4.8(a)	-361.6	-228.1	-192.5	-348.7	-314.8
4.8(b)	-	-315.5	-288.1	-391.5	-361.0

**Table 4.1:** The different computational and experimental energies for  $\text{CH}_3$  addition to the (a) Tert-butyl radical (b) The model for the diamond (100) surface dimer reconstruction used in Chapter 3. Computational results compare the effects of including the zero point energy correction (ZPE) upon the reaction exothermicity. All energies reported are in  $\text{kJ mol}^{-1}$ .

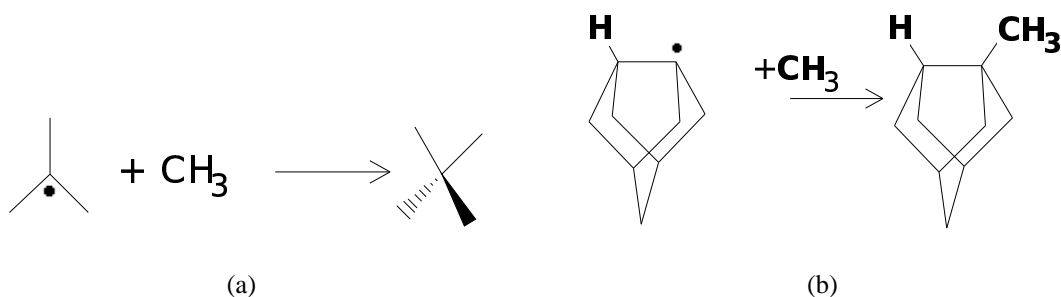


**Figure 4.8:** Two reactions used to compare the relative energetics of PM3 and B3LYP calculations

The results for methyl addition to the Tert-butyl radical  $C_4H_9$ , Figure 4.8(a), indicate that the PM3 level of theory dramatically underestimates the strength of the carbon-carbon bond formation by  $\sim 120 \text{ kJ mol}^{-1}$  when compared to the experimental value compiled from heat of formation data [36] – [38]. The inclusion of a correction factor for the zero point energy increases the discrepancy. B3LYP calculations performed with the 6-311G\*\* basis set, performed better under the same conditions with a 4% discrepancy increasing to 13 % ( $45 \text{ kJ mol}^{-1}$ ) when the zero point energy correction is included. Applying these observations to the results for the more realistic diamond surface model, Figure 4.8(b), it is apparent that the zero point energy corrected PM3 calculations underestimate the carbon-carbon bond strength. The difference between the two computational protocols is reduced, but the PM3 model underestimates the carbon-carbon bond strength by at least  $65 \text{ kJ mol}^{-1}$ . This implies that the PM3 models overestimate the ease (and hence the rate) of  $CH_3$  dissociation from a diamond surface. The accuracy of the B3LYP DFT calculations has been previously discussed in Chapter 3.

To confirm the energetics of the QM / MM system, the initial surface activation by a gaseous hydrogen abstraction was modelled. These hydrogen abstraction reactions have been intensively discussed within the literature, especially with respect to the abstraction from a dimer reconstruction. The IMOMM calculations presented here show that the hydrogen abstraction reaction is virtually thermoneutral ( $\Delta E = -0.7 \text{ kJ mol}^{-1}$ ,  $E_a = 26.4 \text{ kJ mol}^{-1}$ ). This showed that the model is in good agreement with the results for the isolated QM cluster at the same level of theory ( $\Delta E = -7.6 \text{ kJ mol}^{-1}$ ,  $E_a = 22.9 \text{ kJ mol}^{-1}$ ) and similar to the work by Kang and Musgrave ( $E_a = 28.5 \text{ kJ mol}^{-1}$ ) [32].

Tamura and Gordon also suggest that the abstraction process is virtually thermoneutral, but with a large activation energy (CASSCF (3,3)  $\Delta E = 17.3 \text{ kJ mol}^{-1}$ ,  $E_a = 94.6 \text{ kJ mol}^{-1}$ ; MRMP2  $\Delta E = -1.7 \text{ kJ mol}^{-1}$ ,  $E_a = 51.1 \text{ kJ mol}^{-1}$ ). The high

abstraction energy values for the model system were justified by comparison with similar results by Brown *et al.* obtained using MP2 single point calculations with HF optimised structures [39]. However, Brown *et al.* have questioned the accuracy of the absolute values of their calculations and the computational method used by this group has been suggested to introduce errors [40].

### 4.3.2 Incorporation into the reconstructed surface carbon-carbon bond.

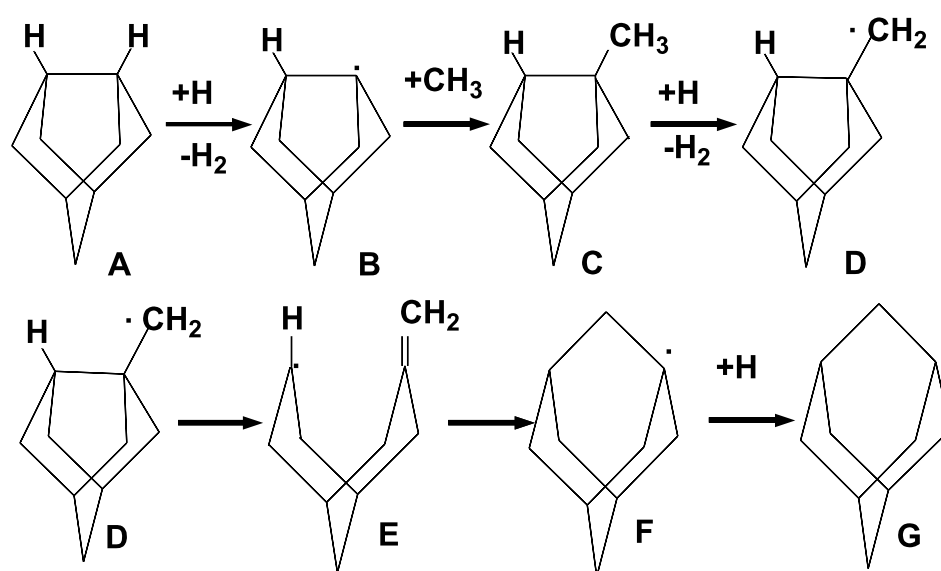


**Figure 4.9:** Recapitulation of Figure 1.17 showing one mechanism by which carbon can be incorporated into the  $\{100\}$  surface

The initial QM calculations performed on a small cluster (Chapter 3) confirmed that the incorporation of carbon in the  $\{100\}$  reconstructed diamond surface can occur by the ring opening / closing mechanism, Figure 4.9. This QM / MM study has revisited this mechanism and investigated the effects that (i) steric interactions from the neighbouring surface atoms, and (ii) constraining the QM region within a rigid diamond lattice, have on the reaction energetics. The results for the initial  $\text{CH}_3$  incorporation into a pristine  $\{100\}$  diamond surface are summarised in Table

## 4.2.

Reaction	IMOMM		QM cluster	
	Carbon	Boron <sup>a</sup>	Carbon	Boron <sup>a</sup>
A → B	-0.7	-0.7	-7.6	-7.6
<i>ts</i>	26.4	26.4	22.9	22.9
B → C	-373.2	-434.5	-383.7	-431.2
<i>ts</i>	-	-	-	-
C → D	-30.1	-9.8	-20.1	-10.9
<i>ts</i>	29.5	-	49.0	-
D → E	28.0	79.1	1.4	55.1
<i>ts</i>	43.4	-	49.0	88.3
E → F	-78.4	-157.3	-52.9	-144.6
<i>ts</i>	53.1	-	58.0	25.6
D → F	-	-78.3	-	-89.5
<i>ts</i>	-	26.3	-	41.2

<sup>a</sup> Incorporation of BH<sub>2</sub> using the direct insertion mechanism shown in Figure 3.4, Chapter 3.

**Table 4.2:** Summary of results for incorporation of CH<sub>3</sub> & BH<sub>x</sub> into the reconstructed dimer bond upon a pristine surface together with comparable results from Chapter 3 and from the literature. To be read in conjunction with Figure 4.9. All energies in kJ mol<sup>-1</sup> and QM cluster calculations contain no zero point energy corrections.

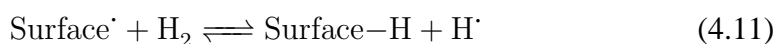
CH<sub>3</sub> readily adds to the activated surface radical site (B → C, Figure 4.9;  $\Delta E = -373.2$  kJ mol<sup>-1</sup>,  $E_a = 0$  kJ mol<sup>-1</sup>) but can be removed from the surface as methane, following a radical displacement reaction with an H atom. ( $\Delta E = -44.8$  kJ mol<sup>-1</sup>,  $E_a = 134.4$  kJ mol<sup>-1</sup>).

Activation of the pendant methyl group (C → D) by a hydrogen abstraction reaction ( $\Delta E = -30.1$  kJ mol<sup>-1</sup>,  $E_a = 29.5$  kJ mol<sup>-1</sup>) is more favourable than the similar process described by the QM cluster model ( $\Delta E = -20.1$  kJ mol<sup>-1</sup>,  $E_a = 49.0$  kJ mol<sup>-1</sup>). All processes discussed so far involve interaction with the uppermost layer of the QM region of diamond model, away from any interactions with

the surrounding MM region.

The pendant methylene radical is incorporated into the dimer reconstruction by the ring opening / closing process as previously discussed (Chapter 1 & 3). The calculated energetics for the ring opening ( $\Delta E = 28.0 \text{ kJ mol}^{-1}$ ,  $E_a = 43.4 \text{ kJ mol}^{-1}$ ) and closing ( $\Delta E = -78.4 \text{ kJ mol}^{-1}$ ,  $E_a = 53.1 \text{ kJ mol}^{-1}$  (relative to the ring opened intermediate)) processes suggest that steric interactions with the neighbouring reconstructions, involving hydrogen on the adjacent dimer row, destabilises the ring opened intermediate (E in Figure 4.9) by preventing full relaxation of the ring opened species. The steric effect from the neighbouring rows reduces the separation between the surface radical and the ethylene group (structure E, Figure 4.9) from 3.00 Å (Cluster) to 2.55 Å (IMOMM), as well as reducing the angle that the unsaturated ethylene group makes with the diamond surface from 105.4° (Cluster) to 101.9° (IMOMM). These effects favour the formation of the closed ring radical species (F). The reduction in the activation energy for the ring opening step is due to the relief of strain caused by the reconstruction.

The quenching of the closed ring radical species (F) can occur by the addition of a methyl radical or the formation of a carbon-hydrogen bond. Within diamond growing CVD reactors, H<sub>2</sub> is the most abundant species but there are also high levels of atomic H so the formation of a carbon-hydrogen bond can occur in two ways, (4.10), (4.11).



Addition of atomic hydrogen, (4.10), to the incorporated surface radical (Pro-

cess  $F \rightarrow G$  in Figure 4.9) is a barrierless exothermic process ( $\Delta E = -441.2 \text{ kJ mol}^{-1}$ ) whilst the abstraction of hydrogen from the more abundant molecular hydrogen species, (4.10), is an endothermic process with an unfavourable activation energy ( $\Delta E = 38.5 \text{ kJ mol}^{-1}$ ,  $E_a = 78.6 \text{ kJ mol}^{-1}$ ).

However, in order for further incorporation of carbon species to occur into a neighbouring site, there must be a surface radical site (F) where an incident  $\text{CH}_3$  radical can form a bond. Under standard conditions, further hydrogen abstraction reactions must occur similar to the initial surface activation (the reverse of (4.11)), as the high abundance of atomic hydrogen and the ease of addition implies that, for the majority of the time, this site should be saturated. This hydrogen abstraction process is slightly more exoergic than abstraction from the pristine surface ( $\Delta E = -38.5 \text{ kJ mol}^{-1}$ ,  $E_a = 40.1 \text{ kJ mol}^{-1}$ ). This is due to the removal of unfavourable steric interaction between the pendant hydrogen and the neighbouring dimer row, Figure 4.10(a). The activation energy is increased because the transition state for abstracting the atomic hydrogen is forced into adopting a bent geometry (C–H–H bond angle  $157.6^\circ$ ) by the steric interaction with the neighbouring dimer row, Figure 4.10(b).

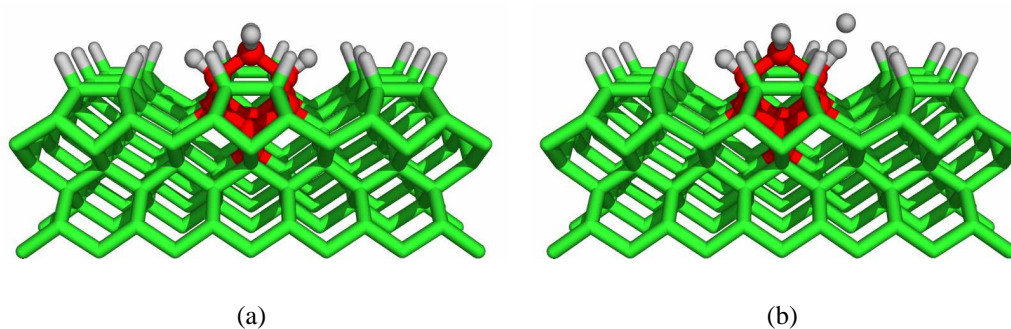


**Figure 4.10:** (a) Figure showing the QM region and the surrounding MM region (truncated for clarity) of structure G from Figure 4.9, (b) The transition state for the post insertion hydrogen abstraction reaction from structure G, Figure 4.9.

Addition of  $\text{CH}_3$  to the radical site formed from the incorporation of methyl into a reconstructed bond is not as favourable as initial incorporation on the pristine surface, as the resulting carbon-carbon bond is weaker ( $\Delta E = -235.1 \text{ kJ mol}^{-1}$ ). The reduction in the stability of the carbon bond is due to a steric interaction between the pendant hydrogens on the adsorbed methyl group interacting with the hydrogen terminated diamond surface, Figure 4.11. These ideas are investigated and expanded in Section 4.3.3 as further studies on this initial model would lead to a large DFT region which would be computationally expensive and continuation with the current model would lead to the main steric interactions being described by molecular mechanics.

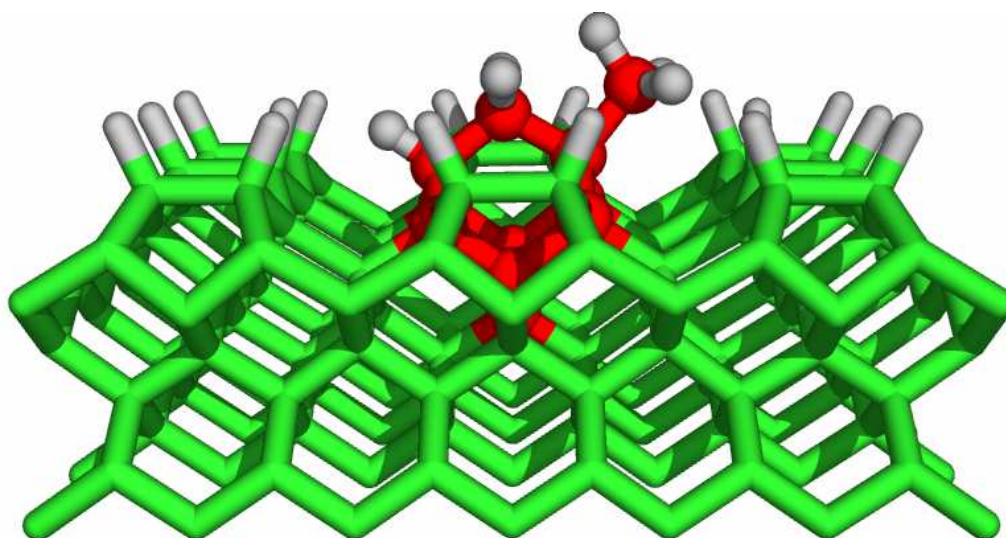


**Figure 4.11:**  $\text{CH}_3$  bound to a surface site after an initial carbon insertion into a dimer reconstruction. Note the induced displacement from the normal geometries for hydrogen bound to neighbouring dimer reconstructions.

Chapter 3 showed that  $\text{BH}_x$  species could be incorporated into a reconstructed carbon-carbon bond. These calculations have been repeated using the large QM / MM model; the results are summarised in Table 4.2. Boron species ( $\text{BH}_2$ ) can readily add to the surface radical ( $\Delta E = -434.5 \text{ kJ mol}^{-1}$ ). Hydrogen abstraction reactions with the pendant  $\text{BH}_2$  species are virtually thermoneutral ( $\Delta E = -9.8 \text{ kJ}$

mol<sup>-1</sup>) and the resulting BH species directly inserts into the dimer reconstruction ( $\Delta E = -78.3$  kJ mol<sup>-1</sup>,  $E_a = 26.3$  kJ mol<sup>-1</sup>). The direct insertion process is slightly less favourable than the isolated QM cluster model predicted due to the extra rigidity of the QM region caused by the surrounding MM region. The ring opening / closing process mirroring the carbon inclusion process is a less favourable pathway as steric interactions from neighbouring rows (as previously discussed for the carbon inclusion study) increase the endothermicity of the process (D  $\rightarrow$  E,  $\Delta E = 79.1$  kJ mol<sup>-1</sup>)

	Tamura & Gordon <sup>a</sup>			Oleinik <i>et al.</i> <sup>b</sup>	Skokov <i>et al.</i>
	IMOMM	CASSCF(3,3)	MRMP2	DFT hybrid	PM3
A $\rightarrow$ B	-0.7	17.3	-1.7	-36.7	-
<i>ts</i>	26.4	94.6	51.1		-
B $\rightarrow$ C	-373.2	-372.4	-372.4	-311.7	-307.9 <sup>d</sup>
<i>ts</i>	0.0	0.0	0.0		0.0 <sup>d</sup>
C $\rightarrow$ D	-30.1	-20.5	-34.7	-79.1	-
<i>ts</i>	29.5	83.3	45.2		-
D $\rightarrow$ E	28.0	83.3	74.1		51.9 <sup>c</sup>
<i>ts</i>	43.4	20.2	15.1		64.0 <sup>c</sup>
E $\rightarrow$ F	-78.4	-78.7	-72.4		-100.4 <sup>d</sup>
<i>ts</i>	53.1	72.4	50.6		51.5 <sup>d</sup>
D $\rightarrow$ F				-29.3	
<i>ts</i>				54.4	

<sup>a</sup> from ref [31].

<sup>b</sup> from ref [41].

<sup>c</sup> from ref [16].

<sup>d</sup> from ref [17].

**Table 4.3:** Comparison of energetics for methyl incorporation into a dimer reconstruction. To be read in conjunction with Figure 4.12.

Table 4.3 compares the IMOMM results for methyl incorporations into a dimer reconstruction with comparable data from the literature. As mentioned previously, the strength of the carbon-carbon bond predicted by the B3LYP level of theory

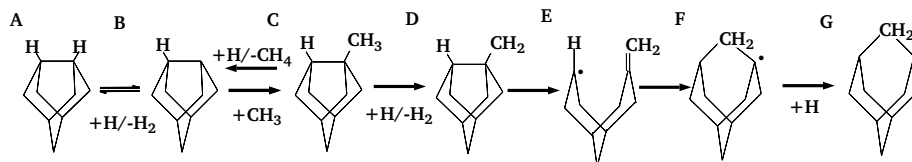


**Figure 4.12:** Recapitulation of mechanism shown in Figure 4.9

(now embedded within an IMOMM protocol) is much greater than predicted by the calculations at the PM3 level. However, the calculations of Tamura and Gordon compute the energetics of the bond formation at a comparable value. The implication of the underestimation of bond strength by the PM3 calculation is that the reverse reaction, the dissociation of  $\text{CH}_3$  from the surface becomes less favourable. This has been considered by many KMC protocols as the final step in the etching process (the reverse of Figure 4.12) and hence the feasibility of the reverse reaction being an etching process for  $\text{CH}_2$  species in such calculations is reduced. The other removal mechanism for carbon from the surface is as methane, via a radical displacement reaction with hydrogen and a pendant methyl group. This process has a high activation barrier, rendering this etching process unlikely.

The direct surface activation of a pendant methyl species by hydrogen abstraction is not mentioned within the works of Frenklach as they generate the pendant radical species from the migration of hydrogen to a surface radical site. The comparable reaction from Tamura and Gordon overestimates the activation barrier and the magnitude of the exothermicity.

The key difference between the IMOMM and PM3 calculation for the incorporation of methylene into the dimer reconstruction is the ring opening process ( $\text{D} \rightarrow \text{E}$ ) with the formation of the unsaturated ethylene group (structure E) within the IMOMM calculation being  $\sim 20 \text{ kJ mol}^{-1}$  less endoergic than the calculations at the PM3 level. The PM3 calculations also overestimate the barrier for the ring opening reaction, by approximately  $20 \text{ kJ mol}^{-1}$ . This results in the rate constant

for this pathway being  $\sim 16\%$  too slow (this value is calculated using the Arrhenius equation for reaction  $D \rightarrow E$  and assuming identical prefactors and conditions). These factors may reduce the population of the surface bound  $\text{CH}_2$  species and make the ring closing step the rate limiting step for the inclusion of  $\text{CH}_2$  via this mechanism.

There is, however, good agreement regarding the value of the activation energy for the final ring closing step, between the PM3 and B3LYP calculations. The ring opening / closing step calculations by Tamura and Gordon overestimate the endoergic nature of the ring opening process but predict a comparable exothermicity for the ring closing step as the IMOMM calculation. The reason for this divergence from the IMOMM data can be traced to steric interactions from the MM region of the calculations; this region contributes approximately  $60 \text{ kJ mol}^{-1}$  to the activation energy process. These interactions prevent full relaxation of the geometries, and thus increases the ring opening energy to unrealistic levels.

The work of Oleinik *et al.* [41] has been included for comparison, as these energetics provided the basis for the etching mechanism for the KMC models of Battaile *et al.*[26]. Contrary to other results presented within the literature, Oleinik *et al.* find that the incorporation mechanism occurs through a direct process with a single transition state (akin to the  $\text{BH}_x$  mechanism discussed in Chapter 3). Their calculated activation barrier for this process, is wrongly compared to the ring opening process of Frenklach [16] which has been shown to be inaccurate. This is clearly erroneous, and the inference that carbon species can be etched by the reversal of the insertion mechanism is also suspicious as their calculations underestimate the enthalpy change for the incorporation of a pendant methyl radical into a reconstructed bond by approximately a factor of 2 ( $-29.3 \text{ kJ mol}^{-1}$ (Oleinik *et al.*),  $-50.4 \text{ kJ mol}^{-1}$  (IMOMM)).

## Neighbouring group effects

Studies within this thesis so far have focused upon the dynamics of the ring opening / closing mechanism for incorporating carbon species into a pristine diamond surface. Two further scenarios have been modelled. These investigate (i) the energetics for incorporation of a  $\text{CH}_3$  group into a dimer reconstruction after insertion has occurred into the neighbouring dimer reconstruction, Figure 4.13(a), and (ii) the incorporation dynamics associated with a reconstruction as part of a 1D growing chain progressing across the reconstructed dimers and troughs, Figure 4.13(b). Both situations would be key situations in a step-wise growth model for diamond CVD. Table 4.4 compares the energetics of these two processes with that for  $\text{CH}_2$  inclusion into the pristine  $\{100\}$  surface. Calculations have focused upon the energies only as transition states were mostly low in energy.

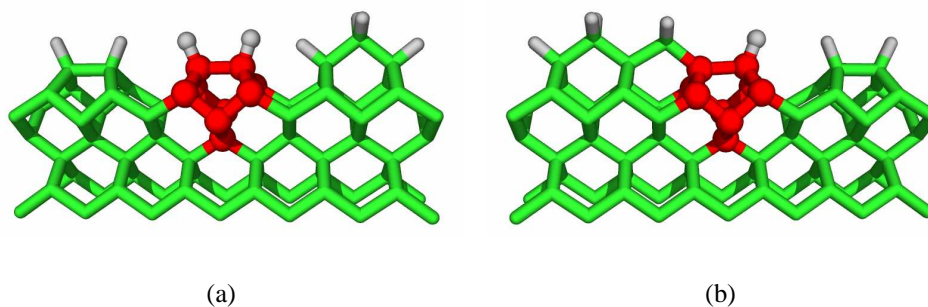


**Figure 4.13:** Cross sections through QM / MM models showing the MM modifications for modelling the effects on incorporation energetics (a) insertions into a neighbouring reconstructed dimer (b) 1D chain, growing across dimers and troughs.

The results show that the surrounding environment to a dimer reconstruction can affect the reaction dynamics of the ring opening / closing mechanism. For a reconstruction adjacent to a carbon inclusion (Figure 4.13(a)), the distance separating the dimer rows is reduced from 2.57 Å (Pristine surface) to 1.93 Å. This causes an

Reaction	Pristine surface	Neighbouring Incorporation <sup>a</sup>	1D Chain <sup>b</sup>
A → B	-0.7	-2.5	15.7
B → C	-373.2	-347.1	-390.5
C → D	-30.1	-37.3	-86.9
D → E	28.0	45.2	
E → F	-78.4	-106.3	
D → F			-103.5

<sup>a</sup> Figure 4.13(a)

<sup>b</sup> Figure 4.13(b)

**Table 4.4:** The energetics for CH<sub>3</sub> incorporation upon three different diamond surface environments using the mechanism shown in Figure 4.12.

increase in the local steric interaction. Hence, processes which reduce these interactions, like the abstraction of a surface hydrogen, become favourable ( $\Delta E = -2.5 \text{ kJ mol}^{-1}$ ). However, the reduction in the size of the dimer trough can also hinder some processes, including the methyl absorption to a surface radical site and the ring opening mechanism. These steric interactions cause the formation of a weaker carbon-carbon bond by  $\sim 30 \text{ kJ mol}^{-1}$ . This weakening occurs from the steric interaction from the protruding surface bound hydrogen, preventing the incident methyl group from forming a bond with the surface radical at the favourable angle of  $71.4^\circ$  (pristine surface) and forces the adoption of a surface angle of  $88.6^\circ$ . The same steric effects increases the endoergicity of forming the ring opened radical species by  $\sim 20 \text{ kJ mol}^{-1}$ . The extra energy costs arise from the steric interactions restricting the separation of the radical and surface bound ethylene group to  $2.48 \text{ \AA}$  instead of the usual  $2.56 \text{ \AA}$  for the pristine surface.

Figure 4.13(b) shows a structure that could be important in the growth of a chain of CH<sub>2</sub> incorporations along dimer chains. The process is perceived to start with incorporation into a dimer reconstruction followed by incorporation of a methylene group across a dimer trough. This species would be a key part of a step-growth

model for diamond. The model for the growing 1D chain shows that the surface dimer bond is under high levels of strain as the carbon atom at the opposing end of the reconstruction is impeded from relaxing to the normal reconstruction geometry. This is shown by the elongation of the dimer bond, to 1.715 Å, and by the bond adopting an angle of 4.7° below the {100} diamond surface.

Methyl addition to a surface radical site, formed by an endoergic hydrogen abstraction reaction ( $\Delta E = 15.7 \text{ kJ mol}^{-1}$ ) results in the formation of a strong carbon-carbon bond ( $\Delta E = -390.5 \text{ kJ mol}^{-1}$ ) and hydrogen abstraction from the pendant  $\text{CH}_3$  group results in the spontaneous relaxation to a ring opened structure. A stable structure with a pendant  $\text{CH}_2$  group (akin to D, Figure 4.9) was not found. The ring closing process is also favourable as it reduces the overall steric interaction on the system to a level similar to that found in the pristine diamond surface.

However, both scenarios are found to involve similar energetics to the simple incorporation into the pristine diamond. In neither case do we find any evidence that the ring opening / closing mechanism shows a preference for incorporation into a site adjacent to a previous incorporation rather than a random incorporation into any other site on a pristine surface.

### 4.3.3 The dimer trough bridging mechanism

Other possibilities for formation of a smooth surface of diamond include preferential carbon incorporation into a site next to previous carbon adsorption. The mechanism discussed here is derived from the HH mechanism first proposed by Harris in 1989 [42] and later modified in 1993 by Harris & Goodwin [29]. The process involves the formation of a bridging methylene group across the trough between dimer rows, Figure 4.14. This can occur by two possible mechanisms: a bi-radical pathway (A  $\rightarrow$  E) or a sterically hindered addition (B  $\rightarrow$  D). The actual mech-



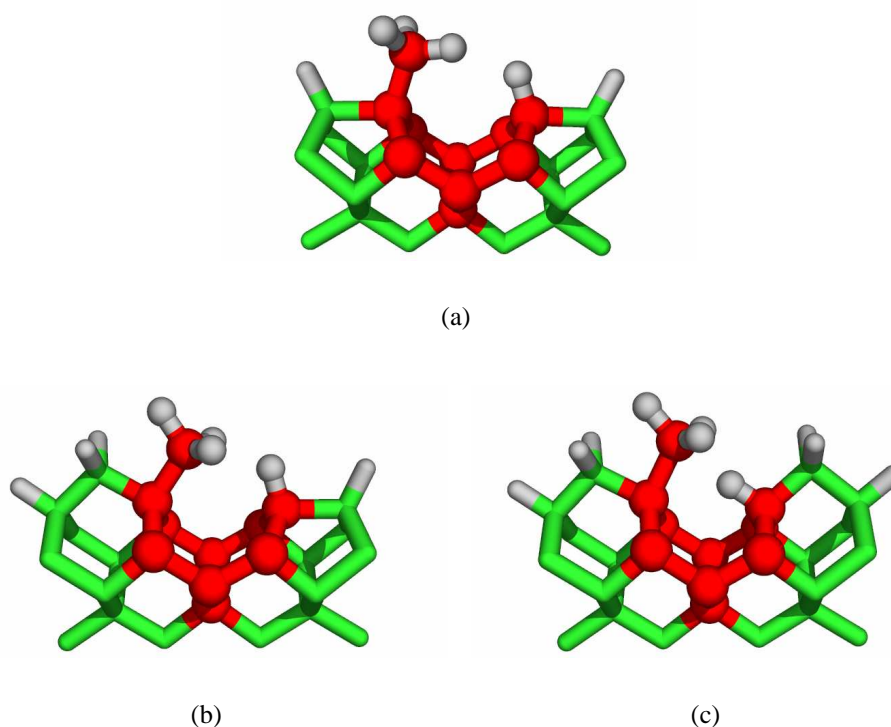


**Figure 4.15:** The three environments used for modelling the row bridging mechanism for carbon incorporation: (a) nucleation; (b) propagation; (c) the termination step. The structure shown relates to step D from Figure 4.14 with the QM region highlighted in red.

sition states have also been located using a larger cluster model of the propagation scenario for comparison. In this new model the QM region has been expanded to include the neighbouring features on each side of the dimer trough, Figure 4.16.

The sterically hindered pathway for incorporation across the dimer trough involves the formation of a carbon-carbon bond with the incident  $\text{CH}_3$  competing for space with a hydrogen atom bonded to the neighbouring dimer row (B  $\rightarrow$  D, Figure 4.14). The local diamond surface environment connecting to the pendant methyl group and the surface hydrogen atom determines the proximity of groups and thus their competition for space. The removal of strain from surface carbon atoms held in a dimer reconstruction by inclusion of a carbon by the ring opening / closing mechanism allows the resultant surface bound hydrogen to adopt the more

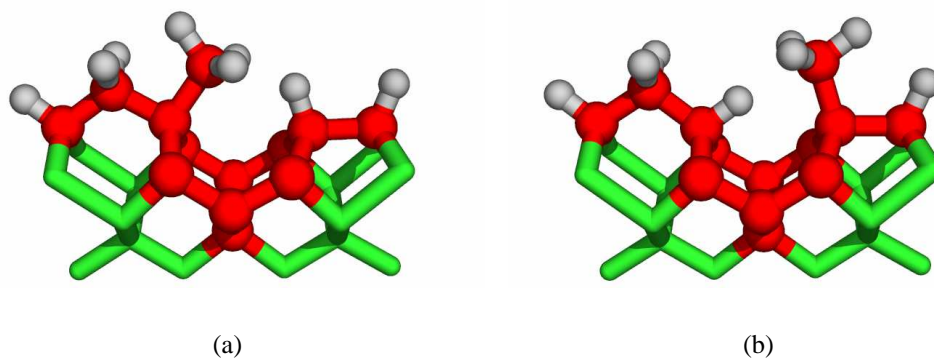


**Figure 4.16:** (a) The larger QM region used to model the propagation step in the trough bridging mechanism; (b) The “mirrored” arrangement. QM region highlighted in red.

favourable  $sp^3$  geometry. This has the consequence that both the carbon and the hydrogen encroach into the dimer trough. These differences in surface geometries are reflected in the strength of the carbon-carbon bonding to the adsorbed methyl group, ranging from a strong bond ( $-389.7 \text{ kJ mol}^{-1}$ ) for adsorption onto the pristine surface (Figure 4.15(a)) to the weak ( $-149.3 \text{ kJ mol}^{-1}$ ) for methyl addition between two previously incorporated reconstructions.

Table 4.5 compares the energies derived using two different QM / MM models, used for a methyl addition reaction to a single surface radical site with differing neighbouring environments.

The results show that there is a fairly good agreement between the three different QM / MM models. All models show a similar trend, i.e. that the most favourable addition of methyl occurs upon the pristine diamond surface and that further incorporations in the neighbouring vicinity results in a weakening of the resultant carbon-carbon bond.

Differences in the absolute values arise from two factors - the description of the surface radical site within the QM region of each model and the manner in which

Local environment	Initial	Trough bridging	
	Cluster <sup>a</sup>	Small <sup>b</sup>	Large <sup>c</sup>
Pristine surface (- · -) <sup>1</sup>	-373.2	-389.7	-345.7
One inclusion (∧ · -) <sup>2</sup>	-235.0	-245.6	-219.1
One inclusion (- · ∧) <sup>3</sup>	-347.1	-340.0	-317.9
Two inclusions (∧ · ∧) <sup>4</sup>	-119.8	-149.3	-101.7

<sup>a</sup> from Section 4.3.2.

<sup>b</sup> from Figure 4.15.

<sup>c</sup> from Figure 4.16.

<sup>1</sup> as in Figure 4.15(a).

<sup>2</sup> as in Figure 4.16(a).

<sup>3</sup> as in Figure 4.16(b).

<sup>4</sup> as in Figure 4.15(c).

**Table 4.5:** Table comparing different QM / MM IMOMM models for the addition of methyl to a single radical site with different neighbouring environments.

steric interaction is conveyed in the individual systems. The QM / MM model used for modelling carbon incorporation into the reconstructed dimer bond models the surface radical as a tertiary species, but all steric interactions are described by the MM force field. The small trough bridging model describes the steric interactions between the dimer rows within the QM region, but describes the surface radical as a secondary radical. These species are inherently less stable than tertiary radicals. The larger QM model for the trough bridging scenario rectifies this problem to being a tertiary radical by the inclusion of the neighbouring reconstructions and / or the incorporated carbon species within the QM region and this change can explain the difference in energies between the large and the small models.

The results indicate that MM steric interactions have a larger effect upon the overall energetics of carbon additions than the precise QM description of these interactions. These effects are manifested in the bond angle for the resultant carbon-carbon bond for one inclusion (∧ · -), where the initial model (MM steric interaction) has a bond angle of 76.8° whilst the full QM description of the interaction

within the larger QM model computes the bond angle to be  $74.0^\circ$ .

Attention now switches to the possible surface rearrangement reactions involving the pendant methyl group and the surface bound hydrogen atom (processes  $D \rightarrow E$ ). For the scenarios which involve a neighbouring incorporation, the hydrogen abstraction reaction from the sterically restricted adsorbed methyl group ( $D \rightarrow C$ , Figure 4.14) to form the pendant  $\text{CH}_2$  radical is exothermic ( $-21.1 \text{ kJ mol}^{-1}$ ,  $-63.1 \text{ kJ mol}^{-1}$ ,  $-111.7 \text{ kJ mol}^{-1}$ , Figures 4.15(a), 4.15(b) & 4.15(c) respectively) as the induced geometry change reduces the steric interactions across the dimer trough.

Internal hydrogen migrations across the dimer trough from the diamond surface, to the pendant methylene group ( $C \rightarrow E$ , Figure 4.14) are virtually thermoneutral except for the termination scenario which is exothermic ( $\Delta E = 8.5, 6.3, -12.5 \text{ kJ mol}^{-1}$ , Figures 4.15(a), 4.15(b), 4.15(c) respectively). The exothermic migration is due to the decrease in steric interaction between the newly-formed pendant methyl group and the neighbouring dimer row.

The initial starting radical (B) can also undergo a further hydrogen abstraction reaction ( $B \rightarrow A$ , Figure 4.14) to form a bi-radical site, to which methyl addition is possible. This abstraction reaction is effectively a thermoneutral process ( $4.1, 5.2 \text{ kJ mol}^{-1}$ ; Figures 4.15(a) & 4.15(b), respectively). For the most sterically hindered site (Figure 4.15(c)) the process is slightly exothermic ( $-5.1 \text{ kJ mol}^{-1}$ ). The exothermicity is generated from the reduction of steric interaction by the removal of the second hydrogen atom from the diamond surface. Methyl addition to this bi-radical site is much more favourable than to the single radical site, and hence strong carbon-carbon bonds are formed for all scenarios. The observed increase in bond strength is ascribed to the reduction in steric interaction from the neighbouring dimer row. This is highlighted by the change in the angle which the methyl group makes with the surface from  $51.9^\circ$  (D) to  $48.6^\circ$  (E) for the larger model shown

in Figure 4.16(a).

These different mechanisms by which methyl radical species can be adsorbed, together with subsequent rearrangement reactions, lead to the same final ring closing reaction ( $E \rightarrow F$ , Figure 4.14) which is instigated by a hydrogen abstraction reaction. In contrast to the previous steps, the energetics for the final ring closing step become more favourable as the distance between the ring closing carbon atoms is reduced. The large distance between the pendant methyl and the surface radical for the pristine diamond surface (2.68 Å) in conjunction with the large separation between the dimer rows (3.46 Å), results in a highly strained ring closed species held in place with a weak carbon-carbon bond ( $-113.1 \text{ kJ mol}^{-1}$ ; F, Figure 4.14). In contrast, the ring closing step for the termination scenario, where the separation of the surface carbons is much less (2.50 Å) results in a very strong carbon-carbon bond ( $-516.7 \text{ kJ mol}^{-1}$ ). This ring closing step is highly favourable due to the reduction in steric hindrance and the resulting bond is stronger than the initial carbon-carbon bond which attaches the  $\text{CH}_3$  group to the diamond surface.

At CVD temperatures, (700 – 1200 K), entropic changes during a reaction will have a significant effect on reaction dynamics. The corresponding contribution to  $\Delta S$  for reactions which lead to the loss of a gas-phase species (e.g.  $\text{CH}_3$  addition to the surface) is  $\sim -100 \text{ J mol}^{-1} \text{ K}^{-1}$ . This entropic contribution when combined with the elevated reaction temperatures makes the weaker ( $\Delta E < 150 \text{ kJ mol}^{-1}$ ) carbon-carbon bond formation steps unlikely, i.e. reagents are favoured. Therefore, for diamond growth at CVD temperatures, the trough bridging mechanism is not a feasible process for nucleation upon a pristine diamond surface as there is an unfavourable ring closing step. Also, incorporation of a methyl radical to a radical site surrounded by two previous incorporations can only occur through the unlikely bi-radical pathway. Hence, the most likely site for carbon incorporation using the trough bridging mechanism is the single surface radical formed after an inclusion in

dimer reconstruction. The reaction pathway at this site has a minimal steric effect on the initial CH<sub>3</sub> adsorption and has a small distance (3.187 Å) between the dimer rows, enabling the formation of a strong carbon-carbon bond in the ring closing reaction.

	Small QM region			Large QM region	
	Pristine surface <sup>a</sup>	1 inclusion <sup>b</sup>	2 inclusions <sup>c</sup>	1 inclusion <sup>d</sup>	Mirrored <sup>e</sup>
	(- -)	(∧. -)	(∧. ∧)	(∧. -)	(- ∧)
<b>Steric route</b>					
B → D	-389.7	-245.6	-149.3	-219.1	-317.9
<i>ts</i>				0.0	
D → C	-21.1	-67.9	-114.4	-67.7	-41.6
<i>ts</i>				31.1	
C → E	8.5	6.3	-12.5	5.7	-33.6
<i>ts</i>				20.0	
<b>Bi-radical</b>					
B → A	4.1	5.2	-5.1	-7.2	-22.6
<i>ts</i>				6.2	
A → E	-406.4	-297.0	-271.1	-274.0	-367.9
<i>ts</i>				0.0	
<b>Ring closing</b>					
E → F	-113.1	-392.7	-516.7	-369.1	-275.2
<i>ts</i>				0.0	

<sup>a</sup> Figure 4.15(a)

<sup>b</sup> Figure 4.15(b)

<sup>c</sup> Figure 4.15(c)

<sup>d</sup> Figure 4.16(a)

<sup>e</sup> Figure 4.16(b)

**Table 4.6:** Summary of results for incorporation of CH<sub>3</sub> across the trough separating dimer rows. All energies in kJ mol<sup>-1</sup>.

Table 4.6 also compares the results for the inclusion of methyl using the large QM IMOMM model (Figure 4.16). As previously discussed, this model is an expansion of the initial trough bridging QM model to include the neighbouring dimer

reconstruction and inclusions in the same row. Methyl addition to the single radical site is a barrierless process similar to CH<sub>3</sub> addition to the pristine diamond surface. Addition to the energetically favourable bi-radical site is assumed to occur by a similar mechanism. This suggests that CH<sub>3</sub> addition to the surface is only affected by the strength of the resulting carbon-carbon bond, which is determined by the local neighbouring environment. These results are in direct contradiction with the finding of Skokov *et al.* whose work for the addition of methyl radicals is summarised in Table 4.7 and Figure 4.17.

	IMOMM <sup>a</sup>	Skokov <i>et al.</i> <sup>b</sup>	
	$\Delta E / \text{kJ mol}^{-1}$	$E_a / \text{kJ mol}^{-1}$	$\Delta E / \text{kJ mol}^{-1}$
A1	-402.5	0	-307.9
A2	-419.6	0	-315.5
A3	-340.0	0	-274.9
A4	-409.3	0	-308.4
B1	-261.0	61.9	-101.3
B2	-308.6	10.0	-195.8
B3	-158.7	101.3	45.6
B4	-283.25	36.08	-129.3

<sup>a</sup> Data obtained using models in Figure 4.15

<sup>b</sup> Data from [17]

**Table 4.7:** The energetics for methyl adsorption for different radical sites described in Figure 4.17.

For methyl addition to the pristine diamond surface, both models predict that CH<sub>3</sub> addition is a barrierless process with the PM3 model underestimating the resultant carbon-carbon bond strength as previously discussed in Section 4.3.2. However, the models differ when comparing methyl addition to a radical site next to a previous inclusion, scenarios B1 – B4 in Figure 4.17, as the PM3 model predicts considerable activation barriers for these processes. Such erroneous activation barriers for these singlet addition reactions can occur from a poor initial description of

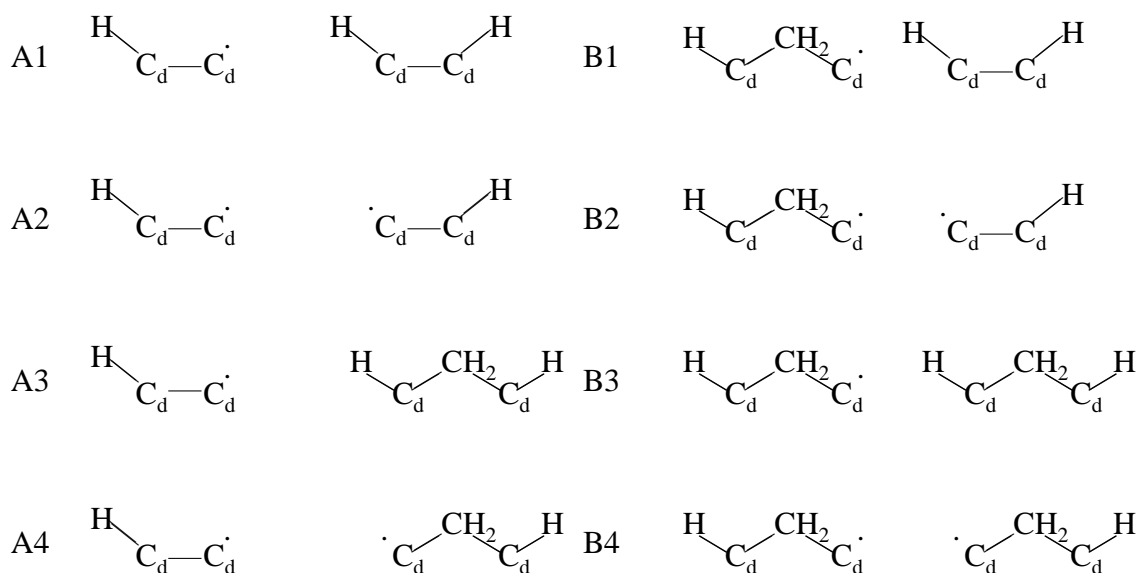


**Figure 4.17:** Surface radical sites investigated for methyl addition in [17]

the occupations of the molecular orbitals of the two incident radical species, resulting in the model being described by a closed shell species. As the PES is probed along the reaction coordinate, the perceived energy barrier occurs from the transition from the closed shell reagents to the singlet state required for carbon-carbon bond formation.

In addition, the underestimate of the strength of the newly formed carbon-carbon bond for species B1 – B4 by the PM3 calculations results in the formation of very weak carbon-carbon bonds when compared with methyl adsorption to the pristine diamond surface. For the B3 scenario, bond formation is considered to be an unfavourable endothermic process with a high activation barrier ( $\Delta E = 45.6 \text{ kJ mol}^{-1}$ ,  $E_a = 101.3 \text{ kJ mol}^{-1}$ ). In reality, these bond forming reactions are all favourable processes which result in weaker carbon-carbon bonds than addition to a pristine surface, but the resultant carbon-carbon bonds (except for the B3 scenario) should be stable under CVD conditions and thus should be included within KMC scenarios.

The focus now returns to the surface modification reactions required for incorporation of methyl using the sterically hindered scenario. The hydrogen abstraction reaction from the pendant methyl group is an energetically favourable step ( $\Delta E = -67.7 \text{ kJ mol}^{-1}$ ,  $E_a = 33.1 \text{ kJ mol}^{-1}$ ) but shows no evidence for preferential activation over the similar abstraction reaction from the pristine diamond surface. The subsequent rearrangement reaction whereby a H atom migrates from the surface to the pendant  $\text{CH}_2$  radical should be a trivial process, as the activation energy for the unimolecular rearrangement ( $\Delta E = -20.5 \text{ kJ mol}^{-1}$ ,  $E_a = 20.0 \text{ kJ mol}^{-1}$ ) is much lower than the ring opening / closing reactions which readily occur upon the diamond surface. Direct abstraction of the surface hydrogen in the sterically unfavoured situation ( $\text{D} \rightarrow \text{E}$ ) is an unlikely process despite being exothermic ( $\Delta E = -61.7 \text{ kJ mol}^{-1}$ ) as the bound  $\text{CH}_3$  group prevents the incident abstracting hydrogen atom from adopting a favourable incident angle, resulting in the high activation energy ( $E_a = 39.4 \text{ kJ mol}^{-1}$ ).

Incorporation of carbon using the bi-radical pathway depends only upon the second hydrogen abstraction which is calculated to be a favourable process with a reduced activation barrier when compared to the radical activation of a pristine surface ( $\Delta E = -7.2 \text{ kJ mol}^{-1}$ ,  $E_a = 6.2 \text{ kJ mol}^{-1}$ ). The final ring closing step ( $\text{E} \rightarrow \text{F}$ ), which is mediated by a hydrogen abstraction reaction, shows a reduction in the hydrogen abstraction activation energy when compared with abstraction from a pristine surface.

For comparison, the trough bridging mechanism has been modelled for a system where the methyl group is bound to a dimer reconstruction which is next to an inclusion, Figure 4.16(b). This “mirror” image of the more preferable trough bridging mechanism would be in direct competition with the ring opening / closing incorporation mechanism. The adsorption of  $\text{CH}_3$  in the “mirror” pathway is  $\sim 100 \text{ kJ mol}^{-1}$  more exothermic than the similar adsorption in the standard scenario. This

increase in the carbon-carbon bond strength is due to the nature of the dimer reconstruction which causes the pendant methyl group to adopt an angle of  $73.1^\circ$  to the surface. This angle moves the pendant methyl group away from the neighbouring incorporation and dramatically reduces the steric interactions with the neighbouring species.

However, the observed difference in geometry for the pendant methyl group results in a weakening of the carbon-carbon bond formed during the ring closing ( $E \rightarrow F$ ) by  $100 \text{ kJ mol}^{-1}$  making this pathway unlikely.

In summary, a strong carbon-carbon bond can form with methyl addition at the bi-radical site (A), but this process is unlikely as the formation of the active site requires two sequential bimolecular hydrogen abstraction reactions in a neighbouring environment, before the methyl adsorption can occur. Methyl addition to the sterically hindered site (B) is energetically possible, but less favourable than addition to the bi-radical site as the resulting carbon bond is relatively weak. Intra-molecular hydrogen migrations are possible but key steps are mediated by hydrogen abstraction, each with an activation barrier.

The most probable scenario where the dimer trough bridging mechanism can occur is the propagation step, with addition of a methyl to a previous incorporation. Both the initiation and termination scenarios have one step which results in a weak carbon-carbon bond ( $113.1, 114.4 \text{ kJ mol}^{-1}$  respectively) which becomes unfavourable at CVD temperatures when entropic effects are considered.

However, these results suggest that there is no activation of the diamond surface for the next  $\text{CH}_3$  incorporation by a previous inclusion (into a dimer reconstruction). Indeed, methyl is preferentially adsorbed onto the single surface radical site upon a pristine diamond surface over a previous incorporation radical site and the probability of this mechanism being the dominant mechanism for carbon inclusion

upon the {100} diamond surface is diminished by the high number of hydrogen abstractions required for the incorporation of one carbon unit in comparison with other processes.

#### 4.3.4 New row nucleation

The mechanisms by which a reconstructed dimer can form upon a diamond surface under CVD conditions is a poorly discussed area of diamond growth. Within this section, we discuss the energetics of a new mechanism by which a new layer within a reconstructed dimer can be created, Figure 4.19.

One view of forming a new dimer reconstruction upon the {100} diamond surface is that two incorporated methylene groups can be in close proximity and that the expulsion of two hydrogen atoms creates a bi-radical site from which the reconstruction is formed, Figure 4.18(a) [43].

Within this section, the QM / MM model from Section 4.3.2 has been modified so that the MM surface region has a row of CH<sub>2</sub> groups incorporated into a dimer chain. The row is located next to the QM region. The QM region is modelled by the cluster from section 4.3.2 expanded to include the appropriate section of the inserted row, structure A in Figure 4.19.

Using the QM / MM model, methyl incorporation into a dimer reconstruction next to the row of incorporated carbons has been modelled using the more favourable ring opening / closing mechanism, Figure 4.18(c), Section 4.3.2. The methyl adsorption, hydrogen abstraction and ring opening steps are energetically feasible but the ring closing step, though possible, has a large activation barrier, Table 4.8.

The large activation barrier results from steric interactions with the methylene

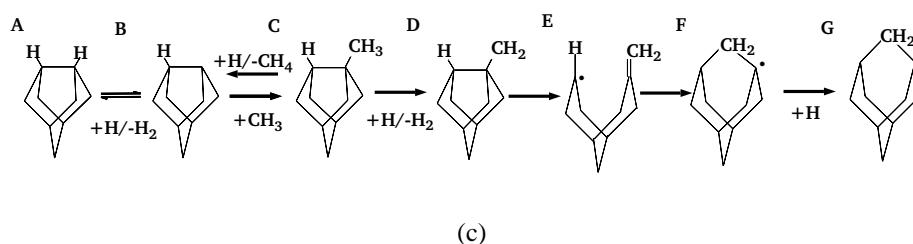
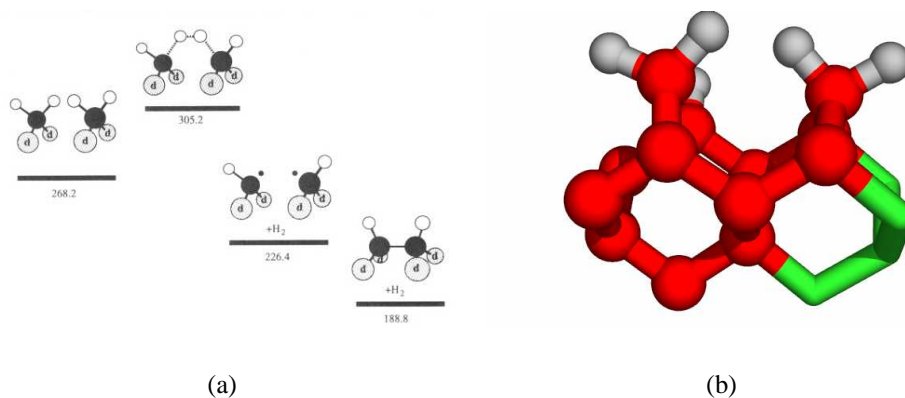


**Figure 4.18:** (a) Recapitulation of Figure 1.15(b) showing a proposed intermediate for formation of the dimer reconstruction from ref [43] (b) The transition state of the ring closing reaction (E  $\rightarrow$  F, Figure 4.18(c)) as part of the incorporation of carbon into a dimer reconstruction (left) next to a row of previously incorporated carbons (c) Recapitulation of the ring opening / closing mechanism (Section 4.3.2).

	IMOMM		Skokov <i>et al.</i> [17]		
	pristine	1 inclusion	pristine	2 inclusions	2 inclusions (1 radical)
Ring closing	-89.5	-49.5	-100.4	18.8	-27.6
<i>ts</i>	49.1	70.5	51.5	132.6	85.8

**Table 4.8:** The effects upon energetics and activation energies for methyl radical incorporation into a dimer reconstruction with 1 or 2 parallel inclusions. All energies are in kJ mol<sup>-1</sup>

group upon the row of incorporated methylenes. This interaction forces the ring closing CH<sub>2</sub> group to adopt an angle of 81.2° to the diamond surface instead of the usual angle of 90°. This high activation barrier renders this pathway an improbable mechanism for generating the reconstructions.

The ring closing reaction is an exothermic process only because the steric interaction from the pendant hydrogens upon the incorporated methylene group is minimised by both CH<sub>2</sub> groups rotating away from each other. This relaxation is only possible because the surrounding environment is a pristine diamond surface, thus further reducing the likelihood of this process happening as part of a growing diamond surface.

Table 4.8 compares these findings with similar studies by Skokov *et al.* [17] at the PM3 level of theory. Their studies sandwiched the studied reconstructed dimer between two inclusions and between one CH<sub>2</sub> and CH radical inclusion. These PM3 results confirm that the ring closing step is not possible for incorporation of methylene radicals in environments where the studied dimer reconstruction has adjacent carbon inclusions in the same dimer row. Thus, the possibility of dimer reconstructions being formed from molecular hydrogen dissociation instigated by steric repulsion is a highly unlikely process.

These results suggest that a different approach is required for the formation of the reconstructed dimers during CVD growth of diamond. Figure 4.19 shows a proposed mechanism which by-passes unfavourable steric interactions caused by two neighbouring methylene groups pendant upon the {100} diamond surface by the incorporation of a methyl radical upon the previously deposited carbon atoms and a neighbouring dimer reconstruction. The mechanism proceeds by the formation of a bridge between the inserted row and the dimer reconstruction using the pendant methyl group and then, upon hydrogen abstraction, the bridging methylene group incorporates into the dimer reconstruction indirectly forming the new reconstruction. This new row nucleation could be envisaged as a step formation. This mechanism is similar to a proposed pathway for the patterned incorporation of a migrated C=CH<sub>2</sub> group (formed from absorption of acetylene), Figure 4.4, [22].

The formation of the pendant methyl group upon the row of previously incor-

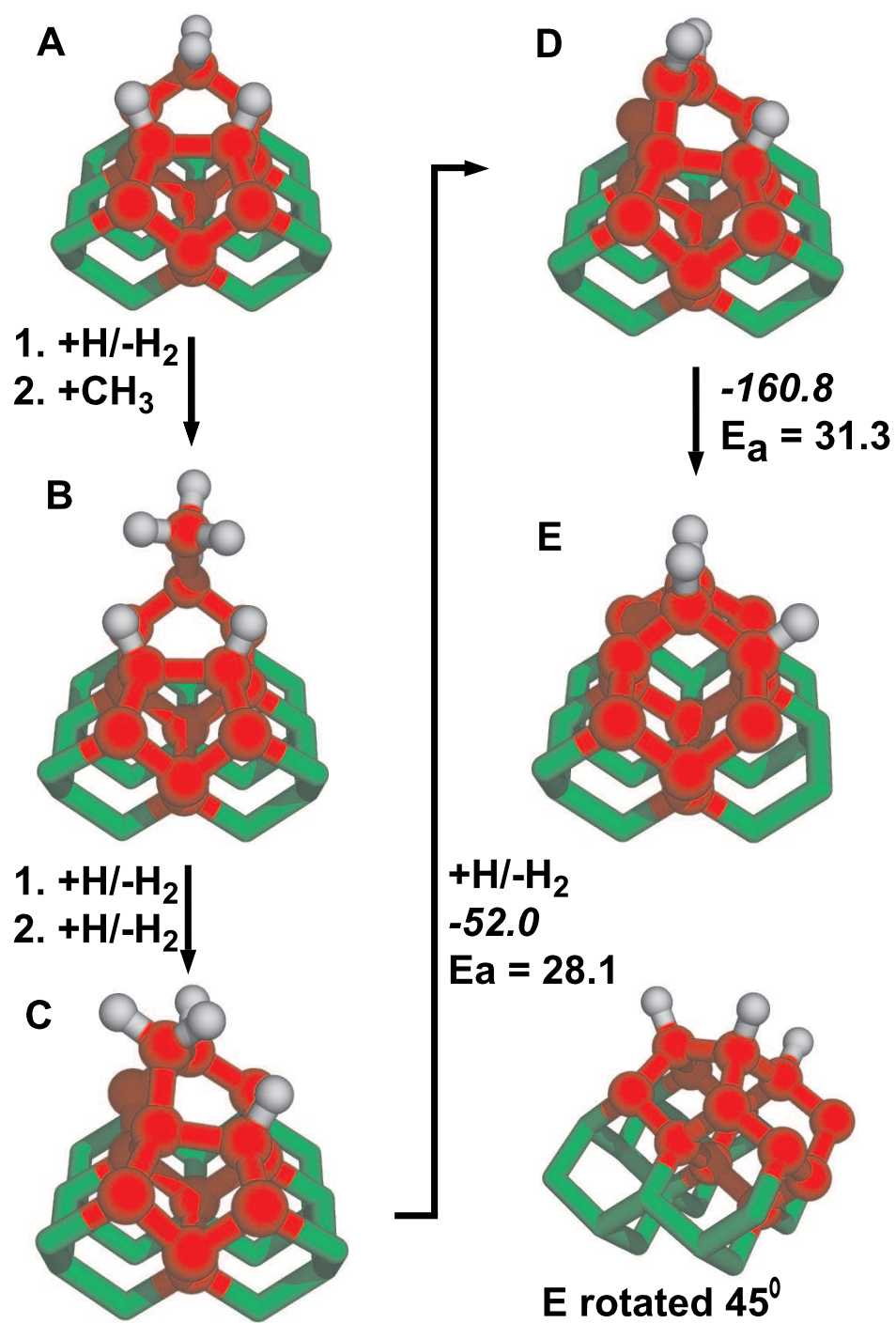


**Figure 4.19:** Proposed mechanism for nucleation of a new dimer reconstruction layer by incorporation of CH<sub>3</sub>. Process energies (in kJ mol<sup>-1</sup>) for inter-conversion between the various species via addition and/or elimination reactions as defined in the figure are indicated in italics

porated carbon atoms ( $A \rightarrow B$ , Figure 4.19) is an exothermic process for both the hydrogen abstraction ( $\Delta E = -25.2 \text{ kJ mol}^{-1}$ ,  $E_a = 30.4 \text{ kJ mol}^{-1}$ ) and methyl adsorption reactions ( $\Delta E = -342.3 \text{ kJ mol}^{-1}$ ,  $E_a = 0 \text{ kJ mol}^{-1}$ ).

The process of forming the bridging  $\text{CH}_2$  species, ( $B \rightarrow C$ , Figure 4.19) is very similar to the  $\text{CH}_3$  incorporation in the trough bridging mechanism, following the sterically hindered pathway, Section 4.3.3. However, in this scenario, the probability of a bi-radical incorporation mechanism being a feasible pathway is unlikely, since this route would require many sequential bimolecular reactions, as there are no mechanisms, except for gas-phase hydrogen abstraction, for forming the initial bi-radical species. There are several possibilities regarding the order in which these hydrogen abstraction reactions can occur (as discussed in Section 4.3.3).

The most favourable pathway for the insertion of a bridging methyl group ( $B \rightarrow C$ , Figure 4.19) is for an initial hydrogen abstraction from the dimer reconstruction ( $\Delta E = -23.1 \text{ kJ mol}^{-1}$ ,  $E_a = 21.8 \text{ kJ mol}^{-1}$ ) followed by a hydrogen abstraction from the pendant methyl group ( $\Delta E = -42.1 \text{ kJ mol}^{-1}$ ,  $E_a = 21.0 \text{ kJ mol}^{-1}$ ). The initial hydrogen abstraction, which was unfavourable in the trough bridging mechanism, is now accessible due to the larger separation between the methyl group and the hydrogen which enables a more orthodox TS geometry and hence a reasonable activation energy.

The possibility of forming the bridging methylene group by a similar mechanism to the sterically hindered trough bridging mechanism (Hydrogen abstraction from pendant  $\text{CH}_3$  followed by hydrogen migration and ring closing induced by a hydrogen abstraction: Pathway  $D \rightarrow F$  via  $C$  in Figure 4.14) is an unlikely process due to the high activation barrier for the endothermic hydrogen migration step ( $\Delta E = 7.5 \text{ kJ mol}^{-1}$ ,  $E_a = 89.0 \text{ kJ mol}^{-1}$ ). The high barrier to the reaction arises from the large distance between the pendant  $\text{CH}_2$  group and the surface hydrogens.

The geometry of the bridging methylene group is such that, upon a favourable hydrogen abstraction ( $\Delta E = -52.0 \text{ kJ mol}^{-1}$ ,  $E_a = 28.1 \text{ kJ mol}^{-1}$ ), the subsequent radical directly inserts into the dimer reconstruction with a similar barrier to that of the ring closing reaction ( $\Delta E = -160.8 \text{ kJ mol}^{-1}$ ,  $E_a = 31.3 \text{ kJ mol}^{-1}$ ). This insertion results in the formation of a reconstructed dimer at  $90^\circ$  to the initial pattern, (E in Figure 4.19). The final insertion mechanism differs from the normal ring opening / closing process because the motion of the inserting radical is restricted by the bridging carbon-carbon bond and this holds the radical in a favourable position for the direct insertion.

### 4.3.5 Surface carbon migration reactions

The results in the previous sections have shown that, despite the numerous surface radical sites to which a gaseous methyl radical can add, the single radical site which results in the strongest carbon-carbon bond is upon a pristine diamond surface. The large number of the energetically favoured pristine surface radical sites available under standard CVD diamond growth conditions suggests that adsorption of  $\text{CH}_3$  will most likely occur at random sites upon a pristine surface, from which carbon will be incorporated into the diamond surface.

In order for these random incorporations to lead to the formation of a smooth  $\{100\}$  surface with rows of reconstructed dimers, we have investigated whether key carbon species can migrate across the diamond surface. During this migration process, individual carbon species can coalesce resulting in the formation of the observed smooth terraces

The carbon migration pathways studied within this thesis were first proposed by Frenklach and Skokov in 1997, and involve the movement of species along and across the dimer rows present upon the  $\{100\}$  diamond surface [21]. As previously

discussed, hydrogen migration processes across a pristine diamond surface are unlikely due to a large activation barrier. This results in the migration processes being controlled by the gas-phase hydrogen abstraction / addition reactions that also govern  $\text{CH}_3$  incorporation. Previous arguments suggest that formation of bi-radical sites is an unlikely random process, requiring two abstraction reactions in a similar location. It can be argued, however, that the lifetime of these bi-radical species is such that only unimolecular reactions, like the methylene migration reactions described below, can occur.

The proposed mechanism for migration of a methylene group is shown in Figure 4.20. The mechanism begins with the incorporated methylene group (F from Figure 4.9) adjacent to a neighbouring radical site. The incorporated  $\text{CH}_2$  group undergoes a ring opening process to form an unsaturated methylene group with a radical upon either side (2 in Figure 4.20).

This intermediate either reforms the dimer reconstruction (3a) or forms a bridging carbon-carbon bond across the dimer trough (3b). The previous steps move the two radicals close enough to form a bond resulting in the strained intermediate 4, which can open in two ways, one of which reverts to 1, and the other leads to the migrated species 5.

The migration mechanism via the pendant  $\text{CH}_2$  radical can occur in two dimensions, both along dimer chains as highlighted in Figure 4.20 as well as along dimer rows as shown in Figure 4.21. Investigations on this mechanism employed the same large QM / MM model used in the trough bridging mechanism, (Section 4.3.3, Figure 4.16(a)).

Table 4.9 compares the results for the ring opening / closing mechanism (1.  $\rightarrow$  4., via 3b.) from the IMOMM model with the published Frenklach data. Both sets of data show that the ring opening step (1.  $\rightarrow$  2.) is an endothermic process with

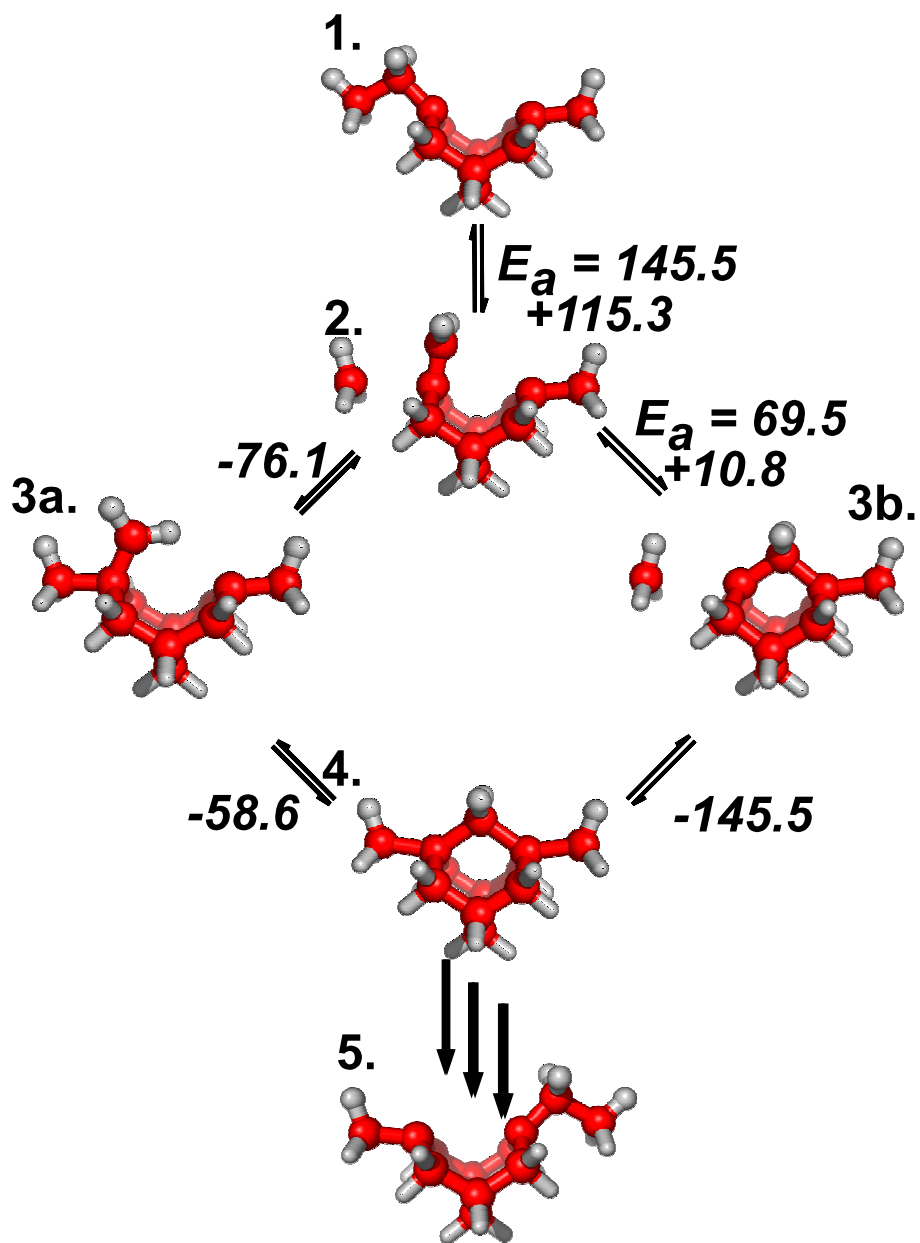


**Figure 4.20:** The CH<sub>2</sub> surface migration mechanism along a dimer chain from ref [21]. The mechanism is highlighted by optimised QM structures from the relevant IMOMM calculation with the QM atoms represented by spheres and the link hydrogen atoms by sticks.

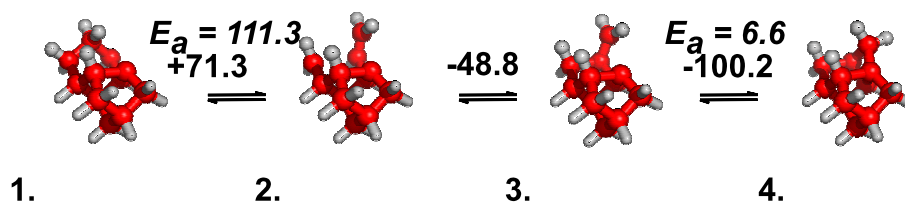


**Figure 4.21:** The  $\text{CH}_2$  surface migration mechanism along a dimer row from ref [21]. The mechanism is highlighted by optimised QM structures from the relevant IMOMM calculation.

similarly high activation barriers. The IMOMM model predicts that the alternative ring closing step (2.  $\rightarrow$  3b.), bridging the dimer trough is effectively an endothermic process with an activation energy barrier slightly higher than the ring closing step within the carbon inclusion step ( $\Delta E = 10.8 \text{ kJ mol}^{-1}$ ,  $E_a = 47.7 \text{ kJ mol}^{-1}$  c.f. ring closing step  $E_a = 53.1 \text{ kJ mol}^{-1}$ ). The regeneration of the reconstructed dimer (3.  $\rightarrow$  4.) by addition of the two radical species is a barrierless exothermic process ( $\Delta E = -145.5 \text{ kJ mol}^{-1}$ ). The IMOMM model thus predicts that the migration of an incorporated  $\text{CH}_2$  species by the ring opening / closing mechanism is less favourable than the initial ring opening / closing incorporation mechanism. These two steps are in contrast to the Frenklach model which predicts an exothermic alternative ring closing step ( $\Delta E = -51.4 \text{ kJ mol}^{-1}$ ,  $E_a = 12.0 \text{ kJ mol}^{-1}$ ) whilst the regeneration of the dimer reconstruction is a thermoneutral process with a very high activation barrier ( $\Delta E = 7.9 \text{ kJ mol}^{-1}$ ,  $E_a = 110.3 \text{ kJ mol}^{-1}$ ) – see Table 4.10.

The migration of carbon as a pendant radical species rather than as an unsaturated methylene group has been considered as a transportation mechanism both along dimer chains, 1.  $\rightarrow$  4. via 3a., Figure 4.20, as well as along dimer rows, Figure 4.21. The main difference with this process and the previously discussed mechanism is that the final bridging species, 4., is generated by the formation of a bridging carbon-carbon bond (3a.  $\rightarrow$  4.). This mechanism is driven by the reformation of the surface reconstruction dimer (2.  $\rightarrow$  3.) which results in the pendant

Radical	IMOMM	Skokov <i>et al.</i> <sup>a</sup>
1. $\longrightarrow$ 2.	115.3	99.6
<i>ts</i>	145.5	150.6
2. $\longrightarrow$ 3.	10.8	-55.6
<i>ts</i>	65.9	61.8
3. $\longrightarrow$ 4.	-145.5	7.9
<i>ts</i>	0.0	45.6

<sup>a</sup> from ref [21]

**Table 4.9:** Results for the ring opening / closing mechanism for surface methylene migration.

CH<sub>2</sub> radical species. The pendant radical can then add to a suitable neighbouring site either across the dimer trough or on the neighbouring dimer reconstruction. This mechanism offers a 2D transportation process across a surface.

Two QM / MM models have been employed to model the radical surface migration along and across the rows of reconstructed dimers upon the diamond surface. The model from the previous section is used to describe the energetics of the dimer trough bridging while the QM / MM model from section 4.3.2 has been modified to include two parallel reconstructions in the QM region to calculate the energetics of migration along dimer rows. The energetics for these migration steps are summarised in Table 4.10. The difference in values for the migration along the dimer row as opposed to along the dimer chains is due to the proximity of the two migration radical sites. These results confirm that methylene migration can occur by these mechanisms and the values for the energetics suggest that the process is more favourable than previously reported Frenklach data.

Also, the termination step involving migration of the pendant CH<sub>2</sub> radical could be responsible for the formation of the reconstructed dimer. Figure 4.22 shows the possible mechanism by which a pendant CH<sub>2</sub> migrating along a dimer row can form

Reaction	Dimer migration	Frenklach & Skokov[21]	Row-bridging migration	Frenklach & Skokov[21]
1. $\longrightarrow$ 2.	71.3	99.6	115.3	99.6
<i>ts</i>	111.3	150.6	145.5	150.6
2. $\longrightarrow$ 3.	-48.8	-51.4	-76.1	-51.4
<i>ts</i>	0.0	12.0	0.0	12.0
3. $\longrightarrow$ 4.	-100.2	14.1	-58.6	3.7
<i>ts</i>	6.6	124.4	0.0	110.3

**Table 4.10:** Results for the methylene radical mechanism for surface migration, showing the energetics for migrations along and across dimer reconstructions.

the bridging methylene structure (Structure C in Figure 4.19) between a previously incorporated carbon and a reconstruction. This bridging species only requires a hydrogen abstraction in order to form a new reconstruction dimer upon a new layer. This termination step assumes that the migration steps leading to the formation of the pendant  $\text{CH}_2$  radical are as facile as the similar reaction upon a pristine surface.

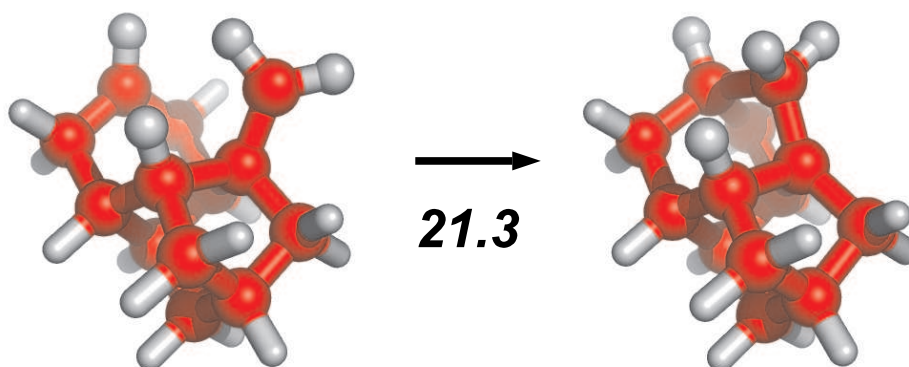


**Figure 4.22:** Possible termination step for methyl radical migration along a dimer row.

The termination step of the migration of a pendant methylene radical is a radical recombination between a previously incorporated carbon radical (this can be easily generated by a hydrogen abstraction reaction, Section 4.3.4) and the pendant

radical. This radical quenching reaction results in a very weak carbon-carbon bond ( $\Delta E = 21.3 \text{ kJ mol}^{-1}$ ), making this an unlikely process.

In summary, this reinvestigation of the previous carbon migration studies has confirmed the feasibility of these carbon migration reactions. The overall activation energy and thermodynamic data, which is calculated at a higher level of theory than hitherto, suggests that migration upon the pristine diamond surface is more facile than previously reported, as many of the key reaction steps are found to have a reduced or no activation energy.

## 4.4 Conclusions

Incorporation of carbon into a growing  $\{100\}$  diamond surface occurs by means of methyl insertion into a reconstructed dimer by the ring opening closing mechanism.  $\text{CH}_3$  radical addition to all of the different surface radical sites occurs without a barrier, hence all the chemistry is controlled by the differences in timescales between unimolecular and bimolecular reactions and the energetics of hydrogen abstraction reactions. The row bridging mechanism is not a favourable pathway for carbon incorporation as it requires too many unlikely bimolecular reactions and there are barriers to key reactions.  $\text{CH}_2$  groups are able to migrate along and across dimer reconstructed chains.

These results hint that, for diamond growth, there is one growth mechanism by which carbon is incorporated randomly into the surface. The incorporated carbon species are able to migrate together, across the diamond surface to form a smooth  $\{100\}$  diamond surface. The use of DFT theory in a QM / MM protocol has dramatically improved the quality of the computational results. These in turn show that methyl incorporation and methylene migration across the diamond surface are

much more facile than previously reported.

## Bibliography

- [1] C. J. Cramer, *Essentials of Computational Chemistry: Theories and Models* (J. Wiley and Sons Inc., 605 Third Avenue, New York, NY., 2002).
- [2] T. L. Hill, *J. Chem. Phys.* **14**, 465 (1946).
- [3] G. Monard and K. M. Merz Jr., *Acc. Chem. Res.* **32**, 904 (1999).
- [4] M. J. Field, P. A. Bash, and M. J. Karplus, *J. Comput. Chem.* **11**, 700 (1990).
- [5] V. Théry, D. Rinaldi, J.-L. Rivail, B. Maigret, and G. G. Ferenczy, *J. Comput. Chem.* **15**, 269 (1994).
- [6] N. Reuter, A. Dejaegere, B. Maigret, and M. Karplus, *Phys. Chem. A.* **104**, 1720 (1999).
- [7] U. C. Singh and P. A. Kollman, *J. Comp. Chem.* **7**, 718 (1986).
- [8] F. Maseras and K. Morokuma, *J. Comp. Chem.* **16**, 1170 (1995).
- [9] J. N. Harvey, *Faraday Discuss.* **127**, 165 (2004).
- [10] A. C. Tsipis, A. G. Orpen, and J. N. Harvey, *Dalton Trans.* (2005).
- [11] S. Humbel, S. Sieber, and K. Morokuma, *J. Chem. Phys.* **105**, 1959 (1996).
- [12] M. Svensson, S. Humbel, R. D. J. Froese, T. Matsubara, S. Sieber, and K. Morokuma, *J. Phys. Chem.* **100**, 19357 (1996).
- [13] K. J. Laidler, *Chemical Kinetics* (HarperCollins Publishers, New York, 3rd edition, 1987).
- [14] J. J. P. Stewart, *J. Comput. Chem.* **10**, 209 (1989).
- [15] S. Skokov, C. S. Carmer, B. Weiner, and M. Frenklach, *Phys. Rev. B* **49**, 5662 (1993).
- [16] S. Skokov, B. Weiner, and M. Frenklach, *J. Phys. Chem* **98**, 8 (1994).
- [17] S. Skokov, B. Weiner, and M. Frenklach, *J. Phys. Chem.* **98**, 7073 (1994).
- [18] S. Skokov, B. Weiner, and M. Frenklach, *J. Phys. Chem.* **99**, 5616 (1995).
- [19] D. Huang and M. Frenklach, *J. Phys. Chem* **95**, 3692 (1991).
- [20] D. Huang, M. Frenklach, and M. Maroncelli, *J. Phys. Chem.* **92**, 6379 (1988).
- [21] M. Frenklach and S. Skokov, *J. Phys. Chem. B.* **101**, 3025 (1997).
- [22] S. Skokov, B. Weiner, M. Frenklach, Th. Frauenheim, and M. Sternberg, *Phys. Rev. B* **52**, 5426 (1995).

- [23] M. Frenklach and H. Wang, *Phys. Rev. B* **43**, 1520 (1991).
- [24] M. E. Coltrin and D. S. Dandy, *J. Appl. Phys.* **74**, 5803. (1993).
- [25] A. Netto and M. Frenklach, *Diamond Relat. Mater.* **14**, 1630 (2005).
- [26] C. C. Battaile, D. J. Srolovitz, I. I. Oleinik, D. G. Pettifor, A. P. Sutton, S. J. Harris, and J. E. Butler, *J. Chem. Phys.* **111**, 4291 (1999).
- [27] R. C. Brown and J. T. Roberts, *J. Phys. Chem. B* **104**, 8420 (2000).
- [28] C. C. Battaile, D. J. Srolovitz, and J. E. Butler, *J. Crystal. Growth.* **194**, 353 (1998).
- [29] S. J. Harris and D. G. Goodwin, *J. Phys. Chem.* **97**, 23 (1993).
- [30] E. J. Dawnkaski, D. Srivastava, and B. J. Garrison, *J. Chem. Phys.* **104**, 5997 (1996).
- [31] H. Tamura and M. S. Gordon, *Chem. Phys. Lett.* **406**, 197 (2005).
- [32] J. K. Kang and C. B. Musgrave, *J. Chem. Phys.* **113**, 7582 (2000).
- [33] M. L. Allinger, *J. Am. Chem. Soc* **99**, 8127 (1977).
- [34] Jaguar, *Schrödinger, Inc., Portland, OR, 2000.*
- [35] J. W. Ponder, *TINKER: Software Tools for Molecular Design, v4.0, Saint Louis, MO, 2003.*
- [36] W. Tsang, in *Energetics of Organic Free Radicals*, (ed. A. Martinho Simoes, A. Greenberg, and J. F. Liebman), Blackie Academic and Professional, London (1996).
- [37] M. Chase Jr., *J. Phys. Chem. Ref. Data* (1998).
- [38] W. Good, *J. Chem. Thermodyn.* **2**, 237 (1970).
- [39] R. C. Brown, C. J. Cramer, and J. T. Roberts, *J. Phys. Chem. B* **101**, 9574 (1997).
- [40] R. F. Frey, J. Coffin, S. Q. Newton, M. Ramek, V. K. W. Cheng, F. A. Momany, and L. Schaefer, *J. Am. Chem. Soc.* **114**, 5369 (1992).
- [41] I. I. Oleinik, D. G. Pettifor, A. P. Sutton, and J. E. Butler, *Diamond Relat. Mater.* **9**, 241 (2000).
- [42] S. J. Harris, *Appl. Phys. Lett.* **56**, 2298 (1990).
- [43] D. Huang and M. Frenklach, *J. Phys. Chem.* **96**, 1868 (1992).

## **Chapter 5**

# **Preliminary diagnostic studies of a high pressure microwave CVD diamond reactor.**

A high-pressure ( $\sim 150$  Torr) microwave plasma CVD system has been constructed and initial studies performed, optimal conditions for diamond deposition have been investigated. Spatially resolved optical emission spectroscopy (OES) studies of the plasma have been conducted. Cavity ring down spectroscopy (CRDS) has been performed upon the  $C_2$  species throughout the region of most intense optical emission. Photography has been used to estimate relative plasma ball sizes under all experimental conditions used.

### **5.1 Spectroscopy**

Spectroscopy is the study of the absorption, emission or scattering of electromagnetic radiation with matter. Spectroscopy theory originates from the quantum me-

chanical description of the probed species. The Schrödinger equation describes the total energy of a system (3.1) and this energy can be expressed as the sum of the constituent physical components (5.1) with each component described by its own Hamiltonian. The application of the Born–Oppenheimer approximation (Chapter 3) enables the decoupling of the electronic and nuclear motion.

$$E_{Total} = E_{Electronic} + E_{Vibrational} + E_{Rotational} + E_{Translational} \quad (5.1)$$

The internal energy of the probed species can be described by the population of quantised energy levels (rotational, vibrational and electronic) and transitions between these levels can be mediated by the absorption or emission of a photon with energy ( $h\nu$ ) that corresponds to the energy difference between the two levels, Figure 5.1. The unique internal energy structure of individual species results in a series of subsequent transitions, which lead to the formation of a species-specific spectrum.

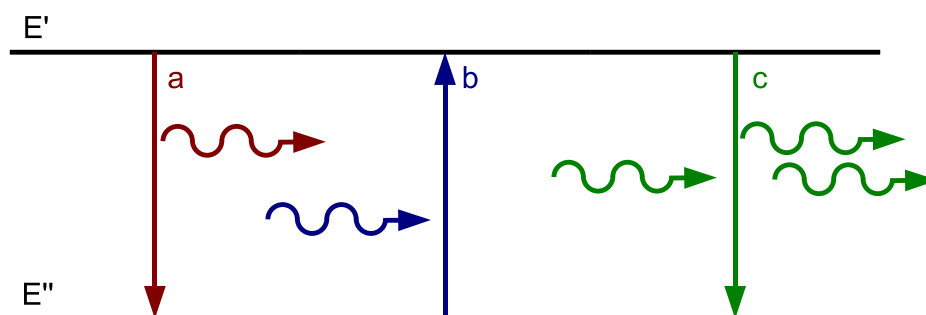


**Figure 5.1:** Three different ways in which electromagnetic radiation can interact with two energy levels (a) Spontaneous emission (b) Absorption (c) Stimulated emission. Colours are used for identification only.

For a system in thermal equilibrium, the population,  $N$ , of these internal energy levels, can be calculated from the Boltzmann distribution at a given temperature

(5.2).

$$\frac{N'}{N''} = \frac{g'}{g''} \exp\left(-\frac{h\nu}{kT}\right) \quad (5.2)$$

where  $N'$  is the population of the higher energy level,  $N''$  is the population of the lower energy level,  $g'$  &  $g''$  correspond to the degeneracy of the relevant energy level,  $h$  is Planck's constant,  $\nu$  is the frequency of the electromagnetic radiation,  $k$  is Boltzmann's constant and  $T$  is the temperature. Consequently, care must be taken when inferring number density from a single spectroscopy transition as within non-thermally equilibrated systems, the relative population of the state probed may not reflect the overall distribution of the species within the system. Chapter 6 highlights these problems within the context of IR absorption spectroscopy.

The rate of change in the population of these levels can be calculated from the population of starting level,  $N'$ , the spectral radiation density of light  $\rho(\nu)$  and the relevant Einstein constant ( $A$  for stimulated emission and  $B$  for absorption / spontaneous emission).

$$\frac{dN}{dt} = N' B' \rho(\nu) \quad (5.3)$$

The transition probability,  $\left| \mathbf{R}' \right|^2$ , (5.4), links the Einstein B constants to the quantum mechanical description of the initial and final energy levels. The transition moment,  $\mathbf{R}'$ , (5.5) is linked to the interaction between the wavefunctions for initial and final state and the associated electric dipole transition moment,  $\boldsymbol{\mu}$  for electronic transitions. For vibrational transitions, the associated change in dipole moment induced by the vibration of interest should be considered. The transition moment must be non-zero in order for a transition between energy levels to occur, and the individual spectroscopic selection rules are derived from this principle.

$$B'' = \frac{8\pi^3}{(4\pi\epsilon_0)3h^2} \left| \mathbf{R}' \right|^2 \quad (5.4)$$

$$\mathbf{R}' = \int \Psi'^* \boldsymbol{\mu} \Psi'' d\tau \quad (5.5)$$

Atomic spectroscopy is based upon the observation of transitions between electronic states, whereas spectroscopic studies of molecular species are complicated by the presence of vibrational and rotational interactions and transitions. The translational energy contribution to spectra is neglected, as the translational energy is effectively a continuum under most experimental conditions. A brief summary of the principles of the main forms of spectroscopy relevant to this thesis is presented below.

The individual rotational and vibrational components of the Hamiltonian can be solved separately by describing each type of motion with a simple quantised model of the system. Rotational spectra are commonly addressed by applying the rigid rotor approximation and vibrational features are described by a harmonic oscillator model [1]. Both approaches lead to an exact solution of the individual components of the Schrödinger equation, (5.6), (5.7) respectively, but both models fail to be an accurate description of each physical process. These approximations can be refined by the addition of further terms (c.f the use of harmonic oscillators within Molecular Mechanics computational modelling, Chapter 4). The  $J(J + 1)$  dependency of the rotational energy,  $E_r$  (5.6), leads to a divergence of the corresponding energy levels whilst the harmonic oscillator description of vibrational energy  $E_v$  (5.7) leads to

evenly spaced energy levels.

$$E_r = \frac{h^2}{8\pi^2 I} J(J + 1) \quad (5.6)$$

where  $I$  is the moment of inertia and  $J$  is the rotational quantum number.

$$E_\nu = h\nu(v + \frac{1}{2}) \quad (5.7)$$

where  $v$  is the vibrational quantum number (which can be 0, or a positive integer value) and  $\nu$  is the classical vibrational frequency of the bond being studied.

Transitions between vibrational states are feasible between adjacent vibrational energy levels ( $\Delta v = \pm 1$ ). However, other weaker transitions are possible,  $\Delta v > 1$ , and the transitions are ascribed to the breakdown in the harmonic oscillator model. Likewise, pure rotational transitions can occur between adjacent rotational energy levels ( $\Delta J = \pm 1$ ) and the  $\Delta J = 0, \pm 1$  selection rules apply for rotational transitions which occur in concert with a vibration or electronic state change.

Spectroscopic transitions between electronic states in atoms are complicated as an electron possesses both orbital,  $l$ , and spin,  $s$ , angular momentum, each with a corresponding quantum number,  $l$  and  $s$  respectively. (The value of  $l$  corresponds to the common s, p, d ... orbital labelling system where  $l = 0, 1, 2 \dots$  respectively). These electronic angular momentum vectors are commonly expressed by the total quantised angular momentum  $\mathbf{j}$  vector with a resultant quantum number  $j$  (5.8).

$$j = l + s, l + s - 1, \dots |l - s| \quad (5.8)$$

The Russell–Saunders coupling approximation is the most commonly used description for multiple-electron system. Within this construct, the total orbital angular momentum  $\mathbf{L}$ , is expressed as the quantised sum of  $l$  for all electrons and by

similar means, the resultant spin  $\mathbf{S}$  component is formed from the summation of the individual spin angular momenta. Each momentum vector term has a corresponding quantum number,  $L$  and  $S$  respectively. The total resultant angular momentum,  $\mathbf{J}$ , is quantised with the resulting quantum number,  $J$ , taking values from the combination of the quantum numbers of the individual total orbital momenta, in a similar manner to (5.8) [2].

Electronic states are commonly labelled by  $^{2S+1}L_J$ , where  $L = 0, 1, 2, 3 \dots$  is represented by S, P, D, F  $\dots$  mirroring the labels for atomic orbitals. For multi-electron systems, numerous terms can exist and the empirically-derived Hund's rules are used to identify the lowest energy configurations. These rules state :

1. The lowest energy configuration has the highest spin multiplicity ( $2S + 1$ ) value.
2. For systems with the same multiplicity, the highest value of  $L$  has the lowest energy.
3. For half filled shells, the lowest  $J$  value results in the lowest energy whilst for shells which are more than half full, the lowest energy configuration has the highest  $J$  value.

These rules originate from the minimisation of the spin interaction between electrons (1), maximisation of the orbital momentum,  $\mathbf{L}$ , (2) and the scalar product of the spin-orbit  $J$  coupling interactions (3). These rules can break down however when studying "heavy" atomic species, where magnetic effects involving  $j - j$  coupling dominate.

In order for transitions to occur between electronic states, the transition moment, (eq. (5.5)) must be non-zero, which involves a change in the local electric dipole moment. The subsequent photon absorption / emission process also requires

a change in the total electronic angular momentum to ensure conservation of momentum. These principles are summarised as the atomic selection rules, as shown below [1].

1.  $\Delta l = \pm 1, \Delta L = 0, \pm 1$ .
2. The adsorption / emission of a photon must result in a change in parity of the wavefunction for a non-zero change in electric dipole moment. This is commonly known as Laporte's rule and thus wavefunction mapping must take the following forms: odd $\leftrightarrow$ even; even $\leftrightarrow$ even, odd $\leftrightarrow$ even .
3.  $\Delta J = 0, \pm 1$  except  $J=0 \leftrightarrow J=0$
4.  $\Delta S = 0$ .

The electronic spectroscopy of a diatomic species is further complicated by the presence of rotational and vibrational effects, which increase the complexity of recorded spectra. (Molecular spectroscopy theory is beyond the scope of this thesis). The electronic momentum vectors ( $L, S$ ) can couple with the inter-atomic axis and the strength of these coupling interactions are categorised into three environments labelled Hund's case (a), (b) and (c). The first case relates to a strong interaction where both  $L$  and  $S$  couple along the axis to produce  $\Lambda\hbar, \Sigma\hbar$  terms respectively; the second case is partial coupling where only  $L$  couples, while the third describes situations where the spin-orbital coupling between  $L$  and  $S$  is stronger than the coupling between either of these and the molecular axis.  $J$  then couples to the axis resulting in  $\Omega\hbar$  vector. Each vector product has an associated quantum number and the associated  $\Omega\hbar$  quantum number,  $\Omega$ , relates to the coupled total momentum quantum number (5.9).

$$\Omega = |\Lambda + \Sigma| \tag{5.9}$$

The labelling of diatomic electronic states mirrors the atomic electronic state description and has the common form  $^{2S+1}\Lambda_{\Omega}$ , where  $\Lambda = 0, 1, 2, 3 \dots$  is represented by the Greek equivalent of S, P, D, F  $\dots$ , i.e.  $\Sigma, \Pi, \Delta, \dots$ . For homonuclear diatomic species, the symmetry of the electronic wavefunction, with respect to a centre of inversion, is expressed by the addition of a g (symmetric) or u (asymmetric) subscript to the term symbol. The electronic diatomic selection rules are analogous to the atomic selections rules.

1.  $\Delta\Lambda = 0, \pm 1$ .
2.  $g \leftrightarrow u; g \leftrightarrow g, u \leftrightarrow u$ .
3.  $\Delta\Sigma = 0, \Delta\Omega = 0, \pm 1$
4.  $\Delta S = 0$ .

Electronic transitions within diatomic molecules can lead to vibration excitation. The most favourable electronic transition between different vibrational states is determined by the Franck-Condon principle. This relies on the fact that electronic transitions occur on a timescale that is much shorter than that for nuclear motion. The Franck-Condon factor is a measure of the overlap of the vibrational wavefunctions of the initial and final states (5.10).

$$\mathbf{R}'_{ev} = \mathbf{R}'_e \int \Psi'_v{}^* \Psi''_v d\tau \quad (5.10)$$

Within this thesis, three optical spectroscopic techniques have been used to profile the species densities within the microwave plasma reactor.

### 5.1.1 Optical Emission Spectroscopy (OES)

Operationally, this is the simplest form of spectroscopy, which monitors the light emitted as a species relaxes from a highly excited state. This technique is generally limited to atomic and diatomic systems, as triatomic and other larger multiple-atom species generally have impenetrably complex spectra, due to the numerous possible rovibronic transitions, and in many cases, decay non-radiatively rather than emission. In practice, OE spectra are recorded by passing the emitted light through a monochromator and onto a suitable detector.

However, care is required in the interpretations of the results from OES as species have different intensities of emission, which makes the determination of number densities a complex and difficult process. In summary, OES is a simple, quick technique which enables qualitative probing of selected species within an electronically excited sample.

### 5.1.2 Absorption Spectroscopy

Absorption spectroscopy is based upon the absorption of incident radiation resulting in an internal promotion between two states. The Beer–Lambert law correlates the absorbance,  $A$ , (the logarithm of the ratio of the initial and transmitted light intensities, typically from a laser source) to the concentration,  $[X]$  in the initial state of the absorbing species with the cross sectional absorption,  $\sigma$ , and the path length of the light through the medium,  $L$ , (5.11). The cross section and concentration terms are combined and commonly referred to as the absorption coefficient,  $\alpha$ .

$$A = \ln \frac{I_0}{I} = \sigma [X] L \quad (5.11)$$

Absorption spectroscopy is a species selective technique, which can lead to quantitative measurement of species concentration profiles, and is relatively simple to implement. Chapter 6 shows the application of absorption spectroscopy within a microwave plasma system using a new IR spectral region enabled by the development of quantum cascade lasers.

However, there are a few inherent issues with absorption spectroscopy. The detection of species present at low concentrations is problematic as this requires the measurement of a small change in the intensity (due to the absorption) of a high intensity light source. Absorption spectroscopy is thus highly dependable on the intensity of the radiation source and any instability within that source propagates into the absorption measurements. In addition, absorption spectra can be complicated by the presence of overlapping bands from different species.

### 5.1.3 Cavity Ring-Down Spectroscopy

Cavity ring-down spectroscopy (CRDS) is a highly sensitive, non-intrusive multiple pass absorption measurement technique based upon the construction of an optical cavity by two high reflectivity mirrors ( $\mathfrak{R} > 99\%$ ) in which a laser pulse is trapped. The laser pulse slowly decays by transmission through the mirrors and is detected, usually by a photo-multiplier tube, which measures the rate of decay. Like conventional absorption spectroscopy, CRDS is a line of sight technique which projects quantitative 3D data into a 2D representation, the column density.

For an “empty” cavity the intensity of transmitted light can be expressed as an exponential decay (5.12) [3] and the ring-down time for this decay,  $\tau$ , solely depends upon the reflectivity of the mirrors,  $\mathfrak{R}$ , the total length of the cavity,  $L$  and the speed of light,  $c$ , (5.13) [4].

$$I(t) = I_0 \exp\left(\frac{-t}{\tau}\right) \quad (5.12)$$

$$\tau = \frac{L}{c(1 - \mathfrak{R})} \quad (5.13)$$

The ring-down time is the time it takes for the intensity to decrease to  $1/e$  of the initial signal; the rate is the reciprocal of this time. The presence of an absorbing medium in the cavity increases the rate at which light is lost from the cavity (5.14), and thus decreases the ring-down time.

$$I(t) = I_0 \exp\left(\frac{-t}{\tau} - \frac{\alpha cl}{L}\right) \quad (5.14)$$

where  $\alpha$  is the absorption coefficient and  $l$  is the sample length.

CRDS experiments measure the rate of light escaping from the optical cavity and the data is described by an exponential decay using the ring-down rate,  $k = 1/\tau$ . Changes in ring-down rate due to the presence of an absorbing medium at any particular frequency, ( $\Delta k$ , (5.12) – (5.14)) is shown in equation (5.15). The measurement of the change in the decay rates removes the dependency for stability with the incident radiation source and also causes an increase in sensitivity enabling CRDS techniques to probe weak “forbidden” spectroscopic transitions.

$$\alpha = \frac{L\Delta k}{cl} \quad (5.15)$$

### 5.1.4 Applying spectroscopy to plasmas used in Diamond CVD

CVD diamond growth occurs from highly activated hydrocarbon / hydrogen gas mixtures and spectroscopy techniques are the natural methods for probing the gas-phase composition and reactions that drive the process. Techniques that have been used to shed light on such issues span optical emission spectroscopy, in situ mass spectrometry, [5] and a number of laser spectroscopy methods. Included among the latter are the pioneering infrared (IR) diode laser absorption studies of stable hydrocarbons and hydrocarbon radicals (e.g.,  $C_2H_2$ ,  $C_2H_4$ , and  $CH_3$ ) by Butler's group [6], [7].

CRDS has been successfully applied to the measurement of  $CH_3$  radicals in a hot filament (HF) system [8],  $CH$  radicals in a HF reactor [9] and to  $C_2$  radicals in a microwave reactor used for ultrananocrystalline diamond (UNCD) film growth [10], an oxyacetylene flame [11] and in a DC arc-jet reactor [12].

Spectroscopic data would, ideally, consist of spatially resolved absolute number densities, measured as a function of process conditions. In practice, only absorption methods are well-suited to absolute concentration measurements, and the densities returned are normally line-of-sight column densities. Without very careful calibration studies, the other methods will generally only provide relative concentrations. These data, taken in conjunction with complementary two- (2-D) or three-dimensional (3-D) reactor modelling, [13], [14] are largely responsible for the current level of understanding of the gas-phase chemistry underpinning diamond CVD [15], [16].

Within this chapter, the initial profiling of the optically accessible species present within a microwave generated plasma using OES and CRDS is discussed. Chapter 6 will describe the IR absorption measurements that shed light on the interconversion between stable hydrocarbon species. Below, is a brief description of the some of the

more important species commonly observed within CVD growing environments.

### Atomic hydrogen

Historically, spectroscopic studies of atomic hydrogen have been at the forefront of the development of quantum mechanics, e.g. Balmer's empirical description of its optical emission spectrum (5.16). With one electron, atomic hydrogen is the only system for which the Schrödinger equation can be solved precisely, because of the lack of electronic repulsions. The standard description of atomic orbitals is derived from this solution. This lack of electronic interactions also maximises all orbital degeneracy within the hydrogen atom, and to a very high level of approximation, the term energies depend only upon  $n$  (5.16). Figure 5.2 shows the most common electronic transitions.

$$\nu = R_H \left( \frac{1}{2^2} - \frac{1}{n^2} \right) \quad (5.16)$$

where  $\nu$  is the frequency, and  $R_H$  is the Rydberg constant.

### C<sub>2</sub> species

Figure 5.3 shows the molecular orbital (MO) diagram for the electronic ground state for C<sub>2</sub>,  $^1\Sigma_g^+$ , and the low lying excited state  $a^3\Pi_u$  only 716 cm<sup>-1</sup> above ground state, [18].

The C<sub>2</sub> radical species is of interest because of the characteristic green optical emission observed during CVD growth cycles which provides clear evidence of its presence. This emission is due to the  $d^3\Pi_g - a^3\Pi_u$  vibronic transition, commonly known as the Swan band. The intensity of such optical emissions has led to sugges-

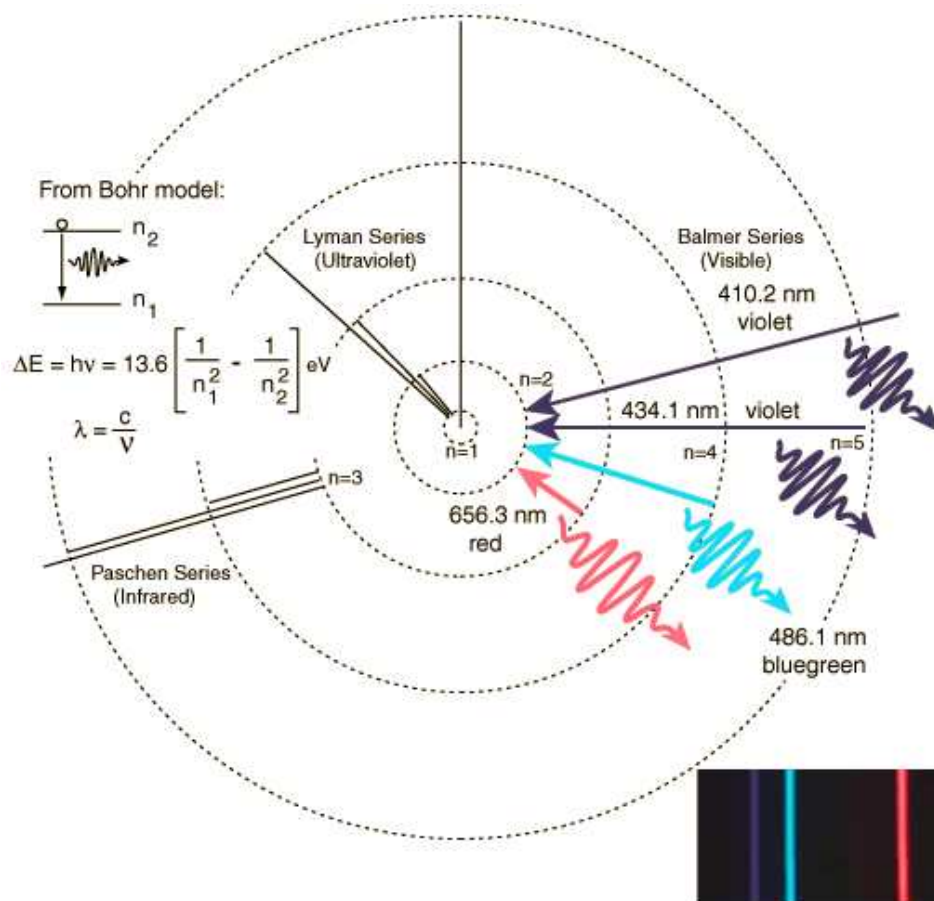


**Figure 5.2:** The more commonly observed electronic series of atomic hydrogen [17].

tions - based both on experiment [19] - [21], and theory [22]- [25] - that  $C_2$  may be an important growth species. The  $C_2$  radical has been intensively probed within the DC arc-jet reactor at Bristol using both OES and CRDS [10], [12].

There have been suggestions that the population of the ground state of  $C_2$  within a CVD diamond growing environment is reduced relative to that predicted on the basis of local thermodynamics equilibrium. This depopulation is proposed to originate from ground state  $C_2$  reacting faster with atomic and molecular hydrogen species than the excited  $a^3\Pi_u$  state [26]. However, CRDS studies of ground and excited state  $C_2$  radicals within a DC arc-jet reactor at Bristol, have revealed  $X : a$  state populations ratios comparable with a Boltzmann distribution and  $T \sim 3000 \text{ K}$  [27].

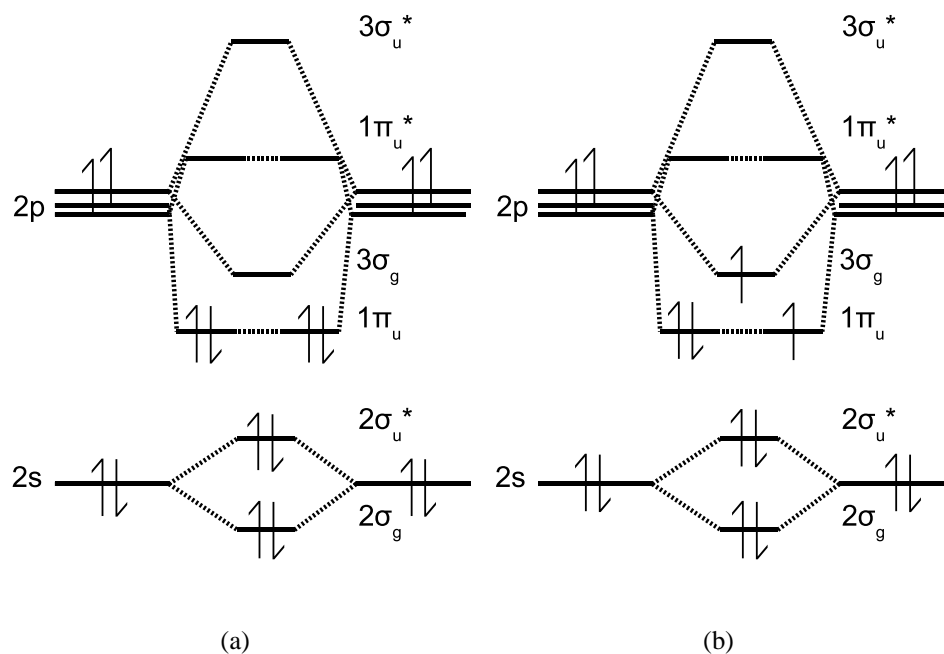


**Figure 5.3:** The MO electronic structure for the (a)  $X^1\Sigma_g^+$  ground state (b) first excited state,  $a^3\Pi_u$ , for the  $C_2$  diatomic. Core 1s electrons omitted.

## 5.2 Experimental construction

A custom designed and built microwave reactor which operates with mixtures of hydrocarbon ( $CH_4$  or  $C_2H_2$ ), Ar, and  $H_2$  has been installed. The microwave reactor has the general form of a vertically aligned cylinder of volume  $\sim 600\text{ cm}^3$ , with microwaves (2.45 GHz from a Muegge power supply and generator) fed from above through a quartz window by an antenna system. The respective gas flows are metered through individual mass flow controllers (MFCs) and mixed prior to introduction into the reactor through two 6.25 mm diameter stainless steel inlet pipes located near the top, and on opposite sides, of the reactor. The chamber walls are water cooled (water flow  $6\text{ l min}^{-1}$ ). The chamber is exhausted through six, radially symmetric, 6.25 mm diameter pumping ports machined into its base, using a two-stage rotary pump (Edwards E2M8). An in-line feedback controlled throttle valve between the reactor and this pump enables stable operation at any user-

specified pressure in the range  $40 \leq P \leq 200$  Torr. Diamond is typically deposited on a polished Mo substrate (30 mm diameter) mounted centrally on the (detachable) water-cooled base of the reactor. The substrate temperature is monitored by a single colour optical pyrometer.

The reactor has been designed with two vertical slots (30mm  $\times$  6mm) which lie along the central plane of the reactor and these viewing ports have been used to probe along the vertical axis of the generated plasma. The microwave reactor is held within a rigid aluminium frame to which all subsequent spectroscopic equipment can be firmly mounted.

### **5.3 Optimisation of process conditions for CVD diamond growth in CRDS Microwave Reactor by the Taguchi method**

The Taguchi method of robust product design is an engineering method for multi component optimisation of a system. Taguchi developed a practical approach in which the theories of statistical design of experiments could easily be incorporated into modern engineering.

The framework of the system is the identification of control parameters which affect measurable quality of the product. The control parameters are then simultaneously manipulated and the product quality is measured for each sample. The mathematical backbone to the Taguchi approach is the construction and manipulation of arrays containing system variables. This enables a vast reduction in the number of samples that need to be prepared and also enables a quantitative prediction of the optimum conditions. This technique has been successfully applied to

Diamond CVD growth [28], [29].

The four main parts of implementing of the Taguchi approach are highlighted below [30], [31].

1. Identification of quality control.
2. Design of experimental conditions and control parameters.
3. Data analysis.
4. Predictions of optimal conditions.

### **5.3.1 Identification of quality control**

Within current literature there is a variation in the reported optimum conditions for diamond CVD growth. Part of the problem is recognising the effects of a variable; whether the observed change is due to the specifics of the reactor used or relates to a global growth process factor.

The aim of this investigation is to identify the best process window for CVD diamond growth. The quality of CVD diamond can be quantified via the ratio of  $sp^3$  to  $sp^2$  carbon present in each sample. The ratios can be measured by comparison of the areas of the diamond Raman peak ( $1332\text{ cm}^{-1}$ ) and the graphite D and G band Raman peaks ( $1355, 1575\text{ cm}^{-1}$ ) [32], [33]. The growth rate of diamond films is a secondary factor and will only be used to distinguish samples of comparable quality.

### 5.3.2 Design of experimental conditions and control parameters

In order to optimise the experimental conditions, it is necessary to identify system variables whilst minimising the introduction of noise. The main variables in CVD diamond growth within the microwave reactor are highlighted and discussed below.

1. Substrate Temperature,  $T_{\text{sub}}$ . The substrate temperature is regulated by the thermal conductivity between the molybdenum substrate and the water cooled surface on which it sits. The current reactor design uses a ring of molybdenum wire of various thickness as a spacer to create a trapped volume of gas under the substrate, which regulates the substrate temperature. The current reactor design has no method for maintaining a constant  $T_{\text{sub}}$  during a growth run and  $T_{\text{sub}}$  is measured by a pyrometer focused on the edge of the substrate. During the growth process, deposition may occur which may change the emissivity of the substrates and the growing film is encroaching further into the plasma - both of which factors can lead to variability and uncertainty in surface temperature [34]. There is evidence that temperature affects the ratio of  $\{100\} / \{111\}$  growth features [35] and that the ideal substrate temperature for CVD diamond growth is near 800°C [36].
2. Microwave input power & background gas pressure. The microwave plasma density is directly related to the input power coupled into the microwave reactor and the pressure at which the plasma is maintained. The literature suggests that an increase in the plasma density causes an increase in the local concentration of atomic hydrogen and thereby enhances the methyl radical density [37] – [40]. This has been linked to an increase in the growth rate and quality of a CVD diamond film [41].
3. Gas mixture compositions. As shown in Chapter 1, the methane concentration within a CVD reactor affects the level of diamond nucleation and the

growth rate. Thus the  $\text{CH}_4$  flow rate controls the subsequent quality of the grown diamond films, with higher percentages ( $> 4\%$ ) of  $\text{CH}_4$  resulting in a poorer quality diamond and a higher growth rate and vice versa. Argon addition is suggested to improve the growth rates of CVD diamond, as well as the quality, due to the addition of ionic and Penning reactions into the gas-phase chemistry [42].

Highly polished Molybdenum substrates (30 mm diam, 3 mm thickness) are cleaned with non-polar and polar solvents before being abraded with a suspension of  $6\ \mu\text{m}$  diamond dust in ultra pure water ( $18\ \text{M}\Omega$ ) in an ultrasonic bath. To ensure a reproducible positioning of the spacer wire, a light groove (29 mm diam) is applied to the reverse side of the substrate, to which the spacer is attached by silver dag after being shaped to the same diameter by means of a former, Figure 5.4. The substrate position is fixed in the centre of the reactor by a removable template.

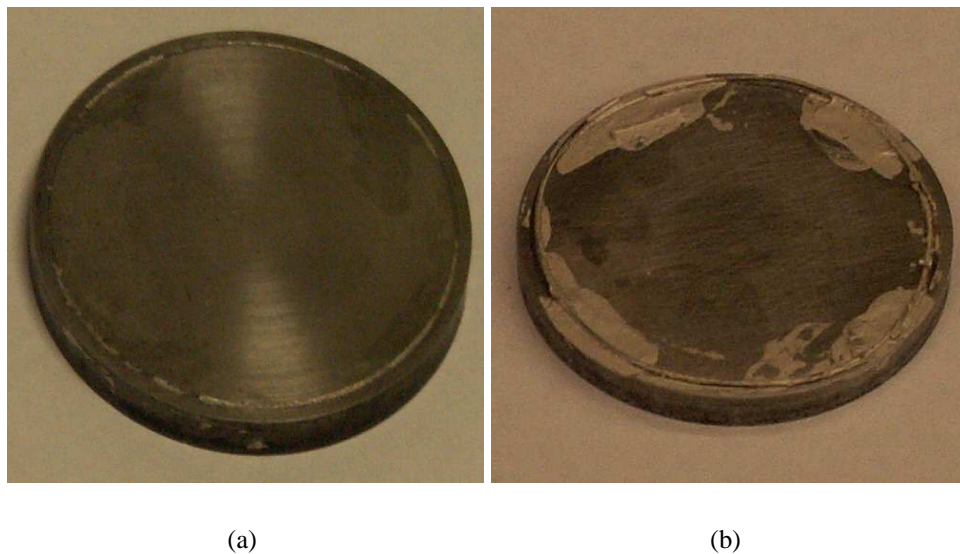


**Figure 5.4:** Photos showing the reverse of a Molybdenum substrate (a) the groove (b) spacer mounted upon a substrate.

For any chosen set of gas reagent ratios, a standard flow of 565 sccm of premixed gas entered the chamber and was maintained at the allocated pressure. A microwave plasma was struck in a low pressure mixture of argon and hydrogen (typically 10 Torr), and pressure was increased to the desired level. Methane introduction into the system defines the beginning of the growth run which lasted for 6 hours. This period of time was deemed appropriate for minimising the effects of diamond growth into the plasma yet still creating a free standing diamond film, leaving the substrate suitable for further use.

Table 5.1 shows the incorporation of the afore mentioned variables with five levels into a  $L'_{16}$  array. This reduces the number of experimental permutations from 625 to just 16.

### 5.3.3 Data Analysis & Predictions

The analysis of the means (ANOM) method is the preferred way of interpreting the experimental results. For each level of each variable, the average Raman  $sp^3 / sp^2$  carbon ratio,  $\bar{y}_a$ , is calculated from all experimental runs grown under that particular condition, Table 5.2. (Appendix E contains the Raman spectrum for each sample). Quantitative predictions for the  $sp^3 / sp^2$  carbon ratio, for a given set of experimental conditions,  $y_{predicted}$ , can be made by the summation of the individual deviation of each variable,  $\bar{y}_a$  from the experimental average value  $\bar{y}_{exp}$ , (5.17).

$$y_{predicted} = \bar{y}_{exp} + (\bar{y}_a - \bar{y}_{exp}) + (\bar{y}_b - \bar{y}_{exp}) + \dots \quad (5.17)$$

Table 5.3 lists the calculated individual contribution that each variable makes to the  $sp^3 / sp^2$  ratio. Simple analysis of these results show that, for the conditions

Sample Number	Spacer height / inches	Microwave power / kW	Pressure / Torr	%CH <sub>4</sub>	%Ar
1	0.008	1.00	75	2	2
2	0.008	1.25	100	3	4
3	0.008	1.50	125	4	6
4	0.008	1.75	150	5	8
5	0.009	1.00	100	3	8
6	0.009	1.25	75	5	6
7	0.009	1.50	150	2	4
8	0.009	1.75	125	3	2
9	0.010	1.00	125	5	4
10	0.010	1.25	150	4	2
11	0.010	1.50	75	3	8
12	0.010	1.75	100	2	6
13	0.012	1.00	150	3	6
14	0.012	1.25	125	2	8
15	0.012	1.50	100	5	2
16	0.012	1.75	75	4	4

**Table 5.1:** L<sub>16</sub> Taguchi Array used for optimisation of CRDS microwave system

studied, the best quality diamond films should be grown using the 0.012” spacer, with a plasma maintained at 1.75 kW with a gas mixture consisting of 3% CH<sub>4</sub> / 2% Ar / balance H<sub>2</sub>, and a pressure of 125 Torr. The Taguchi optimisation method suggests that the input microwave power have the greatest effect upon the diamond quality, and that there is an optimum methane concentration. There is a modest effect on quality with the variation of the spacer height, the large value for the the 0.009“ spacer height is slightly distorted by the large sp<sup>3</sup> / sp<sup>2</sup> ratio for sample 8. Any effects of argon concentration and overall system pressure on the quality of the diamond films are not resolvable from this data set and further investigations are required.

However, caution must be taken in extrapolating these results for longer growth periods, due to the relatively short timescale of each experimental run, which may be comparable with the nucleation phase of CVD diamond growth. Hence, it is conceivable that the optimisation process has identified the experimental conditions suitable for nucleation and the formation of many small crystallites rather than for fewer larger crystals. These results show that diamond growth is possible for all the process gas conditions studied and that the nearest approximation to the standard conditions (4% CH<sub>4</sub>; 7% Ar; 150 Torr; 1.50 kW; 0.012” substrate spacer) used within the spectroscopic investigation of the plasma should lead to a high quality CVD diamond film, ( $y_{predicted} = 15.88\%$ ).

Sample	sp <sup>3</sup> / sp <sup>2</sup> ratio	Sample	sp <sup>3</sup> / sp <sup>2</sup> ratio
1	1.45%	9	3.14%
2	0.51%	10	0.26%
3	0.43%	11	1.01%
4	0.42%	12	0.54%
5	0.00%	13	2.48%
6	4.33%	14	7.79%
7	2.31%	15	3.75%
8	16.97%	16	10.77%
		$\bar{y}_{exp}$	3.51%

**Table 5.2:** The calculated sp<sup>3</sup> / sp<sup>2</sup> ratio for samples listed in Table 5.1.

Spacer height / inches	$\bar{y}$	% CH <sub>4</sub>	$\bar{y}$	Microwave power / kW	$\bar{y}$	% Ar	$\bar{y}$	Pressure / Torr	$\bar{y}$
1	0.70%	2	3.02%	1	1.77%	2	5.61%	75	4.39%
2	5.90%	3	5.24%	1.25	3.22%	4	4.18%	100	1.20%
3	1.24%	4	2.86%	1.5	3.51%	6	1.94%	125	7.08%
4	6.20%	5	2.91%	1.75	7.18%	8	2.30%	150	1.37%

**Table 5.3:** Summary of the calculated ANOM data.

## 5.4 Optical Emission Spectroscopy

### 5.4.1 Experimental Method

Initial OE spectra were recorded by probing a 3 mm column (defined by 2 irises aligned in front of an optic fibre bundle). Light was coupled through the quartz fibre optic bundle (diam 3 mm), into a 12.5 cm monochromator (Oriel Instaspec IV, 600 lines  $\text{mm}^{-1}$  grating) which enabled the simultaneous recording of a 300 nm wide portion of the spectrum onto a UV extended CCD device. This experimental setup enabled the vertical profiling OES which was performed in 3 mm steps.

High resolution spectra of  $\text{C}_2$  species present within a plasma generated within the microwave reactor were taken by focusing the emitted light from the reactor, through a chopper system (operating at 100Hz) into the quartz fibre optic bundle (diam 3 mm). The optical bundle was connected into a 0.5m Spex 1870 spectrometer (slits size of 100  $\mu\text{m}$ , 2400 lines  $\text{mm}^{-1}$  holographic grating) and the light was detected by a photo-multiplier tube operating at 1 kV. The signal was processed by a lock in amplifier (Stanford Research Systems), linked to the chopper system, and data was recorded on a LeCroy wavesurfer 424 oscilloscope, in conjunction with the in-house "Drive" data collection program. Spectral wavelength scales were provided by comparison with spectral features computed by the PGOPHER program [43] using previously compiled spectroscopic constants [44].

### 5.4.2 Results

#### Low Resolution OES

Figure 5.5 compares optical emission spectra from a diamond growing CVD plasma at three different pressures. All spectra show emissions at 656.3, 486.1, 434.1 nm,

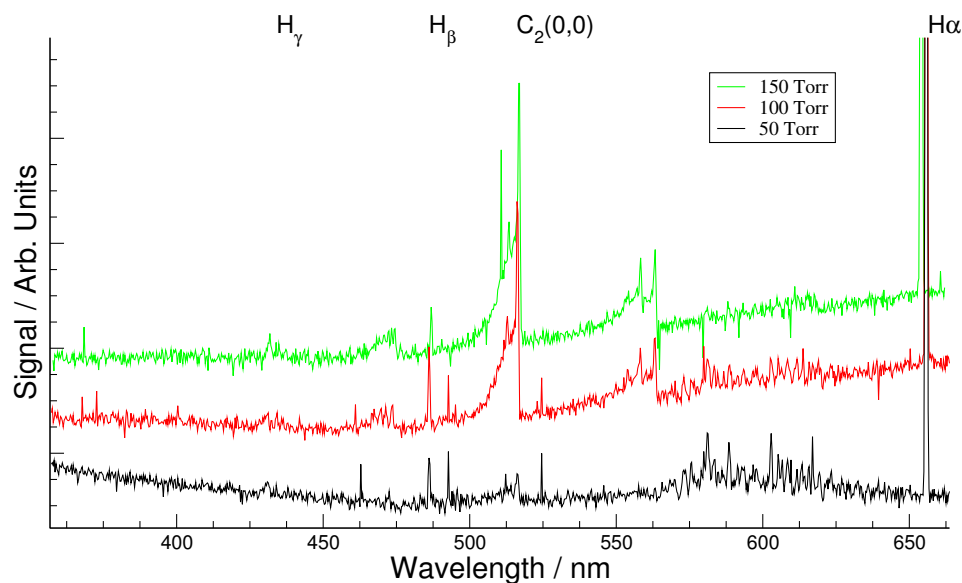


**Figure 5.5:** Low resolution optical emission spectra from a 4.4% CH<sub>4</sub> / 7% Ar / balance H<sub>2</sub> plasma generated within the microwave system, sustained at 1.45 kW, measured at a height of 4 mm above the substrate, at pressures of (a) 50 (b) 100 (c) 150 Torr. The H<sub>α</sub> OES signals have been truncated to retain clarity.

which correlate to the hydrogen Balmer alpha, beta and gamma (H<sub>α</sub>, H<sub>β</sub> and H<sub>γ</sub>) emissions respectively, with decreasing relative intensities. The strength of the optical emission from the C<sub>2</sub>  $d^3\Pi_g - a^3\Pi_u$  Swan band shows a strong pressure dependence, increasing in intensity with pressure, accompanied by comparable rises in the associated  $\Delta\nu=1$  and  $\Delta\nu=-1$  bands. For the lower pressure regimes, a complex spectral pattern can also be seen between 566 – 644 nm, which has been seen in in Ar: H<sub>2</sub> plasma and hence is tentatively ascribed to emissions from complexes arising from interactions between argon and hydrogen species. There is a lack of discernible optical emission signal from CH ( $A^2\Delta \rightarrow X^2\Pi$ , ~431 nm) or any CN ( $B^2\Sigma^+ \rightarrow X^2\Sigma^+$ , ~388 nm) species within the spectral window studied. This phenomenon may be explained by a poor level of light transmission through the optical bundle and a poor UV response from the CCD device

Figure 5.6 compares the intensities for the three brightest emitting species (H<sub>α</sub>, H<sub>β</sub> and C<sub>2</sub> Swan band head) as a function of distance from the substrate for the three

pressures shown in Figure 5.5. For plasmas sustained at 50 Torr, the maximum  $H_\alpha$ ,  $H_\beta$  and  $C_2$  optical emission intensity is 1 mm above the substrate and the intensities of these peaks decay with increasing distance from the substrate. At 100 Torr, the same overall trend of decreasing emission intensity with vertical height occurs but  $H_\alpha$  and  $C_2$  emissions have different profiles. However, at 150 Torr, there is a local maxima in both the  $H_\alpha$  and  $C_2$  emission intensity located at 7 mm and 10 mm respectively from the substrate.

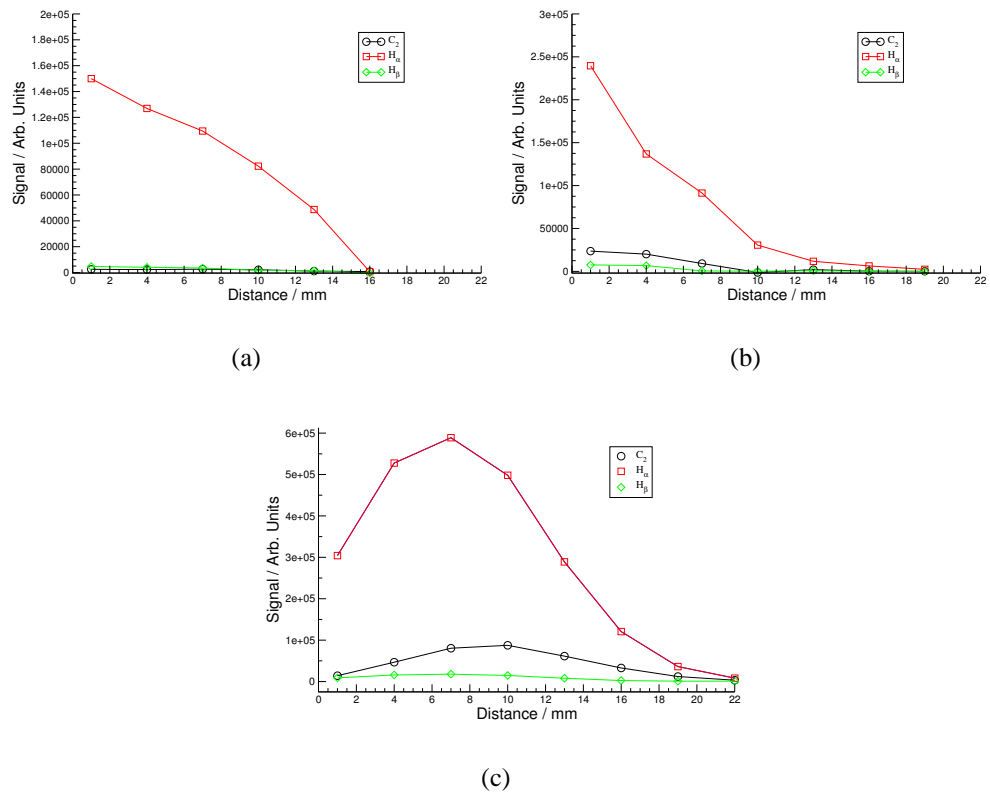


**Figure 5.6:** The measured optical emissions from the  $C_2$  Swan band,  $H_\alpha$  and  $H_\beta$  transitions as a function of distance from the substrate (distance = 0 mm) at (a) 50 Torr (b) 100 Torr (c) 150 Torr. All emission spectra were recorded under the standard condition with a gas mixture of 4.4 %  $CH_4$  / 7% Ar in a balance of  $H_2$  at a total flow rate of 565 sccm with 1.50 kW of microwave power.

## High Resolution OES

The comparatively low levels of emitted light from the microwave reactor coupled with the poor transmission of light through the optical bundle prevented the recording of a vertical profile of  $C_2$  using the high resolution OES experimental setup. Figure 5.7 shows a typical high resolution spectrum of the  $C_2$  ( $d^3\Pi_g - a^3\Pi_u$ ) Swan band transition recorded from the focused optical emissions from the centre of the plasma.

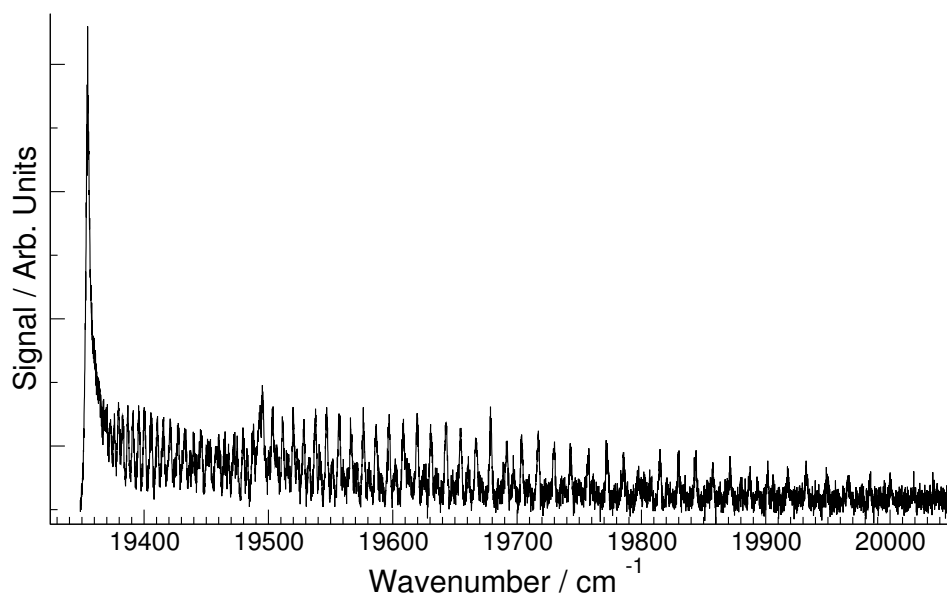


**Figure 5.7:** High Resolution optical emission spectrum of the  $C_2$   $d^3\Pi_g - a^3\Pi_u$  Swan band emission from a plasma resulting from a 4.4 %  $CH_4$  / 7 % Ar in a balance of  $H_2$  gas mixture, sustained at 1.45 kW microwave power, at a pressure of 150 Torr.

## 5.5 Cavity Ring-Down spectroscopy

### 5.5.1 Experiment

Measurements of the  $C_2(d-a)$  Swan band were performed in the custom made high pressure microwave reactor by pulsed laser CRDS as shown in Figure 5.8.

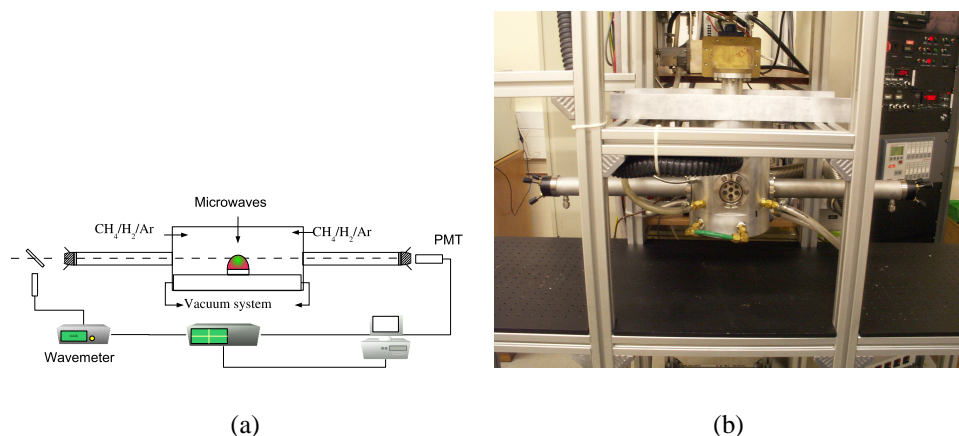


**Figure 5.8:** (a) Systematic drawing showing CRDS set up (b) experimental apparatus (guiding optics omitted for clarity).

Highly reflective concave mirrors (diam. 26.3 mm, radius of curvature 1 m) are mounted at the ends of tubular stainless steel side arms 50 cm from the centre of the plasma so as to form an optical cavity. Each mirror is held in place within a three-way screw construct which enables fine tuning of the cavity alignment. Argon purges are present in front of each mirror, thereby minimising deposition on the mirror surface during measurement. Laser light is from a mains frequency triggered (stepped down to 10 Hz) Nd:YAG pumped dye laser (Continuum Surelite; Sirah Cobra) using Coumarin 307 dye, to produce tunable radiation at wavelengths  $\sim 516$  nm. The light (Energy  $< 11$  mJ / pulse, bandwidth =  $0.09\text{ cm}^{-1}$  (FWHM)) is coupled into the optical cavity through one of the mirrors by means of a lens ( $f = 50$  cm) and steering prisms. Subsequent light decay from the cavity is measured using

a photo-multiplier tube, the output of which is recorded on a fast digital oscilloscope (LeCroy 9361). The centre of the optical cavity is  $\sim 10$  mm above the centre of the substrate surface, at which point the laser beam waist is  $\sim 0.5$  mm diameter. Typical ring-down times were in the order of  $5 \mu\text{s}$ . The ring-down signals were recorded by the in house program “Drive” which also calculated the changes in ring-down rates, ( $\Delta k$ ), whilst scanning the dye-laser (typical scan rates  $0.01 \text{ cm}^{-1} \text{ s}^{-1}$ ). Individual rotational lines in the  $\Delta k$  versus wavelength spectra were fitted to Gaussian functions, (5.18).

$$f(x) = \frac{a}{\sigma\sqrt{2\pi}} e^{-(x-\mu)^2/2\sigma^2} + c \quad (5.18)$$

where  $a$  is the area of the peak;  $c$  is the vertical offset ;  $\sigma^2$  is the variance of the Gaussian function and  $\mu$  is the location of the centre of the peak.

## 5.5.2 Results

Spectra of the  $\text{C}_2$   $d^3\Pi_g - a^3\Pi_u$  (0,0) band have been recorded over a wide wavenumber range, with the detection of rotational lines involving  $J'' > 67$ . Figure 5.9 shows a typical example. The assignment of these lines was made using the PGOPHER simulation program [43] and spectroscopic constants taken from previous work within the group [12]. Spectra were analysed as a function of process conditions; %  $\text{CH}_4$ ; % Ar; microwave power and total chamber pressure.

### Plasma temperature

The gas temperature of the plasma can be estimated from the rotational temperature of  $\text{C}_2$  species present within the reactor. This rotational temperature can be computed from the population of the rotational states within the  $\text{C}_2$  species and

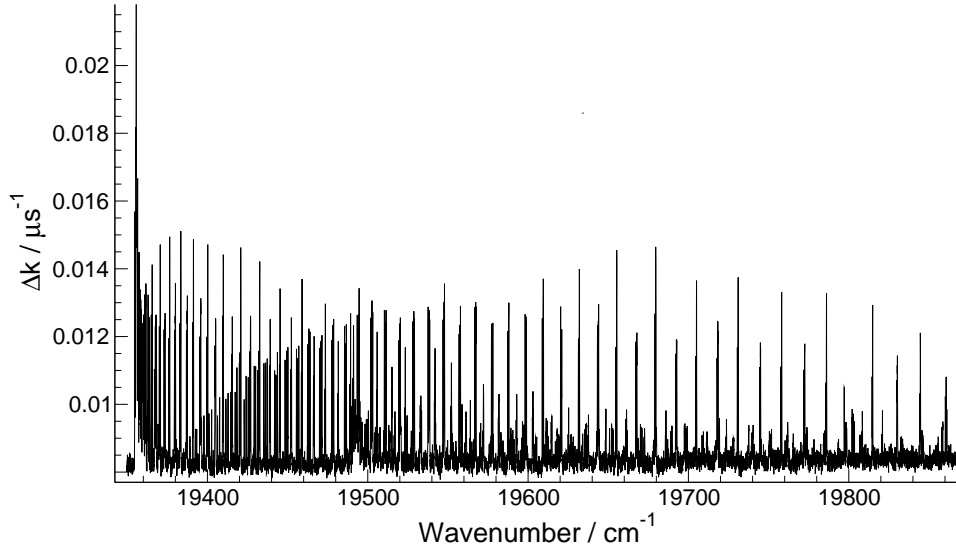


**Figure 5.9:** CRDS spectra of the  $C_2 d^3\Pi_g - a^3\Pi_u$  origin band under typical operating conditions of power of 1.5 kW, with gas composition of 4.4%  $CH_4$ ; 7 % Ar; balance of  $H_2$  at a pressure of 150 Torr measured at a distance of  $\sim 10$  mm from the substrate.

is calculated from the measurement of the  $C_2$  line intensity,  $I_{J'J''}$ , the calculated lines strength,  $S_{J'J''}$ , and the rotational energy of the various absorbing level,  $E_{J''}$ , (5.19).

$$\frac{I_{J'J''}}{S_{J'J''}} = \exp(-E_{J''}/k_bT) \quad (5.19)$$

The resulting Boltzmann plot for the standard conditions is shown in Figure 5.10 resulting in an average gas temperature of  $3520 \pm 260$  K. The linear correlation implies that the hot region of gas is highly localised and it can be inferred that the “hot”  $C_2$  species are solely located within the plasma, in the centre of the optical cavity. This recorded temperature is comparable with values measured within the DC arc-jet and with experiment modelling of this experiment [12].

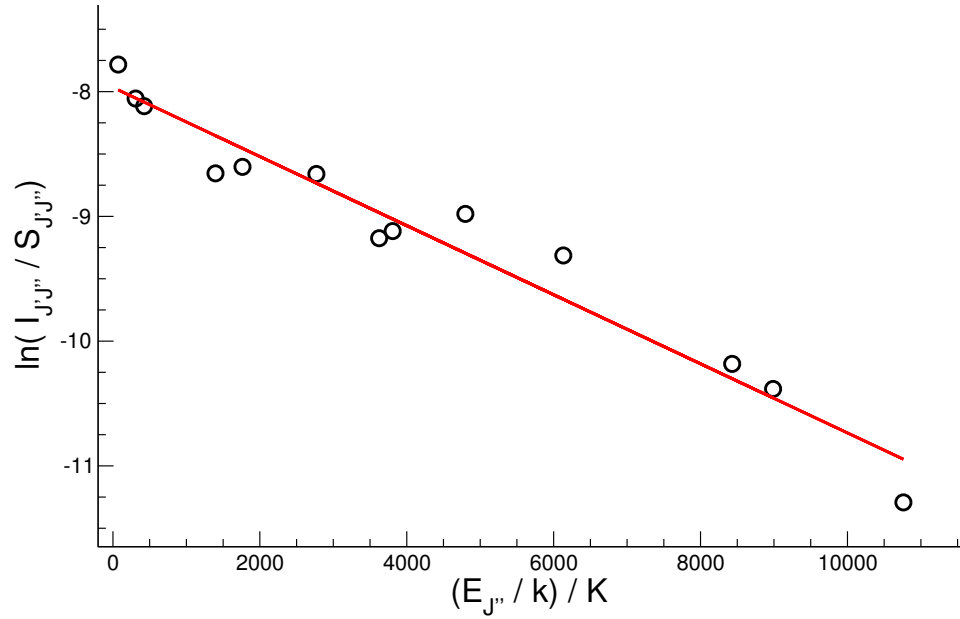


**Figure 5.10:** A Boltzmann plot comparing C<sub>2</sub> line intensity, the calculated line strength and the energy of rotational transitions. The studied plasma is running under the typical operating conditions, with gas composition of 4.4% CH<sub>4</sub>; 7 % Ar; balance of H<sub>2</sub> at a pressure of 150 Torr sustained at 1.5 kW. The line of sight column was measured at a distance of ~10 mm from the substrate.

### CRDS spectra

Figure 5.11 shows a portion of the C<sub>2</sub>(*d-a* 0,0) band which contains transitions from both low and high rotational states, which were used to monitor C<sub>2</sub> column densities as a function of process parameters.

Accurate measurements of the length of the absorbing medium, *l*, are problematic and a source of major errors in such CRDS measurements of localised plasmas. Hence, for these initial studies, column densities have been considered. The absorption coefficients are related to the C<sub>2</sub>(*a*, *v*=0) column density by equation 5.20 [45].

$$\int_{line} \alpha_{\bar{\nu}} d\bar{\nu} = \frac{\lambda^2}{8\pi c} \frac{g_d}{g_a} [C_2(a, v=0)] A_{00} p \quad (5.20)$$

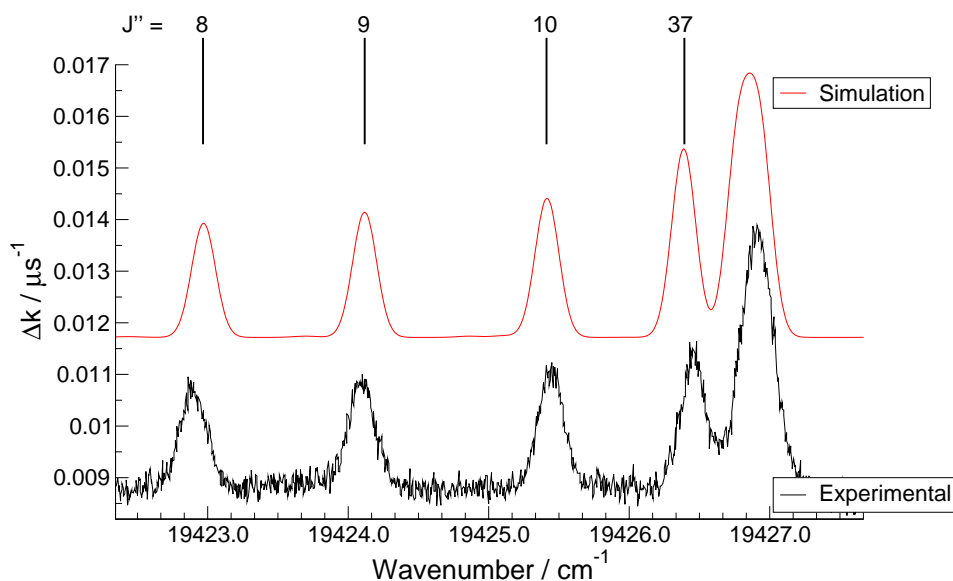


**Figure 5.11:** CRD spectrum of a small portion of the  $C_2 d^3\Pi_g - a^3\Pi_u$  origin band under typical operating conditions, with gas composition of 4.4%  $CH_4$ ; 7% Ar; balance of  $H_2$  at a pressure of 150 Torr, maintained with an input power of 1.5 kW. The column probed was a distance of  $\sim 10$  mm from the substrate. A PGOPHER simulation of this region of the spectrum, assuming  $T_{rot} = 3500$  K, is shown above.

where  $p$  is the fraction of the total band oscillator strength in the rotational line under investigation (which can be calculated from the PGOPHER simulation of the  $C_2$  spectrum provided that  $T_{rot}$  is known);  $\lambda$  is the wavelength of the absorption;  $A$  is the Einstein A coefficient for this band; and  $g_a/g_a$  is the ratio of the electronic state degeneracies.  $C_2$  column densities for the typical operating conditions specified in the caption to Figure 5.11 are found to be  $3.62 \times 10^{12} \text{ cm}^{-2}$ . For any given run under these standard conditions, the standard deviation in the derived  $C_2$  column densities on any one day is only  $\sim 2\%$ .

### Process conditions effects

Column densities for the variations in process conditions have been calculated at 3500 K. Modelling of the plasma ball as having a constant gas temperature is a reasonable approximation as the rotation temperature derived from the Boltzmann plot

is a weighted average value for the distribution of  $C_2(a)$  radicals along the viewing column. This spread (likely to be a few 100 K at most) leads to a relatively small uncertainty in the value  $p$ . Figures 5.12(a), 5.12(b), 5.12(c) & 5.12(d) show the measured variation in  $C_2(a)$  column densities as a function of process conditions. All show linear correlations. Figure 5.12(b) shows that the  $C_2(a)$  column density is rather insensitive to changing the Ar : H<sub>2</sub> ratio while all other variations investigated thus far cause similar increases in  $C_2(a)$  column densities from  $\sim 1 \times 10^{12} \text{ cm}^{-2}$  to  $\sim 7 \times 10^{12} \text{ cm}^{-2}$ .

There is a difference of  $\sim 20\%$  between the column densities calculated from measurements of the low and high J transitions. This difference varies as a function of process conditions. This effect may be due to changes in the gas temperature as the calculated column densities assume a constant gas-phase temperature of 3500 K derived from the Boltzmann's temperature analysis. It is also possible that there is a non-linear temperature distribution through the plasma ball and this results in further distortions in the calculated column densities.

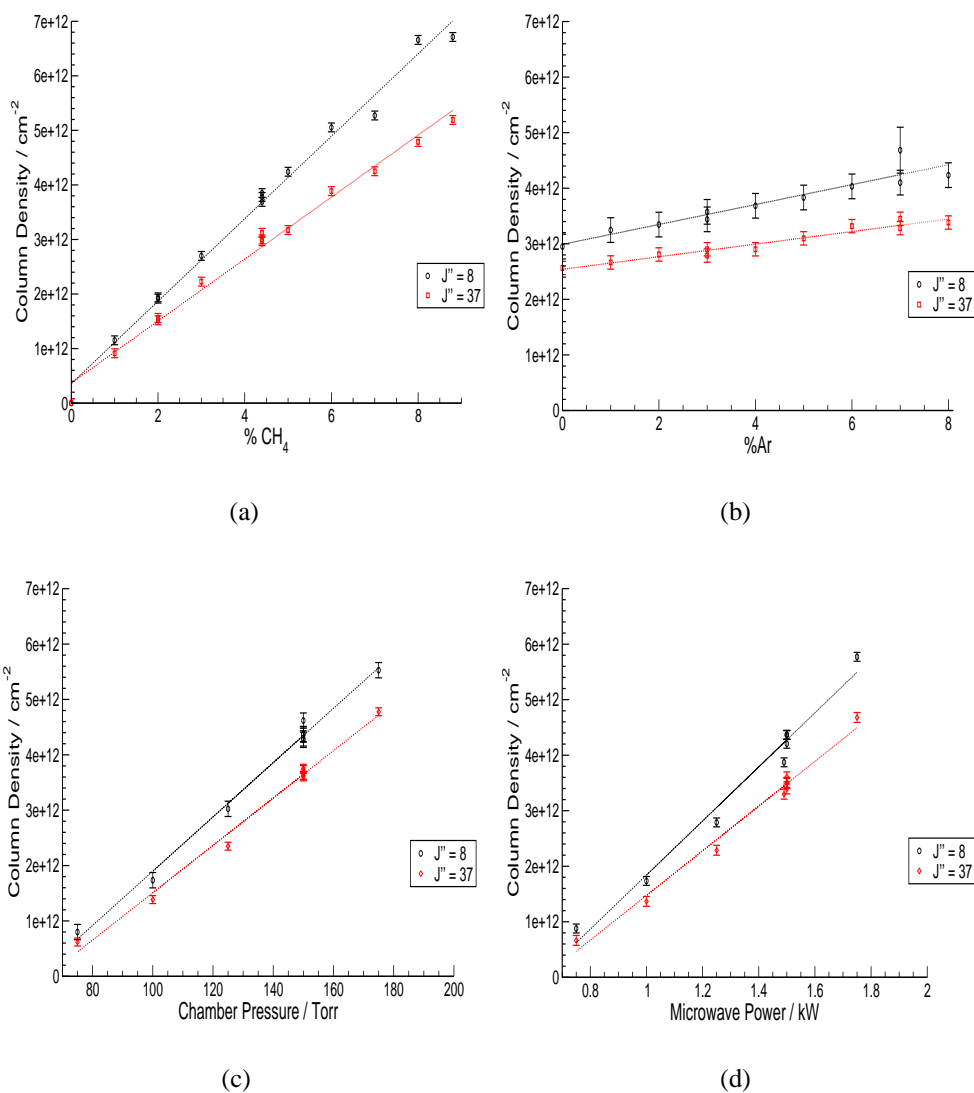


**Figure 5.12:** Variation of  $C_2(a)$  column density with (a) % methane (7 % Ar, balance  $H_2$ ) and (b) % argon (4.4%  $CH_4$ , balance  $H_2$ ), at a total pressure 150 Torr (c) total pressure,  $p$ , ( $P = 1.5$  kW) and (d) applied microwave power,  $P$ , ( $p = 150$  Torr). The effect of the individual variables was assessed as a deviation from the standard conditions of a gas composition of 4.4%  $CH_4$ ; 7 % Ar; balance of  $H_2$  at a pressure of 150 Torr sustained at 1.5 kW and the column density measurements were made at a distance of  $\sim 10$  mm above the substrate surface.

## Numbers densities

Translating the  $C_2$  column densities into an effective number density is a complex process requiring accurate modelling of the plasma chemistry and reaction dynamics. However, the calculation of the gas temperature based upon the Boltzmann rotational state population distribution of  $C_2$ , Figure 5.10, highlights the localised nature of the hot  $C_2$  species. It is thus reasonable to assume that the majority of the  $C_2$  present within the reactor will be in the plasma ball. A simple approximation for the modelling of number density would be to assume a uniform distribution of  $C_2(a)$  within the observed plasma ball and that the size of the plasma correlates to the diameter of the molybdenum substrates and to the experimental conditions.

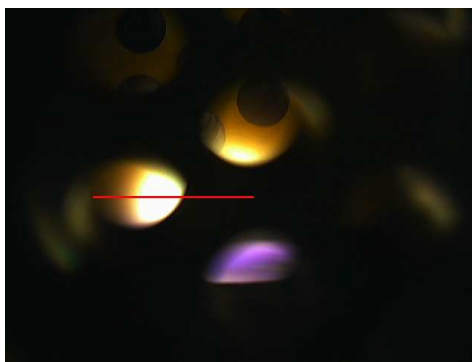


**Figure 5.13:** Photo of the side view of a plasma operating under standard conditions (i.e gas composition of 4.4%  $CH_4$ ; 7 % Ar; balance of  $H_2$  at a pressure of 150 Torr sustained at 1.5 kW). The bar shows the path along which the plasma is measured and all subsequent plasma images are scaled to this image.

In order to resolve these issues, direct monitoring of the plasma emission with a CCD camera array has been used to size the plasma ball under the full range of experimental conditions. These relative sizes are then used to calculate an effective number density using the  $\Delta k$  and column density data for the  $J'' = 8$  transition, from the previous section (The  $J'' = 37$  data follow a similar pattern). Figure 5.13 shows a typical side image of the plasma under the standard conditions, against which all images are sized. (Appendix F contains all images used for processing the number

densities)

The two assumptions made in this work are that the  $C_2$  species probed by CRDS are confined within the plasma ball and for a plasma maintained under standard conditions, the absorbing path length is 30 mm, the diameter of the molybdenum substrate. The relative absorption lengths of  $C_2$  are incorporated into eq (5.15) and Figure 5.14(a), 5.14(b) & 5.14(c) shows the resultant number densities as a function of pressure, power and the methane concentration. These results are compared with number densities calculated assuming a constant path length,  $l$  of 30 mm. (The effects of argon upon the size of the plasma ball were below the resolution of the experimental setup and hence negligible.) These results show that changes in pressure and methane concentrations have minimal effects on the size of the luminous plasma ball and thus on the assumed size of the column of absorbing  $C_2$ . This explains the similarities between the calculated number densities shown in Figure 5.14(a) & 5.14(c). However, Figure 5.14(b) shows a clear difference between the number densities calculated by the two methods, indicating that the size of the plasma ball is sensitive to the input power.

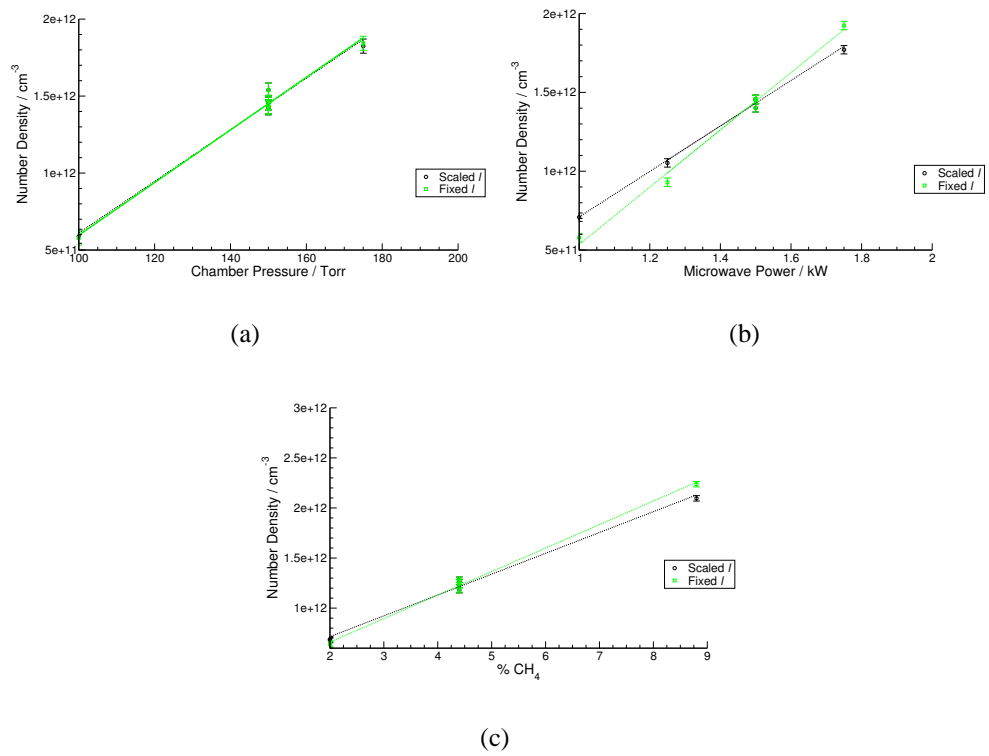
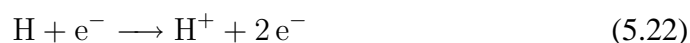
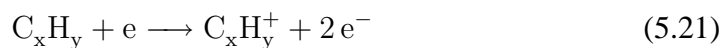


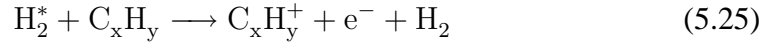
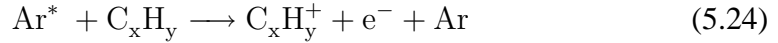
**Figure 5.14:** Comparison of the variation of  $C_2(a)$  number densities from probing on the  $J'' = 8$  transition, using the scaled absorption path length  $l$  and a fixed  $l$  of 30 mm for (a) total pressure,  $p$ , (b) applied microwave power and (c) %  $CH_4$ . These results were obtained from deviations from the standard conditions of 4.4 %  $CH_4$ , 7 % Ar, balance  $H_2$  gas mixture at a gas pressure of 150 Torr with an input power of 1.5 kW. Measurements were performed at a distance of  $\sim 10$  mm above the substrate surface.

## 5.6 Initial thermodynamical and kinetic modelling of gas-phase chemical processes

At Bristol, OES and CRDS measurements on HF and DC arc-jet reactors have shown a high level of agreement with the predictions from modelling work by Mankelevich [13], [15], [46] – [48]. These results imply that the model used includes a good understanding of the gas-phase chemistry occurring within the CVD environment. Within this section, modifications to and preliminary results from, modelling of the gas-phase chemistry in a high-pressure microwave reactor are presented.

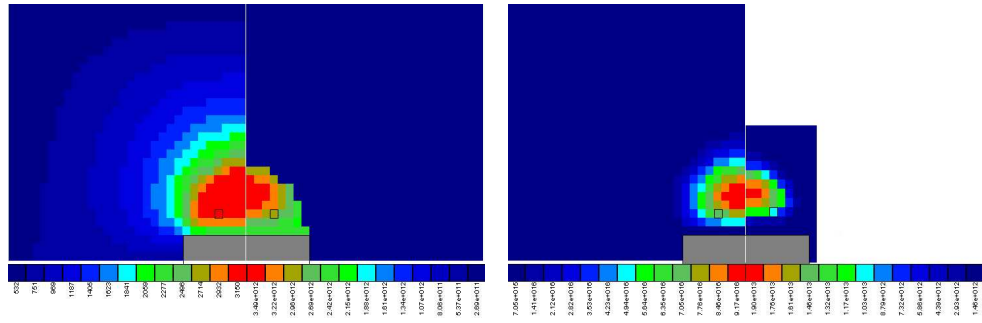
Initial modelling has focussed upon replicating the standard conditions, (4.4 % CH<sub>4</sub>, 7 % Ar, balance H<sub>2</sub> gas mixture, at a gas pressure of 150 Torr with an input power of 1.5 kW) Based on power balance considerations, the plasma within the microwave system is estimated to have an electronic temperature, T<sub>e</sub> = 1.5 eV and a power density of 200 W cm<sup>-3</sup>. This energy is absorbed by electrons, which lead to vibrational and rotational excitation of H<sub>2</sub> (~62% and 26% of the total absorbed energy respectively); the dissociation of molecular species (~6.5%, H<sub>2</sub>, ~1.5%, C<sub>x</sub>H<sub>y</sub>) and the ionisation and excitation of gas-phase species (~4%). The most important reactions are highlighted in (5.21)–(5.25)).





However, the initial model is lacking one or more cooling pathways as it currently leads to unrealistically high  $T_{\text{gas}}$  ( $\sim 4000$  K) and hydrogen atom mole fractions ( $> 50\%$  in the plasma ball). An initial spatial model of the microwave reactor and the chemistry occurring within it can be made by limiting the gas-phase temperature within the plasma to 3000 K. Figure 5.15(a) shows the spatial distribution of the local gas-phase temperature and electron distribution that results, confirming that the fixed probing through the centre of emission intensity of the plasma, ( $\sim 10$  mm from the substrate), is through the hottest region of the gas mixture. Figure 5.6 shows the predicted distribution of the H atom and  $\text{C}_2$  radicals within the reactor, which is in good qualitative agreement with the experiment OES measurement at this pressure, Figure 5.6(c). The two species show different number density profiles, both of which maximise away from the substrate. The model also emphasises the inhomogeneous nature of the plasma ball and suggests a column density of  $\text{C}_2$  radicals over the total substrate of  $\sim 1.3 \times 10^{14} \text{cm}^{-3}$ .

Table 5.4 shows predicted number densities of selected species, 1 mm from the substrate under standard conditions, with molecular  $\text{C}_2\text{H}_2$  being the most abundant species present. This model also suggests the main possible growth species present as  $\text{CH}_3$  and  $\text{C}_2\text{H}$  with relatively low  $\text{C}_2$  concentrations.



(a)

**Figure 5.15:** Calculated  $(r,z)$  distribution for (a) gas temperature,  $T_g$  (left) and electron distribution (right) (b) hydrogen (left) and  $C_2$  (right), within microwave reactor under standard conditions.

Species	Concentration $\text{cm}^{-3}$
H	4.31E+15
$\text{CH}_3$	2.37E+13
$\text{C}_2\text{H}_2$	1.15E+16
$\text{CH}_2$	2.60E+11
$\text{C}_2$	6.74E+09
$\text{C}_2\text{H}$	1.77E+12
$\text{C}_2\text{H}_4$	7.58E+12
$\text{CH}_4$	1.70E+14
$\text{C}_3\text{H}_2$	2.39E+13
$\text{C}_4\text{H}_2$	2.95E+13
$\text{H}_2$	6.17E+17

**Table 5.4:** Table summarising the predicted number densities for the major CVD species, present within the plasma ball, at 1 mm above the substrate within microwave reactor under standard conditions.

## 5.7 Conclusions

The installation and optimisation of a high pressure CVD microwave reactor has been performed. OES studies show that the main emitting species present in the plasma are hydrogen ( $H_{\alpha}$ ,  $H_{\beta}$ ) and  $C_2(a)$ . Vertical profiling using OES has revealed the structure of the plasmas at different pressures.

CRDS has been shown to be a viable technique for measuring column densities of  $C_2(a)$  radicals over a wide range of process conditions. CRDS measurements of  $C_2$  rotational temperature have found the plasma temperature to be  $3520 \pm 260$  K.  $C_2(a, v=0)$  column densities under the base operating conditions (applied microwave power  $P = 1.5$  kW, gas composition 4.4 %  $CH_4$ , 7% Ar, balance  $H_2$ ,  $p = 150$  Torr, and measuring at a distance of  $\sim 10$  mm from the substrate) are found to be  $\sim 3.62 \times 10^{-12} \text{ cm}^{-2}$ . Optical measurements of the microwave plasma have shown that there is minimal variation in the size of the plasma ball as  $CH_4$  flow rate or total pressure are varied, but that the applied power has more affect on the plasma ball size. All observations are in good agreement with the initial modelling predictions by Mankelevich.

## Bibliography

- [1] J. M. Hollas, *Modern Spectroscopy* (Wiley, 4th edition, 2004).
- [2] W. G. Richards and P. R. Scott, *Energy Levels in Atoms and Molecules* (Oxford Science Publications, 1994).
- [3] D. Romanini and K. K. Lehmann, *J. Chem. Phys.* **99**, 6287 (1993).
- [4] M. D. Wheeler, S. M. Newman, M. N. R. Ashfold, and A. J. Orr-Ewing, *J. Chem. Soc. Faraday Trans.* **94**, 337 (1998).
- [5] C. A. Rego, P. W. May, C. R. Henderson, M. N. R. Ashfold, K. N. Rosser, and N. M. Everitt, *Diamond Relat. Mater.* **4** (1995).
- [6] F. G. Celii and J. E. Butler, *Annu. Rev. Phys. Chem.* **42**, 643 (1991).
- [7] F. G. Celii, P. E. Pehrsson, H. t. Wang, and J. E. Butler, *Appl. Phys. Letts.* **52**, 2043 (1988).
- [8] P. Zalicki, Y. Ma, R. N. Zare, E. H. Wahl, J. R. Dadamio, T. G. Owano, and C. H. Kruger, *Chem. Phys. Letts.* **234**, 269 (1995).
- [9] U. Lommatzsch, E. H. Wahl, D. Aderhold, T. G. Owano, C. H. Kruger, and R. N. Zare, *Appl. Phys. A.* **73**, 27 (2001).
- [10] P. John, J. Rabeau, and J. Wilson, *Diamond Relat. Mater.* **11**, 608 (2002).
- [11] A. Staicu, R. L. Stolk, and J. J. ter Meulen, *J. Appl. Phys.* **96**, 969 (2002).
- [12] J. B. Wills, J. A. Smith, W. E. Boxford, J. M. F. Elks, M. N. R. Ashfold, and A. J. Orr-Ewing, *J. Appl. Phys.* **92**, 4213 (2002).
- [13] Yu. A. Mankelevich, N. V. Suetin, M. N. R. Ashfold, J. A. Smith, and E. Cameron, *Diamond Relat. Mater.* **10**, 364 (2001).
- [14] C. J. Rennick, A. G. Smith, J. A. Smith, J. B. Wills, A. J. Orr-Ewing, M. N. R. Ashfold, Yu. A. Mankelevich, and N. V. Suetin, *Diamond Relat. Mater.* **13**, 561 (2004).
- [15] M. N. R. Ashfold, P. W. May, J. R. Petherbridge, K. N. Rosser, J. A. Smith, Yu. A. Mankelevich, and N. V. Suetin, *Phys. Chem. Chem. Phys.* **3**, 3471 (2001).
- [16] D. G. Goodwin and J. E. Butler, in *Handbook of Industrial Diamonds and Diamond Films*, (ed. M. A. Prelas, G. Popovici, and L. G. Bigelow), Marcel Dekker Inc. (1998).
- [17] <http://hyperphysics.phy-astr.gsu.edu/hbase/hyde.html#c2>

- [18] K. P. Huber and G. Herzberg, *Molecular spectra and molecular structure.4, Constants of diatomic molecules* (Van Nostrand Reinhold, New York, 1979).
- [19] G. Lombardi, F. Bénédic, F. Mohasseb, K. Hassouni, and A. Gicquel, *Plasma Sources Sci. Technol.* **13**, 375 (2004).
- [20] A. N. Goyette, Y. Matsuda, L. W. Anderson, and J. E. Lawler, *J. Vacuum Sci. Tech. A* **16**, 337 (1998).
- [21] K. Larsson, *Phys. Rev. B* **56**, 15452 (1997).
- [22] D. A. Horner, L. A. Curtiss, and D. M. Gruen, *Chem. Phys. Letts.* **233**, 243 (1995).
- [23] M. Sternberg, P. Zapol, and L. A. Curtiss, *Mol. Phys.* **6-8**, 1017 (2005).
- [24] S. W. Yang, X. Xie, P. Wu, and K. P. Loh, *J. Phys. Chem. B*, **107**, 985 (2003.).
- [25] M. Sternberg, M. Kaukonen, R. M. Nieminen, and T. Frauenheim, *Phys. Rev. B* **63**, 165414 (2001).
- [26] J. Luque, W. Juchmann, and J. B. Jeffries, *J. Appl. Phys.* **82**, 2072 (1997).
- [27] C. J. Rennick, J. A. Smith, M. N. R. Ashfold, and A. J. Orr-Ewing, *Chem. Phys. Letts.* **383**, 518 (2004).
- [28] N. Ali, F. Neto, S. Mei, G. Cabral, Y. Kousar, E. Titus, A. A. Ogwu, D. S. Misra, and J. Gracio, *Thin Solid Films* **469-70**, 154 (2004).
- [29] M.-J. Youh, *Development of Microwave Absorbing Diamond Coated Fibres*, Ph.D thesis, University of Bristol, 2000.
- [30] W. Y. Fowlkes and C. M. Creveling, *Engineering methods for robust product design : using Taguchi methods in technology and product development* (Addison-Wesley, 1995).
- [31] A. Bendell, J. Disney, and W. A. Pridmore (editors), *Taguchi methods : applications in world industry* (Springer, 1989).
- [32] R. E. Shroder, R. J. Nemanich, and J. T. Glass, *Phys. Rev. B* **41**, 3738 (1990).
- [33] J. W. Ager, D. K. Veirs, and G. M. Rosenblatt, *Phys. Rev. B* **43**, 6491 (1991).
- [34] M. Wakagi, B. Hong, H. V. Nguyen, R. W. Collins, W. Drawl, and R. Messier, *J. Vac. Sci. Tech. A.* **13** (1995).
- [35] C. Wild, P. Koidl, W. Müller-Sebert, H. Walcher, R. Kohl, N. Herres, R. Locher, R. Samlenski, and R. Brenn, *Diamond Relat. Mater.* **2**, 158 (1993).
- [36] J. Achard, A. Tallaire, R. Sussmann, F. Silva, and A. Gicquel, *J. Cryst. Growth.* **284**, 396 (2005).

- [37] T. Teraji, S. Mitani, and T. Ito, *Phys. Stat. Sol. (a)*. **198**, 395 (2003).
- [38] K. Hassouni, X. Duten, A. Rousseau, and A. Gicquel, *Plasma Sources Sci. Technol.* **10**, 61 (2001).
- [39] A. Gicquel, M. Chenevier, K. Hassouni, A. Tserepi, and M. Dubus, *J. Appl. Phys.* **83**, 7504 (1998).
- [40] F. Silva, A. Gicquel, A. Tardieu, P. Cledat, and T. Chauveau, *Diamond. Relat. Mater.* **5**, 338 (1996).
- [41] A. Tallaire, J. Achard, F. Silva, and A. Gicquel, *Phys. Stat. Sol. (a)*. **202**, 2059.
- [42] W. Zhu, A. Inspektor, A. R. Badzian, T. McKenna, and R. Messier, *J. Applied Phys.* **68**, 1489 (1990).
- [43] C. M. Western, *PGOPHER, a Program for Simulating Rotational Structure*, University of Bristol.
- [44] J. B. Wills, *Laser diagnostics of chemical vapour deposition of diamond films*, Ph.D thesis, University of Bristol, 2002.
- [45] A. P. Thorne, *Spectrophysics* (Chapman and Hall, New York, 1998).
- [46] J. A. Smith, E. Cameron, M. N. R. Ashfold, Yu. A. Mankelevich, and N. V. Suetin, *Diamond Relat. Mater.* **10**, 358 (2001).
- [47] C. J. Rennick, R. Engeln, J. A. Smith, A. J. Orr-Ewing, M. N. R. Ashfold, and Yu. A. Mankelevich, *J. Appl. Phys* **97**, 113306 (2005).
- [48] D. W. Comerford, A. Cheesman, T. P. F. Carpenter, D. M. E. Davies, N. A. Fox, R. S. Sage, J. A. Smith, M. N. R. Ashfold, and Yu. A. Mankelevich, *J. Phys. Chem. A* **110**, 2868 (2006).

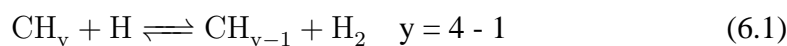
## **Chapter 6**

# **Monitoring of CH<sub>4</sub> and C<sub>2</sub>H<sub>2</sub> column densities in CH<sub>4</sub> / Ar / H<sub>2</sub> and C<sub>2</sub>H<sub>2</sub> / Ar / H<sub>2</sub> gas mixtures in the microwave CVD reactor using an Infrared Quantum Cascade Laser**

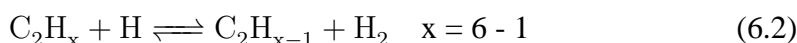
This chapter reports the first illustrations of the use of pulsed quantum cascade lasers for in situ probing of the chemistry prevailing in microwave plasma activated hydrocarbon / Ar / H<sub>2</sub> gas mixtures used for diamond thin film growth. CH<sub>4</sub> and C<sub>2</sub>H<sub>2</sub> molecules, and their interconversion, have been monitored by line-of-sight single pass absorption methods, as a function of process conditions (e.g., choice of input hydrocarbon (CH<sub>4</sub> or C<sub>2</sub>H<sub>2</sub>), hydrocarbon mole fraction, total gas pressure, and applied microwave power).

## 6.1 Introduction

The important role of atomic hydrogen in the CVD growth of diamond has been shown throughout this thesis, highlighting the role it plays in controlling the growth of the diamond surface, Chapters 3, 4, as well as controlling the nature of gas-phase dopants, Chapter 2. Attention now shifts to the role of atomic hydrogen as a gas-phase reagent with hydrocarbon species. Chapter 1 showed that most diamond CVD is brought about by using activated dilute methane / H<sub>2</sub> gas mixtures. Activation leads to dissociation of molecular hydrogen, and formation of H atoms. The most important role of these atoms, in the context of the gas-phase chemistry involved with CVD diamond growth, is activation of gas-phase hydrocarbon species via the sequence of H-shifting reactions (6.1).



Self-reactions between the resulting CH<sub>y-1</sub> radicals can yield C<sub>2</sub>H<sub>x</sub> (x ≤ 6) species, which participate in a similar sequence of H-shifting reactions (6.2).



Any thorough understanding of the diamond CVD process thus requires rather detailed knowledge of the chemical environment immediately adjacent to the growing film surface. Chapter 1 has highlighted the main research impetus in studying the CVD environment and Chapter 5 has highlighted the main uses of spectroscopic techniques within a CVD diamond growing environment.

A key feature of understanding the CVD process is the recognition of high H atom number densities throughout the reactor – even in the peripheral, cooler regions, where the H atom densities far exceed those expected on the basis of local

thermodynamic equilibrium. This reflects the paucity of efficient H atom loss processes in these gas mixtures (which typically contain 95 – 99% H<sub>2</sub>). These H atoms not only drive the families of radical forming H shifting abstraction reactions (6.1) and (6.2) but also, in the cooler regions, participate in H addition reactions that convert C<sub>2</sub>H<sub>2</sub> (the most stable C<sub>2</sub>H<sub>x</sub> species at high gas temperatures) back to the CH<sub>y</sub> family [1] [2]. If the CH<sub>y</sub>  $\rightleftharpoons$  C<sub>2</sub>H<sub>x</sub> interconversions are sufficiently rapid, it follows that the detailed distribution of CH<sub>y</sub>, C<sub>2</sub>H<sub>x</sub>, etc. species present in an activated hydrocarbon / H<sub>2</sub> gas mixture should be relatively insensitive to the precise choice of hydrocarbon feedstock gas. In support of this view, a number of early diamond film growth studies demonstrated that similar morphologies and growth rates could indeed be obtained by using different hydrocarbon source gases (at a constant input carbon mole fraction) [3]. While qualitatively correct, there is a wealth of available data to suggest that this assumption cannot be correct in detail. For example, earlier comparison of HF activated 1% CH<sub>4</sub> / H<sub>2</sub> and 0.5% C<sub>2</sub>H<sub>2</sub> / H<sub>2</sub> gas mixtures indicated that there were 3 times higher CH<sub>3</sub> radical number densities near the filament in the former [4]. There remains a continuing need for new and improved, non-intrusive, in situ probes of the gas-phase chemistry and compositions, not just to quantify such differences better and to move our understanding of the diamond CVD process to a higher level, but also from the viewpoint of improved process control.

Here we provide the first illustrations of the potential of quantum cascade (QC) laser technology to address some of these issues. The theory behind quantum cascade lasing has been well described in the literature [5], however the physical construction of these devices has only recently been realised [6], [7]. Quantum cascade lasers work on a basic 3 level laser principle based on transitions across very thin layers of different semiconductors, Figure 6.1. The construction of the semiconductor layers generates a series of square well potentials within the device, which

directly control the lasing wavelength and offer a narrow laser line width laser. This process avoids using the natural band-gap of the optical medium and thus offers new lasing regions. The laser works by an optical lasing transition between levels 3 and 2 producing one photon followed by a fast electronic transition from level 2 to 1 which then populates the next upper level of the next construct. The optic flux of the laser is determined by the number of the cascading units. Application of a fast square wave potential pulse across the laser leads to a current sweep in the laser which lowers the lasing frequency and produces a distinct non-linear frequency “chirp” pulse.

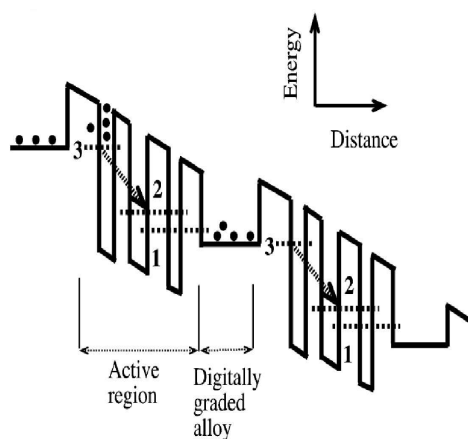


**Figure 6.1:** Schematic of the quantum cascade laser energy profile from ref [7]

Specifically, we have employed a pulsed QC laser operating at  $\sim 1275 \text{ cm}^{-1}$  to probe  $\text{CH}_4$  and  $\text{C}_2\text{H}_2$  molecules, and their interconversion, in a 1.5 kW microwave reactor operating with both  $\text{CH}_4 / \text{Ar} / \text{H}_2$  and  $\text{C}_2\text{H}_2 / \text{Ar} / \text{H}_2$  gas mixtures, as a function of process conditions (e.g., input hydrocarbon mole fraction, total gas pressure, and applied MW power). In addition, the rapid sweep rate of such pulsed QC lasers has enabled new insights into the time evolution of the  $\text{CH}_4 / \text{C}_2\text{H}_2$  ratio when either is introduced into (or removed from) an established  $\text{Ar} / \text{H}_2$  plasma.

## 6.2 Experimental Details

The plasma of interest was maintained in a custom designed and built MW reactor operating with mixtures of hydrocarbon ( $\text{CH}_4$  or  $\text{C}_2\text{H}_2$ ), Ar, and  $\text{H}_2$  (BOC, with respective stated purities of 99.5% ( $\text{CH}_4$ ), 98.5% ( $\text{C}_2\text{H}_2$ ), 99.995% (Ar), and 99.995% ( $\text{H}_2$ )). The design specification and initial characterisation of this reactor are discussed in Chapter 5. Those studies provide the basis for the adoption of the following standard conditions: a gas mixture consisting of 4.4%  $\text{CH}_4$  / 7 % Ar / balance  $\text{H}_2$ , maintained at 150 Torr and the plasma sustained by a 1.5 kW microwave source.

The column probed by the laser is defined by two 4 mm-diameter apertures mounted on opposite sides of the reactor, allowing single-pass line-of-sight monitoring along an axis parallel to, and 13 mm above, the substrate surface. In the present experiments, these apertures were sealed by thin, polished CVD diamond windows (Element Six Ltd) mounted on wedged flanges so as to minimise etaloning effects. The window-window separation, and thus the length of the sampled column, was = 19.0 cm, of which the luminous plasma ball appeared to span the central  $\sim 30$  mm. The QC laser spectrometer and its operation have been described elsewhere [7] – [9]. The present experiments employed an 8  $\mu\text{m}$  laser, mounted in a compact QC laser head and driver developed by Cascade Technologies Ltd [10]. When operating at  $-2$  °C, the output wavenumber from the laser could be swept from 1277.6 to 1273.0  $\text{cm}^{-1}$  (a 140 GHz tuning range) in 2  $\mu\text{s}$  by applying a square voltage of this duration to the laser head. This wavenumber sweep is repeated, typically at a frequency of 5 kHz, thereby enabling rapid acquisition of infrared spectra with good signal-to-noise ratio by averaging many successively acquired spectra. The linearly polarised, unfocused laser output was attenuated by using a rotatable linear polariser (to avoid saturating the detector), and aligned along the viewing axis

by using two 90° turning mirrors. The transmitted light was focused onto a liquid nitrogen cooled detector (Kolmar Technologies KV104-0.1-1A-3) with a parabolic mirror, and the detector output passed through a fast amplifier (Femto Messtechnik HAS-Y-1-40) to a fast data collection card (Acqiris DP210) in a PC running under Labview control. Spectra were transformed and linearised from time to wavenumber space by periodically measuring the interference fringes produced by inserting a Ge Etalon (free spectral range = 0.0481 cm<sup>-1</sup>) into the laser beam path.

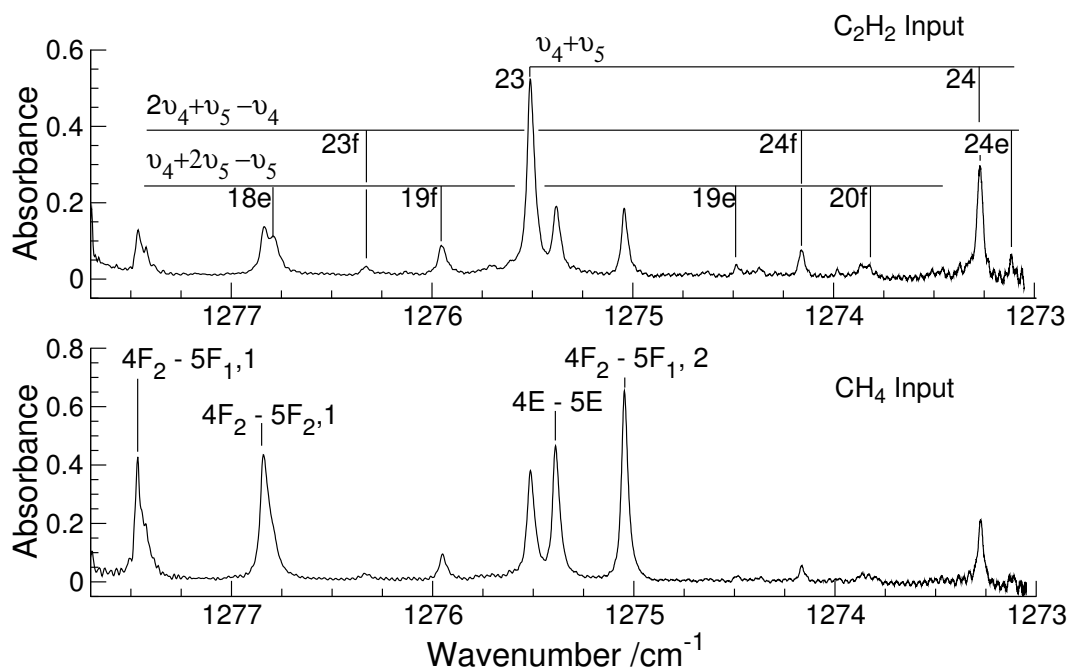
### 6.3 Results

Figure 6.2 shows measured single pass, line-of-sight absorption spectra of MW activated 4.4% C<sub>2</sub>H<sub>2</sub> / 7% Ar in H<sub>2</sub> (upper panel) and 8.8% CH<sub>4</sub> / 7% Ar in H<sub>2</sub> (lower panel) gas mixtures.

wavenumber/ cm <sup>-1</sup> [11]	vibrational transition	rotational transition
1277.47335	4 <sub>0</sub> <sup>1</sup>	4F <sub>2</sub> – 5F <sub>1,1</sub>
1276.84431	4 <sub>0</sub> <sup>1</sup>	4F <sub>1</sub> – 5F <sub>2,1</sub>
1275.38678	4 <sub>0</sub> <sup>1</sup>	4E – 5E
1275.04168	4 <sub>0</sub> <sup>1</sup>	4F <sub>2</sub> – 5F <sub>1,2</sub>

**Table 6.1:** Assignments of observed CH<sub>4</sub> absorption lines.

The carbon mole fraction in each case is thus the same, as is the total flow rate (565 sccm), pressure (150 Torr), and applied MW power (1.5 kW). The same spectral features are evident in both spectra, but their relative intensities show significant variations. The displayed wavenumber range includes four strong absorption lines of the  $\nu_4$  band of CH<sub>4</sub> and two strong lines of the  $\nu_4 + \nu_5$  combination band of C<sub>2</sub>H<sub>2</sub>. Several other absorption lines attributable to vibrationally excited C<sub>2</sub>H<sub>2</sub> molecules



**Figure 6.2:** Line-of-sight absorption spectra of MW activated 4.4 %  $C_2H_2$  7% Ar /  $H_2$  (upper panel) and 8.8%  $CH_4$  / 7% Ar /  $H_2$  (lower panel) gas mixtures. The carbon fraction, the total flow rate (565 sccm), total pressure (150 Torr), and applied MW power (1.5 kW) are the same in both cases.  $C_2H_2$  and  $CH_4$  absorptions are present in both spectra, with different relative intensities. Features due to  $C_2H_2$  and to  $CH_4$  are indicated in the upper and lower panels respectively. Details of these assignments are given in Tables 6.1 & 6.2.

with  $\nu_4 = 1$  or  $\nu_5 = 1$  are also evident. The vibrational origins of these two levels lie respectively 614.0 and 731.5  $cm^{-1}$  above the vibrational ground state [12]. Absolute wavenumbers for the  $C_2H_2$  transitions were determined by fitting against literature values for the four  $CH_4$  transitions [11]. This served to validate the  $CH_4$  and  $C_2H_2$  line assignments indicated in Figure 6.2 (on the upper and lower spectra, respectively) and detailed in Tables 6.1 & 6.2 respectively.

No absorptions associated with vibrationally excited  $CH_4$  molecules have been identified under the prevailing conditions, though  $CH_4$  hot-band absorptions have been observed in this wavenumber region in long path length absorption measurements of other environments [13].

obsd wave- number / $\text{cm}^{-1}$	lit. value/ $\text{cm}^{-1}$ [12]	vibrational transition	rotational transition <sup>a</sup>
1276.7807	1276.79005	$4_0^1 5_1^2 (\Pi_g - \Pi_u)$	P (18,e)
1276.3284	1276.33656	$4_1^2 5_0^1 (\Pi_u - \Pi_g)$	P (23,f)
1275.9443	1275.95852	$4_0^1 5_1^2 (\Pi_g - \Pi_u)$	P (19,f)
1275.5006	1275.51215	$4_0^1 5_0^1 (\Sigma_u^+ - \Sigma_g^+)$	P (23)
1275.3725	1275.37459	$4_1^2 5_0^1 (\Pi_u - \Pi_g)$	P (23,e)
1274.4764	1274.47943	$4_0^1 5_1^2 (\Pi_g - \Pi_u)$	P (19,e)
1274.1521	1274.15632	$4_1^2 5_0^1 (\Pi_u - \Pi_g)$	P (24,f)
1273.8193	1273.81965	$4_0^1 5_1^2 (\Pi_g - \Pi_u)$	P (20,f)
1273.2646	1273.26188	$4_0^1 5_0^1 (\Sigma_u^+ - \Sigma_g^+)$	P (24)
1273.1024	1273.10380	$4_1^2 5_0^1 (\Pi_u - \Pi_g)$	P (24,e)

<sup>a</sup> *e* and *f* indicate the  $\Pi$ -type doubling components of the vibrational states

**Table 6.2:** Assignments of observed  $\text{C}_2\text{H}_2$  absorption lines.

The rest of this chapter illustrates some of the opportunities afforded by this new, sensitive, non-intrusive, optical diagnostic method. The rapid sweep facility enables essentially simultaneous monitoring of the dominant hydrocarbons ( $\text{CH}_4$  and  $\text{C}_2\text{H}_2$ ) in these activated gas mixtures as a function of process conditions (source gas, gas mixing ratios, chamber pressure, applied MW power, etc.) and can provide insight into the time-dependence of interconversion between  $\text{CH}_4$  and  $\text{C}_2\text{H}_2$ .

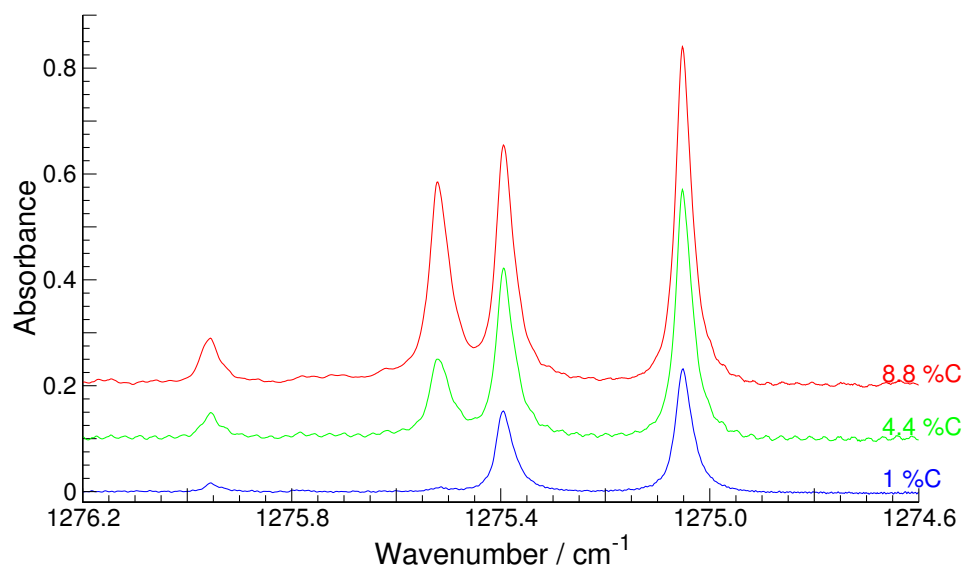
However, the line-of-sight nature of the experiment returns absorbances of the various target species in the particular quantum states probed. Inverting such measurements into (non-quantum state resolved) column densities of a chosen target molecule, or position dependent species number densities, requires detailed knowledge of the gas composition and the temperature distribution along the viewing column. Without detailed modelling of the local gas-phase chemistry, (the flow fields, stagnation volumes, etc.) within the present reactor, the very evident differences between the spectra recorded with the same input carbon mole fraction but

different hydrocarbon process gases (Figure 6.2) do not necessarily contradict the view that the gas phase composition immediately adjacent to the growing diamond surface (and the details of ensuing microcrystalline diamond film growth) depends only on the local C:H ratios, and not the specific chemical identities of the feedstock gases.

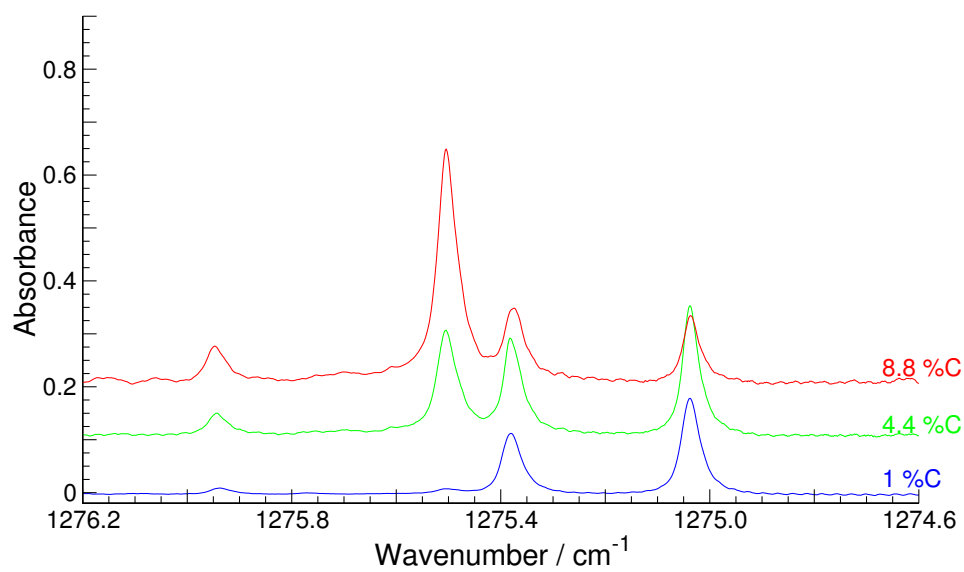
More detailed studies were performed using the smaller wavenumber region between 1276.2 and 1274.6  $\text{cm}^{-1}$ . Figures 6.3(a) & 6.3(b) show absorption spectra measured over this range for three different  $\text{CH}_4 / \text{Ar} / \text{H}_2$  and  $\text{C}_2\text{H}_2 / \text{Ar} / \text{H}_2$  gas mixtures, chosen so as to allow comparison between samples containing input carbon fractions of 1%, 4.4%, and 8.8%. Ar constituted 7% of the total gas flow in each case, with  $\text{H}_2$  making up the balance. The plasma composition was left to equilibrate for at least 5 min after each change in gas mixing ratio prior to recording the various spectra .

The following discussion focuses attention on the relative behaviours of the three spectral lines with wavenumbers of (literature values) 1275.9585  $\text{cm}^{-1}$  (due to vibrationally excited  $\text{C}_2\text{H}_2(\nu_5 = 1)$  molecules ( $\text{C}_2\text{H}_2^\ddagger$ )), 1275.5122  $\text{cm}^{-1}$  (associated with ground ( $\nu = 0$ ) state  $\text{C}_2\text{H}_2$  molecules), and 1275.0417  $\text{cm}^{-1}$  (due to ground-state  $\text{CH}_4$  molecules). The fourth line within the spectral window, centred at  $\sim 1275.38 \text{ cm}^{-1}$ , consists of contributions from overlapping  $\text{CH}_4$  ( $\nu = 0$ ) and  $\text{C}_2\text{H}_2$  ( $\nu_4 = 1$ ) absorptions.

Figures 6.3(c) & 6.3(d) show how the measured absorbances of the selected lines vary as a function of percent C in the input gas mixture, for both  $\text{CH}_4$  and  $\text{C}_2\text{H}_2$  source gases. At low (1%) input carbon fractions, the dominant absorption feature is attributable to  $\text{CH}_4$ , irrespective of the identity of the input hydrocarbon. The absorbance associated with  $\text{C}_2\text{H}_2^\ddagger$  molecules under these conditions is actually greater than that due to ground-state  $\text{C}_2\text{H}_2$  and is insensitive to the choice of hydrocarbon source gas. As percent C increases, however, differences between  $\text{CH}_4$  and  $\text{C}_2\text{H}_2$

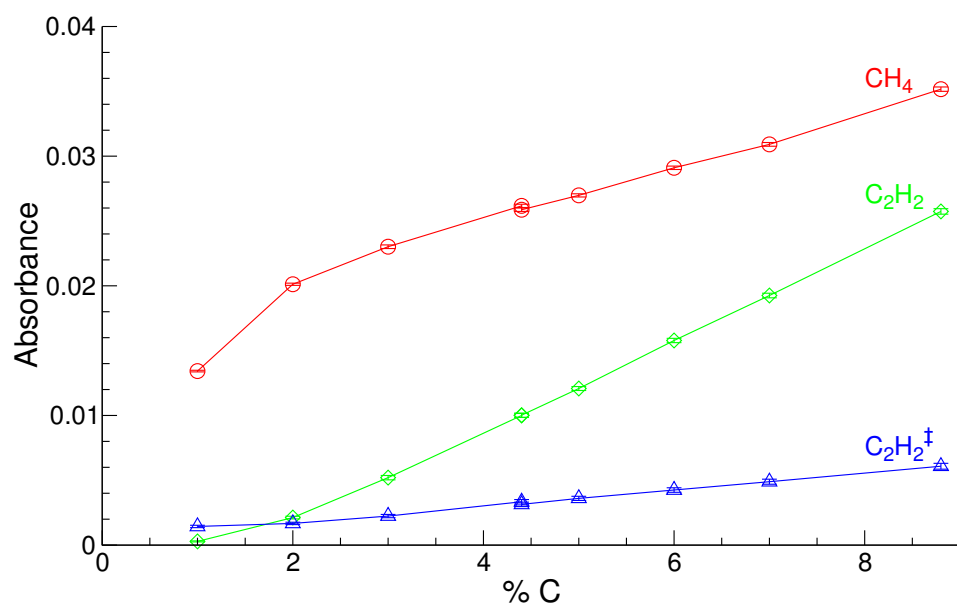


(a)

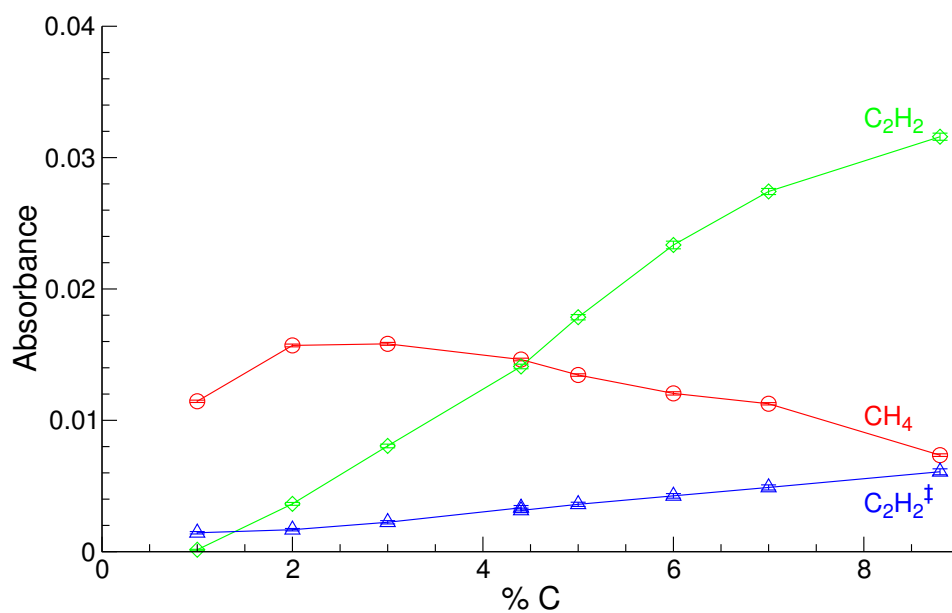


(b)

**Figure 6.3:** Absorption spectra measured over the range 1276.2 – 1274.6  $\text{cm}^{-1}$  for (a)  $\text{CH}_4 / \text{Ar} / \text{H}_2$  and (b)  $\text{C}_2\text{H}_2 / \text{Ar} / \text{H}_2$  gas mixtures containing, respectively, C input fractions of 1%, 4.4%, and 8.8%. The respective spectra have been offset vertically, by 0.1 absorbance unit, for clarity.



(c)



(d)

**Figure 6.3:** continued, Plots c and d show how the absorbances of the  $1275.9585\text{ cm}^{-1}$  (due to  $\text{C}_2\text{H}_2^\dagger$   $\triangle$ ),  $1275.5122$  ( $\text{C}_2\text{H}_2$   $\diamond$ ), and  $1275.0417\text{ cm}^{-1}$  ( $\text{CH}_4$   $\circ$ ) lines vary with percent C in the input gas mixture when using, respectively,  $\text{CH}_4 / \text{Ar} / \text{H}_2$  and  $\text{C}_2\text{H}_2 / \text{Ar} / \text{H}_2$  input gas mixtures.

input gas mixtures become apparent. Absorption due to  $C_2H_2^\ddagger$  increases steadily with percent C in both cases, but much less steeply than does the absorption due to ground-state  $C_2H_2$  molecules. The trend in  $CH_4$  absorption with increasing percent C provides the clearest distinction between the two input gases. With  $CH_4$  as the source gas, the  $CH_4$  absorption rises steadily with increasing percent C (though less steeply than the  $C_2H_2$  absorption), whereas with  $C_2H_2$  as the hydrocarbon source, the  $CH_4$  absorbance maximises at  $\sim 2\%$  input C, and gently declines as percent C is increased further. Conversion of these measured integrated absorbances,  $A$ , into column densities of  $CH_4$  and  $C_2H_2$  is far from straightforward, as the viewing column in the present experiment spans very inhomogeneous distributions of species number densities and gas temperatures.

Chapter 5 has shown from cavity ring down spectroscopy measurements of  $C_2(a)$  radicals that the temperature of the plasma ball is  $\sim 3500$  K, but such measurements are heavily biased toward the centre of the plasma ball where the temperature and the radical concentrations are highest. In contrast, the highest densities of stable molecules such as  $CH_4$  and  $C_2H_2$  will be in the coolest regions of the reactor. The HITRAN database [11] lists temperature-dependent line intensities,  $S(T)$  (in units of  $cm^{-1} / (molecule\ cm^{-2})$ ), for individual rovibrational transitions within both the  $4_0^1$  band of  $CH_4$  and the  $4_0^1 5_0^1$  combination band of  $C_2H_2$ .  $S$  provides a measure of the absorption intensity per molecule of the target species; its  $T$  dependence arises via the Boltzmann factor and the vibrational and rotational partition functions. Given a sample in thermal equilibrium at temperature,  $T$ , the column density of the species of interest can be obtained simply by dividing the measured absorbance by the appropriate  $S(T)$  value. Unfortunately, when the plasma is running, the probed column spans inhomogeneous distributions of species number densities and local gas temperatures and, as Figure 6.4 shows, the  $S$  values for the P(23) line of the  $C_2H_2$   $4_0^1 5_0^1$  band at  $1275.5122\ cm^{-1}$  and for the  $4F_2-5F_1$ , 2 transi-

tion of the  $\text{CH}_4$   $4_0^1$  band at  $1275.0417 \text{ cm}^{-1}$  monitored in this study show markedly different temperature dependences.

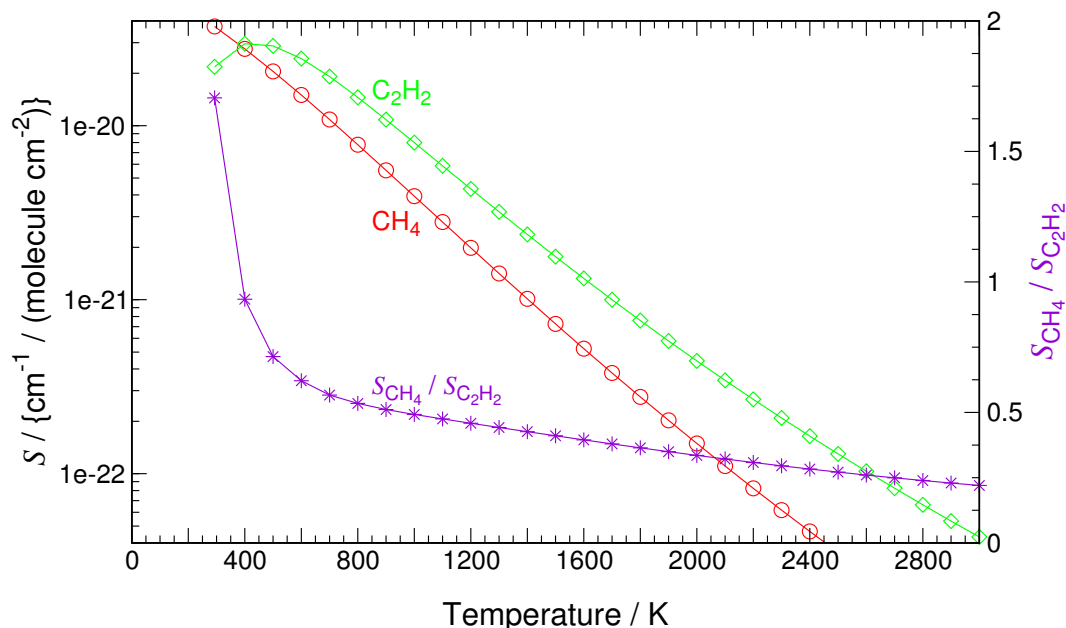


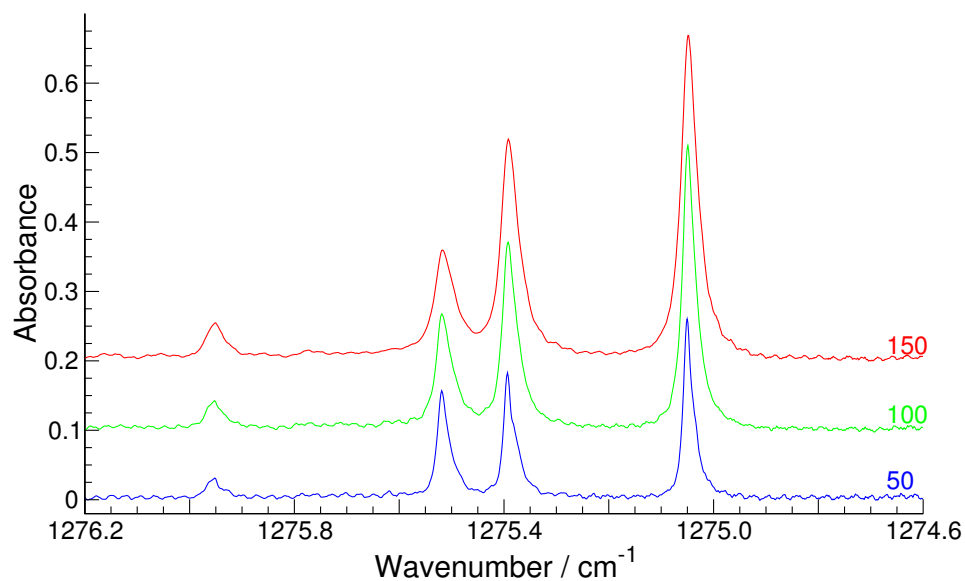
**Figure 6.4:** Semilogarithmic plot showing the temperature dependence of  $S$ , the intensity per molecule in units of  $\text{cm}^{-1} / (\text{molecule cm}^{-2})$  when probing  $\text{C}_2\text{H}_2$  ( $\diamond$ ) via the P (23) line of the  $4_0^1 5_0^1$  band at  $1275.5122 \text{ cm}^{-1}$  and  $\text{CH}_4$  ( $\circ$ ) by the  $4F_2$ - $5F_{1,2}$  transition of the  $4_0^1$  band at  $1275.0417 \text{ cm}^{-1}$  (left-hand axis). Also shown is the ratio of the respective  $S$  (T) values ( $*$ ), plotted on a linear scale (right-hand axis).

$S(\text{CH}_4)$  is  $\sim 1.7 \times$  larger than  $S(\text{C}_2\text{H}_2)$  at room temperature, but is some  $5 \times$  smaller than  $S(\text{C}_2\text{H}_2)$  at the highest gas temperatures relevant to the present reactor. Quantitative conversion of measured absorbances into column densities is thus not possible, and detailed concentration profiling must await comparison with detailed reactor modelling calculations. Figure 6.3(d) shows that  $\text{C}_2\text{H}_2$  is the dominant absorbing species in the probed column within the activated 4.4%  $\text{C}_2\text{H}_2 / 7\% \text{ Ar} / \text{H}_2$  gas mixture. Neglecting non- $\text{C}_2\text{H}_2$  contributions to the total carbon balance, mass dependent thermal diffusion effects, etc., the measured integrated absorbance ( $A \sim 0.031$ ) can be reproduced assuming ideal gas behaviour and a (not implausible) “effective” gas temperature of  $\sim 700 \text{ K}$ . The  $S(\text{CH}_4) / S(\text{C}_2\text{H}_2)$  ratio at this temper-

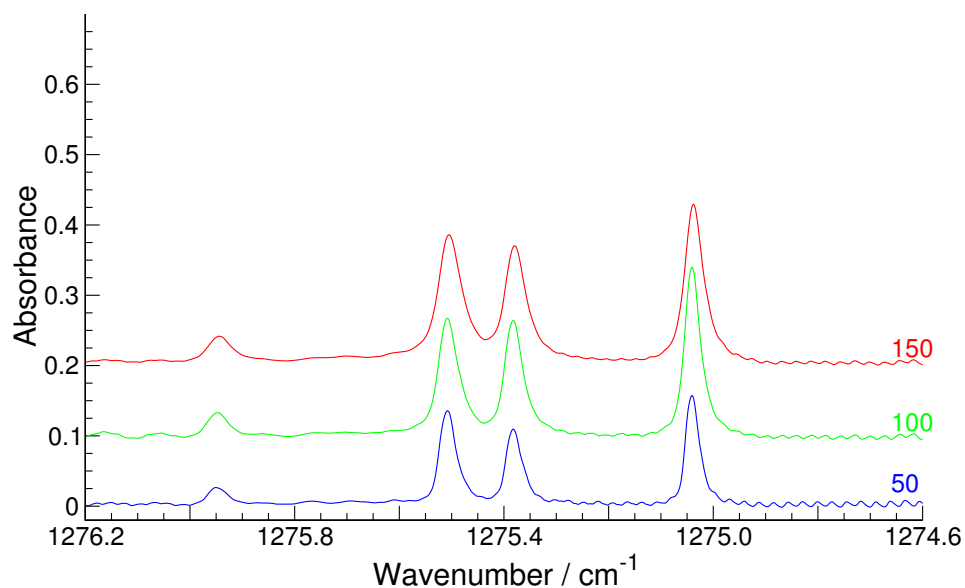
ature is  $\sim 0.57$ . Assuming that the spatial distributions for  $\text{CH}_4$  and  $\text{C}_2\text{H}_2$  along the viewing column are broadly similar, the relative column densities of  $\text{CH}_4$  and  $\text{C}_2\text{H}_2$  can be roughly assessed by doubling the vertical scale for the  $\text{CH}_4$  data in Figure 6.3(c) & 6.3(d). Hence, the  $\text{CH}_4$  column density exceeds that of  $\text{C}_2\text{H}_2$  not just for all  $\text{CH}_4 / \text{Ar} / \text{H}_2$  input gas mixtures investigated here, but also for all  $\text{C}_2\text{H}_2 / \text{Ar} / \text{H}_2$  gas mixtures containing less than  $\sim 6\%$  C (i.e.  $< 3\%$   $\text{C}_2\text{H}_2$ ). At low percent C, the absorbance of the  $\text{C}_2\text{H}_2^\ddagger$  hot band feature at  $1275.9585 \text{ cm}^{-1}$  is consistently larger than that of the  $\text{C}_2\text{H}_2 (\nu = 0)$  feature at  $1275.5122 \text{ cm}^{-1}$ . These transitions both involve excitation of the  $\nu_4 + \nu_5$  combination, and differ only in the identity of the starting level. The respective transition dipole moments are expected to be very similar. The former originates from a slightly lower rotational state ( $J = 19$ ), so its Hönl-London line strength factor will be  $\sim 0.83 \times$  that of the  $1275.5122 \text{ cm}^{-1}$  feature. This is a small difference compared with the difference in the displayed absorbance at low percent C. The most likely location of the vibrationally excited  $\text{C}_2\text{H}_2$  molecules is in the hotter regions of the probed column, but the weakness of the  $\text{C}_2\text{H}_2 (\nu = 0)$  absorption when using 1% C input gas mixtures (see Figure 6.3) can only be accommodated by assuming an inverted (i.e. nonthermal) population distribution over the  $\text{C}_2\text{H}_2$  vibrational states.

Figure 6.5 illustrates the sensitivity of this same spectral region to the total gas pressure,  $p$ . The three spectra displayed in each of panels of Figure 6.5(a) & 6.5(b) were measured using, respectively, equilibrated  $\text{CH}_4 / \text{Ar} / \text{H}_2$  and  $\text{C}_2\text{H}_2 / \text{Ar} / \text{H}_2$  gas mixtures that both contained 4.4% input fraction C, 7% Ar with the balance  $\text{H}_2$ , and  $P = 50, 100, \text{ and } 150 \text{ Torr}$ .

The absorption features are described well by Lorentzian line shapes and Figure 6.6(a) shows an example fit to experimental data. The suitability of the Lorentzian fitting is understandable given the relative magnitudes of the instrumental, Doppler, and pressure broadening contributions to the total line shape under the prevailing



(a)



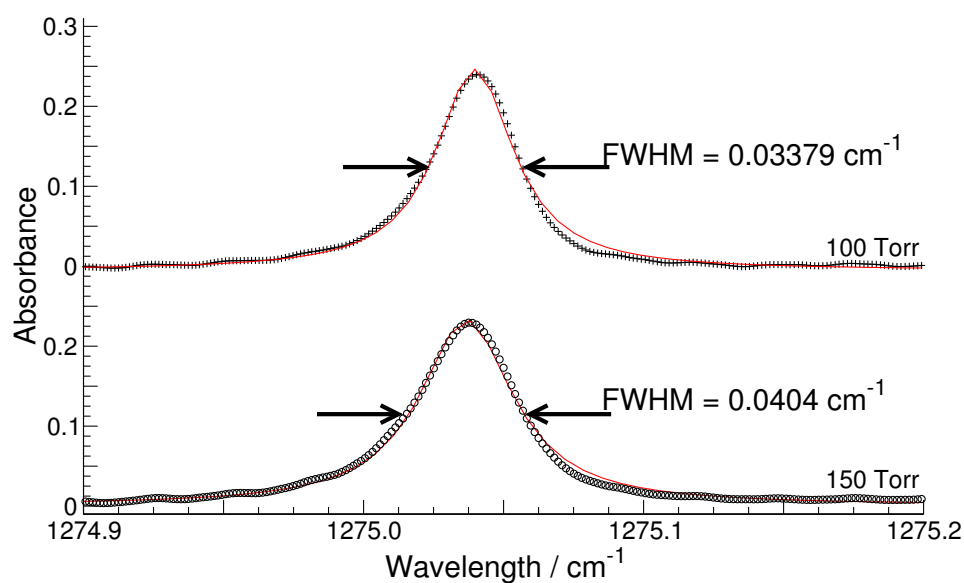
(b)

**Figure 6.5:** Absorption spectra measured over the range 1276.2-1274.6  $\text{cm}^{-1}$  for (a)  $\text{CH}_4 / \text{Ar} / \text{H}_2$  and (b)  $\text{C}_2\text{H}_2 / \text{Ar} / \text{H}_2$  gas mixtures containing 4.4% C input fractions at total gas pressures of 50, 100, and 150 Torr (as indicated at the right-hand end of each spectrum). The respective spectra have each been offset vertically by 0.1 absorbance unit for ease of display.

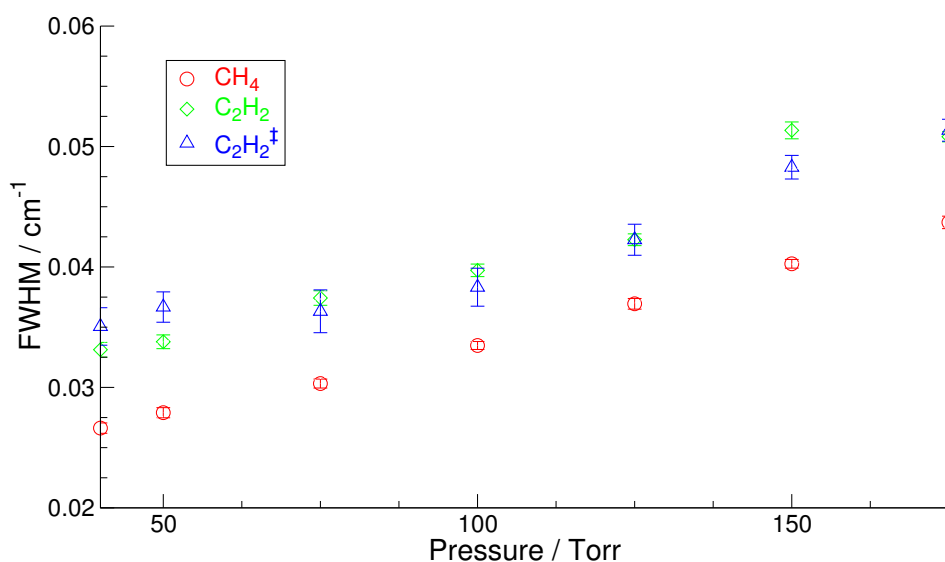
experimental conditions. The intrinsic bandwidth of the QC laser is of the order of 100 kHz, but the instrumental resolution is limited by the rate of change of the device temperature (and thus output frequency), ranging from  $\sim 0.008$  to  $\sim 0.004$   $\text{cm}^{-1}$  (fwhm) during the  $2 \mu\text{s}$  current pulse. Estimating the Doppler broadening contribution requires an “effective” value for the gas temperature,  $T_{\text{gas}}$ , which is the assumed  $T_{\text{gas}} = 700$  K.

Doppler broadening should thus give a (Gaussian) contribution to the width of a  $\text{CH}_4$  line at  $\sim 1275$   $\text{cm}^{-1}$  of  $\sim 0.006$   $\text{cm}^{-1}$  (fwhm). The corresponding contribution to a  $\text{C}_2\text{H}_2$  line would be  $\sim 0.005$   $\text{cm}^{-1}$  (fwhm). Doppler and instrumental contributions are thus both small compared with the measured line widths of the  $\text{CH}_4$  and  $\text{C}_2\text{H}_2$  transitions, all of which increase with  $p$  as shown in Figure 6.6(b). Pressure broadening coefficients,  $\gamma$ , derived from such data are of limited value given the ( $p$  dependent) variation in species (and total) number densities, and temperature, along the viewing column, but the gradient of the line width versus  $p$  plot for the  $\text{CH}_4$  line, for example, equates to  $\gamma \sim 3.9$  MHz / Torr. The collision frequencies at the pressures used in the present experiments are sufficiently high to obviate line shape complications due to effects of rapid adiabatic passage, such as have been observed when using a frequency chirped QC laser to probe much lower pressure gas samples [7].

Figures 6.7(a) & 6.7(b) show the pressure dependent absorbances due to the  $\text{C}_2\text{H}_2^\ddagger$ ,  $\text{C}_2\text{H}_2$ , and  $\text{CH}_4$  features of interest. The total carbon content in these gas mixtures increases 3-fold as  $p$  is raised from 50 and 150 Torr. This increase is roughly mirrored by the  $\text{CH}_4$  and  $\text{C}_2\text{H}_2^\ddagger$  absorbances measured when using  $\text{CH}_4$  as the input hydrocarbon, but the absorption associated with ground-state  $\text{C}_2\text{H}_2$  molecules increases less steeply. Different behaviour is observed with  $\text{C}_2\text{H}_2$  as the source hydrocarbon. In this scenario, the  $\text{C}_2\text{H}_2$  and  $\text{C}_2\text{H}_2^\ddagger$  absorbances increase with  $p$ , while the  $\text{CH}_4$  absorption appears to plateau at  $p \sim 100$  Torr. The detailed

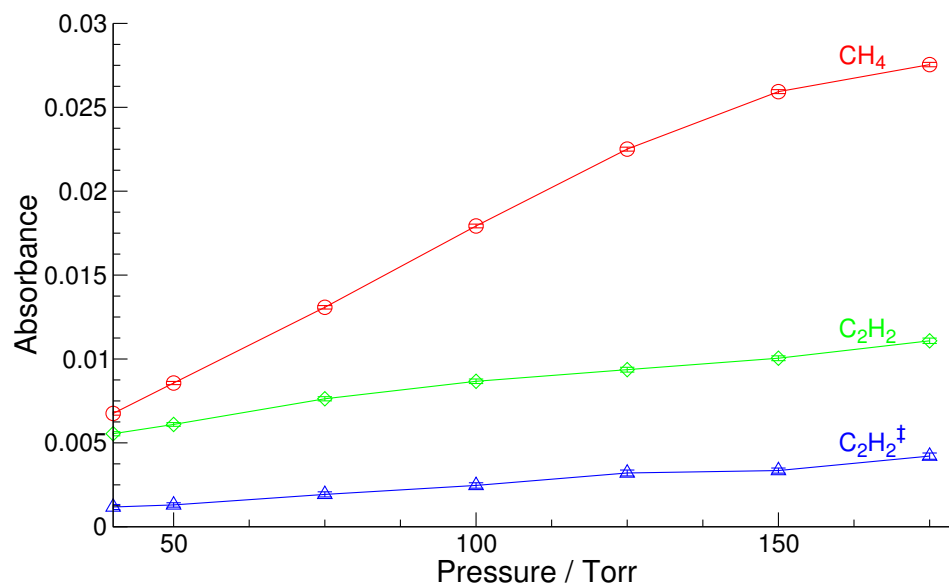


(a)

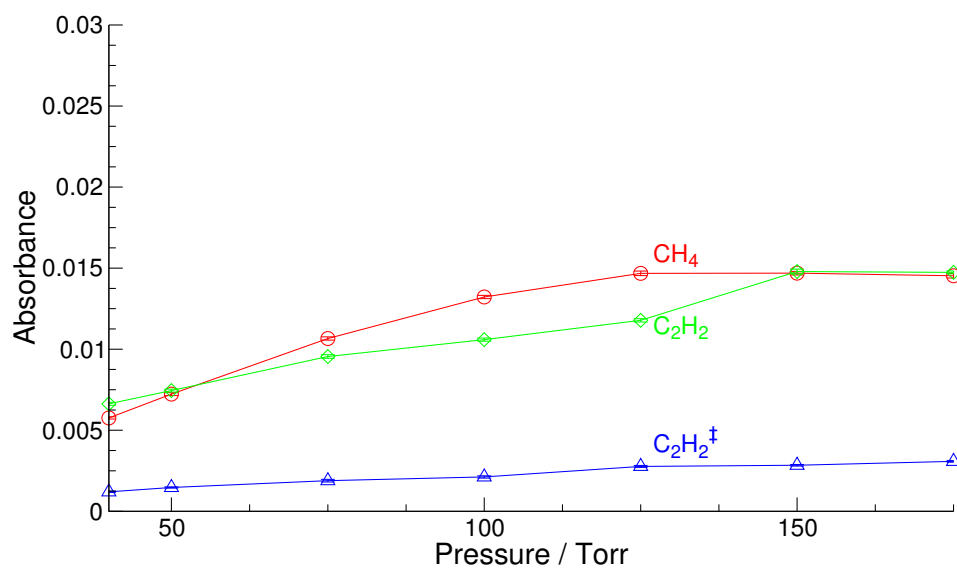


(b)

**Figure 6.6:** (a) Example spectra demonstrating the quality of the Lorentzian fits to the  $1275.0417 \text{ cm}^{-1}$  ( $\text{CH}_4$ ) line shapes measured using the 2.2%  $\text{C}_2\text{H}_2 / \text{Ar} / \text{H}_2$  gas mixture at  $p = 100$  and  $150$  Torr. (b) The pressure dependence of the full width half-maximum (fwhm) values obtained by fitting the  $1275.9585$  ( $\text{C}_2\text{H}_2^\ddagger$   $\triangle$ ),  $1275.5122$  ( $\text{C}_2\text{H}_2$   $\diamond$ ), and  $1275.0417 \text{ cm}^{-1}$  ( $\text{CH}_4$   $\circ$ ) line shapes in spectra obtained using the same mixing ratio as in Figure 6.6(a).



(a)



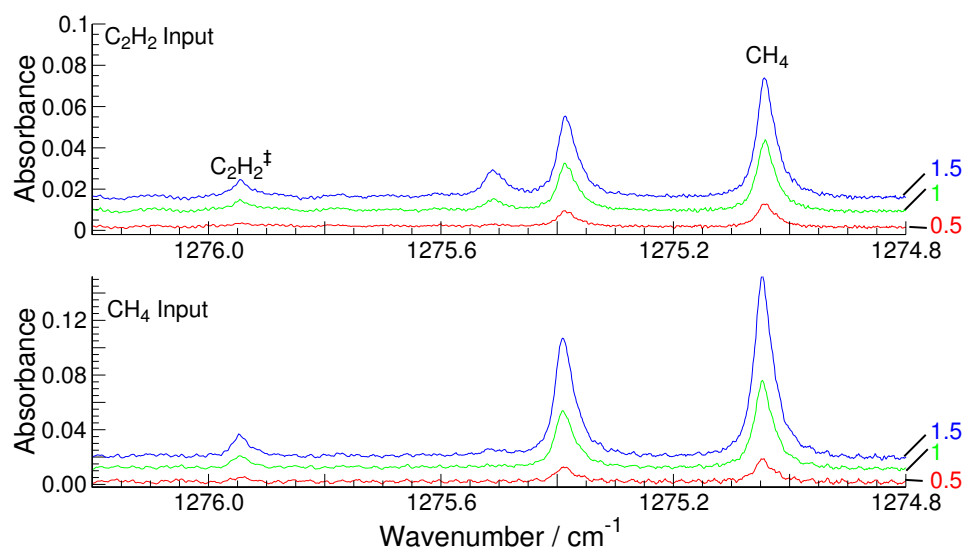
(b)

**Figure 6.7:** Plots showing the p dependence of the respective  $C_2H_2^\ddagger$ ,  $C_2H_2$ , and  $CH_4$  absorbances when using (a) 4.4%  $CH_4$  / Ar /  $H_2$  and (b) 2.2%  $C_2H_2$  / Ar /  $H_2$  input gas mixtures.

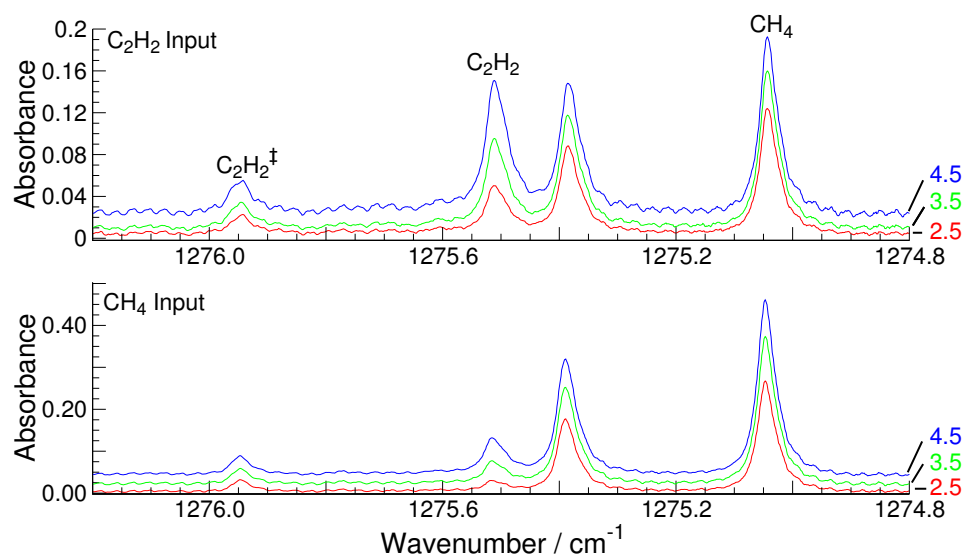
discussion of these observations, and their conversion to column densities, must await more detailed modelling of the temperature and species number density distributions within this reactor.

The rapid spectral acquisition rate achievable with a frequency chirped QC laser has also allowed investigation of the way the column density approaches equilibrium after introduction (or cessation) of the hydrocarbon flow into a pre-established 7% Ar in H<sub>2</sub> plasma. Illustrative data following introduction of 4.4% C<sub>2</sub>H<sub>2</sub> (upper traces) and 8.8% CH<sub>4</sub> (lower traces) are given in each of the three panels displayed in Figure 6.8. The number appearing at the right-hand end of each trace indicates the time, *t* (in seconds), at which the spectrum was recorded following introduction of the hydrocarbon flow into the premixing manifold (at *t* = 0). Detailed interpretation of these observations will also require more thorough modelling and understanding of the reactor flow fields and the distributions of species population and temperature along the probed column than is currently available but a number of striking and hitherto unreported trends are immediately apparent.

No CH<sub>4</sub> or C<sub>2</sub>H<sub>2</sub> signals are observed at *t* < 0, even when the substrate is covered by a pre-grown CVD diamond film, implying that etching processes make negligible contribution to the present absorption measurements and that these are sensitive solely to gas-phase chemistry. Even at the earliest time after opening the hydrocarbon MFC (*t* < 0.5 s), carbon has reached the probed column but the dominant absorptions are those of CH<sub>4</sub>, even when C<sub>2</sub>H<sub>2</sub> is used as the source gas. Additionally, the absorption due to C<sub>2</sub>H<sub>2</sub><sup>‡</sup> is greater than that from ground-state C<sub>2</sub>H<sub>2</sub>. These trends are very reminiscent of those observed under equilibrium conditions, when using dilute (e.g. 1% C content) gas mixtures, Figure 6.3. With C<sub>2</sub>H<sub>2</sub> as source gas, the absorption due to ground-state C<sub>2</sub>H<sub>2</sub> molecules has overtaken that due to C<sub>2</sub>H<sub>2</sub><sup>‡</sup> by *t* = 1.5 s; when using CH<sub>4</sub>, ~3.5 s are required to achieve a C<sub>2</sub>H<sub>2</sub> absorption greater than that from C<sub>2</sub>H<sub>2</sub><sup>‡</sup>.



(a)



(b)

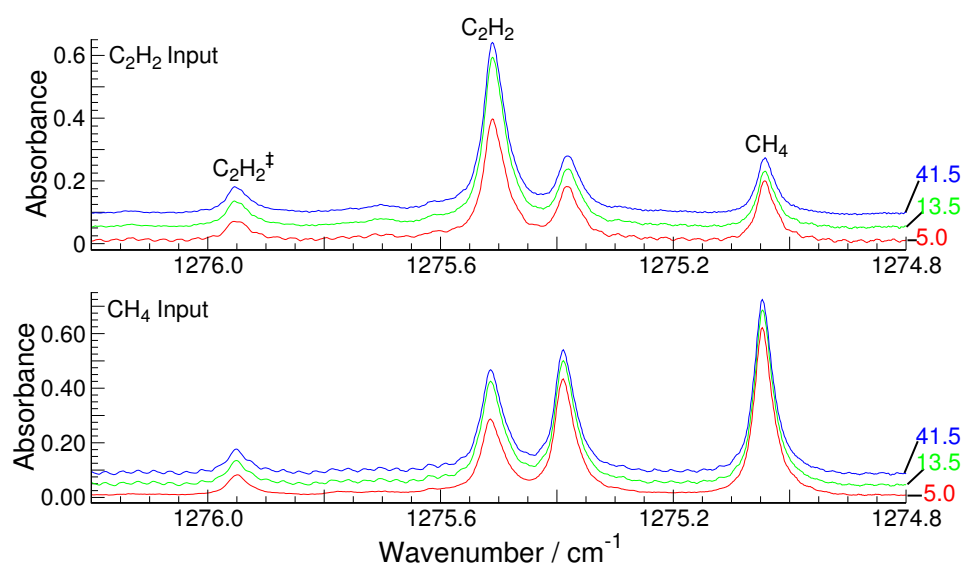
**Figure 6.8:** Absorption spectra measured over the range 1276.2-1274.6  $\text{cm}^{-1}$ , as a function of time (in s, indicated at the right-hand end of each trace) following addition of 4.4%  $\text{C}_2\text{H}_2$  (upper traces in each panel) and 8.8%  $\text{CH}_4$  (lower traces) to a pre-established Ar /  $\text{H}_2$  plasma. Spectra shown in panels a, b, and c (on the following page) were recorded at progressively later times after the instant of hydrocarbon addition to the mixing manifold, and the spectra displayed in any one panel have been coloured and offset vertically for display purposes.

Thereafter, in both cases, the  $\text{CH}_4$  and  $\text{C}_2\text{H}_2^\ddagger$  absorptions both reach their steady-state values faster than does the  $\text{C}_2\text{H}_2$  absorption. When  $\text{CH}_4$  is used as the source gas, the  $\text{CH}_4$  absorption barely increases after  $t = 5$  s. In both cases, the various line intensities in the spectra recorded at  $t = 41.5$  s are in quantitative accord with those shown in Figure 6.3. This validates the earlier assumption that equilibrium conditions are reached well within 5 minutes of any change in gas mixing ratio.

These trends are summarised in Figure 6.9, which shows the measured  $t$  dependent rise in  $\text{CH}_4$ ,  $\text{C}_2\text{H}_2$ , and  $\text{C}_2\text{H}_2^\ddagger$  absorbances when 8.8%  $\text{CH}_4$  is introduced to a pre-established 7% Ar in  $\text{H}_2$  plasma, and the subsequent fall in these signals from their equilibrium values when the hydrocarbon feed is cut (at  $t = 70$  s). The  $\text{CH}_4$  and  $\text{C}_2\text{H}_2^\ddagger$  absorptions are seen to exhibit a qualitatively different time response to the change in hydrocarbon feed than does the  $\text{C}_2\text{H}_2$  signal.

## 6.4 Discussion

This study provides the first illustration of the use of pulsed QC lasers for in situ probing of the gas-phase chemistry prevailing in a 2 kW MW plasma enhanced reactor during diamond CVD. Specifically, both  $\text{CH}_4$  and  $\text{C}_2\text{H}_2$  molecules, and their interconversion, have been monitored as a function of process conditions (e.g., choice of input hydrocarbon ( $\text{CH}_4$  or  $\text{C}_2\text{H}_2$ ), hydrocarbon mole fraction, total gas pressure, and applied MW power). The measured quantities are line-of-sight absorbances and, as pointed out previously, the conversion of such measurements into absolute column densities is hampered by the inhomogeneous species number density and temperature distributions along the viewing column. The absolute sensitivity achieved in these preliminary investigations could be much improved, by multipassing the probe beam and by more careful design and mounting of the windows (so as to obviate etaloning effects). Vertical profiling of the plasma ball will



(c)

**Figure 6.8:** continued

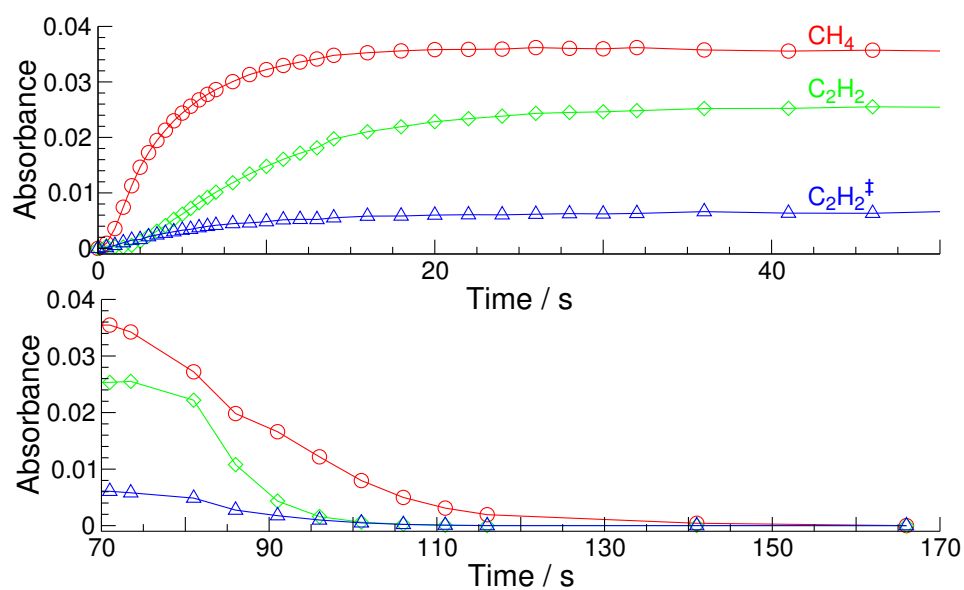


**Figure 6.9:** Plot showing variation of  $\text{CH}_4$  ( $\circ$ ),  $\text{C}_2\text{H}_2$  ( $\diamond$ ), and  $\text{C}_2\text{H}_2^{\ddagger}$  ( $\triangle$ ) absorbances with time after the introduction (at  $t = 0$  s) of 8.8%  $\text{CH}_4$  to a pre-established 7% Ar in  $\text{H}_2$  plasma and, below, the subsequent fall in these signals from their equilibrium values when the hydrocarbon feed is cut (at  $t = 70$  s).

be trivial to implement.

Key new findings from these preliminary studies are the very obvious preference for C to be present as CH<sub>4</sub> in the more dilute hydrocarbon gas mixtures, irrespective of the hydrocarbon source gas, the inverted C<sub>2</sub>H<sub>2</sub> vibrational state population distribution when using low C fractions, and the progressive switch toward C<sub>2</sub>H<sub>2</sub> as the input C fraction increases.

These trends are all understandable, qualitatively, within the framework of existing models of the gas-phase chemistry prevailing in activated hydrocarbon / H<sub>2</sub> mixtures under conditions appropriate for diamond CVD. As shown previously, interconversion between CH<sub>4</sub> and C<sub>2</sub>H<sub>2</sub> involves a multistep reaction sequence, the overall rate (and even the sign) of which is sensitively dependent upon the local hydrocarbon and H atom number densities, and the local gas temperature all of which are reactor and process specific. Of particular relevance to the present observations was the finding that C<sub>2</sub>H<sub>2</sub> → CH<sub>4</sub> conversion can be driven by a sequence of (third body stabilised) H atom addition reactions at low (< 1000 K) gas temperatures [1], [2]. High H atom concentrations, and such comparatively low gas temperatures, are precisely the conditions that will be encountered at the top of the reactor when C<sub>2</sub>H<sub>2</sub> is first introduced into a pre-existing Ar / H<sub>2</sub> plasma (Figure 6.5(a)). Similar trends were observed under steady-state conditions when using low input flow rates of C<sub>2</sub>H<sub>2</sub> (Figure 6.3(b)). This can be understood also by recognising that similar C<sub>2</sub>H<sub>2</sub> → CH<sub>4</sub> conversions will occur in regions distant from the plasma ball (e.g. at both ends of the viewing column) where, because the gas is cooler, most of the total number density will be concentrated.

Increasing the hydrocarbon input will increase the rates of reactions (6.1) and (6.2), and thus lead to a reduction in the H atom concentrations throughout the reactor. This, and the associated increase in CH<sub>y</sub> radical concentrations, will both serve to shift the equilibrium back in favour of C<sub>2</sub>H<sub>2</sub>, as observed. The dominant show-

ing of the respective source gases in spectra recorded at high (8.8%) C input ratios (Figure 6.3(c)) is most readily understandable by assuming that, in these cases, the hydrocarbon / H atom ratios are becoming large enough that a significant fraction of the input hydrocarbon flow escapes processing on route to the viewing column.

The observed trends in  $C_2H_2^\ddagger$  can be ascribed to the  $CH_4 \longrightarrow C_2H_x$  interconversion which occurs via the H-shifting reactions (6.1) and (6.2).  $C_2H_2$  ( $x = 2$ ) is the more stable species at high T, so this interconversion will occur preferentially in the hottest regions of the reactor. However, the  $C_2H_2^\ddagger$  and  $C_2H_2$  ( $\nu = 0$ ) absorbances should be fairly reliable indicators of their respective column densities as shown. The  $C_2H_2^\ddagger$  column density actually exceeds that of  $C_2H_2$  ( $\nu = 0$ ) in dilute hydrocarbon /  $H_2$  mixtures.

There are plenty of possible reasons for this deduced population inversion. The last step in the kinetic scheme driving  $CH_4 \longrightarrow C_2H_2$  in hot regions of the reactor involves the conversion  $C_2H_3 + H \rightleftharpoons C_2H_2 + H_2$ . This reaction is fast and exothermic by  $\sim 290 \text{ kJ mol}^{-1}$  [14]. The present measurements suggest that at least some of this reaction exoergicity is channelled into vibrational excitation of the nascent  $C_2H_2$  products and probably into many excited vibrational levels additional to the  $\nu_5=1$  level probed in this work. That being so, diagnostic methods that sample just  $C_2H_2$  ( $\nu = 0$ ) molecules may yield serious underestimates of the total  $C_2H_2$  column (or number) density in situations where the rate of  $C_2H_2$  production via reaction (6.2) significantly exceeds the vibrational relaxation (and thermal equilibration) rates of the resulting  $C_2H_2^\ddagger$  species.

Quantitative analysis of these measurements is beyond the scope of this thesis but it is intended that analysis of this and related future datasets will proceed in tandem with detailed modelling of the plasma chemical transformations and heat and mass transfer processes within these MW activated gas mixtures as in our recent combined experimental and modelling studies of a diamond depositing DC arc jet

reactor operating with CH<sub>4</sub> / Ar / H<sub>2</sub> gas mixtures [15], [16].

## 6.5 Conclusions

The use of a quantum cascade laser has offered a unique spectral window through which the chemistry of the interconversion between C<sub>2</sub>H<sub>2</sub> and CH<sub>4</sub> species within a CVD diamond growing reactor can be observed as a function of process conditions. Column densities of vibrationally excited C<sub>2</sub>H<sub>2</sub> ( $\nu_5 = 1$ ) molecules at low input carbon fractions are shown to be far higher than expected on the basis of local thermodynamic equilibrium. The observed trends can be rationalised, qualitatively, within the framework of the previously reported modelling of the gas-phase chemistry prevailing in hot filament activated hydrocarbon/H<sub>2</sub> gas mixtures [1]. The presence of vibrationally excited C<sub>2</sub>H<sub>2</sub> molecules (C<sub>2</sub>H<sub>2</sub><sup>‡</sup>) can be attributed to the exothermicity of the C<sub>2</sub>H<sub>3</sub> + H  $\rightleftharpoons$  C<sub>2</sub>H<sub>2</sub> + H<sub>2</sub> elementary reaction within the overall multistep CH<sub>4</sub>  $\rightarrow$  C<sub>2</sub>H<sub>2</sub> conversion. Diagnostic methods that sample just C<sub>2</sub>H<sub>2</sub> ( $\nu = 0$ ) molecules thus run the risk of underestimating total C<sub>2</sub>H<sub>2</sub> column densities in hydrocarbon / H<sub>2</sub> mixtures operated under conditions where the production rate of C<sub>2</sub>H<sub>2</sub><sup>‡</sup> molecules exceeds their vibrational relaxation (and thermal equilibration) rates.

## Bibliography

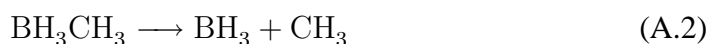
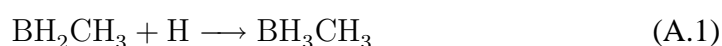
- [1] M. N. R. Ashfold, P. W. May, J. R. Petherbridge, K. N. Rosser, J. A. Smith, Yu. A. Mankelevich, and N. V. Suetin, *Phys. Chem. Chem. Phys.* **3**, 3471 (2001).
- [2] Yu. A. Mankelevich, N. V. Suetin, M. N. R. Ashfold, J. A. Smith, and E. Cameron, *Diamond Relat. Mater.* **10**, 364 (2001).
- [3] P. K. Bachmann, D. Leers, and H. Lydtin, *Diamond Relat. Mater.* **1**, 1 (1991).
- [4] J. A. Smith, E. Cameron, M. N. R. Ashfold, Yu. A. Mankelevich, and N. V. Suetin, *Diamond Relat. Mater.* **10**, 358 (2001).
- [5] R. F. Kazarinov and R. A. Suris, *Sov. Phys. Semicond.* **5**, 707 (1971).
- [6] J. Faist, F. Capasso, D. L. Sivco, C. Sirtori, A. L. Hutchinson, and A. Y. Cho, *Science* **264**, 553 (1994).
- [7] G. Duxbury, N. Langford, M. T. McCulloch, and S. Wright, *Chem. Soc. Rev.* **34**, 1 (2005).
- [8] M. T. McCulloch, E. L. Normand, N. Langford, G. Duxbury, and D. A. Newnham, *J. Opt. Soc. Am. A* **20**, 1761 (2003).
- [9] M. T. McCulloch, N. Langford, and G. Duxbury, *Appl. Opt.* **44**, 2887 (2005).
- [10] Cascade Technologies Ltd, 141 St James Road, Glasgow G4 0LT.
- [11] HITRAN 2000., L. S. Rothman, A. Barbe, D. C. Benner, L. R. Brown, C. Camy-Peyret, M. R. Carleer, K. Chance, C. Clerbaux, V. Dana, V. M. Devi, A. Fayt, J.-M. Flaud, R. R. Gamache, A. Goldman, D. Jacquemart, K. W. Jucks, W. J. Lafferty, J.-Y. Mandin, S. T. Massie, V. Nemtchinov, D. A. Newnham, A. Perrin, C. P. Rinsland, J. Schroeder, K. M. Smith, M. A. H. Smith, K. Tang, R. A. Toth, J. Vander Auwera, P. Varanasi, and K. Yoshino, *J. Quant. Spectrosc. Radiat. Transfer* **82**, 5 (2003).
- [12] Y. Kabbadi, M. Herman, G. di Lonardo, L. Fusina, and J. W. C. Johns, *J. Mol. Spectrosc.* **150**, 535 (1991).
- [13] M. T. McCulloch, S. Wright, N. Langford, and G. Duxbury, Unpublished work.
- [14] D. L. Baulch, C. J. Cobos, R. A. Cox, C. Esser, P. Frank, T. Just, J. A. Kerr, M. J. Pilling, J. Troe, R. W. Walker, and J. Warnatz, *J. Phys. Chem. Ref. Data* **21**, 411 (1992).
- [15] C. J. Rennick, A. G. Smith, J. A. Smith, J. B. Wills, A. J. Orr-Ewing, M. N. R. Ashfold, Yu. A. Mankelevich, and N. V. Suetin, *Diamond Relat. Mater.* **13**, 561 (2004).

- [16] C. J. Rennick, R. Engeln, J. A. Smith, A. J. Orr-Ewing, M. N. R. Ashfold, and Yu. A. Mankelevich, *J. Appl. Phys* **97**, 113306 (2005).

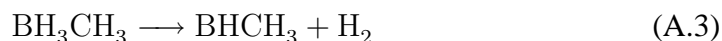
# Appendix A

## Coupled cluster calculation of boron-carbon bond fission reaction

Chapter 3 has shown that a possible pathway for the loss of  $\text{BH}_3$  from the diamond surface involves boron-carbon bond fission reactions. To ensure that the DFT level of theory chosen can adequately describe the energetics of this process, a small system has been studied using coupled cluster theory. These investigations into the nature of the boron-carbon bond fission were required as there were no suitable experimental or theoretical studies for comparison at the time of writing. The boron-carbon bond fission reactions occurring upon a diamond surface can be modelled by the decomposition of the  $\text{BH}_2\text{CH}_3$  molecule mediated by the addition of atomic hydrogen (A.1) (A.2).



The decomposition of  $\text{BH}_3\text{CH}_3$  by elimination of molecular hydrogen dissociation (akin to reactions (2.5)) has also been modelled (A.3).



The potential energy surface minima were calculated using the standard B3LYP functional with the 6-31G\* basis set. Single point calculations using DFT and the coupled cluster theory were calculated using the 6-31G\* geometries and performed

using the GAUSSIAN 03 program package[1] and MOLPRO program package [2] respectively.

Reaction	B3LYP		CCSD(T)		
	6-31G*	6-311+G(2df,p)	cc-PVDZ	cc-PVTZ	cc-pVQZ
<b>A.1</b>	-43.35	-40.27	-40.67	-43.94	-43.36
<b>A.2</b>	31.95	24.36	48.32	58.38	59.5
<b>A.3</b>	106.76	92.53	161.37	144.56	142.28

**Table A.1:** Summary of the coupled cluster energetics calculations, in kJ mol<sup>-1</sup>

The results in Table **A.1** show that the DFT level of theory overpredicts the strength of the boron-carbon bond whilst underestimating the energetics of the boron-hydrogen bonds. However, the maximum discrepancy is less than 50 kJ mol<sup>-1</sup> and acceptable.

## Appendix B

# Optimised structures for DFT cluster models for the incorporation of $\text{CH}_3$ and $\text{BH}_x$ into a diamond surface

Chapter 3 discusses the mechanisms by which gaseous  $\text{CH}_3$  and  $\text{BH}_x$  can be incorporated into the diamond surface. This chapter records the optimised geometries for the key structures involved in these processes as bond lengths and bond angles within each cluster. Figures B.1 – B.2 and corresponding tables show the geometries of the cluster model for the surface hydrogen abstraction reaction; Figures B.3 – B.7 are the related structures for the mechanism for incorporating  $\text{CH}_3$  into the  $\{100\}$  diamond surface; Figures B.8 – B.11 are the structures for surface bound  $\text{BH}_x$  species and Figures B.12 – B.15 show the structures for incorporated  $\text{BH}_x$  species.

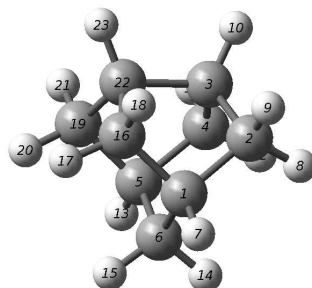


**Figure B.1:** The optimised geometry for structure A in Figure 3.2

Bond	Bond length / Å	Bond Angle	°	Bond Angle (cont)	°
R(1,2)	1.540	A(2,1,6)	109.782	A(6,5,13)	110.419
R(1,6)	1.554	A(2,1,7)	113.486	A(6,5,19)	109.782
R(1,7)	1.097	A(2,1,16)	99.392	A(13,5,19)	113.486
R(1,16)	1.540	A(6,1,7)	110.419	A(1,6,5)	112.005
R(2,3)	1.549	A(6,1,16)	109.782	A(1,6,14)	109.510
R(2,8)	1.096	A(7,1,16)	113.486	A(1,6,15)	109.510
R(2,9)	1.098	A(1,2,3)	100.755	A(5,6,14)	109.510
R(3,4)	1.549	A(1,2,8)	113.968	A(5,6,15)	109.510
R(3,10)	1.094	A(1,2,9)	110.226	A(14,6,15)	106.648
R(3,22)	1.594	A(3,2,8)	112.301	A(1,16,17)	113.968
R(4,5)	1.540	A(3,2,9)	112.008	A(1,16,18)	110.226
R(4,11)	1.098	A(8,2,9)	107.581	A(1,16,22)	100.755
R(4,12)	1.096	A(2,3,4)	107.074	A(17,16,18)	107.581
R(5,6)	1.554	A(2,3,10)	113.446	A(17,16,22)	112.301
R(5,13)	1.097	A(2,3,22)	104.109	A(18,16,22)	112.008
R(5,19)	1.540	A(4,3,10)	113.446	A(5,19,20)	113.968
R(6,14)	1.099	A(4,3,22)	104.109	A(5,19,21)	110.226
R(6,15)	1.099	A(10,3,22)	113.756	A(5,19,22)	100.755
R(16,17)	1.096	A(3,4,5)	100.755	A(20,19,21)	107.581
R(16,18)	1.098	A(3,4,11)	112.008	A(20,19,22)	112.301
R(16,22)	1.549	A(3,4,12)	112.301	A(21,19,22)	112.008
R(19,20)	1.096	A(5,4,11)	110.226	A(3,22,16)	104.109
R(19,21)	1.098	A(5,4,12)	113.968	A(3,22,19)	104.109
R(19,22)	1.549	A(11,4,12)	107.581	A(3,22,23)	113.756
R(22,23)	1.094	A(4,5,6)	109.782	A(16,22,19)	107.074
		A(4,5,13)	113.486	A(16,22,23)	113.446
		A(4,5,19)	99.392	A(19,22,23)	113.446

**Table B.1:** Bond lengths and angles for Figure B.1

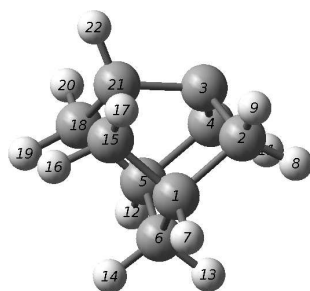


**Figure B.2:** The optimised geometry for structure B in Figure 3.2

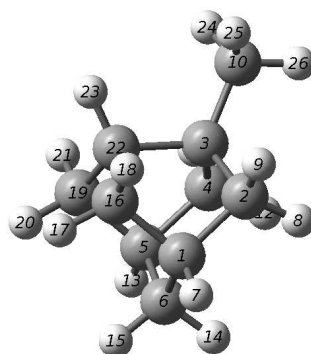


**Figure B.3:** The optimised geometry for structure C in Figure 3.2

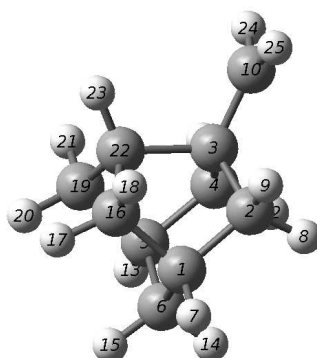


**Figure B.4:** The optimised geometry for structure D in Figure 3.2

Bond	Bond length / Å	Bond Angle	°	Bond Angle (cont)	°
R(1,2)	1.557	A(2,1,6)	109.384	A(6,5,12)	110.659
R(1,6)	1.558	A(2,1,7)	113.452	A(6,5,18)	109.775
R(1,7)	1.097	A(2,1,15)	99.290	A(12,5,18)	113.728
R(1,15)	1.543	A(6,1,7)	110.659	A(1,6,5)	112.415
R(2,3)	1.515	A(6,1,15)	109.775	A(1,6,13)	109.507
R(2,8)	1.095	A(7,1,15)	113.728	A(1,6,14)	109.316
R(2,9)	1.099	A(1,2,3)	97.893	A(5,6,13)	109.507
R(3,4)	1.515	A(1,2,8)	114.041	A(5,6,14)	109.316
R(3,21)	1.562	A(1,2,9)	109.753	A(13,6,14)	106.611
R(4,5)	1.557	A(3,2,8)	113.055	A(1,15,16)	113.945
R(4,10)	1.099	A(3,2,9)	113.839	A(1,15,17)	110.274
R(4,11)	1.095	A(8,2,9)	108.102	A(1,15,21)	100.450
R(5,6)	1.558	A(2,3,4)	110.956	A(16,15,17)	107.663
R(5,12)	1.097	A(2,3,21)	107.263	A(16,15,21)	112.445
R(5,18)	1.543	A(4,3,21)	107.263	A(17,15,21)	112.046
R(6,13)	1.099	A(3,4,5)	97.893	A(5,18,19)	113.945
R(6,14)	1.099	A(3,4,10)	113.839	A(5,18,20)	110.274
R(15,16)	1.096	A(3,4,11)	113.055	A(5,18,21)	100.450
R(15,17)	1.097	A(5,4,10)	109.753	A(19,18,20)	107.663
R(15,21)	1.552	A(5,4,11)	114.041	A(19,18,21)	112.445
R(18,19)	1.096	A(10,4,11)	108.102	A(20,18,21)	112.046
R(18,20)	1.097	A(4,5,6)	109.384	A(3,21,15)	102.932
R(18,21)	1.552	A(4,5,12)	113.452	A(3,21,18)	102.932
R(21,22)	1.095	A(4,5,18)	99.290	A(3,21,22)	115.268
				A(15,21,18)	107.258
				A(15,21,22)	113.647
				A(18,21,22)	113.647

**Table B.2:** Bond lengths and angles for Figure B.2

Bond	Bond length / Å	Bond Angle	°	Bond Angle (cont)	°
R(1,2)	1.539	A(2,1,6)	109.840	A(6,5,19)	109.840
R(1,6)	1.554	A(2,1,7)	113.421	A(13,5,19)	113.472
R(1,7)	1.097	A(2,1,16)	99.299	A(1,6,5)	111.748
R(1,16)	1.541	A(6,1,7)	110.468	A(1,6,14)	109.557
R(2,3)	1.553	A(6,1,16)	109.842	A(1,6,15)	109.584
R(2,8)	1.097	A(7,1,16)	113.471	A(5,6,14)	109.558
R(2,9)	1.099	A(1,2,3)	101.596	A(5,6,15)	109.583
R(3,4)	1.553	A(1,2,8)	114.067	A(14,6,15)	106.679
R(3,10)	1.525	A(1,2,9)	110.121	A(3,10,24)	111.362
R(3,22)	1.602	A(3,2,8)	112.169	A(3,10,25)	111.357
R(4,5)	1.539	A(3,2,9)	111.443	A(3,10,26)	111.134
R(4,11)	1.099	A(8,2,9)	107.454	A(24,10,25)	107.785
R(4,12)	1.097	A(2,3,4)	105.969	A(24,10,26)	107.505
R(5,6)	1.554	A(2,3,10)	114.015	A(25,10,26)	107.505
R(5,13)	1.097	A(2,3,22)	103.312	A(1,16,17)	114.005
R(5,19)	1.541	A(4,3,10)	114.027	A(1,16,18)	110.174
R(6,14)	1.099	A(4,3,22)	103.312	A(1,16,22)	100.740
R(6,15)	1.099	A(10,3,22)	114.971	A(17,16,18)	107.534
R(10,24)	1.097	A(3,4,5)	101.596	A(17,16,22)	112.372
R(10,25)	1.097	A(3,4,11)	111.443	A(18,16,22)	112.017
R(10,26)	1.098	A(3,4,12)	112.174	A(5,19,20)	114.004
R(16,17)	1.097	A(5,4,11)	110.119	A(5,19,21)	110.175
R(16,18)	1.098	A(5,4,12)	114.065	A(5,19,22)	100.740
R(16,22)	1.547	A(11,4,12)	107.454	A(20,19,21)	107.534
R(19,20)	1.097	A(4,5,6)	109.842	A(20,19,22)	112.372
R(19,21)	1.098	A(4,5,13)	113.419	A(21,19,22)	112.017
R(19,22)	1.547	A(4,5,19)	99.299	A(3,22,16)	104.493
R(22,23)	1.095	A(6,5,13)	110.467	A(3,22,19)	104.494
				A(3,22,23)	113.076
				A(16,22,19)	107.140
				A(16,22,23)	113.412
				A(19,22,23)	113.411

**Table B.3:** Bond lengths and angles for Figure B.3

Bond	Bond length / Å	Bond Angle	°	Bond Angle (cont)	°
R(1,2)	1.538	A(2,1,6)	109.9	A(6,5,13)	110.46
R(1,6)	1.553	A(2,1,7)	113.25	A(6,5,19)	109.88
R(1,7)	1.097	A(2,1,16)	99.44	A(13,5,19)	113.42
R(1,16)	1.540	A(6,1,7)	110.46	A(1,6,5)	111.77
R(2,3)	1.555	A(6,1,16)	109.88	A(1,6,14)	109.55
R(2,8)	1.096	A(7,1,16)	113.42	A(1,6,15)	109.58
R(2,9)	1.098	A(1,2,3)	102	A(5,6,14)	109.55
R(3,4)	1.555	A(1,2,8)	114.12	A(5,6,15)	109.58
R(3,10)	1.480	A(1,2,9)	110.25	A(14,6,15)	106.68
R(3,22)	1.633	A(3,2,8)	111.7	A(3,10,24)	120.96
R(4,5)	1.538	A(3,2,9)	111.28	A(3,10,25)	120.99
R(4,11)	1.098	A(8,2,9)	107.51	A(24,10,25)	117.43
R(4,12)	1.096	A(2,3,4)	106.24	A(1,16,17)	113.91
R(5,6)	1.553	A(2,3,10)	114.42	A(1,16,18)	110.24
R(5,13)	1.097	A(2,3,22)	102.57	A(1,16,22)	101.04
R(5,19)	1.540	A(4,3,10)	114.41	A(17,16,18)	107.56
R(6,14)	1.099	A(4,3,22)	102.57	A(17,16,22)	112.12
R(6,15)	1.099	A(10,3,22)	115.21	A(18,16,22)	111.97
R(10,24)	1.087	A(3,4,5)	102	A(5,19,20)	113.91
R(10,25)	1.087	A(3,4,11)	111.27	A(5,19,21)	110.24
R(16,17)	1.097	A(3,4,12)	111.7	A(5,19,22)	101.04
R(16,18)	1.097	A(5,4,11)	110.25	A(20,19,21)	107.56
R(16,22)	1.544	A(5,4,12)	114.13	A(20,19,22)	112.12
R(19,20)	1.097	A(11,4,12)	107.51	A(21,19,22)	111.98
R(19,21)	1.097	A(4,5,6)	109.9	A(3,22,16)	104.11
R(19,22)	1.544	A(4,5,13)	113.25	A(3,22,19)	104.11
R(22,23)	1.093	A(4,5,19)	99.44	A(3,22,23)	112.65
				A(16,22,19)	107.6
				A(16,22,23)	113.73
				A(19,22,23)	113.74

**Table B.4:** Bond lengths and angles for Figure B.4

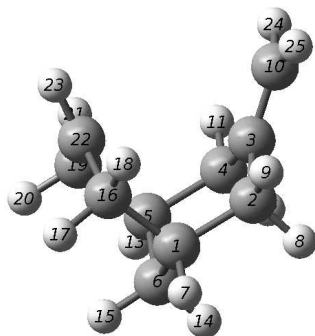


**Figure B.5:** The optimised geometry for structure E in Figure 3.2

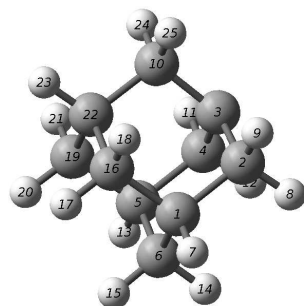


**Figure B.6:** The optimised geometry for structure F in Figure 3.2

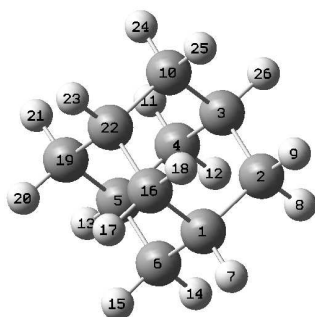


**Figure B.7:** The optimised geometry for structure G in Figure 3.2

Bond	Bond length / Å	Bond Angle	°	Bond Angle (cont)	°
R(1,2)	1.548	A(2,1,6)	109.478	A(13,5,19)	108.368
R(1,6)	1.541	A(2,1,7)	107.952	A(1,6,5)	109.791
R(1,7)	1.098	A(2,1,16)	112.155	A(1,6,14)	110.043
R(1,16)	1.548	A(6,1,7)	109.345	A(1,6,15)	110.072
R(2,3)	1.514	A(6,1,16)	109.490	A(5,6,14)	110.043
R(2,8)	1.102	A(7,1,16)	108.368	A(5,6,15)	110.072
R(2,9)	1.097	A(1,2,3)	112.606	A(14,6,15)	106.778
R(3,4)	1.514	A(1,2,8)	107.576	A(3,10,24)	121.724
R(3,10)	1.337	A(1,2,9)	110.508	A(3,10,25)	121.724
R(4,5)	1.548	A(3,2,8)	108.795	A(24,10,25)	116.553
R(4,11)	1.097	A(3,2,9)	110.426	A(1,16,17)	107.427
R(4,12)	1.102	A(8,2,9)	106.699	A(1,16,18)	110.198
R(5,6)	1.541	A(2,3,4)	114.501	A(1,16,22)	112.535
R(5,13)	1.098	A(2,3,10)	122.743	A(17,16,18)	105.545
R(5,19)	1.548	A(4,3,10)	122.743	A(17,16,22)	110.319
R(6,14)	1.099	A(3,4,5)	112.606	A(18,16,22)	110.539
R(6,15)	1.099	A(3,4,11)	110.426	A(5,19,20)	107.427
R(10,24)	1.088	A(3,4,12)	108.795	A(5,19,21)	110.198
R(10,25)	1.088	A(5,4,11)	110.508	A(5,19,22)	112.535
R(16,17)	1.109	A(5,4,12)	107.576	A(20,19,21)	105.545
R(16,18)	1.099	A(11,4,12)	106.699	A(20,19,22)	110.319
R(16,22)	1.496	A(4,5,6)	109.478	A(21,19,22)	110.539
R(19,20)	1.109	A(4,5,13)	107.952	A(16,22,19)	120.126
R(19,21)	1.099	A(4,5,19)	112.155	A(16,22,23)	119.438
R(19,22)	1.496	A(6,5,13)	109.345	A(19,22,23)	119.438
R(22,23)	1.087	A(6,5,19)	109.490		

**Table B.5:** Bond lengths and angles for Figure B.5

Bond	Bond length / Å	Bond Angle	°	Bond Angle (cont)	°
R(1,2)	1.563	A(2,1,6)	108.866	A(1,6,5)	110.171
R(1,6)	1.544	A(2,1,7)	109.815	A(1,6,14)	110.089
R(1,7)	1.099	A(2,1,16)	108.962	A(1,6,15)	109.868
R(1,16)	1.545	A(6,1,7)	109.847	A(5,6,14)	110.065
R(2,3)	1.507	A(6,1,16)	109.452	A(5,6,15)	109.840
R(2,8)	1.099	A(7,1,16)	109.878	A(14,6,15)	106.749
R(2,9)	1.098	A(1,2,3)	106.103	A(3,10,22)	106.156
R(3,4)	1.506	A(1,2,8)	109.703	A(3,10,24)	111.763
R(3,10)	1.507	A(1,2,9)	109.771	A(3,10,25)	111.792
R(4,5)	1.563	A(3,2,8)	111.770	A(22,10,24)	109.734
R(4,11)	1.099	A(3,2,9)	111.824	A(22,10,25)	109.757
R(4,12)	1.098	A(8,2,9)	107.665	A(24,10,25)	107.636
R(5,6)	1.545	A(2,3,4)	112.958	A(1,16,17)	109.768
R(5,13)	1.099	A(2,3,10)	112.982	A(1,16,18)	110.124
R(5,19)	1.545	A(4,3,10)	113.006	A(1,16,22)	110.206
R(6,14)	1.099	A(3,4,5)	106.128	A(17,16,18)	106.727
R(6,15)	1.099	A(3,4,11)	111.764	A(17,16,22)	109.788
R(10,22)	1.563	A(3,4,12)	111.764	A(18,16,22)	110.165
R(10,24)	1.099	A(5,4,11)	109.762	A(5,19,20)	109.836
R(10,25)	1.099	A(5,4,12)	109.741	A(5,19,21)	110.119
R(16,17)	1.099	A(11,4,12)	107.678	A(5,19,22)	110.203
R(16,18)	1.099	A(4,5,6)	108.844	A(20,19,21)	106.749
R(16,22)	1.545	A(4,5,13)	109.813	A(20,19,22)	109.804
R(19,20)	1.099	A(4,5,19)	108.878	A(21,19,22)	110.069
R(19,21)	1.099	A(6,5,13)	109.905	A(10,22,16)	108.891
R(19,22)	1.544	A(6,5,19)	109.507	A(10,22,19)	108.877
R(22,23)	1.099	A(13,5,19)	109.871	A(10,22,23)	109.826
				A(16,22,19)	109.421
				A(16,22,23)	109.883
				A(19,22,23)	109.920

**Table B.6:** Bond lengths and angles for Figure B.6

Bond	Bond length / Å	Bond Angle	°	Bond Angle (cont)	°
R(1,2)	1.544	A(2,1,6)	109.348	A(1,6,5)	109.731
R(1,6)	1.544	A(2,1,7)	109.598	A(1,6,14)	110.063
R(1,7)	1.098	A(2,1,16)	109.347	A(1,6,15)	110.042
R(1,16)	1.544	A(6,1,7)	109.589	A(5,6,14)	110.070
R(2,3)	1.544	A(6,1,16)	109.363	A(5,6,15)	110.051
R(2,8)	1.099	A(7,1,16)	109.582	A(14,6,15)	106.846
R(2,9)	1.099	A(1,2,3)	109.711	A(3,10,22)	109.729
R(3,4)	1.544	A(1,2,8)	110.056	A(3,10,24)	110.056
R(3,10)	1.544	A(1,2,9)	110.069	A(3,10,25)	110.036
R(3,26)	1.098	A(3,2,8)	110.063	A(22,10,24)	110.090
R(4,5)	1.544	A(3,2,9)	110.058	A(22,10,25)	110.069
R(4,11)	1.099	A(8,2,9)	106.846	A(24,10,25)	106.821
R(4,12)	1.099	A(2,3,4)	109.337	A(1,16,17)	110.070
R(5,6)	1.544	A(2,3,10)	109.331	A(1,16,18)	110.060
R(5,13)	1.098	A(2,3,26)	109.596	A(1,16,22)	109.705
R(5,19)	1.544	A(4,3,10)	109.372	A(17,16,18)	106.865
R(6,14)	1.099	A(4,3,26)	109.590	A(17,16,22)	110.044
R(6,15)	1.099	A(10,3,26)	109.600	A(18,16,22)	110.058
R(10,22)	1.544	A(3,4,5)	109.729	A(5,19,20)	110.054
R(10,24)	1.099	A(3,4,11)	110.077	A(5,19,21)	110.068
R(10,25)	1.099	A(3,4,12)	110.048	A(5,19,22)	109.747
R(16,17)	1.099	A(5,4,11)	110.078	A(20,19,21)	106.833
R(16,18)	1.099	A(5,4,12)	110.046	A(20,19,22)	110.033
R(16,22)	1.544	A(11,4,12)	106.823	A(21,19,22)	110.066
R(19,20)	1.099	A(4,5,6)	109.330	A(10,22,16)	109.326
R(19,21)	1.099	A(4,5,13)	109.624	A(10,22,19)	109.352
R(19,22)	1.544	A(4,5,19)	109.359	A(10,22,23)	109.605
R(22,23)	1.098	A(6,5,13)	109.607	A(16,22,19)	109.348
		A(6,5,19)	109.312	A(16,22,23)	109.608
		A(13,5,19)	109.595	A(19,22,23)	109.587

**Table B.7:** Bond lengths and angles for Figure B.7

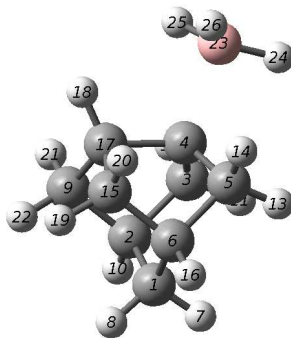


**Figure B.8:** The optimised geometry for surface bound  $\text{BH}_3$  on the diamond  $\{100\}$  surface (Figure 3.4)

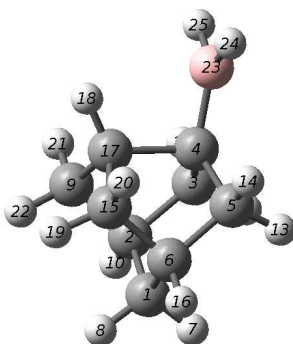


**Figure B.9:** The optimised geometry for surface bound  $\text{BH}_2$  on the diamond  $\{100\}$  surface (Figure 3.4)

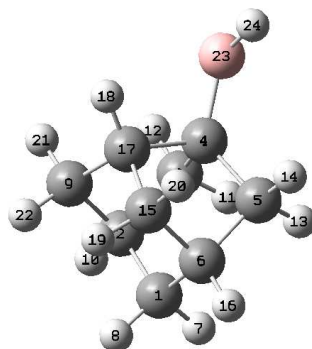


**Figure B.10:** The optimised geometry for surface bound  $\text{BH}$  on the diamond  $\{100\}$  surface (Figure 3.4)

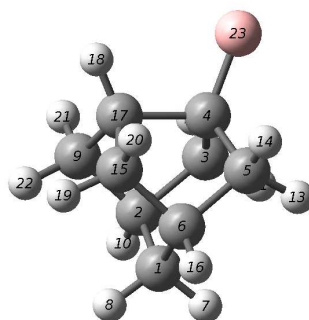


**Figure B.11:** The optimised geometry for surface bound B on the diamond {100} surface (Figure 3.4)

Bond	Bond length / Å	Bond Angle	°	Bond Angle (cont)	°
R(1,2)	1.554	A(2,1,6)	112.059	A(6,5,14)	109.675
R(1,6)	1.554	A(2,1,7)	109.642	A(13,5,14)	108.663
R(1,7)	1.098	A(2,1,8)	109.329	A(1,6,5)	109.637
R(1,8)	1.099	A(6,1,7)	109.642	A(1,6,15)	110.139
R(2,3)	1.560	A(6,1,8)	109.329	A(1,6,16)	110.928
R(2,9)	1.543	A(7,1,8)	106.693	A(5,6,15)	99.312
R(2,10)	1.096	A(1,2,3)	109.636	A(5,6,16)	112.333
R(3,4)	1.515	A(1,2,9)	110.139	A(15,6,16)	113.931
R(3,11)	1.094	A(1,2,10)	110.928	A(2,9,17)	100.593
R(3,12)	1.095	A(3,2,9)	99.312	A(2,9,21)	110.393
R(4,5)	1.515	A(3,2,10)	112.334	A(2,9,22)	113.936
R(4,17)	1.572	A(9,2,10)	113.931	A(17,9,21)	111.930
R(4,23)	1.991	A(2,3,4)	97.542	A(17,9,22)	112.150
R(5,6)	1.560	A(2,3,11)	114.687	A(21,9,22)	107.813
R(5,13)	1.094	A(2,3,12)	109.676	A(6,15,17)	100.593
R(5,14)	1.095	A(4,3,11)	112.782	A(6,15,19)	113.935
R(6,15)	1.543	A(4,3,12)	113.240	A(6,15,20)	110.393
R(6,16)	1.096	A(11,3,12)	108.663	A(17,15,19)	112.150
R(9,17)	1.550	A(3,4,5)	110.807	A(17,15,20)	111.930
R(9,21)	1.096	A(3,4,17)	107.449	A(19,15,20)	107.813
R(9,22)	1.096	A(3,4,23)	110.187	A(4,17,9)	102.541
R(15,17)	1.550	A(5,4,17)	107.450	A(4,17,15)	102.541
R(15,19)	1.096	A(5,4,23)	110.180	A(4,17,18)	114.409
R(15,20)	1.096	A(17,4,23)	110.700	A(9,17,15)	107.529
R(17,18)	1.091	A(4,5,6)	97.542	A(9,17,18)	114.262
R(23,24)	1.204	A(4,5,13)	112.782	A(15,17,18)	114.262
R(23,25)	1.203	A(4,5,14)	113.240	A(4,23,24)	96.856
R(23,26)	1.203	A(6,5,13)	114.687	A(4,23,25)	98.428
				A(4,23,26)	98.433
				A(24,23,25)	118.234
				A(24,23,26)	118.234
				A(25,23,26)	117.952

**Table B.8:** Bond lengths and angles for Figure B.8

Bond	Bond length / Å	Bond Angle	°	Bond Angle (cont)	°
R(1,2)	1.552	A(2,1,6)	111.938	A(6,5,13)	113.613
R(1,6)	1.552	A(2,1,7)	109.456	A(6,5,14)	110.342
R(1,7)	1.095	A(2,1,8)	109.571	A(13,5,14)	107.554
R(1,8)	1.095	A(6,1,7)	109.456	A(1,6,5)	109.933
R(2,3)	1.536	A(6,1,8)	109.571	A(1,6,15)	109.888
R(2,9)	1.535	A(7,1,8)	106.709	A(1,6,16)	110.442
R(2,10)	1.093	A(1,2,3)	109.933	A(5,6,15)	99.370
R(3,4)	1.548	A(1,2,9)	109.888	A(5,6,16)	113.494
R(3,11)	1.093	A(1,2,10)	110.442	A(15,6,16)	113.228
R(3,12)	1.094	A(3,2,9)	99.370	A(2,9,17)	101.419
R(4,5)	1.548	A(3,2,10)	113.494	A(2,9,21)	110.415
R(4,17)	1.651	A(9,2,10)	113.228	A(2,9,22)	114.040
R(4,23)	1.537	A(2,3,4)	102.029	A(17,9,21)	111.974
R(5,6)	1.536	A(2,3,11)	113.613	A(17,9,22)	111.250
R(5,13)	1.093	A(2,3,12)	110.342	A(21,9,22)	107.752
R(5,14)	1.094	A(4,3,11)	111.414	A(6,15,17)	101.419
R(6,15)	1.535	A(4,3,12)	111.926	A(6,15,19)	114.040
R(6,16)	1.093	A(11,3,12)	107.554	A(6,15,20)	110.415
R(9,17)	1.541	A(3,4,5)	106.965	A(17,15,19)	111.250
R(9,21)	1.093	A(3,4,17)	102.474	A(17,15,20)	111.974
R(9,22)	1.093	A(3,4,23)	120.686	A(19,15,20)	107.752
R(15,17)	1.541	A(5,4,17)	102.474	A(4,17,9)	103.380
R(15,19)	1.093	A(5,4,23)	120.686	A(4,17,15)	103.379
R(15,20)	1.093	A(17,4,23)	99.669	A(4,17,18)	115.195
R(17,18)	1.093	A(4,5,6)	102.029	A(9,17,15)	108.311
R(23,24)	1.196	A(4,5,13)	111.414	A(9,17,18)	112.846
R(23,25)	1.196	A(4,5,14)	111.926	A(15,17,18)	112.846
				A(4,23,24)	120.571
				A(4,23,25)	120.570
				A(24,23,25)	118.571

**Table B.9:** Bond lengths and angles for Figure B.9

Bond	Bond length / Å	Bond Angle	°	Bond Angle (cont)	°
R(1,2)	1.552	A(2,1,6)	111.938	A(4,5,14)	111.926
R(1,6)	1.552	A(2,1,7)	109.456	A(6,5,13)	113.613
R(1,7)	1.095	A(2,1,8)	109.571	A(6,5,14)	110.342
R(1,8)	1.095	A(6,1,7)	109.456	A(13,5,14)	107.554
R(2,3)	1.536	A(6,1,8)	109.571	A(1,6,5)	109.933
R(2,9)	1.535	A(7,1,8)	106.709	A(1,6,15)	109.888
R(2,10)	1.093	A(1,2,3)	109.933	A(1,6,16)	110.442
R(3,4)	1.548	A(1,2,9)	109.888	A(5,6,15)	99.370
R(3,11)	1.093	A(1,2,10)	110.442	A(5,6,16)	113.494
R(3,12)	1.094	A(3,2,9)	99.370	A(15,6,16)	113.228
R(4,5)	1.548	A(3,2,10)	113.494	A(2,9,17)	101.419
R(4,17)	1.651	A(9,2,10)	113.228	A(2,9,21)	110.415
R(4,23)	1.537	A(2,3,4)	102.029	A(2,9,22)	114.040
R(5,6)	1.536	A(2,3,11)	113.613	A(17,9,21)	111.974
R(5,13)	1.093	A(2,3,12)	110.342	A(17,9,22)	111.250
R(5,14)	1.094	A(4,3,11)	111.414	A(21,9,22)	107.752
R(6,15)	1.535	A(4,3,12)	111.926	A(6,15,17)	101.419
R(6,16)	1.093	A(11,3,12)	107.554	A(6,15,19)	114.040
R(9,17)	1.541	A(3,4,5)	106.965	A(6,15,20)	110.415
R(9,21)	1.093	A(3,4,17)	102.474	A(17,15,19)	111.250
R(9,22)	1.093	A(3,4,23)	120.686	A(17,15,20)	111.974
R(15,17)	1.541	A(5,4,17)	102.474	A(19,15,20)	107.752
R(15,19)	1.093	A(5,4,23)	120.686	A(4,17,9)	103.380
R(15,20)	1.093	A(17,4,23)	99.669	A(4,17,15)	103.379
R(17,18)	1.093	A(4,5,6)	102.029	A(4,17,18)	115.195
R(23,24)	1.196	A(4,5,13)	111.414	A(9,17,15)	108.311
				A(9,17,18)	112.846
				A(15,17,18)	112.846
				A(4,23,24)	120.571

**Table B.10:** Bond lengths and angles for Figure B.10

Bond	Bond length / Å	Bond Angle	°	Bond Angle (cont)	°
R(1,2)	1.555	A(2,1,6)	112.09	A(4,5,13)	111.49
R(1,6)	1.555	A(2,1,7)	109.55	A(4,5,14)	112.46
R(1,7)	1.098	A(2,1,8)	109.43	A(6,5,13)	114.14
R(1,8)	1.098	A(6,1,7)	109.55	A(6,5,14)	110.54
R(2,3)	1.540	A(6,1,8)	109.43	A(13,5,14)	107.51
R(2,9)	1.538	A(7,1,8)	106.64	A(1,6,5)	109.87
R(2,10)	1.097	A(1,2,3)	109.87	A(1,6,15)	109.87
R(3,4)	1.564	A(1,2,9)	109.87	A(1,6,16)	110.52
R(3,11)	1.095	A(1,2,10)	110.52	A(5,6,15)	99.68
R(3,12)	1.098	A(3,2,9)	99.68	A(5,6,16)	113.03
R(4,5)	1.564	A(3,2,10)	113.03	A(15,6,16)	113.41
R(4,17)	1.621	A(9,2,10)	113.41	A(2,9,17)	101.21
R(4,23)	1.543	A(2,3,4)	100.74	A(2,9,21)	110.46
R(5,6)	1.540	A(2,3,11)	114.14	A(2,9,22)	113.95
R(5,13)	1.095	A(2,3,12)	110.54	A(17,9,21)	111.92
R(5,14)	1.098	A(4,3,11)	111.49	A(17,9,22)	111.67
R(6,15)	1.538	A(4,3,12)	112.46	A(21,9,22)	107.65
R(6,16)	1.097	A(11,3,12)	107.51	A(6,15,17)	101.21
R(9,17)	1.546	A(3,4,5)	106.62	A(6,15,19)	113.95
R(9,21)	1.097	A(3,4,17)	103.59	A(6,15,20)	110.46
R(9,22)	1.096	A(3,4,23)	115.78	A(17,15,19)	111.67
R(15,17)	1.546	A(5,4,17)	103.59	A(17,15,20)	111.92
R(15,19)	1.096	A(5,4,23)	115.78	A(19,15,20)	107.65
R(15,20)	1.097	A(17,4,23)	110.12	A(4,17,9)	103.59
R(17,18)	1.095	A(4,5,6)	100.74	A(4,17,15)	103.59
				A(4,17,18)	114.1
				A(9,17,15)	108.07
				A(9,17,18)	113.29
				A(15,17,18)	113.29

**Table B.11:** Bond lengths and angles for Figure B.11

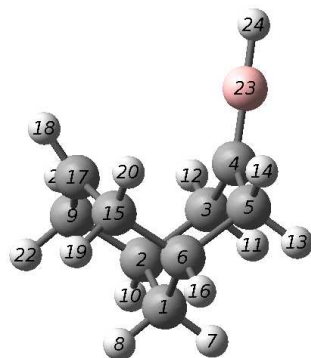


**Figure B.12:** The optimised geometry for unsaturated ring opened boron intermediate for boron inclusion on diamond {100} surface (Figure 3.4)

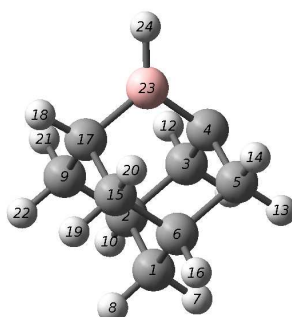


**Figure B.13:** The optimised geometry for boron containing radical intermediate involved in boron inclusion on diamond {100} surface (Figure 3.4)

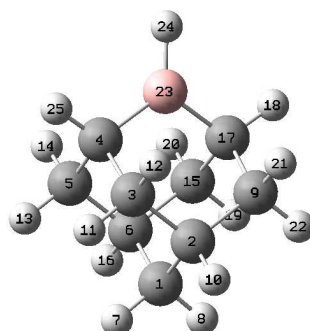


**Figure B.14:** The optimised geometry for boron containing intermediate involved in boron inclusion on diamond {100} surface (Figure 3.4)

Bond	Bond length / Å	Bond Angle	°	Bond Angle (cont)	°
R(1,2)	1.541	A(2,1,6)	109.832	A(6,5,14)	109.794
R(1,6)	1.541	A(2,1,7)	110.033	A(13,5,14)	106.308
R(1,7)	1.099	A(2,1,8)	110.072	A(1,6,5)	109.501
R(1,8)	1.099	A(6,1,7)	110.033	A(1,6,15)	109.507
R(2,3)	1.548	A(6,1,8)	110.072	A(1,6,16)	109.263
R(2,9)	1.547	A(7,1,8)	106.755	A(5,6,15)	112.513
R(2,10)	1.099	A(1,2,3)	109.501	A(5,6,16)	107.562
R(3,4)	1.525	A(1,2,9)	109.507	A(15,6,16)	108.428
R(3,11)	1.103	A(1,2,10)	109.263	A(2,9,17)	112.778
R(3,12)	1.097	A(3,2,9)	112.513	A(2,9,21)	110.152
R(4,5)	1.525	A(3,2,10)	107.562	A(2,9,22)	107.314
R(4,23)	1.387	A(9,2,10)	108.428	A(17,9,21)	110.450
R(5,6)	1.548	A(2,3,4)	112.024	A(17,9,22)	110.445
R(5,13)	1.103	A(2,3,11)	107.807	A(21,9,22)	105.399
R(5,14)	1.097	A(2,3,12)	109.795	A(6,15,17)	112.778
R(6,15)	1.547	A(4,3,11)	108.992	A(6,15,19)	107.314
R(6,16)	1.099	A(4,3,12)	111.675	A(6,15,20)	110.152
R(9,17)	1.497	A(11,3,12)	106.308	A(17,15,19)	110.445
R(9,21)	1.099	A(3,4,5)	113.949	A(17,15,20)	110.449
R(9,22)	1.109	A(3,4,23)	123.033	A(19,15,20)	105.399
R(15,17)	1.497	A(5,4,23)	123.018	A(9,17,15)	120.441
R(15,19)	1.109	A(4,5,6)	112.024	A(9,17,18)	119.191
R(15,20)	1.099	A(4,5,13)	108.992	A(15,17,18)	119.191
R(17,18)	1.087	A(4,5,14)	111.675		
R(23,24)	1.176	A(6,5,13)	107.807		

**Table B.12:** Bond lengths and angles for Figure B.12

Bond	Bond length Å	Bond Angle	°	Bond Angle (cont)	°
R(1,2)	1.542	A(2,1,6)	109.945	A(13,5,14)	107.054
R(1,6)	1.542	A(2,1,7)	110.098	A(1,6,5)	108.921
R(1,7)	1.099	A(2,1,8)	109.926	A(1,6,15)	109.606
R(1,8)	1.099	A(6,1,7)	110.098	A(1,6,16)	109.834
R(2,3)	1.562	A(6,1,8)	109.926	A(5,6,15)	109.897
R(2,9)	1.544	A(7,1,8)	106.799	A(5,6,16)	109.272
R(2,10)	1.099	A(1,2,3)	108.921	A(15,6,16)	109.297
R(3,4)	1.519	A(1,2,9)	109.606	A(2,9,17)	111.241
R(3,11)	1.100	A(1,2,10)	109.834	A(2,9,21)	109.881
R(3,12)	1.099	A(3,2,9)	109.898	A(2,9,22)	109.579
R(4,5)	1.519	A(3,2,10)	109.272	A(17,9,21)	110.522
R(4,23)	1.545	A(9,2,10)	109.296	A(17,9,22)	109.277
R(5,6)	1.562	A(2,3,4)	106.971	A(21,9,22)	106.210
R(5,13)	1.100	A(2,3,11)	109.687	A(6,15,17)	111.241
R(5,14)	1.099	A(2,3,12)	109.528	A(6,15,19)	109.578
R(6,15)	1.544	A(4,3,11)	111.400	A(6,15,20)	109.881
R(6,16)	1.099	A(4,3,12)	112.198	A(17,15,19)	109.278
R(9,17)	1.560	A(11,3,12)	107.054	A(17,15,20)	110.522
R(9,21)	1.099	A(3,4,5)	111.896	A(19,15,20)	106.210
R(9,22)	1.100	A(3,4,23)	111.709	A(9,17,15)	108.673
R(15,17)	1.560	A(5,4,23)	111.711	A(9,17,18)	109.662
R(15,19)	1.100	A(4,5,6)	106.971	A(9,17,23)	107.140
R(15,20)	1.099	A(4,5,13)	111.400	A(15,17,18)	109.662
R(17,18)	1.098	A(4,5,14)	112.198	A(15,17,23)	107.143
R(17,23)	1.590	A(6,5,13)	109.687	A(18,17,23)	114.386
R(23,24)	1.200	A(6,5,14)	109.528	A(4,23,17)	108.476
				A(4,23,24)	127.471
				A(17,23,24)	124.053

**Table B.13:** Bond lengths and angles for Figure B.13

Bond	Bond length / Å	Bond Angle	°	Bond Angle (cont)	°
R(1,2)	1.541	A(2,1,6)	109.569	A(6,5,13)	109.848
R(1,6)	1.541	A(2,1,7)	110.099	A(6,5,14)	109.880
R(1,7)	1.099	A(2,1,8)	110.098	A(13,5,14)	106.336
R(1,8)	1.099	A(6,1,7)	110.099	A(1,6,5)	109.410
R(2,3)	1.543	A(6,1,8)	110.098	A(1,6,15)	109.407
R(2,9)	1.543	A(7,1,8)	106.844	A(1,6,16)	109.487
R(2,10)	1.099	A(1,2,3)	109.410	A(5,6,15)	110.486
R(3,4)	1.559	A(1,2,9)	109.407	A(5,6,16)	109.020
R(3,11)	1.100	A(1,2,10)	109.487	A(15,6,16)	109.014
R(3,12)	1.099	A(3,2,9)	110.486	A(2,9,17)	110.635
R(4,5)	1.559	A(3,2,10)	109.020	A(2,9,21)	109.873
R(4,23)	1.576	A(9,2,10)	109.014	A(2,9,22)	109.837
R(4,25)	1.097	A(2,3,4)	110.634	A(17,9,21)	110.512
R(5,6)	1.543	A(2,3,11)	109.848	A(17,9,22)	109.568
R(5,13)	1.100	A(2,3,12)	109.880	A(21,9,22)	106.323
R(5,14)	1.099	A(4,3,11)	109.548	A(6,15,17)	110.636
R(6,15)	1.543	A(4,3,12)	110.503	A(6,15,19)	109.837
R(6,16)	1.099	A(11,3,12)	106.336	A(6,15,20)	109.873
R(9,17)	1.559	A(3,4,5)	108.570	A(17,15,19)	109.568
R(9,21)	1.099	A(3,4,23)	107.362	A(17,15,20)	110.512
R(9,22)	1.101	A(3,4,25)	109.581	A(19,15,20)	106.323
R(15,17)	1.559	A(5,4,23)	107.364	A(9,17,15)	108.610
R(15,19)	1.101	A(5,4,25)	109.581	A(9,17,18)	109.582
R(15,20)	1.099	A(23,4,25)	114.218	A(9,17,23)	107.356
R(17,18)	1.097	A(4,5,6)	110.634	A(15,17,18)	109.582
R(17,23)	1.576	A(4,5,13)	109.548	A(15,17,23)	107.357
R(23,24)	1.201	A(4,5,14)	110.503	A(18,17,23)	114.192
				A(4,23,17)	112.854
				A(4,23,24)	123.562
				A(17,23,24)	123.584

**Table B.14:** Bond lengths and angles for Figure B.14

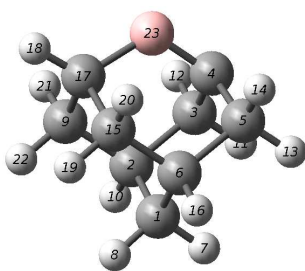


**Figure B.15:** The optimised geometry for atomic boron inclusion on diamond {100} surface (Figure 3.4)

Bond	Bond length / Å	Bond Angle	°	Bond Angle (cont)	°
R(1,2)	1.542	A(2,1,6)	109.945	A(13,5,14)	107.054
R(1,6)	1.542	A(2,1,7)	110.098	A(1,6,5)	108.921
R(1,7)	1.099	A(2,1,8)	109.926	A(1,6,15)	109.606
R(1,8)	1.099	A(6,1,7)	110.098	A(1,6,16)	109.834
R(2,3)	1.562	A(6,1,8)	109.926	A(5,6,15)	109.897
R(2,9)	1.544	A(7,1,8)	106.799	A(5,6,16)	109.272
R(2,10)	1.099	A(1,2,3)	108.921	A(15,6,16)	109.297
R(3,4)	1.519	A(1,2,9)	109.606	A(2,9,17)	111.241
R(3,11)	1.100	A(1,2,10)	109.834	A(2,9,21)	109.881
R(3,12)	1.099	A(3,2,9)	109.898	A(2,9,22)	109.579
R(4,5)	1.519	A(3,2,10)	109.272	A(17,9,21)	110.522
R(4,23)	1.545	A(9,2,10)	109.296	A(17,9,22)	109.277
R(5,6)	1.562	A(2,3,4)	106.971	A(21,9,22)	106.210
R(5,13)	1.100	A(2,3,11)	109.687	A(6,15,17)	111.241
R(5,14)	1.099	A(2,3,12)	109.528	A(6,15,19)	109.578
R(6,15)	1.544	A(4,3,11)	111.400	A(6,15,20)	109.881
R(6,16)	1.099	A(4,3,12)	112.198	A(17,15,19)	109.278
R(9,17)	1.560	A(11,3,12)	107.054	A(17,15,20)	110.522
R(9,21)	1.099	A(3,4,5)	111.896	A(19,15,20)	106.210
R(9,22)	1.100	A(3,4,23)	111.709	A(9,17,15)	108.673
R(15,17)	1.560	A(5,4,23)	111.711	A(9,17,18)	109.662
R(15,19)	1.100	A(4,5,6)	106.971	A(9,17,23)	107.140
R(15,20)	1.099	A(4,5,13)	111.400	A(15,17,18)	109.662
R(17,18)	1.098	A(4,5,14)	112.198	A(15,17,23)	107.143
R(17,23)	1.590	A(6,5,13)	109.687	A(18,17,23)	114.386
R(23,24)	1.200	A(6,5,14)	109.528	A(4,23,17)	108.476
				A(4,23,24)	127.471
				A(17,23,24)	124.053

**Table B.15:** Bond lengths and angles for Figure B.15

## Appendix C

# Canonical Transition State Theory rate coefficients for inclusion of carbon and boron species into the {100} diamond reconstructed surface

Simple canonical transition state theory has been used in conjunction with the calculated energetics for incorporation of carbon and boron species into a {100} reconstructed diamond surface taken from Chapter 3. 3D modelling of the high pressure microwave system (Section 5.6), indicates that the atomic hydrogen density is  $\sim 2 \times 10^{13} \text{ cm}^{-3}$  for typical CVD growth of diamond. Using this value for the abundance of Hydrogen atoms, the deduced difference in the rate of the Hydrogen abstraction reaction compared with all of the unimolecular processes implies that, on the timescale of a bimolecular reaction, the insertion and the reverse unimolecular reactions may occur numerous times.

For example, at 1200 K, the lifetime with respect to the the hydrogen abstraction reaction is calculated at  $4.34 \times 10^{-2} \text{ s}$  whilst the lifetime for the carbon ring opening and closing species are  $9.43 \times 10^{-11} \text{ s}$  and  $7.35 \times 10^{-9} \text{ s}$ , respectively.

Temperature / K	Hydrogen abstraction	Carbon	
		ring opening	ring closing
200	5.72E-17	1.45E+00	3.17E-05
300	1.70E-15	1.11E+04	3.94E+00
400	1.04E-14	1.03E+06	1.32E+03
500	3.33E-14	1.59E+07	4.25E+04
600	7.68E-14	1.00E+08	4.27E+05
700	1.46E-13	3.75E+08	2.22E+06
800	2.44E-13	1.02E+09	7.63E+06
900	3.74E-13	2.21E+09	1.99E+07
1000	5.38E-13	4.13E+09	4.30E+07
1100	7.37E-13	6.90E+09	8.07E+07
1200	9.72E-13	1.06E+10	1.36E+08
1300	1.24E-12	1.52E+10	2.12E+08
1400	1.55E-12	2.08E+10	3.11E+08
1500	1.90E-12	2.73E+10	4.32E+08
1600	2.28E-12	3.46E+10	5.77E+08
1700	2.70E-12	4.27E+10	7.44E+08
1800	3.15E-12	5.14E+10	9.34E+08
1900	3.65E-12	6.08E+10	1.14E+09
2000	4.17E-12	7.07E+10	1.37E+09

**Table C.1:** The bimolecular reaction rate coefficients (in  $\text{cm}^3\text{s}^{-1}$ ) for surface activation reactions by hydrogen abstraction and the RRKM unimolecular rate coefficient (in  $\text{s}^{-1}$ ) for carbon inclusion via the ring opening and closing mechanism.

Temperature / K	BH			Atomic B
	direct insertion	ring opening	ring closing	direct insertion
200	7.15E+02	2.40E-09	5.55E+04	4.65E-02
300	5.66E+05	2.73E-02	8.06E+06	1.05E+03
400	1.61E+07	1.04E+02	9.50E+07	1.65E+05
500	1.20E+08	1.55E+04	4.15E+08	3.50E+06
600	4.61E+08	4.49E+05	1.11E+09	2.71E+07
700	1.20E+09	5.03E+06	2.24E+09	1.17E+08
800	2.47E+09	3.11E+07	3.79E+09	3.54E+08
900	4.34E+09	1.29E+08	5.72E+09	8.36E+08
1000	6.79E+09	4.04E+08	7.95E+09	1.67E+09
1100	9.81E+09	1.03E+09	1.04E+10	2.93E+09
1200	1.33E+10	2.25E+09	1.31E+10	4.69E+09
1300	1.73E+10	4.36E+09	1.58E+10	6.99E+09
1400	2.16E+10	7.70E+09	1.86E+10	9.84E+09
1500	2.62E+10	1.26E+10	2.15E+10	1.32E+10
1600	3.10E+10	1.95E+10	2.43E+10	1.72E+10
1700	3.60E+10	2.85E+10	2.72E+10	2.16E+10
1800	4.10E+10	4.00E+10	3.00E+10	2.65E+10
1900	4.62E+10	5.43E+10	3.27E+10	3.18E+10
2000	5.14E+10	7.14E+10	3.54E+10	3.74E+10

**Table C.2:** RRKM unimolecular reaction rate coefficients for boron species (in  $\text{s}^{-1}$ ) incorporating in the  $\{100\}$  reconstruction via a direct insertion process; the ring opening / closing mechanism analogous to the carbon mechanism and direct insertion of atomic boron bound on the surface.

# Appendix D

## Thermochemical Data for $\text{BH}_x$ , $x = 0 - 4$

Thermodynamic studies of  $\text{B}_y\text{H}_x$  species have been collated by Yu & Bauer [3]. The temperature range over which species have been studied however is below the temperature window of CVD growth of boron doped diamond. Thermodynamic data ( $C_v$ ,  $S$  and  $H$ ) for  $\text{BH}_x$  species have been calculated using DFT methods as described in Chapter 3 for a larger temperature range than previously reported. The consistency of the generated data was tested by comparison with previously published data [3]. All extended datasets fitted the published data within the limits of the accuracy of the calculations used.

Non-SI units have been used for easy integration into the NASA polynomial typically used in this field. The values found for these species have been used by Mankelevich in his modelling in his modelling of  $\text{BH}_x$  species degradation under CVD conditions.

Temperature / K	$C_v$ / cal mol <sup>-1</sup>	$S$ / cal mol <sup>-1</sup>	$H$ / kcal mol <sup>-1</sup>	Temperature / K	$C_v$ / cal mol <sup>-1</sup>	$S$ / cal mol <sup>-1</sup>	$H$ / kcal mol <sup>-1</sup>
298	2.981	33.085	133.843	2100	2.981	42.785	142.796
300	2.981	33.118	133.853	2200	2.981	43.016	143.293
400	2.981	34.547	134.350	2300	2.981	43.237	143.789
500	2.981	35.656	134.847	2400	2.981	43.449	144.286
600	2.981	36.561	135.344	2500	2.981	43.651	144.783
700	2.981	37.327	135.841	2600	2.981	43.846	145.280
800	2.981	37.991	136.338	2700	2.981	44.034	145.777
900	2.981	38.576	136.834	2800	2.981	44.214	146.274
1000	2.981	39.099	137.331	2900	2.981	44.389	146.771
1100	2.981	39.573	137.828	3000	2.981	44.557	147.267
1200	2.981	40.005	138.324	3100	2.981	44.720	147.764
1300	2.981	40.403	138.821	3200	2.981	44.878	148.261
1400	2.981	40.771	139.318	3300	2.981	45.031	148.757
1500	2.981	41.114	139.815	3400	2.981	45.179	149.254
1600	2.981	41.434	140.312	3500	2.981	45.323	149.751
1700	2.981	41.735	140.809	3600	2.981	45.463	150.248
1800	2.981	42.019	141.306	3700	2.981	45.599	150.745
1900	2.981	42.288	141.802	3800	2.981	45.732	151.242
2000	2.981	42.543	142.299	3900	2.981	45.861	151.739
				4000	2.981	45.986	152.235

**Table D.1:** Calculated thermodynamic data for atomic boron.

Temperature / K	$C_v$ / cal mol <sup>-1</sup>	$S$ / cal mol <sup>-1</sup>	$H$ / kcal mol <sup>-1</sup>	Temperature / K	$C_v$ / cal mol <sup>-1</sup>	$S$ / cal mol <sup>-1</sup>	$H$ / kcal mol <sup>-1</sup>
298	4.970	40.984	105.808	2100	6.553	55.752	119.961
300	4.970	41.030	105.822	2200	6.584	56.150	120.817
400	4.992	43.034	106.519	2300	6.612	56.531	121.675
500	5.057	44.598	107.219	2400	6.638	56.898	122.536
600	5.167	45.891	107.929	2500	6.660	57.250	123.400
700	5.307	47.004	108.651	2600	6.680	57.590	124.265
800	5.459	47.988	109.388	2700	6.699	57.917	125.133
900	5.609	48.874	110.140	2800	6.716	58.234	126.003
1000	5.750	49.681	110.907	2900	6.731	58.539	126.874
1100	5.877	50.425	111.687	3000	6.744	58.835	127.746
1200	5.990	51.114	112.480	3100	6.757	59.121	128.620
1300	6.090	51.757	113.282	3200	6.768	59.399	129.495
1400	6.178	52.359	114.095	3300	6.779	59.669	130.371
1500	6.255	52.925	114.915	3400	6.789	59.931	131.248
1600	6.322	53.459	115.743	3500	6.798	60.185	132.126
1700	6.380	53.964	116.577	3600	6.806	60.433	133.005
1800	6.432	54.444	117.416	3700	6.813	60.674	133.885
1900	6.477	54.901	118.260	3800	6.821	60.909	134.766
2000	6.517	55.336	119.109	3900	6.827	61.138	135.647
				4000	6.833	61.361	136.528

**Table D.2:** Calculated thermodynamic data for BH.

Temperature / K	$C_v$ / cal mol <sup>-1</sup>	$S$ / cal mol <sup>-1</sup>	$H$ / kcal mol <sup>-1</sup>	Temperature / K	$C_v$ / cal mol <sup>-1</sup>	$S$ / cal mol <sup>-1</sup>	$H$ / kcal mol <sup>-1</sup>
298	6.292	44.941	76.004	2100	10.868	65.111	96.025
300	6.299	44.996	76.020	2200	10.949	65.711	97.315
400	6.668	47.430	76.867	2300	11.021	66.288	98.612
500	7.042	49.401	77.751	2400	11.086	66.843	99.916
600	7.421	51.081	78.673	2500	11.145	67.378	101.227
700	7.804	52.560	79.633	2600	11.198	67.894	102.543
800	8.184	53.892	80.631	2700	11.246	68.392	103.864
900	8.547	55.112	81.666	2800	11.289	68.875	105.189
1000	8.884	56.239	82.737	2900	11.329	69.341	106.519
1100	9.191	57.290	83.840	3000	11.365	69.793	107.852
1200	9.465	58.275	84.972	3100	11.398	70.232	109.189
1300	9.709	59.201	86.129	3200	11.428	70.657	110.529
1400	9.925	60.076	87.310	3300	11.455	71.070	111.872
1500	10.115	60.904	88.511	3400	11.481	71.472	113.218
1600	10.282	61.691	89.730	3500	11.504	71.863	114.566
1700	10.429	62.439	90.964	3600	11.526	72.243	115.916
1800	10.560	63.153	92.212	3700	11.546	72.614	117.268
1900	10.675	63.834	93.473	3800	11.565	72.975	118.622
2000	10.777	64.486	94.744	3900	11.582	73.327	119.978
				4000	11.598	73.671	121.336

**Table D.3:** Calculated thermodynamic data for BH<sub>2</sub>.

Temperature / K	$C_v$ / cal mol <sup>-1</sup>	$S$ / cal mol <sup>-1</sup>	$H$ / kcal mol <sup>-1</sup>	Temperature / K	$C_v$ / cal mol <sup>-1</sup>	$S$ / cal mol <sup>-1</sup>	$H$ / kcal mol <sup>-1</sup>
298	6.540	44.929	21.319	2100	16.112	70.630	26.641
300	6.556	44.987	21.336	2200	16.251	71.476	28.458
400	7.460	47.563	22.234	2300	16.374	72.289	30.288
500	8.450	49.778	23.228	2400	16.485	73.073	32.130
600	9.411	51.766	24.321	2500	16.584	73.829	33.982
700	10.310	53.592	25.506	2600	16.673	74.559	35.843
800	11.136	55.288	26.777	2700	16.754	75.265	37.713
900	11.881	56.878	28.128	2800	16.827	75.948	39.591
1000	12.543	58.374	29.548	2900	16.894	76.609	41.476
1100	13.126	59.787	31.031	3000	16.954	77.251	43.367
1200	13.636	61.124	32.569	3100	17.009	77.872	45.264
1300	14.080	62.393	34.154	3200	17.060	78.476	47.167
1400	14.467	63.598	35.780	3300	17.106	79.063	49.074
1500	14.805	64.745	37.443	3400	17.149	79.634	50.985
1600	15.099	65.838	39.137	3500	17.188	80.189	52.901
1700	15.356	66.882	40.859	3600	17.225	80.730	54.820
1800	15.582	67.880	42.605	3700	17.258	81.257	56.743
1900	15.781	68.835	44.372	3800	17.289	81.770	58.669
2000	15.957	69.751	46.157	3900	17.318	82.272	60.599
				4000	17.345	82.761	62.530

**Table D.4:** Calculated thermodynamic data for BH<sub>3</sub>.

Temperature / K	$C_v$ / cal mol <sup>-1</sup>	$S$ / cal mol <sup>-1</sup>	$H$ / kcal mol <sup>-1</sup>	Temperature / K	$C_v$ / cal mol <sup>-1</sup>	$S$ / cal mol <sup>-1</sup>	$H$ / kcal mol <sup>-1</sup>
298	8.017	50.294	56.501	2100	21.786	83.871	91.567
300	8.052	50.361	56.521	2200	21.949	84.981	93.953
400	9.822	53.492	57.614	2300	22.095	86.048	96.355
500	11.475	56.308	58.879	2400	22.225	87.076	98.769
600	12.964	58.897	60.301	2500	22.341	88.067	101.197
700	14.290	61.303	61.863	2600	22.446	89.023	103.634
800	15.457	63.554	63.550	2700	22.540	89.947	106.083
900	16.475	65.669	65.347	2800	22.626	90.840	108.540
1000	17.355	67.661	67.238	2900	22.703	91.705	111.005
1100	18.112	69.541	69.211	3000	22.774	92.544	113.478
1200	18.762	71.318	71.254	3100	22.838	93.357	115.957
1300	19.320	73.002	73.358	3200	22.897	94.146	118.442
1400	19.800	74.599	75.513	3300	22.950	94.912	120.934
1500	20.214	76.116	77.713	3400	23.000	95.658	123.430
1600	20.572	77.561	79.952	3500	23.046	96.383	125.931
1700	20.883	78.938	82.224	3600	23.088	97.088	128.436
1800	21.155	80.253	84.524	3700	23.126	97.776	130.946
1900	21.392	81.511	86.851	3800	23.162	98.446	133.459
2000	21.601	82.716	89.199	3900	23.196	99.100	135.976
				4000	23.227	99.738	138.496

**Table D.5:** Calculated thermodynamic data for BH<sub>4</sub>.

## Appendix E

# Raman spectroscopy of thin diamond films grown for the Taguchi optimisation of the CVD microwave plasma reactor

Chapter 5 discusses the use of the Taguchi approach as a method for optimising the process conditions for the CVD growth of diamond. Within this chapter, the Raman spectra of the individual samples grown under the conditions specified within Table 5.1 are presented and Figure E.17 shows a typical multi-component curve fit to the experimental data.

Solid-state Raman spectroscopy is based upon the inelastic scattering of photons caused by structural vibrational features. Upon illumination, samples are excited into a virtual state from which subsequent relaxations to the initial state results in the scattering of light at the initial wavelength. This is commonly referred to as Rayleigh scattering. However, a small percentage of relaxations from the virtual state leads to the internal excitation or relaxation of vibrational states resulting in scattering of lower (Stokes radiation) and higher (anti-Stokes radiation) frequencies of light, respectively. The frequencies of the Stokes and anti-Stokes radiation depends upon the composition of the probed sample and Figure E.1 shows the common  $sp^3$  and  $sp^2$  features present in CVD diamond from diamond and graphite.

Raman spectra were recorded using a Renishaw inVia (488 nm  $Ar^+$ , 2400 l / mm grating) spectrometer and at Stokes shifted wavenumbers between 1000 –

2000  $\text{cm}^{-1}$ . All spectra presented have had a background correction (typically an exponential function) applied to remove the underlying photoluminescence emission.

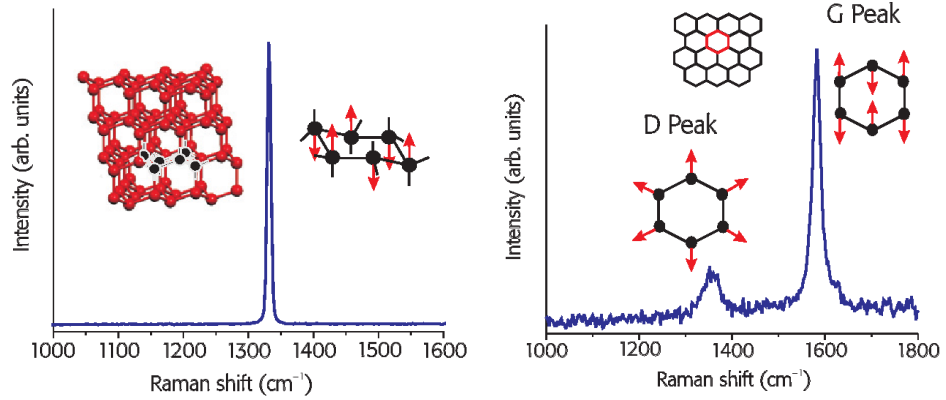


**Figure E.1:** Raman spectra of (a) diamond (b) graphite with insets showing the respective nuclear motions associated with each band, from ref [4].

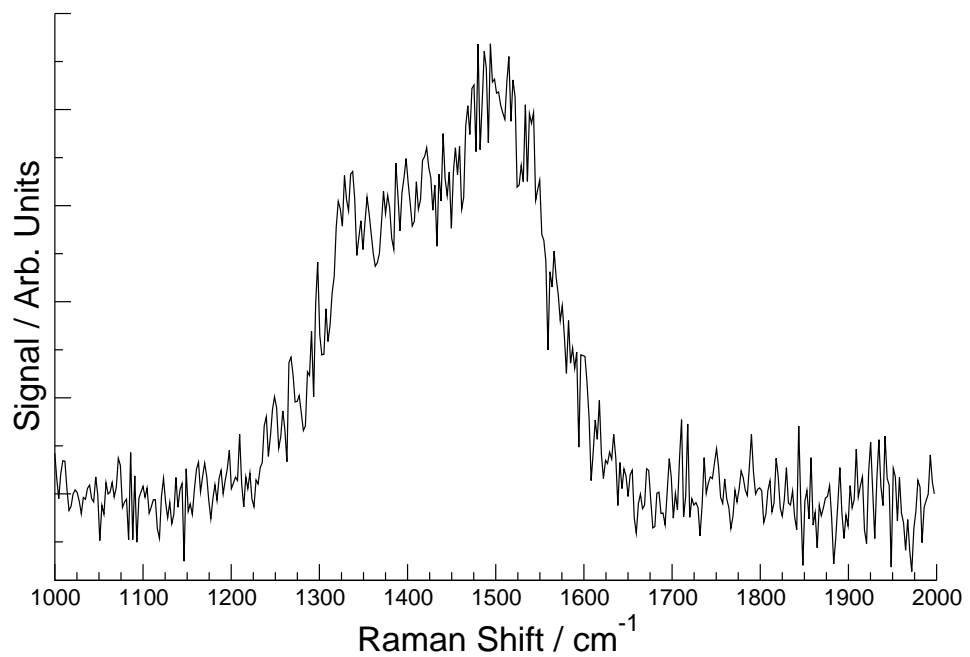


**Figure E.2:** Raman spectrum of sample 1.

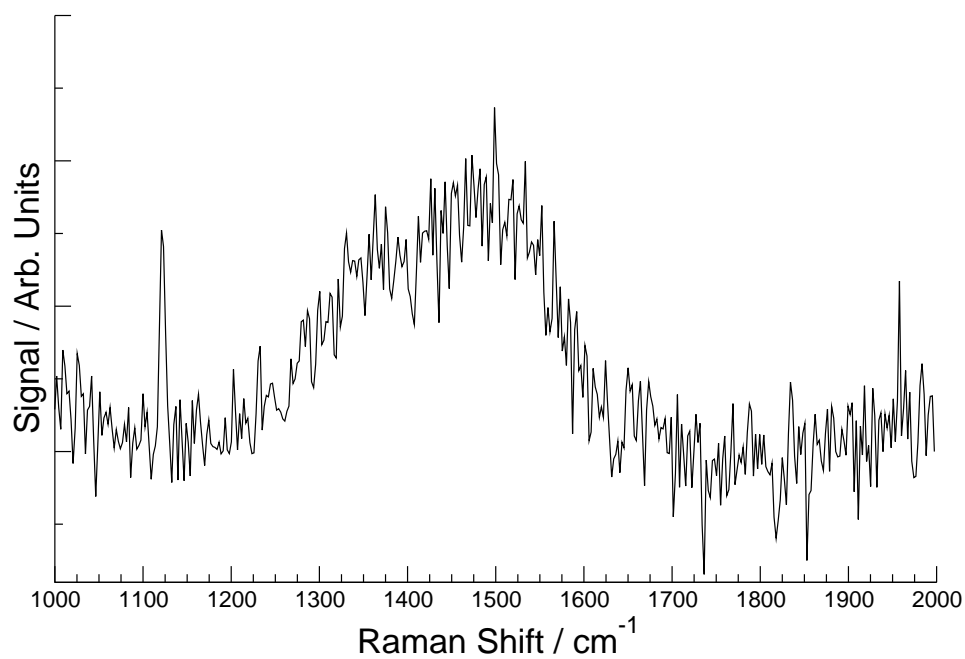


**Figure E.3:** Raman spectrum of sample 2.

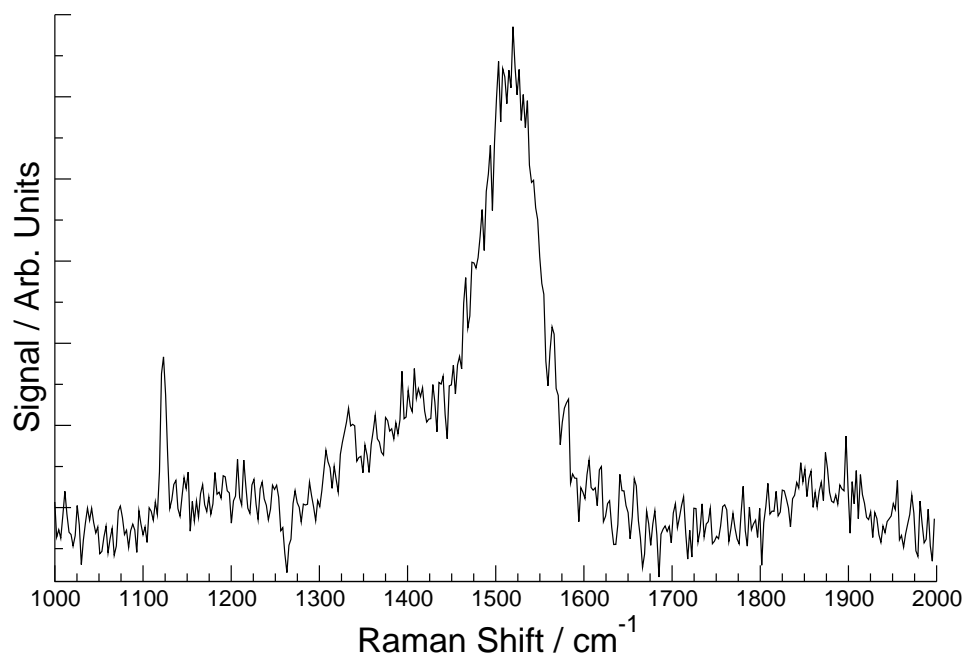


**Figure E.4:** Raman spectrum of sample 3.

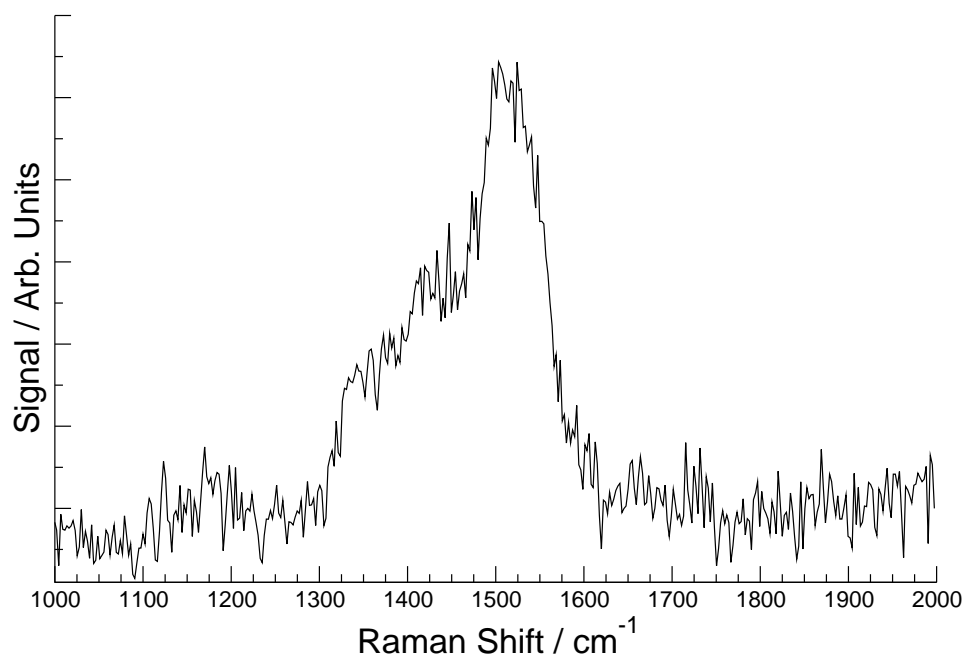


**Figure E.5:** Raman spectrum of sample 4.

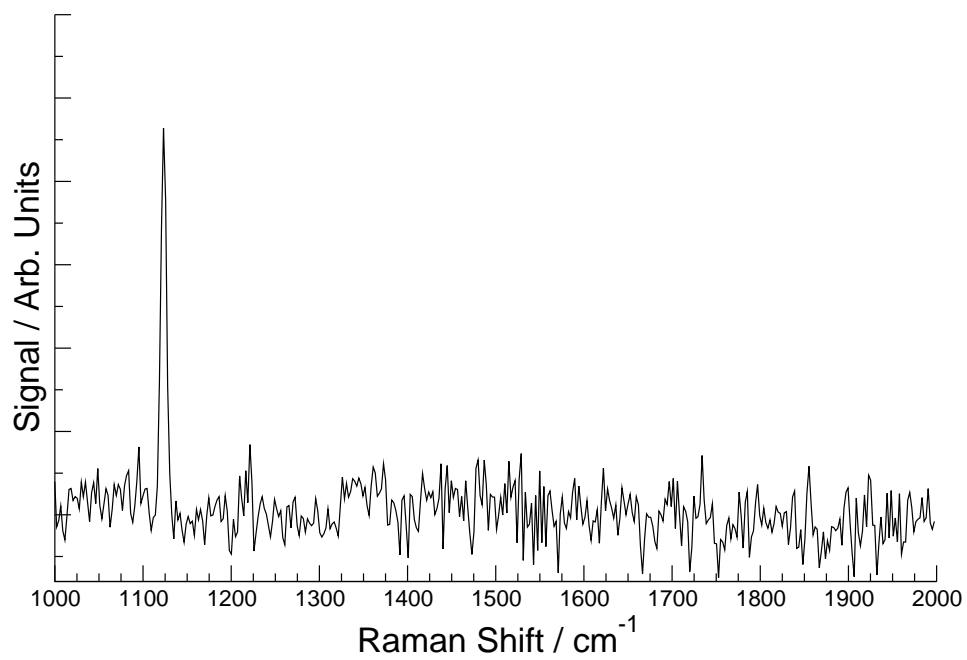


**Figure E.6:** Raman spectrum of sample 5.

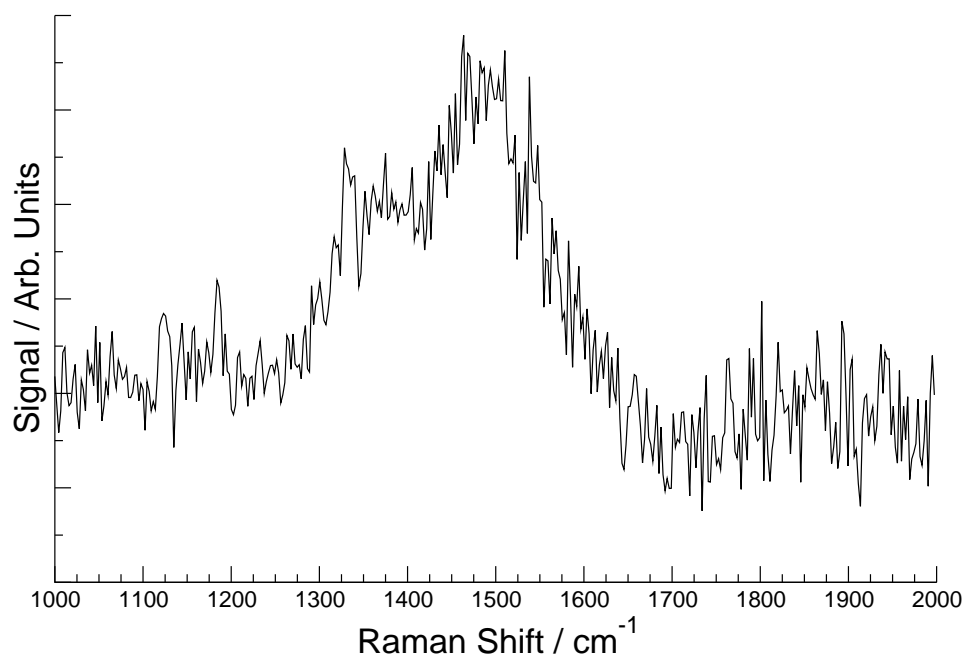


**Figure E.7:** Raman spectrum of sample 6.

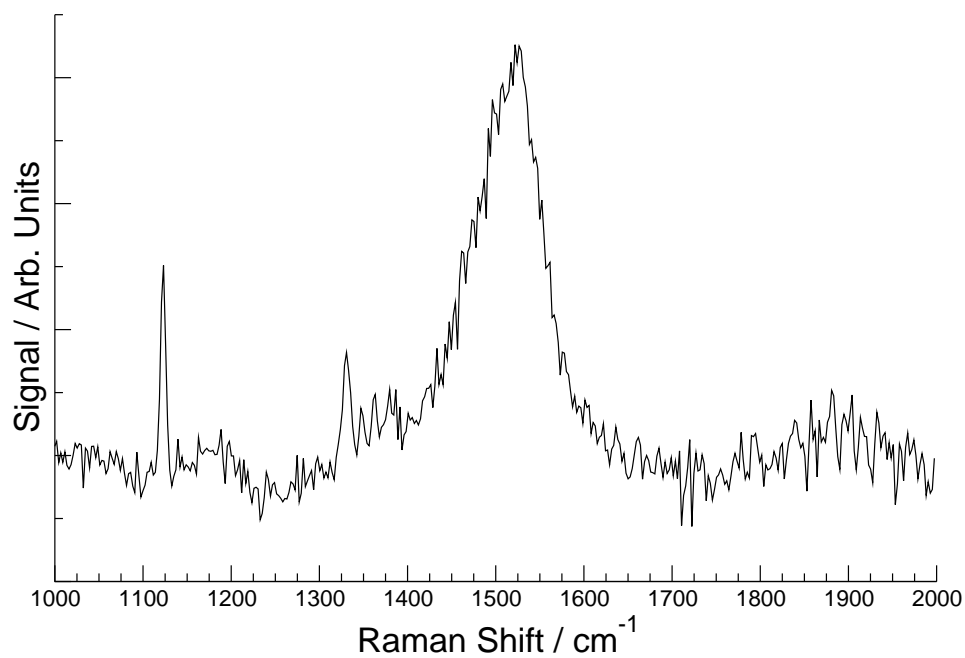


**Figure E.8:** Raman spectrum of sample 7.

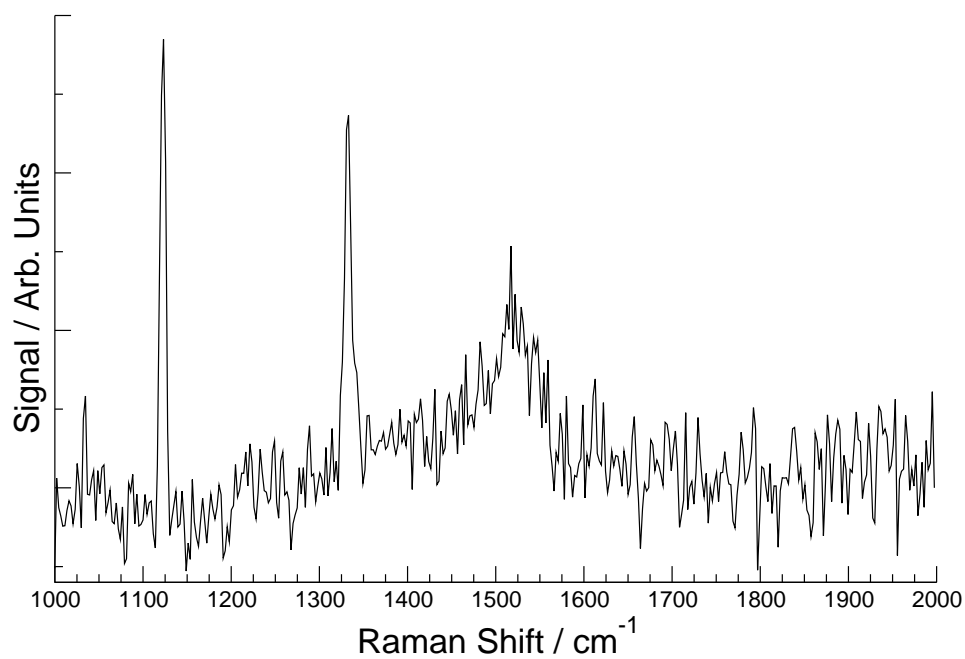


**Figure E.9:** Raman spectrum of sample 8.

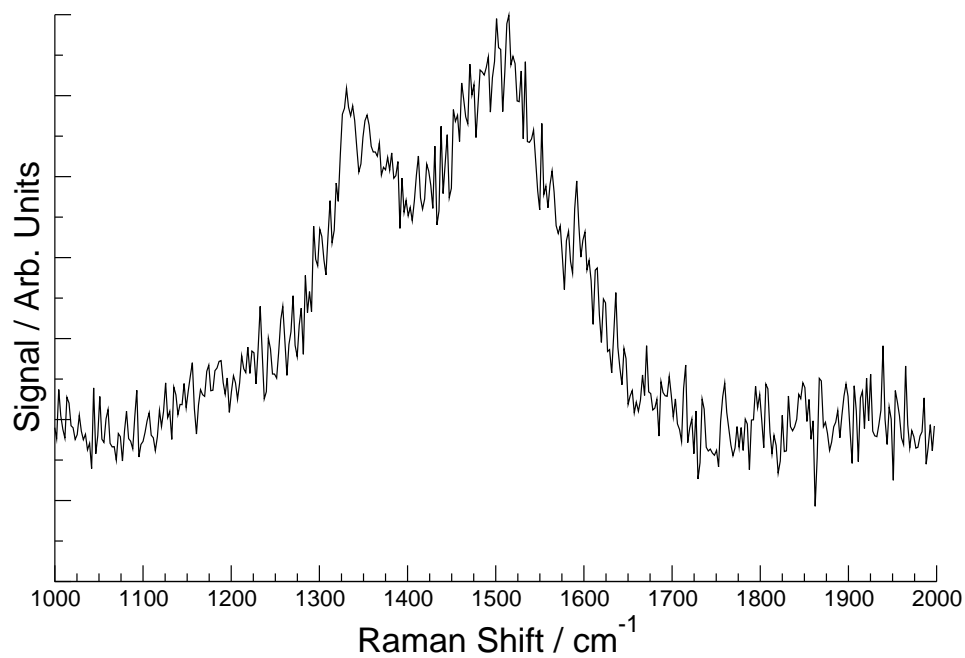


**Figure E.10:** Raman spectrum of sample 9.

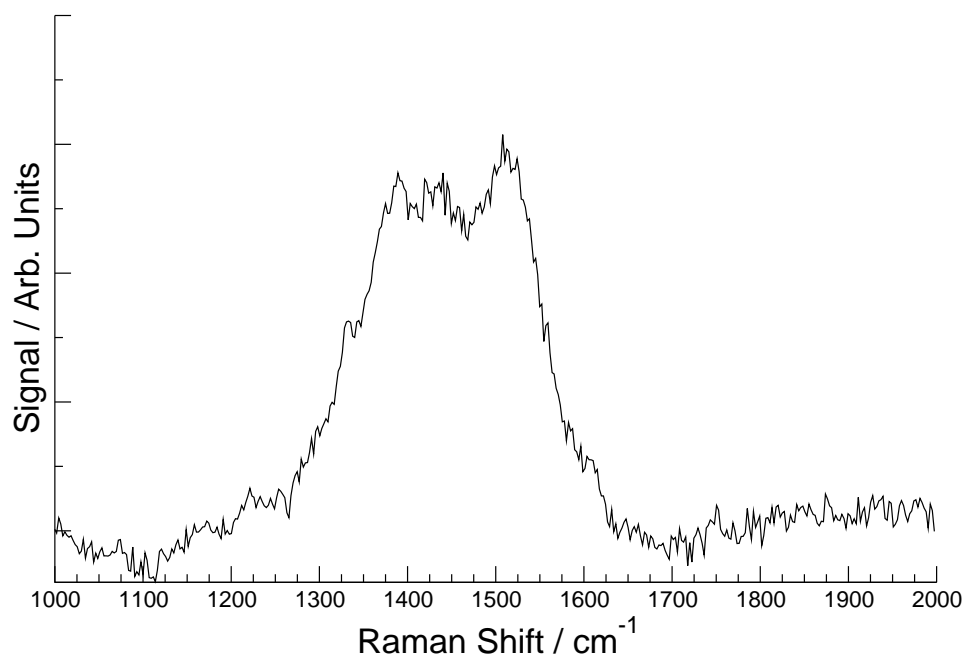


**Figure E.11:** Raman spectrum of sample 10.

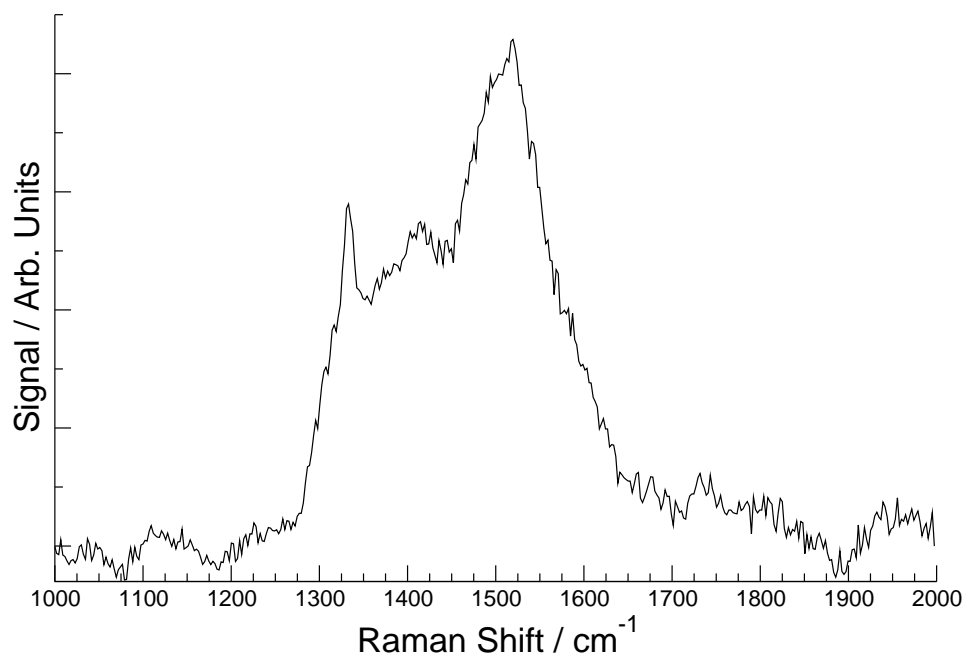


**Figure E.12:** Raman spectrum of sample 11.

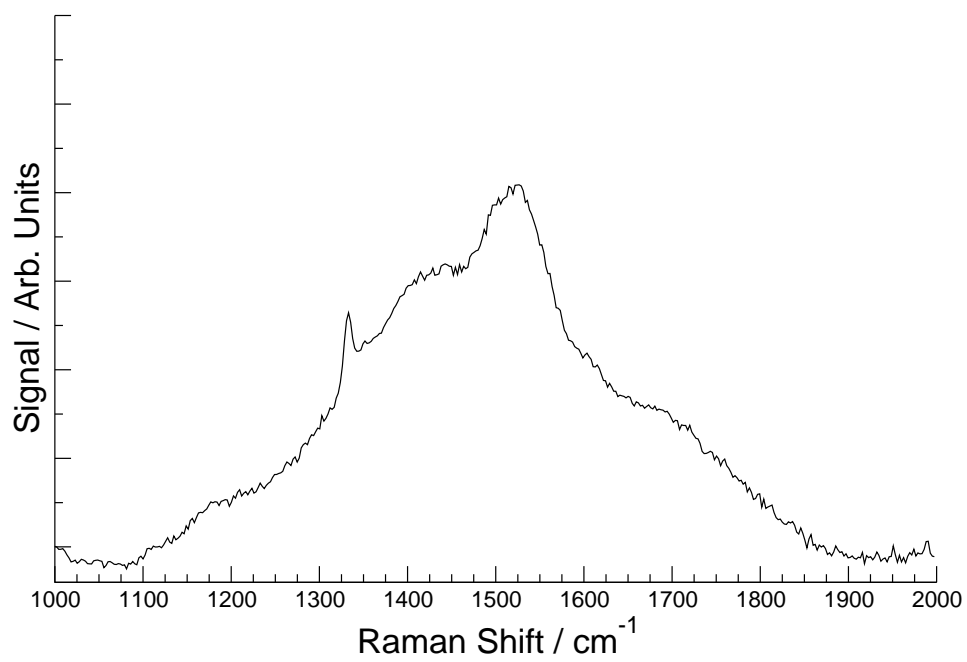


**Figure E.13:** Raman spectrum of sample 12.

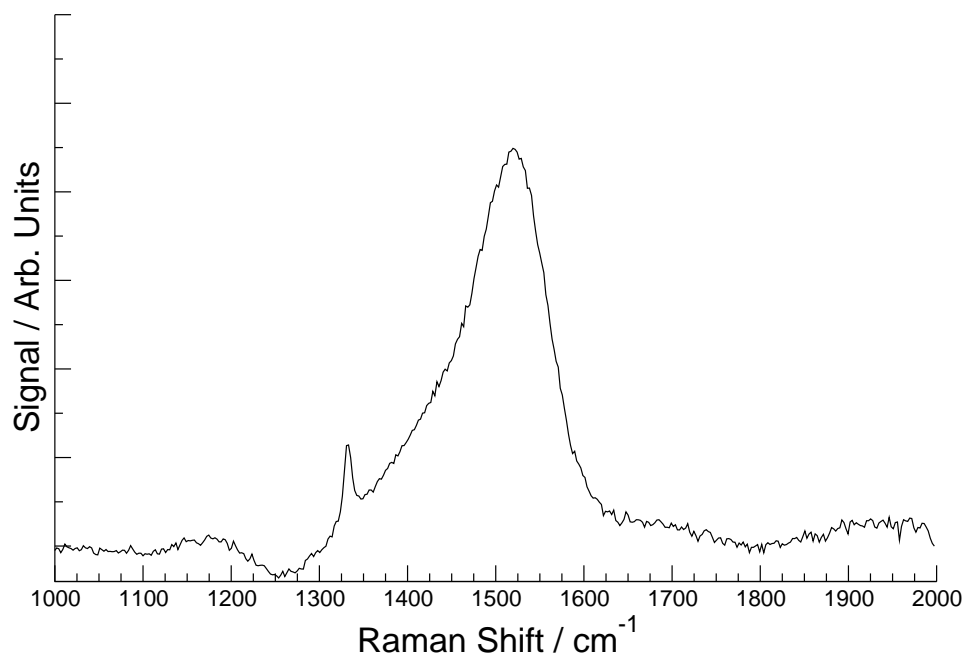


**Figure E.14:** Raman spectrum of sample 13.

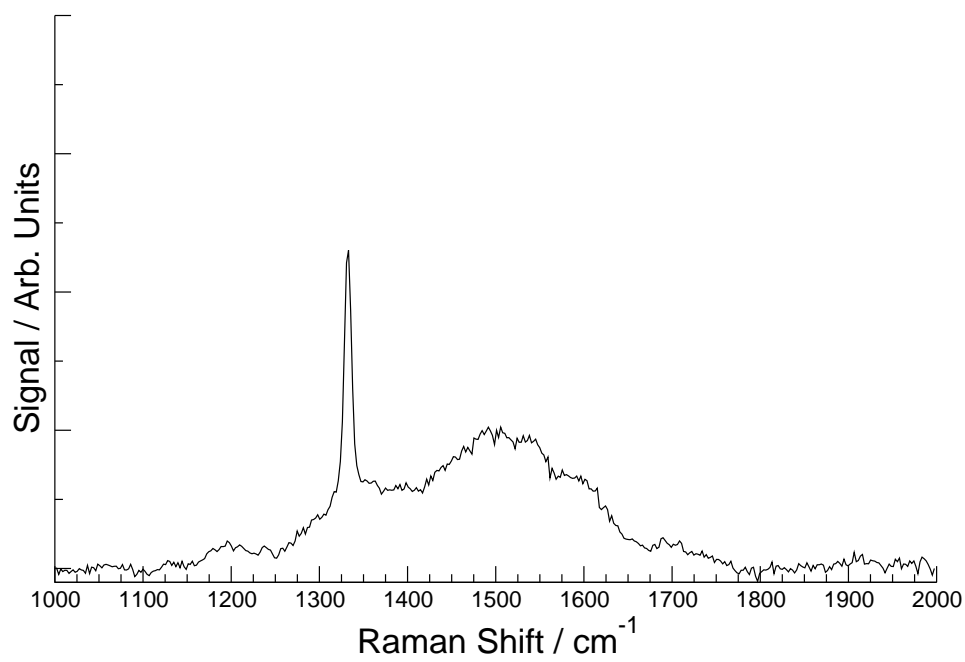


**Figure E.15:** Raman spectrum of sample 14.

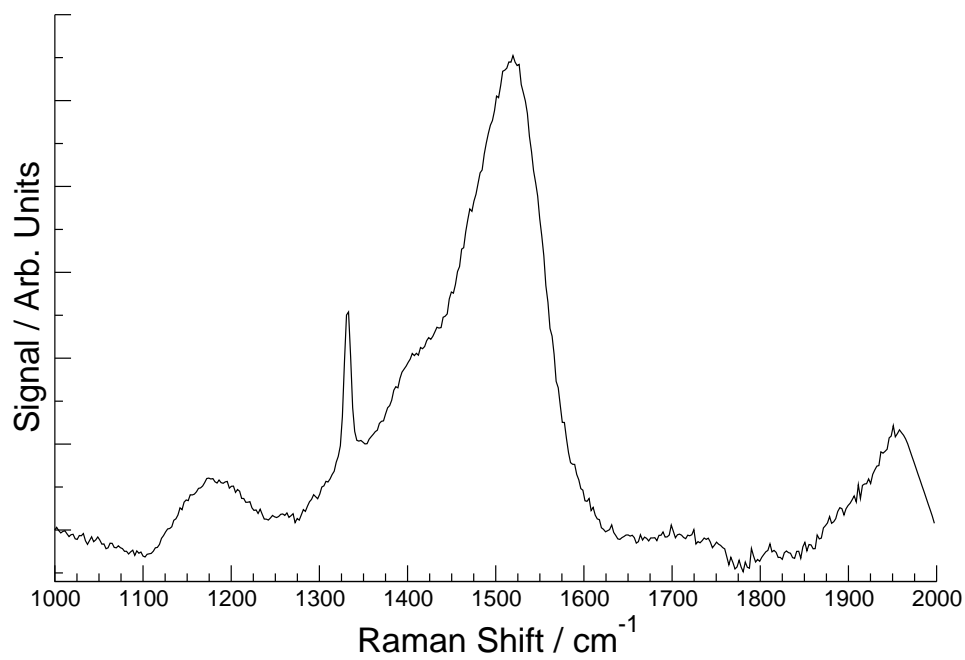


**Figure E.16:** Raman spectrum of sample 15.

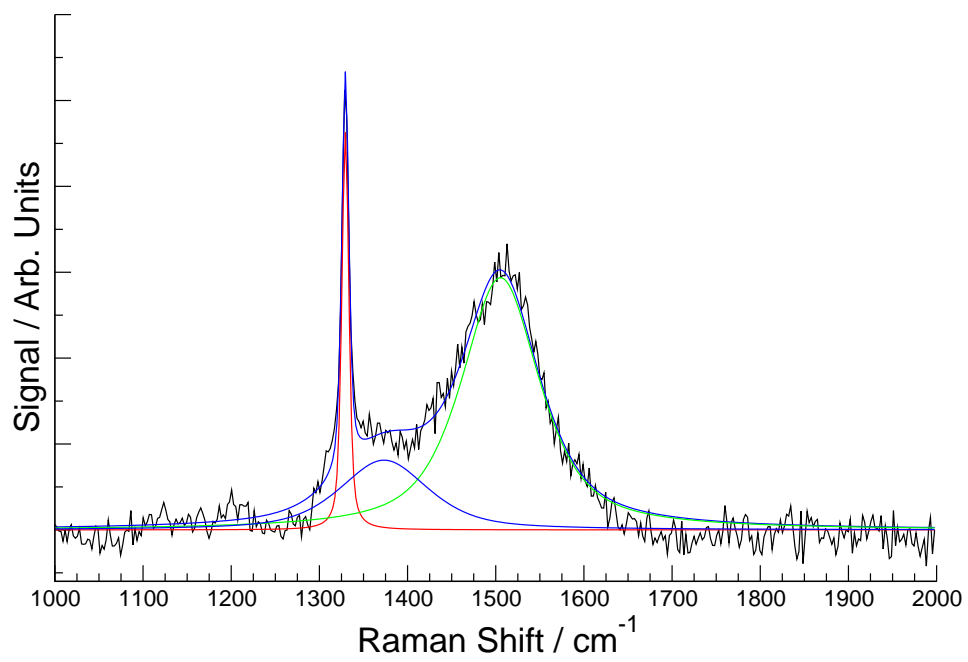


**Figure E.17:** Raman spectrum of sample 16, with curve fitting highlighted.

## Appendix F

### Photos of Plasma ball as a function of process conditions

This appendix displays images of the plasma ball recorded as a function of process conditions. The observed variations in the size of the luminescence ball were used for estimating the  $C_2$  number densities reported in Chapter 5. Images were taken with a Sony DFW-VL500 camera, using Unibrain's Fire-i frame capture software.

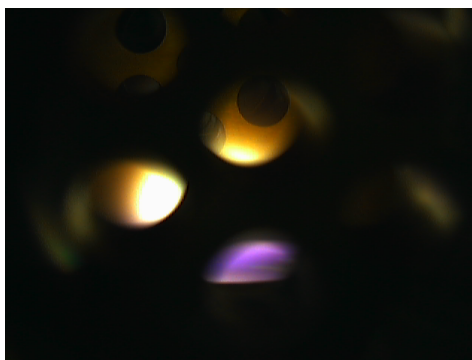


**Figure F.1:** Side image of plasma sustained under the standard conditions of a gas composition of 4.4%  $CH_4$ ; 7 % Ar; balance of  $H_2$  at a pressure of 150 Torr sustained at 1.5 kW.

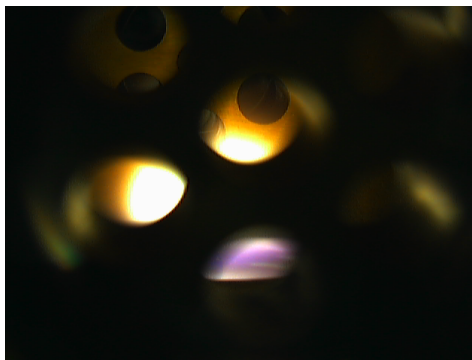


**Figure F.2:** Side image of plasma sustained with a gas composition of 8.8%  $\text{CH}_4$ ; 7 % Ar; balance of  $\text{H}_2$  at a pressure of 150 Torr sustained at 1.5 kW.



**Figure F.3:** Side image of plasma sustained with a gas composition of 2%  $\text{CH}_4$ ; 7 % Ar; balance of  $\text{H}_2$  at a pressure of 150 Torr sustained at 1.5 kW.



**Figure F.4:** Side image of plasma sustained with a gas composition of 7 % Ar; balance of  $\text{H}_2$  at a pressure of 150 Torr sustained at 1.5 kW.

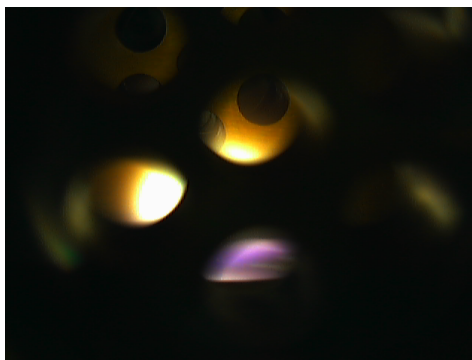


**Figure F.5:** Side image of plasma sustained with a gas composition of 4.4% CH<sub>4</sub>, 7 % Ar; balance of H<sub>2</sub> at a pressure of 175 Torr sustained at 1.5 kW.

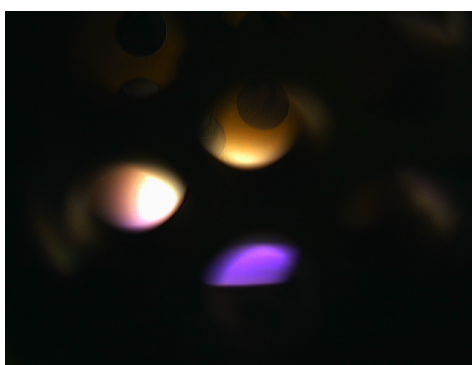


**Figure F.6:** Side image of plasma sustained with a gas composition of 4.4% CH<sub>4</sub>, 7 % Ar; balance of H<sub>2</sub> at a pressure of 100 Torr sustained at 1.5 kW.

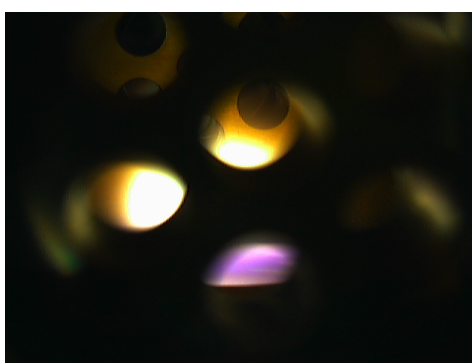


**Figure F.7:** Side image of plasma sustained with a gas composition of 4.4% CH<sub>4</sub>, 7 % Ar; balance of H<sub>2</sub> at a pressure of 150 Torr sustained at 1.75 kW.



**Figure F.8:** Side image of plasma sustained with a gas composition of 4.4% CH<sub>4</sub>, 7 % Ar; balance of H<sub>2</sub> at a pressure of 150 Torr sustained at 1.0 kW.



**Figure F.9:** Side image of plasma sustained with a gas composition of 4.4% CH<sub>4</sub>, 7 % Ar; balance of H<sub>2</sub> at a pressure of 150 Torr sustained at 1.25 kW.

## Bibliography

- [1] M. J. Frisch, G. W. Trucks, H. B. Schlegel, G. E. Scuseria, M. A. Robb, J. R. Cheeseman, J. A. Montgomery Jr., T. Vreven, K. N. Kudin, J. C. Burant, J. M. Millam, S. S. Iyengar, J. Tomasi, V. Barone, B. Mennucci, M. Cossi, G. Scalmani, N. Rega, G. A. Petersson, H. Nakatsuji, M. Hada, M. Ehara, K. Toyota, R. Fukuda, J. Hasegawa, M. Ishida, T. Nakajima, Y. Honda, O. Kitao, H. Nakai, M. Klene, X. Li, J. E. Knox, H. P. Hratchian, J. B. Cross, C. Adamo, J. Jaramillo, R. Gomperts, R. E. Stratmann, O. Yazyev, A. J. Austin, R. Cammi, C. Pomelli, J. W. Ochterski, P. Y. Ayala, K. Morokuma, G. A. Voth, P. Salvador, J. J. Dannenberg, V. G. Zakrzewski, S. Dapprich, A. D. Daniels, M. C. Strain, O. Farkas, D. K. Malick, A. D. Rabuck, K. Raghavachari, J. B. Foresman, J. V. Ortiz, Q. Cui, A. G. Baboul, S. Clifford, J. Cioslowski, B. B. Stefanov, G. Liu, A. Liashenko, P. Piskorz, I. Komaromi, R. L. Martin, D. J. Fox, T. Keith, M. A. Al-Laham, C. Y. Peng, A. Nanayakkara, M. Challacombe, P. M. W. Gill, B. Johnson, W. Chen, M. W. Wong, C. Gonzalez, and J. A. Pople, *Gaussian 03, Revision B.04*, Gaussian, Inc., Pittsburgh PA, 2003.
- [2] R. D. Amos, A. Bernhardsson, A. Berning, P. Celani, D. L. Cooper, M. J. O. Deegan, A. J. Dobbyn, F. Eckert, C. Hampel, G. Hetzer, P. J. Knowles, T. Korona, R. Lindh, A. W. Lloyd, S. J. McNicholas, F. R. Manby, W. Meyer, M. E. Mura, A. Nicklass, P. Palmieri, R. Pitzer, G. Rauhut, M. Schütz, U. Schumann, H. Stoll, A. J. Stone, R. Tarroni, T. Thorsteinsson, and H.-J. Werner, *MOLPRO, a package of ab initio programs designed by H.-J. Werner and P. J. Knowles, Version 2002.1*, 2002.
- [3] C. L. Yu and S. H. Bauer, *J. Phys. Chem. Ref. Data* **27**, 807 (1998).
- [4] J. Filik, *Spectroscopy Europe* **17**, 10 (2005).